

*In situ* investigation of the rapid  
thermal reaction of Cu-In-Ga  
precursors to  $\text{Cu}(\text{In},\text{Ga})\text{Se}_2$   
thin-film solar cell absorbers

im Fachbereich Physik der  
Freien Universität Berlin eingereichte

**Dissertation**

zur Erlangung des akademischen Grades  
Doktor der Naturwissenschaften

- Dr. rer. nat. -

von

**Jan-Peter Bäcker**



Erstgutachter: Prof. Dr. Klaus Lips (Betreuer)  
Zweitgutachter: Prof. Dr. Rutger Schlatmann  
Disputation: 9. Juli 2018



# Contents

<b>Introduction</b>	<b>1</b>
<b>1. Basics of Cu(In,Ga)Se<sub>2</sub> absorber material and preparation</b>	<b>5</b>
1.1. The role of Ga in Cu(In,Ga)Se <sub>2</sub> with respect to material and electrical properties . . . . .	5
1.1.1. Crystal structure of Cu(In,Ga)Se <sub>2</sub> . . . . .	6
1.1.2. Cu(In,Ga)Se <sub>2</sub> -based solar cells and the role of Ga therein . . . . .	7
1.2. Binary and ternary phase diagrams of the Cu-In-Ga-Se system . . . . .	12
1.2.1. Phase diagrams of the Cu-In-Ga system without Se . . . . .	12
1.2.2. Phase diagrams of the Cu-In-Se system . . . . .	14
1.3. Types of Se supply and known effects on CIGS growth . . . . .	16
1.4. Sequential growth of Cu(In,Ga)Se <sub>2</sub> . . . . .	19
1.4.1. Growth of CuInSe <sub>2</sub> . . . . .	20
1.4.2. Growth of CIGS with strong vertical Ga segregation . . . . .	21
1.4.3. Growth of CIGS with less distinct vertical Ga segregation . . . . .	23
<b>2. Experimental and analytical methods</b>	<b>27</b>
2.1. Cu(In,Ga)Se <sub>2</sub> absorber preparation . . . . .	27
2.1.1. Cu-In-Ga metal precursor deposition . . . . .	27
2.1.2. Selenization of metallic precursor layers . . . . .	28
2.1.3. Preparation of solar cells . . . . .	31
2.2. Main characterization methods . . . . .	32
2.2.1. Energy dispersive X-ray diffraction (EDXRD) . . . . .	34
2.2.2. Energy dispersive X-ray fluorescence (EDXRF) . . . . .	35
2.3. Standard characterization methods . . . . .	43
<b>3. Lateral element redistribution during annealing of metal precursors</b>	<b>45</b>
3.1. Influence of precursor stacking sequence on film roughness and homogeneity	47
3.2. Effect of heating rate and temperature on lateral element redistribution	48
3.3. Impact of evaporated NaF on dewetting . . . . .	51
3.4. Non-reversibility of lateral phase separation with selenization . . . . .	53
3.5. Discussion . . . . .	53
3.6. Conclusion . . . . .	55

<b>4. Evolution of crystallographic phases and vertical elemental redistribution during selenization</b>	<b>57</b>
4.1. Thermal treatment of the Cu-In-Ga multilayer precursor without Se . . .	59
4.1.1. Analysis of the <i>in situ</i> EDXRD/EDXRF measurement . . . . .	59
4.1.2. Summary . . . . .	62
4.2. Fast absorber growth with strong vertical Ga segregation . . . . .	63
4.2.1. Analysis of the <i>in situ</i> EDXRD/EDXRF measurement . . . . .	63
4.2.2. Deduced 1D growth schematic . . . . .	70
4.2.3. Summary . . . . .	81
4.3. Fast absorber growth without final vertical Ga segregation . . . . .	82
4.3.1. Analysis of the <i>in situ</i> EDXRD/EDXRF measurement . . . . .	82
4.3.2. Deduced 1D growth schematic . . . . .	89
4.3.3. Summary . . . . .	103
4.4. Discussion of the applied EDXRD/EDXRF method and assumptions . .	103
4.5. Comparison of the two distinct growth paths from <i>in situ</i> investigation	107
4.6. Comparison of the two distinct growth paths from <i>ex situ</i> investigation	110
4.7. CIGS growth model and correlation with the Se supply . . . . .	115
<b>5. Conclusion and outlook</b>	<b>117</b>
<b>Kurzfassung</b>	<b>120</b>
<b>Abstract</b>	<b>121</b>
<b>Bibliography</b>	<b>123</b>
<b>A. Supplementary for Ch. 1</b>	<b>141</b>
<b>B. Supplementary for Ch. 2</b>	<b>145</b>
<b>C. Supplementary for Ch. 3</b>	<b>153</b>
<b>D. Supplementary for Ch. 4</b>	<b>157</b>
D.1. Evaluation of the composition of the $\gamma$ -phase . . . . .	157
D.2. Supplementary for Sec. 4.1 . . . . .	158
D.3. Supplementary for Sec. 4.2 . . . . .	160
D.4. Supplementary for Sec. 4.3 . . . . .	165
D.5. Supplementary for Sec. 4.5 . . . . .	172
D.5.1. Influence of total pressure on the film evolution during selenization	172
<b>E. Data from literature</b>	<b>175</b>

<b>List of Symbols and Abbreviations</b>	<b>I</b>
<b>List of Publications</b>	<b>III</b>
<b>Acknowledgment</b>	<b>V</b>
<b>Curriculum Vitae</b>	<b>VII</b>
<b>Selbständigkeitserklärung</b>	<b>IX</b>



# Introduction

Photovoltaics (PV) in general has evolved from just powering satellites and gadgets towards contribution significantly to the electric energy supply. The demand for renewable energies rises, because conventional energy sources exhibit a finite supply. In addition, green house gas emission and nuclear power plants are urgent safety issues. Overall, the absorber material with the dominant market share is Si. The aim of further reducing production costs led to the concept of thin film technologies. The absorption of light within a thin film of only a few  $\mu\text{m}$  relies on high absorption materials like  $\text{Cu}(\text{In,Ga})\text{Se}_2$  (CIGS) and  $\text{CdTe}$ . This opens up further advantages like less weight and creates new fields of application e.g. flexible modules. In the field of thin film PV technologies, CIGS based cells exhibit the lowest environmental impact in comparison with Si and  $\text{CdTe}$  based thin film technologies [Jungbluth *et al.*, 2008].

However, CIGS also needs to be economically competitive. Especially the costs per output power are relevant. So far, the costs are decreasing by an ongoing upscaling of the production per year [Palm *et al.*, 2015]. Another main lever for profitability is the conversion efficiency. In this respect, CIGS is a promising material, currently exhibiting the highest thin film solar cell efficiency. The highest reported CIGS cell efficiency is 22.9% [K.K., 20]. There is still a high potential for increasing the efficiency, since the theoretical maximum is about 33% [Werner *et al.*, 1995, Werner *et al.*, 2005, Siebentritt, 2011]. Another advantage of CIGS is the possibility to adjust the energy band gap ( $E_g$ ) to optimize the efficiency in regard to the local incoming light spectrum. The  $E_g$  is correlated to the Ga to In ratio in  $\text{Cu}(\text{In}_{1-x}\text{Ga}_x)\text{Se}_2$ . An increasing Ga amount expands the  $E_g$  from 1.00 eV for Ga free  $\text{CuInSe}_2$  to up to 1.68 eV for  $\text{CuGaSe}_2$  [Shay and Wernick, 1975].

An industrially attractive production route is the so called sequential process. It consists of two steps, first a deposition of a precursor and second a reaction with a chalcogen at an elevated temperature. The sequential process is already used by companies, e.g. AVANCIS and Solar Frontier. The central preparation technique in this work is one possible variation of the sequential process. In detail, it consists of the thermally activated and fast reaction of a sputtered Cu-In-Ga precursor in elemental Se vapor (selenization). The selenization is performed within a few minutes via a rapid thermal processing step (RTP), which can be carried out at atmospheric pressure.

The use of elemental Se instead of toxic and explosive gases like  $\text{H}_2\text{Se}$  (and  $\text{H}_2\text{S}$  for the efficiency record) reduces costs and safety risks. Using a sequential process and elemental chalcogenides, an efficiency of 17.3% was reached [Broussillou *et al.*, 2015]. Unfortunately, the preparation technique with fast selenization of a Cu-In-Ga precursor in elemental Se vapor typically leads to a segregation within the CIGS film. This means most of the Ga accumulating at the Mo back contact and an emerging Ga free top part of the film [Chirilă *et al.*, 2011, Palm *et al.*, 2004, Caballero *et al.*, 2006, Weber *et al.*, 2011, Mainz *et al.*, 2015b]. The Ga segregation fundamentally inhibits an adjustment of the Ga depth profile ( $E_g$ , respectively). However, such an adjustment is necessary for a higher efficiency to stay competitive on the market and over other preparation techniques (e.g. vacuum based co-evaporation).

Some approaches have been investigated in the past to promote a more controlled band gap tuning, e.g.:

- Adjusting the Ga depth profile in the precursor  
[Caballero *et al.*, 2006, Hsu *et al.*, 2012, Wu *et al.*, 2014]
- Increasing selenization time and/or temperature  
[Marudachalam *et al.*, 1995, Marudachalam *et al.*, 1997]

So far, all approaches have a draw-back, *i.e.* they are not sufficient, not reproducible, not understood or they suffer from an increase in processing time. Up to now, an adjustment of the Ga in-depth profile during fast selenization in elemental Se vapor has not been achieved.

The formation of CIGS is determined mainly by the thermodynamics and kinetic limitations of the material system. For example, the motion of each element can depend on the possible pathways by either chemical reactions, defects or a diffusion barrier. The possibilities for a direct control of the selenization are limited. The Se partial pressure ( $P_{\text{Se}}$ ) is a possible parameter for controlling the reaction. However, measuring  $P_{\text{Se}}$  is difficult due to the corrosive Se vapor combined with the high temperature required to avoid condensation. An often followed approach to vary the Se supply is therefore to add different amounts of Se onto or next to the precursor and heat up everything together in a closed reaction chamber. In this case, the Se partial pressure and time of Se supply is often directly coupled to the temperature of the reaction chamber. As a result, the Se supply is neither independent from the substrate temperature nor constant throughout the selenization.

The approach in this work is to supply Se by an external Se source to decouple the Se supply as well as possible from the temperature of the reaction chamber. Thus, the  $P_{\text{Se}}$  is defined by the Se source temperature ( $T_{\text{Se}}$ ). A control of the Se supply might allow to influence the CIGS growth. Furthermore, with an external Se source, Se can be provided at an elevated temperature (instead from the beginning at room temperature).

---

This can lead to unwanted side effects like phase separation and dewetting, which are investigated in this thesis.

The aim of this work is to understand the phase formation, its evolution and depth distribution to finally prevent Ga segregation. The reactions during selenization are very fast and the material is highly complex with its large number of elements and various possible phases. For these reasons, an *in situ* approach utilizing synchrotron light was applied: The fast evolution of phases is observed by analyzing the Bragg reflections observed by *in situ* energy dispersive X-ray diffraction (EDXRD). This measurement is performed simultaneously with *in situ* energy dispersive X-ray fluorescence (EDXRF) and hence, the signals can be correlated. A unique combination of the *in situ* EDXRD/EDXRF method with quantitatively calculated fluorescence intensities is used to deduce the phase depth distribution during growth.

The approach in this work is to study the influence on the resulting lateral and vertical Ga distribution of i) different precursor preparations, ii) heating rates, iii) maximum annealing temperatures, iv) NaF supply and most important v) control of Se supply via an external Se source.

## Outline

Chapter 1 introduces relevant information on material properties of CIGS, required for this work. It starts with material properties of CIGS and the role of In and Ga therein as well as related effects on solar cell parameters. The relevant crystallographic phases present during the growth of CIGS are introduced by means of selected phase diagrams. A central control parameter in this work is the Se supply during growth of CIGS. Therefore known influences of Se supply on the Se and Ga diffusion coefficients and on the phase formation are presented. The applied growth method, the sequential processing, is introduced and previous *in situ* and *ex situ* investigations of it from literature are presented.

Chapter 2 presents the sample preparation and the experimental setups that were used for thermal treatments with and without Se supply. Especially, the application of an external Se source, developed at the Helmholtz Zentrum Berlin (HZB), is described. Further, the central applied experimental methods are described: *in situ* Energy dispersive X-ray diffraction (EDXRD) and fluorescence (EDXRF) at the energy dispersive diffraction beamline (EDDI) at the synchrotron BESSY II. A program for calculating EDXRF intensities depending on the elemental depth distribution is introduced, which is used to draw conclusions about the elemental

depth distribution during selenization. This chapter closes with a short overview of the further characterization methods utilized for the present work.

In Chapter 3, lateral elemental separation and dewetting during thermal treatment of Cu-In-Ga precursor layers in Se free atmosphere are studied to gain knowledge about the time during selenization when Se should be supplied. This is performed by means of phase identification using X-ray diffraction (XRD) measurements and by elemental mapping using energy dispersive X-ray spectroscopy (EDX) in a scanning electron microscope (SEM).

Chapter 4 shows *in situ* measurement data from EDXRD and EDXRF during thermal treatment without and with Se atmosphere. Section 4.1 presents the phase evolution of a precursor during heating without Se. The phase evolution during selenization of a sample, which resulted in strong Ga segregation at the back contact is presented in Section 4.2. Section 4.3 reveals, for the first time, the time dependent phase evolution during selenization of a sample without resulting in Ga segregation. Both growth evolutions are compared in Section 4.5. Sec. 4.6 shows an *ex situ* investigation with which the temperature of the Se source, growth path and Ga depth profile are shown to be correlated. The investigations are compared to propose a comprehensive model of growth in Sec. 4.7.

# 1. Basics of Cu(In,Ga)Se<sub>2</sub> absorber material and preparation

This chapter describes material properties of Cu(In,Ga)Se<sub>2</sub> (CIGS), the role of In and Ga therein as well as related effects on solar cells parameters. The relevant crystallographic phases present during the growth of CIGS are introduced by means of selected phase diagrams. A central control parameter in this work is the Se supply during growth of CIGS. Therefore known influences of Se supply on the Se and Ga diffusion coefficients and on the phase formation are presented. Afterwards, the applied growth method, sequential processing, is introduced and previous *in situ* and *ex situ* investigations of it from literature are presented.

## 1.1. The role of Ga in Cu(In,Ga)Se<sub>2</sub> with respect to material and electrical properties

The band gap energy ( $E_g$ ) of the absorber material determines the minimum required energy of photons to create an electron-hole pair. Thus,  $E_g$  is an important design parameter to prepare solar cells with maximum possible efficiency. CIGS is a compound semiconductor of the family of I-III-VI<sub>2</sub> materials, which offer the opportunity of adjusting  $E_g$  by substitution of group I, III or VI elements, *i.e.* forming different compounds within the (Ag, Cu)(In, Ga, Al)(S, Se, Te)<sub>2</sub> system [Wei and Zunger, 1995]. The substitution of In by Ga to increase  $E_g$  is the most common approach and a central topic in this work. First principles calculations and experimental results regarding the functionality of the absorber layer in the solar cell as modified by adding Ga are presented in the following. Further information on the general physics of solar cells are described in more detail in reference [Würfel, 2000] and further chalcogenide-specific details can be found in reference [Scheer and Schock, 2011].

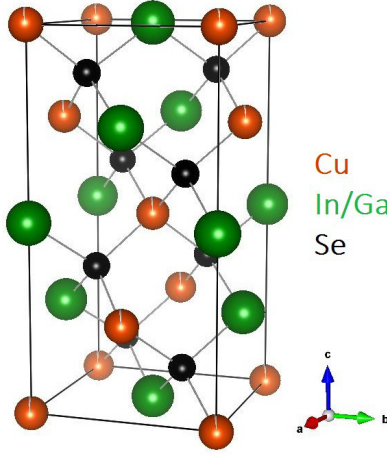


**Figure 1.1.:** Chalcopyrite crystal structure of  $\text{Cu}(\text{In,Ga})\text{Se}_2$ . (Schematic created with VESTA.)

### 1.1.1. Crystal structure of $\text{Cu}(\text{In,Ga})\text{Se}_2$

At room temperature (RT), CIGS exhibits the chalcopyrite crystal structure, as shown in Fig. 1.1. It is a tetragonal crystal system and its space group is  $\bar{I}42d$ . The composition can be described by a solid solution of the miscible compounds  $\text{CuInSe}_2$  and  $\text{CuGaSe}_2$  as  $\text{Cu}(\text{In}_{1-x}\text{Ga}_x)\text{Se}_2$  and  $x$  is also referred to as  $[\text{Ga}]/([\text{Ga}]+[\text{In}])$  (GGI). However, calculations based on Monte Carlo simulations [Xue *et al.*, 2016] and density functional theory [Wei and Zunger, 1995, Ludwig *et al.*, 2010] suggest, that a separation of the solutes is energetically preferred at room temperature.  $\text{CuInSe}_2$  forms clusters in Ga-rich (GGI>0.5) films and  $\text{CuGaSe}_2$  forms clusters in In-rich (GGI<0.5) films. These clusters are decreasing in average size with increasing temperature [Ludwig *et al.*, 2010]. This increasing homogeneity is experimentally confirmed [Haarstrich *et al.*, 2011]. Furthermore, the calculated inhomogeneity is higher for higher Ga content CIGS [Ludwig, 2011], which is in agreement with experimental results [Gütay and Bauer, 2007]. The preservation of the high temperature homogeneity towards a lower temperature can be forced by a fast cool down [Windeln *et al.*, 2009]. The consequence of a formation of clusters is a detrimental band gap fluctuation. A locally decreased  $E_g$  decreases the limit for splitting the quasi-Fermi levels [Siebentritt, 2011] and thus can increase the recombination. It has been found that band gap fluctuations in state-of-the-art devices are in the order of 8 meV [Gütay and Bauer, 2009]. However, it has been shown, that only variations above 25 meV significantly change the efficiency [Rau and Werner, 2004].

The two group three elements (In and Ga) exhibit different atomic radii and occupy the same lattice position. The lattice constants of  $\text{CuInSe}_2$  are larger than those of  $\text{CuGaSe}_2$  (sup. Tab. E.2). The lattice constant of an ideal solid solution can be

approximated by a linear dependence on the percentage  $x$  of the substituting element, according to Vegard's law for two solutes A and B in Eq. 1.1 [Vegard, 1921].

$$a_{A_{1-x}B_x} = (1 - x)a_A + xa_B \quad (1.1)$$

Vegard's law is a suitable approximation in the case of CIGS [Suri *et al.*, 1989], [Choi and Lee, 2007].

The structure of chalcopyrite is closely related to that of zinc blende ZnS (sphalerite). The unit cell of chalcopyrite is approximately twice as big in volume, since  $2a \approx c$  and reflects an alternation of Cu<sup>+</sup> and In/Ga<sup>3+</sup> replacing Zn<sup>2+</sup> in adjacent planes. In fact, CIGS is typically distorted along the  $c$ -axis with the result that  $c/a$  is unequal 2. The strengths of the bonds of the cations with Se (Cu-Se, In-Se and Ga-Se) are different and the anion (Se) is not occupying the ideal lattice position. A consequence is, that some XRD reflections which belong to the sphalerite structure are split into two signals for the chalcopyrite structure.

The crystal structure can also be disturbed by a wide variety of point defects possible in CIGS [Zhang *et al.*, 1998]. The various defects include unoccupied lattices sites (vacancies), atoms in the space between the normal lattice sites (interstitials) and atoms on a different position (antisites). Defects influence e.g. the doping and recombination in a CIGS solar cell as well as the diffusion of elements during growth of CIGS (see Secs. 1.3 and 1.4).

### 1.1.2. Cu(In,Ga)Se<sub>2</sub>-based solar cells and the role of Ga therein

A standard structure of a CIGS solar cell as it is applied in this work is illustrated in Fig. 1.2. Glass, coated with 1  $\mu$ m Mo as back contact typically serves as substrate. A pn heterostructure consisting of a absorber/buffer/window (p/n/n) stack is prepared on top. A front contact and a contact grid are deposited on top.

Contact grid	Ni/Al	
Front contact	Al:ZnO	~1 $\mu$ m
Window	i-ZnO	~130 nm
Buffer	CdS	~60 nm
Absorber	CIGS	~1.5 $\mu$ m
Back contact	Mo	~1 $\mu$ m
	Glass	~3 mm

**Figure 1.2.:** Schematic structure of an in-house Cu(In,Ga)Se<sub>2</sub> based solar cell with exemplary thickness values.

A Ga concentration  $x$  in  $\text{Cu}(\text{In}_{1-x}\text{Ga}_x)\text{Se}_2$  between 0 and 1 is possible.  $\text{CuInSe}_2$  exhibits an  $E_g$  of 1.0 eV in contrast to 1.68 eV for  $\text{CuGaSe}_2$  [Shay and Wernick, 1975, Kulkarni *et al.*, 2009]. The resulting  $E_g$  in a solid solution of them can be described as a function of the GGI by use of a bowing factor with the suggested approximation by Ishizuka *et al.* (2005):

$$E_g = 1 + 0.564 \times \text{GGI} + 0.116 \times \text{GGI}^2 \quad (1.2)$$

This experimental result is supported by first principles calculations [Wei and Zunger, 1995]. The effect of Ga addition on  $E_g$  is mainly due to an increase of the conduction band minimum ( $E_C$ ), while the valence band maximum ( $E_V$ ) is only slightly affected [Wei and Zunger, 1995, Lavrenko *et al.*, 2015].

In view of commercial application, the efficiency ( $\eta$ ) is the most important property of a solar module. The efficiency maximum is the optimum of the tradeoff between the achieved voltage and collected current. Whereas the  $V_{oc}$  increases with  $E_g$  the collected current decreases. Therefore,  $\eta$  is correlated to  $E_g$  and thus to the Ga concentration. The first approximation relating  $E_g$  and efficiency is the well-known limit by Shockley and Queisser (SQL) [Shockley and Queisser, 1961] for single  $E_g$  solar cells. The model is based on black body radiation, a temperature of 6000 °K for the sun surface, a quantum efficiency (QE) of 1 and assuming only radiative recombination. For a refined approximation, a standard AM1.5 spectrum can be applied [Werner *et al.*, 1995, Werner *et al.*, 2005, Siebentritt, 2011]. Their refined approximation shows that highest possible efficiencies are for absorbers with  $E_g$  between 1.15 eV and 1.35 eV.

When correlating experimental findings, Contreras *et al.* used the drop of an EQE measurement to 20 % as a measure for  $E_g$  which is referred to as the effective  $E_g$  in the following. This definition is used since  $E_g$  can vary in the depth of the absorber and laterally. Fig. 1.3 shows achieved efficiencies plotted over the effective  $E_g$ , to demonstrate the experimental correlation between  $\eta$  and  $E_g$ .

The achieved record efficiency of 22.9 % [K.K., 20] is still significantly lower than predicted. This is not surprising due to non-radiative recombination like Auger recombination and in CIGS often dominating Shockley-Read-Hall recombination (SRH) [Lewerenz and Jungblut, 1995, Siebentritt, 2011]. SRH recombination may occur in the bulk [Lewerenz and Jungblut, 1995] as well as at the interfaces with the front and back contact [Siebentritt, 2011, Chirilă *et al.*, 2011]. The broad maximum of the theoretical maximum  $\eta$  (according to [Siebentritt, 2011]) between  $E_g=1.15$  eV and 1.35 eV is not found in the experiment. In the experiment, higher currents (at low  $E_g$ ) were apparently easier to achieve than high  $V_{oc}$  (at wide  $E_g$ ) which shifts the trade-off between both to lower  $E_g$ . The linear approximation of  $V_{oc}(E_g)$  is based on results from Rau and Schock (1999): They showed that for different recombination mechanism,

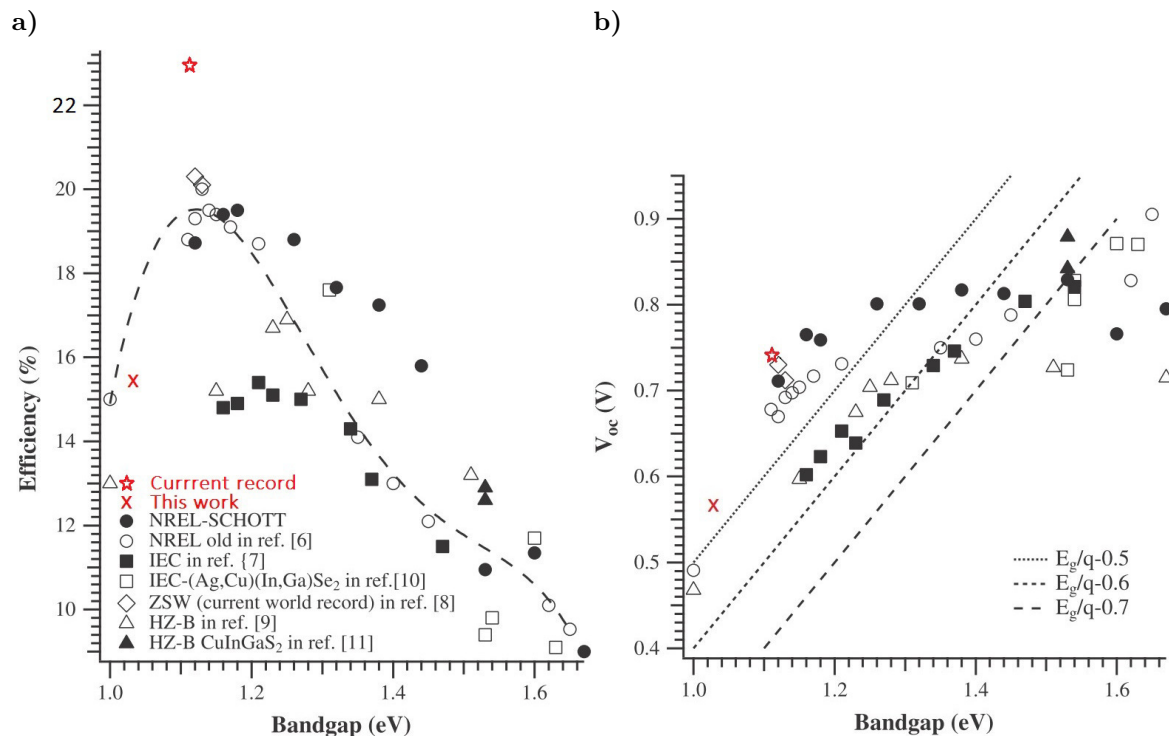


**Figure 1.3.:** a) Solar cell efficiency and b)  $V_{oc}$  versus effective band gap values of CIGS devices, determined on the basis of the EQE according to [Contreras *et al.*, 2012]. Figure taken from [Contreras *et al.*, 2012]. The red x marks the achieved values, presented in this work (Sec. 4.6). Regarding the current record of 22.9% [K.K., 20], the possibly corresponding  $E_g$  and  $V_{oc}$  are taken from [Wu *et al.*, 2018].

typically observed in chalcopyrite solar cells and a dominant recombination in the bulk, that  $V_{oc}$  can be written as  $V_{oc} = \frac{E_g}{q} - \frac{AkT}{q} \ln\left(\frac{j_{00}}{j_{sc}}\right)$  ( $A$ : diode ideality factor,  $k$ : Boltzmann constant,  $j_{00}$ : reference current density). If the recombination process and its main parameters (apart from band gap) stay the same, the second term (the  $V_{oc}$  deficit) should show no distinct variation with the band gap. As Fig. 1.3b) shows, this does not correspond to the experimental result where the  $V_{oc}$  deficit increases from less than 0.5 V to more than 0.7 V with increasing  $E_g$ . The predicted dependence of  $\eta$  and  $E_g$  can only be valid, if Ga modifies just the band gap. However, other consequences of Ga incorporation such as a modified defect distribution, oxidation, morphology and band line up at the heterointerface are known:

Ga influences the energetic position of defects [Heath *et al.*, 2002, Zunger *et al.*, 1997] and the defect concentration. A minimum of the bulk defect concentration was found for an  $E_g \approx 1.15$  eV [Hanna *et al.*, 2001]. Another experimental result is, that  $\text{CuInSe}_2$  can be doped p- and n-type by native point defects resulting from deviations from stoichiometric composition [Noufi *et al.*, 1984] or by doping with  $\text{Cd}_{\text{Cu}}$  or  $\text{Cl}_{\text{Se}}$  [Zhao *et al.*, 2004]. However, n-type doping seems to be impossible for  $\text{CuGaSe}_2$  [Coutts *et al.*, 1986]. This describes a fundamental difference between both chalcopy-

rites regarding the defects without a quantitative correlation with the GGI so far. First-principle calculations show, that n-type doping in  $\text{CuGaSe}_2$  is strongly hampered by a low formation energy (and possibility of spontaneous formation) of  $V_{\text{Cu}}$ , acting as an acceptor [Zhao *et al.*, 2004, Persson *et al.*, 2005]. The calculations also show a remarkably low formation energy for the defect pair ( $2V_{\text{Cu}}^- + \text{III}_{\text{Cu}}^{2+}$ ), which is lower for  $\text{In}_{\text{Cu}}$  than for  $\text{Ga}_{\text{Cu}}$  [Zunger *et al.*, 1997]. This explains the possible formation of ordered vacancy compounds like  $\text{CuIn}_3\text{Se}_5$  (OVC) (see also Sec. 1.2.2).

Regarding the surface properties of CIGS, Ga was found to more quickly oxidize compared with In, forming  $\text{Ga}_2\text{O}_3$  on top of CIGS and a reduction of the Ga concentration in the film [Lehmann *et al.*, 2014, Dirnstorfer *et al.*, 2000, Lehmann, 2010]. Thus, it possibly affects the defect distribution at the interface with the buffer layer.

In regard to the morphology and crystal structure, a similar trend to the efficiency was obtained: A maximum of grain size was found for  $x=0.23$  (corresponds to 1.14 eV) (by electron backscatter diffraction (EBSD) maps) [Abou-Ras *et al.*, 2008, Eisenbarth *et al.*, 2009]. This correlates with results from investigation of the crystal structure in powder samples by XRD [Suri *et al.*, 1989], suggesting a linear dependence of the  $c/a$  ratio on the gallium content. They found, that the ratio of the lattice constants  $c/a$  is equal to 2 for about the same  $x$  value. The authors propose, that this pseudocubic crystal structure at about  $x=0.23$  may lead to reduced strain in the growing  $\text{Cu}(\text{In}_{1-x}\text{Ga}_x)\text{Se}_2$  film and therefore larger average grain sizes.

While in these studies, trying to correlate Ga content and morphology, the biggest grain size was achieved at  $x=0.23$ , the maximum cell efficiency (16.9%) was actually observed at  $x=0.37$  (1.22 eV) [Abou-Ras *et al.*, 2008, Eisenbarth *et al.*, 2009] (in contrast to Fig. 1.3).

In short, the band gap widening from 1.0 eV for  $\text{CuInSe}_2$  towards 1.15 eV is desired for a higher efficiency. This is the most important effect of Ga substitution but certainly not the only one. A fully consistent and comprehensive model of the cell performance as a function of Ga content does not exist.

Due to the limited material quality of CIGS, an approach to increase  $\eta$  is the implementation of a changing  $E_g$  over depth [Dullweber *et al.*, 2000, Song *et al.*, 2004, Huang, 2008, Hirai *et al.*, 2014], which is typical for state-of-the-art devices [Witte *et al.*, 2015, Chirilă *et al.*, 2011].

State-of-the-art CIGS devices include a double  $E_g$  gradient, with the minimum close to the edge of the space charge region. This minimum  $E_g$  typically correlates well to the effective  $E_g$  described above. The gradient towards the back contact is typically achieved by increasing the GGI, while the gradient towards the surface can be realized by S incorporation in case of sequential preparation [Koo *et al.*, 2016]. An increasing  $E_g$  is applied to reduce recombination and minimize interface recombination as well as ensuring a current flow. The gradient towards the back contact has the advantage

of inducing a gradient of the quasi Fermi level (here for electrons:  $E_{fn}$ ) in operation (Fig. 1.4) in the bulk towards the front surface which improves the current collection [Wüffel, 2000]. The gradient also reduces the recombination at the back contact (by reducing the electron density) which can in addition have a positive influence on the saturation current density and therefore  $V_{oc}$ .

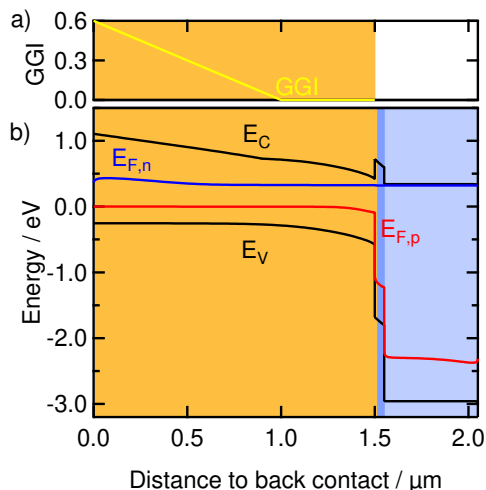


**Figure 1.4.:** Band diagram for a CIGS device with Ga segregation under illumination with a device structure similar to Fig. 1.2, calculated at the maximum power point by use of SCAPS [Burgelman *et al.*, 2000]. Used properties are listed in sup. Tab. A.1. a) GGI plotted over depth. b) Plotted over depth are  $E_V$  and  $E_C$  (valence and conduction band energy) as well as  $E_{fn}$  and  $E_{fp}$  (quasi Fermi level for electrons and holes). The  $E_g$  of the absorber is based on a schematic example for the Ga in-depth profile, as it is observed in Fig. 4.5, with Ga segregation at the back contact. The top 600 nm are at a GGI of 0 and below are 900 nm with an linear increase of the GGI up to 0.6. This diagram demonstrates the effect of Ga on the band structure.

There are different preparation methods for CIGS absorber layers. With a preparation method like co-evaporation of all elements from separate sources, the GGI over film depth can be controlled by the deposition rates of the elements during growth and a sufficiently good homogeneity can be achieved. The largest CIGS industrial production capacity, however, is based on sequential processing [Frontier, 2015]. This preparation method (as described in Sec. 1.4 in more detail) starts with deposition of a Cu-In-Ga-based metal precursor film. This film is then processed via reactive annealing in a Se containing atmosphere. For a sputtered precursor film, Ga is typically present in a Cu-Ga alloy (like  $\text{Cu}_9\text{Ga}_4$ ). During this preparation, the thermodynamics and the formation of several intermediate phases can only be controlled by external parameters in a limited way, such as the temperature profile over processing time. Furthermore, this processing leads to additional kinetic limitations. Sequential processing typically leads to a Ga segregation at the Mo back contact, see Fig. 1.4a) and Sec. 1.4.2. Adjusting the in-depth Ga grading towards a uniform profile afterwards is in principle possible [Marudachalam *et al.*, 1997] but only under specific conditions and with extended processing time. Ga segregation means, most Ga is located at back and a top part is free of Ga and thus, the top part at an  $E_g$  of about  $\text{CuInSe}_2$ , and the  $E_g$  at the back contact is higher than 1.2 eV. Determining a resulting single  $E_g$  for the total

device from a measurement (e.g. by EQE) shows, that the lowest  $E_g$  in the top part determines such an effective  $E_g$  [Dullweber *et al.*, 2001]. This minimal  $E_g$  of 1.0 eV limits the maximum  $V_{oc}$  and efficiency, as explained above.

As in the theoretical predictions, the experiment also shows a steep increase in efficiency between the  $E_g=1.0$  eV and 1.15 eV. That supports the main motivation of this work. Identifying pathways to prevent strong Ga segregation within a fast sequential process is the aim of this thesis.

## 1.2. Binary and ternary phase diagrams of the Cu-In-Ga-Se system

In the following, phase diagrams of the Cu-In-Ga-Se system are presented and discussed to introduce relevant phases present during the investigation in Ch. 3 and Ch. 4. First, the Cu-In-Ga system is presented with the aid of ternary phase diagrams of Cu-In-Ga. A more detailed discussion of phases in the Cu-In-Ga system can be found in [Purwins, 2010, Muzzillo *et al.*, 2015]. Afterwards, the Se containing system is presented on the basis of the ternary phase diagram of Cu-In-Se and the quasi-binary phase diagram of In<sub>2</sub>Se<sub>3</sub>-Cu<sub>2</sub>Se. Further phase diagrams can be found in the supplementary information (sup. Sec. E). All phase diagrams are typically based on results close to thermal equilibrium conditions while the rapid thermal annealing step (RTA) with a heating rate of up to 1 °C/s in the experiments performed for this thesis may be far away from thermal equilibrium.

### 1.2.1. Phase diagrams of the Cu-In-Ga system without Se

Possible phases in a Cu-In-Ga precursor are given by the ternary Cu-In-Ga phase diagram at 150 °C (Fig. 1.5a) and at 550 °C (Fig. 1.5b). At 150 °C, possible precursor phases and solid solutions are  $\eta$ -Cu<sub>16</sub>(In,Ga)<sub>9</sub> (in literature often denoted as Cu<sub>2</sub>In for Cu<sub>16</sub>In<sub>9</sub>), Cu<sub>11</sub>In<sub>9</sub>,  $\gamma_i$ -Cu<sub>9</sub>(In,Ga)<sub>4</sub>, In,  $\alpha$ -Cu(Ga),  $\zeta$ -Cu<sub>778</sub>Ga<sub>222</sub>,  $\delta$ -Cu<sub>7</sub>In<sub>3</sub> and CuGa<sub>2</sub>. The phase  $\eta$ -Cu<sub>16</sub>(In,Ga)<sub>9</sub> is found to form already at RT and the preparation process might induce enough energy for formation of other phases. The development over temperature shows (compare Fig. 1.5), that especially the solubility ranges increase for  $\gamma$ -Cu<sub>9</sub>(In,Ga)<sub>4</sub> and liquid In. Meanwhile the three phase area of In+Cu<sub>16</sub>In<sub>9</sub>+Cu<sub>9</sub>(In,Ga)<sub>4</sub> decreases (see gray area in Fig. 1.5).

Although the typical total film compositions with a GGI about 0.3 and a CGI about 0.9 is often prepared, the reported phases in the precursor vary. This is likely a consequence of different preparation techniques as well as parameters and impurities.

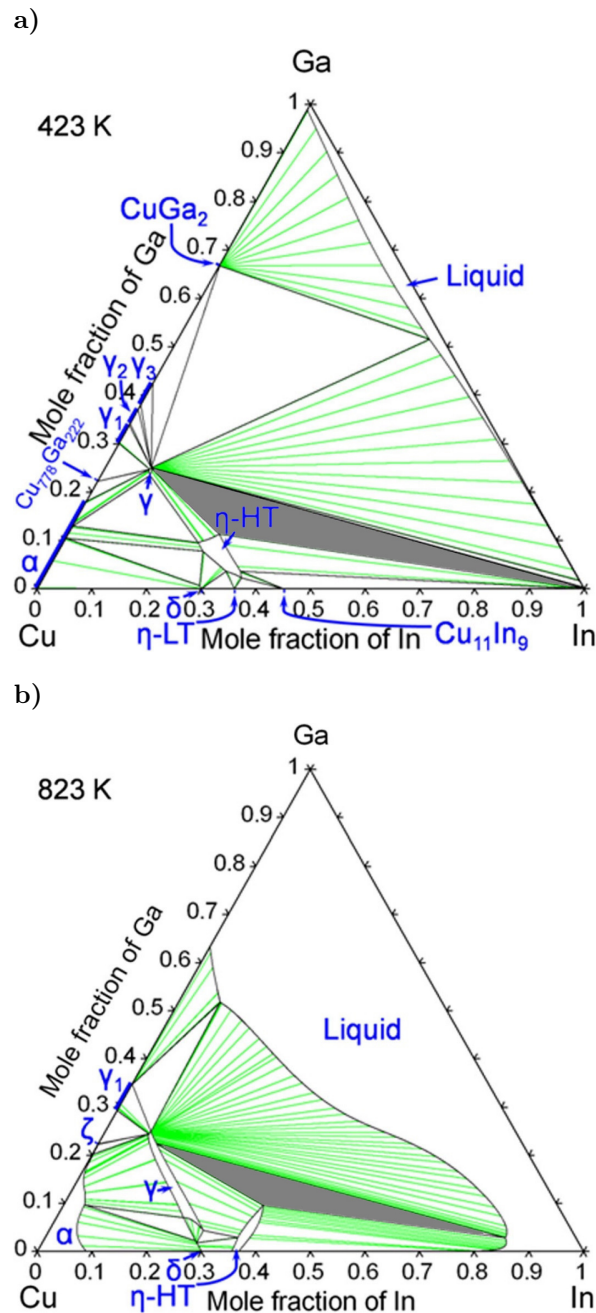


**Figure 1.5.:** Calculated isothermal ternary phase diagram of Cu-In-Ga from Muzzillo *et al.* (2015) at a) 150 °C (423 K), b) 550 °C (823 K). An additional phase diagram for 350 °C (623 K) is shown in sup. Fig. E.4. The greek letters correspond to the following compounds:  $\alpha$ : Cu,  $\gamma_i$ : different  $\text{Cu}_9\text{Ga}_4$  (see text and sup. Fig. E.1) with  $\gamma$  which is denoted as  $\gamma_0$  in this work, a low (LT) and high (HT) temperature phase of  $\eta$ :  $\text{Cu}_{16}\text{In}_9$ ,  $\phi$ :  $\text{Cu}_{11}\text{In}_9$ ,  $\zeta$ :  $\text{Cu}_{778}\text{Ga}_{222}$ . The area of the ternary phase mixture of  $\text{In} + \text{Cu}_{16}\text{In}_9 + \text{Cu}_9(\text{In,Ga})_4$  is colored in gray.

A difficulty for phase identification results from the fact, that most reflections of the two solid solutions, the  $\gamma$ - and the  $\eta$ -phase, may overlap due to the variation of the lattice constants with the Ga/In ratio within their regions of existence. Assignment of reflections to the  $\gamma$ -phase is sometimes possible, because of unique but low intensity reflections like 110, 222 or 321.

Another difficulty rises from  $\text{Cu}_9\text{Ga}_4$ , for which four different structures were found and which are also present in the ternary system. They are denoted as  $\gamma_i\text{-Cu}_9\text{Ga}_4$  (with  $i$  from 0 to 3, in this work  $\gamma$  is denoted as  $\gamma_0$ ), compare Fig. 1.5a) and the details in the Cu-Ga phase diagram in Fig. E.1. They all exhibit a range of phase existence and  $\gamma_1$  transforms to  $\gamma_0$  at higher temperatures, see sup. Fig. E.1. Additionally, the Cu to Ga ratio changes the lattice constant, see sup. Fig. E.2a). In XRD patterns, they can be differentiated only by different relative intensities of side reflections, which have typically low intensities. However, the different reference patterns could not be found in the literature. It seems to be soluble only in  $\gamma_1\text{-Cu}_9(\text{In},\text{Ga})_4$  [Hölzing, 2013]. The solubility of In in  $\text{Cu}_9\text{Ga}_4$  and Ga in  $\text{Cu}_{16}\text{In}_9$  increases with increasing temperature.

No other Cu-In, Cu-Ga or Cu-(In-Ga) phases will be observed during this work. An identification of the structure of  $\text{Cu}_9(\text{In},\text{Ga})_4$  as well as possible will be the basis to determine the composition. The distinction of  $\text{Cu}_{16}(\text{In},\text{Ga})_9$  and  $\text{Cu}_9(\text{In},\text{Ga})_4$  as well as the composition will be important for the calculation of fluorescence intensities.

### 1.2.2. Phase diagrams of the Cu-In-Se system

To describe the complex quaternary system of CIGS, it can be depicted as a binary system of  $\text{CuInSe}_2$  and  $\text{CuGaSe}_2$ . Each ternary compound can be found in a ternary phase diagram (see Fig. 1.6a for Cu-In-Se and [Purwins, 2010] for Cu-Ga-Se). In turn, a ternary phase diagram can be broken down by many possible isopleth lines into pseudo binary systems. One pseudo binary system is  $\text{In}_2\text{Se}_3\text{-Cu}_2\text{Se}$  (see Fig. 1.6b)) (or InSe-CuSe) in which important phases can be found.

Especially, for non-stoichiometric growth ( $\text{CGI} \neq 1$ ) secondary phases were found at the (growth) surface.  $\text{Cu}_{2-x}\text{Se}$  is found in the Cu-rich condition ( $\text{CGI} > 1$ ) [Tuttle *et al.*, 1991], which is highly conductive and can produce shunt paths. In the Cu-poor condition ( $\text{CGI} < 1$ ),  $\text{CuIn}_2\text{Se}_{3.5}$  and  $\text{CuIn}_3\text{Se}_5$  were found [Schmid *et al.*, 1993, Kessler *et al.*, 1993, Marín *et al.*, 1998]. It was suggested that  $\text{Cu}(\text{In}_{1-x}\text{Ga}_x)\text{Se}_2$  exhibits  $\text{Cu}(\text{In}_{1-x}\text{Ga}_x)_3\text{Se}_5$  at the surface [Negami *et al.*, 1995, Schmid *et al.*, 1993] or grain boundaries [Hetzer *et al.*, 2005, Abou-Ras *et al.*, 2012] and therefore it might be important for the growth process. Cho *et al.* assume, that an OVC layer reduces the defect density at the interface to CdS and suppresses the interface recombination

processes of a CIGS solar cell [Cho *et al.*, 2013]. Hence, it is relevant for solar cell preparation.

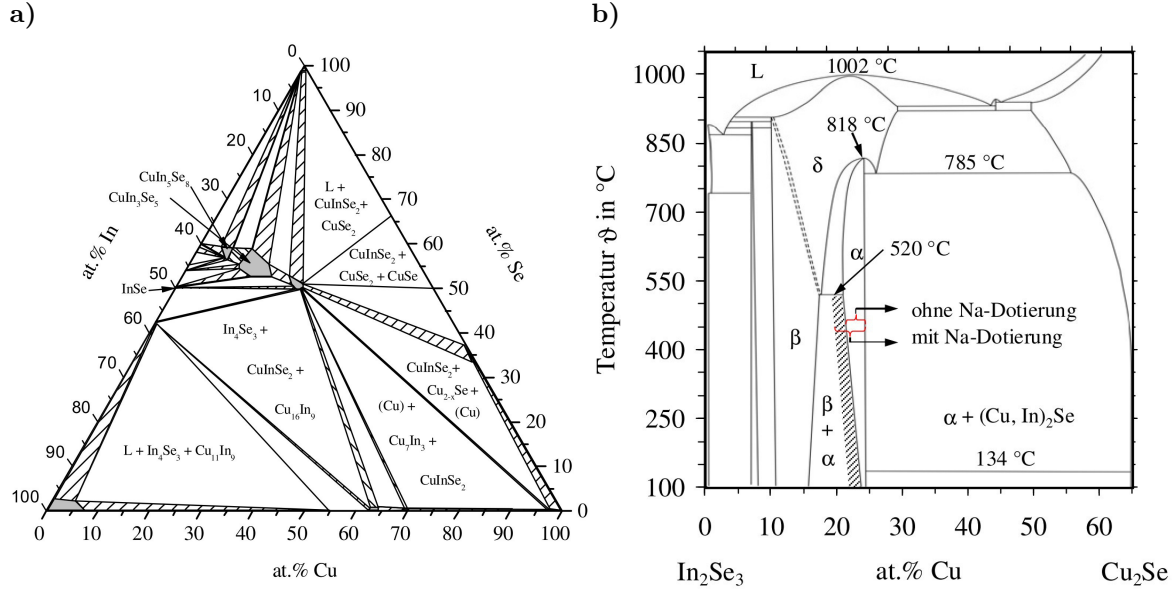


**Figure 1.6.:** Phase diagrams of the Cu-In-Se system. a) Ternary phase diagram of Cu-In-Se at 300 °C, reported in [Purwins, 2010]. Single phase areas like  $\text{CuInSe}_2$  in the center and OVCs are shaded gray. b) The pseudo binary system  $\text{In}_2\text{Se}_3$ - $\text{Cu}_2\text{Se}$  (from reference [Purwins, 2010]) as an exemplary isophlet in the ternary Cu-In-Se phase diagram. The abbreviations of phases are:  $\alpha$ : chalcopyrite- $\text{CuInSe}_2$ ,  $\beta$ :  $\text{CuIn}_3\text{Se}_5$  and  $\delta$ : sphalerite- $\text{CuInSe}_2$ . The range of the existence area of  $\alpha$ - $\text{CuInSe}_2$  increases with addition of Na towards an In richer composition (crosshatched). This suppresses the formation of  $\beta$ - $\text{CuIn}_3\text{Se}_5$  [Haalboom, 1998]. Many more pseudo binary phase diagrams can be found in [Gödecke *et al.*, 2000a, Gödecke *et al.*, 2000b, Gödecke *et al.*, 2000c]. Phase diagrams of the ternary Cu-Ga-Se system can be found in [Purwins, 2010, Mikkelsen, 1981]. An area with green lines indicate a miscibility gap.

Generally,  $\text{CuIn}_3\text{Se}_5$  (and  $\text{CuIn}_5\text{Se}_8$ ) can be described by a solid solution of the quasi binary system  $\text{CuInSe}_2$  -  $\text{In}_2\text{Se}_3$  [Pamplin and Feigelson, 1979]. The structure can be explained with formation and ordering of the defect pair ( $2V_{\text{Cu}}^- + \text{In}_{\text{Cu}}^{2+}$ ) and, accordingly, ordered defect compound (ODC) or ordered vacancy compound (OVC) were suggested as names. First-principle calculations show a remarkably low formation energy for the defect pair ( $2V_{\text{Cu}}^- + \text{III}_{\text{Cu}}^{2+}$ ), which is lower for  $\text{In}_{\text{Cu}}$  than for  $\text{Ga}_{\text{Cu}}$  [Zunger *et al.*, 1997]. This explains the possible formation of ordered vacancy compounds like  $\text{CuIn}_3\text{Se}_5$  (OVC). This defect pair with its unusually low formation energy is favorable over other possible defects [Zhang *et al.*, 1997]. In comparison with  $\text{CuInSe}_2$ ,  $\text{CuIn}_3\text{Se}_5$  exhibits a similar tetragonal lattice in relation to the Se positions. The ordering of  $2V_{\text{Cu}}^-$  and  $\text{In}_{\text{Cu}}^{2+}$  leads to additional reflections in XRD pattern. The additional reflections for  $\text{CuIn}_3\text{Se}_5$  result from planes with hkl-indices

of 002, 110, 200, 202 and 114 which do not fulfill the extinction conditions as the lattices in the space group  $\bar{I}42d$ . Instead  $P\bar{4}2c$  [Marín *et al.*, 1998] was suggested and its accuracy is still under debate.  $\text{CuInSe}_2$  and  $\text{CuIn}_3\text{Se}_5$  were hardly distinguished by TEM [Grigorov *et al.*, 2008].

For  $\text{CuIn}_5\text{Se}_8$  a completely different XRD diagram was found indicating a hexagonal structure [Folmer *et al.*, 1985, Merino *et al.*, 2000] and is not relevant for this work.

OVC were found at the CIGS surface [Negami *et al.*, 1995, Schmid *et al.*, 1993] and are supposed to be present at the CIGS growth front (see below) and grain boundaries [Hetzer *et al.*, 2005, Abou-Ras *et al.*, 2012]. The preferred growth of  $\text{CuInSe}_2$  leading to Ga segregation maybe also explained by the lower formation energy of  $(2V_{\text{Cu}}^- + \text{In}_{\text{Cu}}^{2+})$  than  $(2V_{\text{Cu}}^- + \text{Ga}_{\text{Cu}}^{2+})$ .

### 1.3. Types of Se supply and known effects on CIGS growth

#### Types of Se supply

The way as well as the amount of Se supplied for the selenization can influence the growth of CIGS e.g. via changing the diffusivity of Se in the phases or by triggering a different phase formation of intermediate phases. The growth of CIGS is based on the reactions of metallic and intermediate phases with Se. Hence, the Se supply is a very important experimental factor during the thermal reactive treatment (selenization) and is of particular interest for this work.

In general, Se is required for the complete formation of CIGS. It may be supplied as part of the precursor and/or during selenization via  $\text{H}_2\text{Se}$  or Se vapor. When supplying elemental Se vapor, the Se supply depends on the Se partial pressure ( $P_{\text{Se}}$ ), which in turn is a function of the Se source temperature ( $T_{\text{Se}}$ ) in a constant volume, compare Fig. A.1a).

In many experiments described in the literature, Se is often placed in form of pellets next to or as layer onto the precursor before heating everything together [Mainz *et al.*, 2015b, Koo *et al.*, 2013, Song *et al.*, 2003, Caballero *et al.*, 2006]. This procedure couples the Se partial pressure to the current substrate temperature, which changes during selenization by nearly 600 °C. Besides the influence on  $P_{\text{Se}}$ , this also changes the composition of the  $\text{Se}_i$  molecules ( $i=2-8$ ) in the vapor. Another consequence is a varying amount of Se supplied depending on the position of the Se pellets. Increasing the distance to the sample was found to lead to a decreasing solar cell efficiency [Colombara *et al.*, 2017, Chernomordik *et al.*, 2016]. In addition, Se was found to be

adhering to the inner walls of the chamber acting as an additional and difficult to control source of Se.

The application of an external Se source, as in this work (see Sec. 2.1.2) requires additional expenditure. The most important advantage is to decouple the Se supply from  $T_{\text{sub}}$  and to be able to choose the time of the Se supply. In this work, the Se supply is adjusted via  $T_{\text{Se}}$ .

### Influence of the Se supply on Se and Ga diffusivities

It is known, that  $P_{\text{Se}}$  affects the diffusion coefficient of Se ( $D_{\text{Se}}$ ). The  $D_{\text{Se}}$  in CuInSe<sub>2</sub> was found to be a function of Se<sub>2</sub><sup>1</sup> partial pressure with a square root dependence, formulated as  $D_{\text{Se}} \sim P_{\text{Se}_2}^{0.50 \pm 0.07}$  by Von Bardeleben [von Bardeleben, 1984] (see sup. Fig. A.1b). Von Bardeleben found, that  $D_{\text{Se}}$  is dominated by Se vacancies in case of a low  $P_{\text{Se}}$  while it is dominated by Se interstitials ( $\text{Se}_i$ ) in the case of a high  $P_{\text{Se}}$ . Another investigation was performed with first-principles calculations based on thermal activation energies for mass transport in CIGS. The outcome was, that Se vacancies ( $V_{\text{Se}}$ ) and Se dumbbells (two Se atoms sharing the same lattice site, see [Oikkonen *et al.*, 2012]) exhibit a similar formation energy. However, the diffusion of  $V_{\text{Se}}$  is impeded by a migration barrier of 2.19 eV. A lower migration barrier of 0.24 eV was found for Se dumbbells [Oikkonen *et al.*, 2013]. The authors concluded, that formation of  $V_{\text{Se}}$  is energetically preferred in under-stoichiometric Se conditions. In contrast, Se dumbbells are preferred in case of a high Se supply. They stated, that the dominant mechanism for Se diffusion is independent of the substrate temperature.

The formation of the Ga depth profile (see description of CIGS growth in Sec. 1.4) can be strongly influenced by the elemental diffusion processes [Gabor *et al.*, 1994, Lundberg *et al.*, 2003], which in turn are influenced by substrate temperature [Nishiwaki *et al.*, 2001] and Se supply [Moon *et al.*, 2012, Matsushita and Takizawa, 1997]. During selenization, Se enters the film and forms a reaction front at the depth position, where it encounters the other elements or already formed phases. This depth position might be determined by the relative diffusion coefficients. Furthermore, a diffusion of an element would prevent or exclude it from the reaction front. Hence, a noteworthy aspect is the order of magnitude of the elemental diffusion coefficients in comparison to each other.

The range of measured  $D_{\text{Ga}}$  (and similarly  $D_{\text{In}}$ ) reaches from about  $1 \times 10^{-13} \text{ cm}^2\text{s}^{-1}$  up to  $1 \times 10^{-9} \text{ cm}^2\text{s}^{-1}$ , while  $D_{\text{Se}}$  reaches from  $2 \times 10^{-13} \text{ cm}^2\text{s}^{-1}$  [von Bardeleben, 1984] over  $(6.7 \pm 1.0) \times 10^{-11} \text{ cm}^2\text{s}^{-1}$  [Wang *et al.*, 2013] up to  $1.5 \times 10^{-8} \text{ cm}^2\text{s}^{-1}$

---

<sup>1</sup>Se vapor consists of various molecular species ( $\text{Se}_i$ ) with different thermal energy (due to different mass) and chemical activity. Their relative composition varies according to the temperature, especially within a difference from RT to 600 °C, as shown by [Rau, 1974]. An investigation on the mole fraction of the species in Se vapor from H. Rau [Rau, 1974] showed Se<sub>6</sub> to be the main molecular species in saturated selenium vapors up to 610 °C, above Se<sub>2</sub> becomes the dominant species.

[Kumar and Reddy, 1997], compare overview in sup. Fig. A.2).  $D_{\text{Se}}$  can be orders above or similar to  $D_{\text{Ga}}$ . A relation of  $D_{\text{Se}} > D_{\text{Ga}}$  with a difference in the order magnitude by  $10^2$  has been seen by Wang *et al.* at a temperature of 300 °C [Wang *et al.*, 2013]. Since Se is needed for the formation of CIGS, the magnitude of the different diffusion coefficients especially in relation to each other may determine the growth path. If  $D_{\text{Se}}$  exhibits the highest value, it can diffuse deep into the film to reach the rear side of already formed CIGS. In contrast, if  $D_{\text{Se}}$  gets smaller, other elements, such as Ga, may diffuse quicker through the CIGS layer than Se.

It was found, that  $D_{\text{Ga}}$  can be influenced e.g. by a Se containing / Se free environment, by the CGI as well as  $T_{\text{sub}}$ .

Regarding the Se supply, Marudachalam *et al.* showed, that annealing a film, in which  $\text{CuInSe}_2$  and  $\text{CuGaSe}_2$  are separated (CGI = 0.9-1) in a Se free Ar atmosphere at 500-600 °C for at least 60 min leads to formation of single phase CIGS by inter-diffusion [Marudachalam *et al.*, 1994, Marudachalam *et al.*, 1996, Marudachalam *et al.*, 1997]. Inter-diffusion occurred only in a Se free Ar atmosphere. At the same time, they observed a loss of Se from 51.8 at.% to 50.2 at.% Se in CIGS. They concluded that inter-diffusion is enhanced by the presence of Se vacancies ( $V_{\text{Se}}$ ). Furthermore, it was found by S. M. Wasim, that  $V_{\text{Se}}$  can lead to Se interstitials ( $\text{Se}_i$ ) or vacancies of Cu, In or Ga, with small energies of formation for Cu and In vacancies compared with that of Se interstitials [Wasim, 1986]. The result, that  $V_{\text{Se}}$  can lead to metal vacancies is important for the Ga diffusion, because metal vacancies are a preferred path for Ga and thus influence  $D_{\text{Ga}}$ : The dominant diffusion mechanism for Ga was suggested to be via vacant metal sites in the lattice structure for both cases, a Cu-rich (CGI>1) and Cu-poor (CGI<1) film composition [Lundberg *et al.*, 2003, Marudachalam *et al.*, 1996, Bodegård *et al.*, 2003]. This is also in agreement with an estimation of the diffusivities for Ga in  $\text{Cu}(\text{In},\text{Ga})_3\text{Se}_5$ , Cu-poor CIGS and Cu-rich CIGS (with present  $\text{Cu}_2\text{Se}$  phase) by Rodriguez-Alvarez *et al.* (2014), based on the results in the references [Marudachalam *et al.*, 1997, Schroeder *et al.*, 1996]. They conclude, that  $D_{\text{Ga}}$  increases with temperature and is 20 times higher in OVC (CGI $\approx$ 0.25) than Cu-poor CIGS (CGI $\approx$ 0.9) and 100 times higher in presence of  $\text{Cu}_2\text{Se}$  (CGI>1) than Cu-poor. An overview of the elemental diffusion coefficients found in literature is presented in Fig. A.2.

The film composition is a more important factor than the applied temperature in controlling the diffusion coefficient of Ga in  $\text{CuInSe}_2$ . This is concluded from the different ranges of the diffusion coefficient which is about two decades for varying the composition at each same temperature (500, 570 or 725 °C), while the range of the diffusion coefficients is only about one decade between 400-600 °C (compare Fig. A.2a) and Fig. A.2b)).

### Influence of the Se supply on the phase formation in the Cu-In-Se system

Matsushita *et al.* investigated the phase formation in the Cu-In-Se system with a decoupled Se source [Matsushita and Takizawa, 1997]. The authors varied the  $P_{\text{Se}}$  ( $T_{\text{Se}}$ , respectively) and expressed this value as a ratio  $x$  in  $(\text{CuIn})_{1-x}\text{Se}_{2x}$  ( $x=0-1$ ). The results led to the CuIn-2Se phase diagram, as shown in Fig. 1.7.

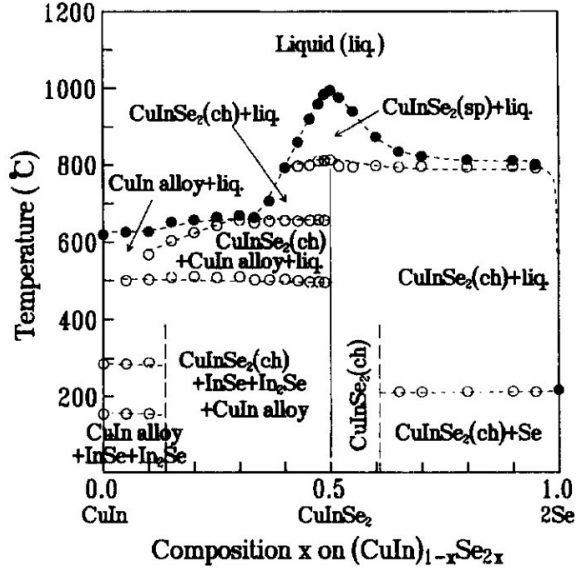


**Figure 1.7:** CuIn-2Se Phase diagram by Matsushita and Takizawa (1997), for which experiments were performed in a differential thermal analysis system (DTA) under controlled Se vapor pressure. The 2Se content corresponds to the Se vapor pressure. An understoichiometric Se offer ( $x < 0.5$ ) is referred to as low Se supply and an excess of Se ( $x > 0.5$ ) is referred to as high Se supply in this work.

The phase diagram shows significant differences for  $x$  below and above 0.5. An understoichiometric Se offer ( $x < 0.5$ ) is referred to as low Se supply and an excess of Se ( $x > 0.5$ ) is referred to as high Se supply in the following. In the range of a low Se supply, a liquid In-Se forms at 500 °C. Furthermore, the liquidus line of  $\text{CuInSe}_2$  decreases by 400 °C. This is not the case in the Se-rich ( $x > 0.5$ ) part.

## 1.4. Sequential growth of $\text{Cu}(\text{In},\text{Ga})\text{Se}_2$

The sequential growth consists of two steps: The first step is the preparation of the precursor. The second step is a reactive thermal treatment to activate chalcogenization. Various preparation methods for the precursor have been investigated in the past, like thermal evaporation [Voorwinden *et al.*, 2003], electrodeposition [Broussillou *et al.*, 2015], ink printing [Wang *et al.*, 2012] and sputtering [Rockett *et al.*, 1989]. The precursor can consist of metals only or may exhibit a chalcogen as capping or within the film. Typically applied chalcogens are Se and S. The chalcogenization is based on thermally activated reactions of the metals with the chalcogen. This thermal treatment has a duration between minutes and hours. The required chalcogen can be supplied either in the precursor or by an application of a

chalcogen containing atmosphere, i.e. Se/S vapor or  $\text{H}_2\text{Se}/\text{H}_2\text{S}$  or by a mixture of both. For this work, a Cu-In-Ga precursor was prepared by sputtering and is combined with the selenization in elemental Se vapor within few minutes. Fast processing is advantageous e.g. to decrease the cycle time and energy consumption for an industrial production.

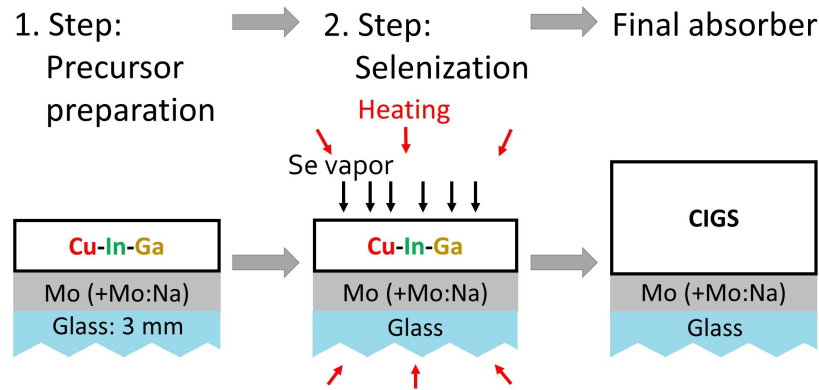


**Figure 1.8.:** Schematic of a sequential processing for the preparation of CIGS thin films, as it is applied in this work.

An overview of the current theory and understanding of the sequential growth of CIGS during selenization is presented in the following. The focus here is on a Cu-poor<sup>2</sup> precursor and Se as chalcogen, since S is not applied in this work. First, the growth of  $\text{CuInSe}_2$  is presented. The growth of CIGS with Ga is presented afterwards, as it increases the complexity. The typical CIGS thin film used for solar cells contains more In than Ga ( $\text{GGI} \approx 0.3$ ). The growth of CIGS typically leads to a segregation of Ga within the film with a higher GGI at the back contact. This chapter starts with describing the Ga free growth paths and continues with the case of Ga addition. Afterwards, results on the growth with resulting single phase CIGS are depicted. Finally, the discussion on the explanations for Ga segregation is summarized.

### 1.4.1. Growth of $\text{CuInSe}_2$

Wolf and Müller [Wolf and Müller, 2000] developed a qualitative model of  $\text{CuInSe}_2$  growth (Ga-free) (see Fig. 1.9). They combined the results from *in situ* thin film calorimetry and *ex situ* XRD obtained on different films. In-Se and Cu-Se films were thermally evaporated and Cu-In-Se films were sputtered. Their model presents a phase evolution, which is divided into four steps. The first step A is defined for the

<sup>2</sup>The Cu-poor precursor was chosen to prevent formation of  $\text{Cu}_2\text{Se}$ , which is highly conductive and produces shunt paths [Hsieh *et al.*, 2011]. Furthermore, Cu deficient surfaces are assumed to enable a Cd in-diffusion, which can decrease the valence band maximum at the interface [Nishimura *et al.*, 2017].

heating from RT to 220 °C. At around 150 °C metallic reactions form  $\text{Cu}_{11}\text{In}_9$  and In. Meanwhile, the layer of deposited Se, which was partly amorphous, crystallizes. In the second step B between 220 °C and 310 °C the former phases transform to  $\text{CuSe}_2$  and

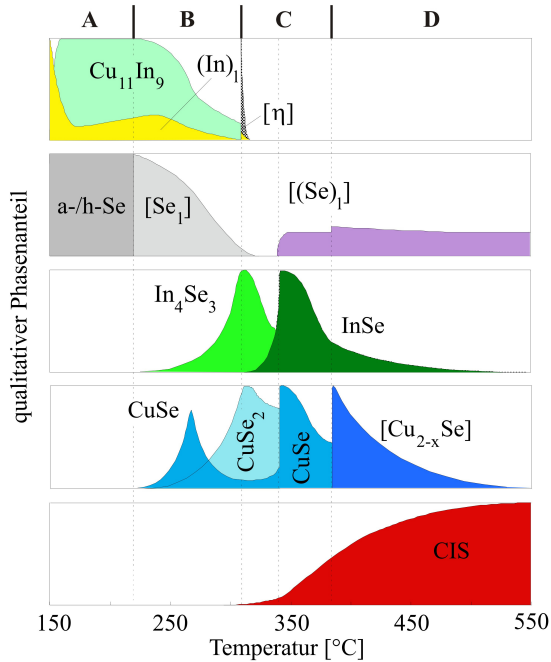


**Figure 1.9:** Evolution of qualitative phase content during reactive annealing of a Cu-In-Se film in a closed chamber (based on [Wolf and Müller, 2000], edited figure taken from [Purwins, 2010]). The compound  $\text{Cu}_{16}\text{In}_9$  is denoted as  $\eta$ . Amorphous and hexagonal Se is indicated as a-/h-Se. Square brackets indicate, that this phase was not found by XRD but is concluded from thin film calorimetry.

$\text{In}_4\text{Se}_3$ . The third step C between 310 °C and 380 °C is described as reactions with a Se exchange.  $\text{In}_4\text{Se}_3$  forms InSe with Se from the peritectic decomposition of  $\text{CuSe}_2$  to CuSe at around 340 °C. CuSe reacts peritectically to  $\text{Cu}_{2-x}\text{Se}$  at around 380 °C. It is concluded that  $\text{CuInSe}_2$  forms from CuSe and InSe in this step. In the last step D for a temperature beneath 380 °C the only existing copper selenide is  $\text{Cu}_{2-x}\text{Se}$  and therefore it reacts with InSe and Se to  $\text{CuInSe}_2$ .

### 1.4.2. Growth of CIGS with strong vertical Ga segregation

The original model from Wolf and Müller (Fig. 1.9) was further investigated by Hack [Hack, 2003]. Hergert *et al.* extended the model by the addition of Ga based on angle dispersive *in situ* XRD [Hergert *et al.*, 2005]. They found that large grains of  $\text{CuInSe}_2$  were formed latest at 377 °C. At 377 °C CuSe decomposes and  $\text{Cu}_2\text{Se}$  forms on top of the  $\text{CuInSe}_2$  crystals [Purwins, 2010]. Afterwards,  $\text{Ga}_2\text{Se}_3$  crystallizes at 400 °C and reacts with  $\text{Cu}_2\text{Se}$  to  $\text{CuGaSe}_2$ . Their models describe a growth with the resulting typical inhomogeneous Ga depth distribution.

Such a selenization with final Ga segregation was investigated by Mainz *et al.* (2015b) with combined *in situ* EDXRD/EDXRF and *ex situ* investigations. The evolution of their observed fluorescence and diffraction peak intensities is shown in Fig. 1.10. They

assume that the separation of  $\text{CuInSe}_2$  and  $\text{CuGaSe}_2$  initiates with In diffusion to the surface and a beginning formation of  $\text{In}_x\text{Se}_y$  (first  $\text{In}_4\text{Se}_3$  followed by  $\text{InSe}$ ). According to the authors, the subsequent stage ( $t=40\text{ s}$ ) involves the formation of  $\text{Cu}_{2-x}\text{Se}$  on top.  $\text{Cu}_{2-x}\text{Se}$  was identified by Raman spectroscopy but could not be observed in *in situ* EDXRD measurements. For  $\text{Cu}_{2-x}\text{Se}$  to be on top, Cu needs to diffuse to the surface which generally might be detected by an increase of  $\text{Cu-K}\alpha$ . Unfortunately, Cu fluorescence could not be detected due to attenuation of low energy photons by the setup. The  $\text{Cu}_x\text{Se}_y$  and  $\text{In}_x\text{Se}_y$  react to  $\text{CuInSe}_2$  while Ga enriches in the metallic phase at the back contact. Further Se diffuses in and  $\text{CuGaSe}_2$  forms. The main selenization reaction takes only a few tens of seconds. Afterwards a slower ordering of Cu and In or Ga occurs.

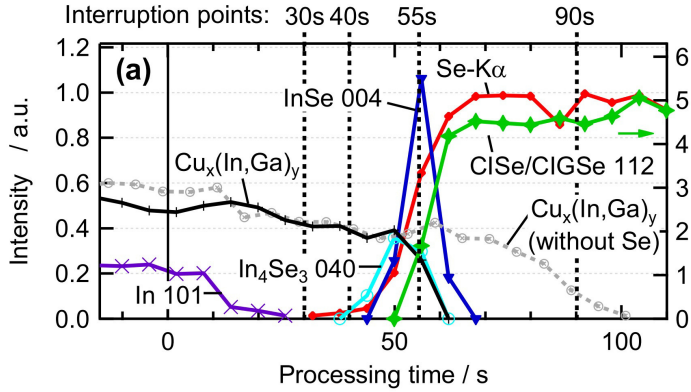


**Figure 1.10:** Evolution of integral reflection and fluorescence peak intensities from *in situ* EDXRD/EDXRF during a selenization of a Cu-In-Ga precursor.  $T_{\text{sub}}$  at 30 s is already above  $500^\circ\text{C}$  and reaches  $\approx 600^\circ\text{C}$  at 90 s. The figure is taken from [Mainz *et al.*, 2015b].

An important difference of the growth of CIGS to the growth of Ga free  $\text{CuInSe}_2$  are possible additional phases and solid solutions like  $\text{Cu}_{16}(\text{In},\text{Ga})_9$ ,  $\text{Cu}_9(\text{In},\text{Ga})_4$  and  $(\text{In},\text{Ga})\text{Se}$ . Only few identical phases are observed always in both cases, *i.e.*  $\text{In}_4\text{Se}_3$ . In the Ga free growth of  $\text{CuInSe}_2$ , Wolf and Müller could identify  $\text{CuSe}_2$ ,  $\text{CuSe}$  and  $\text{Cu}_2\text{Se}$  by thermodynamic and XRD analysis. In contrast to a growth with Ga, Mainz *et al.* found  $\text{Cu}_2\text{Se}$  on top of a film by Raman analysis after an interrupted selenization without any Cu-Se diffraction peaks and Purwins found  $\text{Cu}_{2-x}\text{Se}$  crystals on top of a film by SEM and saw a thermodynamic transition of  $\text{CuSe}$  to  $\text{Cu}_2\text{Se}$  at  $377^\circ\text{C}$ .

The CIGS growth path is still under investigation due to the difficult phase identification. An alternative thermodynamic assessment is also difficult with a quiet large span of standard formation enthalpies of  $\text{CuInSe}_2$  published. This inconsistency is a topic in many publications [Purwins, 2010, Anderson *et al.*, 2003, Guillemoles, 2000].

Gabor *et al.* suggested that the strain energy of the film is reduced by a preferred outdiffusion of In relative to Ga due to the larger atomic radius of In [Gabor *et al.*, 1996]. This assumption is based on similar behavior found in III-V materials [Lin *et al.*, 1987]. Further, Gabor *et al.* state this to be a competing mechanism to the presence of a homogenization force described by Fick's law and the concentration gradients.

### 1.4.3. Growth of CIGS with less distinct vertical Ga segregation

A CIGS film with Ga segregation can be transformed to a single phase CIGS by annealing it in a Se-free Ar atmosphere at 500-600 °C for at least 60 min as shown by Marudachalam *et al.* (1994, 1996, 1997) . They used a sputtered precursor with a CGI of 0.9-1, which was selenized in an  $\text{H}_2\text{Se}$  atmosphere for 90 min. This inter-diffusion of Ga and In could not be obtained in case of a Se containing atmosphere. They typically apply this in a three step process of selenization, homogenization and subsequent  $\text{H}_2\text{S}$  treatment.

Alberts *et al.* reached a single phase  $\text{Cu}(\text{In}, \text{Ga})(\text{S}, \text{Se})_2$  via sequential processing and a chalcogenization at atmospheric pressure with a not further specified gas concentration by a combination of  $\text{H}_2\text{Se}$  and  $\text{H}_2\text{S}$  in Ar [Alberts *et al.*, 2004]. They used a sputtered precursor with a CGI of 0.9 and a GGI of 0.25. Their growth schematic depicts two different approaches for growth of  $\text{Cu}(\text{In}, \text{Ga})(\text{S}, \text{Se})_2$  with either an initial formation of a single phase  $\text{Cu}(\text{In}, \text{Ga})\text{Se}_2$  with a post sulfurization forming a top layer of  $\text{Cu}(\text{In}, \text{Ga})(\text{S}, \text{Se})_2$  or an initial formation of binary selenides ( $\text{CuSe}$ ,  $\text{InSe}$  and  $\text{Ga}_2\text{Se}_3$ ) as well as  $\text{CuInSe}_2$  which is transformed to a single phase by sulfurization. Their tentative schematic for the reaction path shows  $\text{CuInSe}_2$  and intermediate phases like  $\text{Ga}_2\text{Se}_3$ ,  $\text{InSe}$ ,  $\text{CuSe}$  and  $\text{Cu}_2\text{Se}$  [Alberts, 2004]. The parameters for achieving these results are described by “careful optimization of reaction parameters such as temperature profiles, pressures, gas concentrations and durations of selenization/-sulfurization reaction periods” [Alberts, 2007]. They note, that an increase in gas concentration ( $\text{H}_2\text{Se}/\text{H}_2\text{S}/\text{Ar}$ ), reaction temperature or reaction period would increase the reaction between the remaining binary phases and result in  $\text{CuGaSe}_2$  formation. They showed this also for  $\text{Cu}(\text{In}, \text{Ga})(\text{S}, \text{Se})_2$  with an intermediate state, which consisted of  $\text{CuIn}(\text{S}, \text{Se})_2$  and  $\text{CuGa}(\text{S}, \text{Se})_2$  (identified by their 112 reflections in XRD) and a following inter-diffusion via long term processing [Alberts *et al.*, 2006]. Concerning the results from Alberts *et al.*, Hanket *et al.* denote [Hanket *et al.*, 2007], that the identification of phases is complicated due to the possible reflexes of  $\text{InSe}$  at  $2\theta$  angles, which were attributed by Alberts *et al.* to  $\text{CuSe}$  and  $\text{Ga}_2\text{Se}_3$ .

For a selenization with elemental Se, a higher Ga concentration ( $>0$ ) towards the sample surface was proposed to be adjustable by a steep heating ramp [Koo *et al.*, 2013]. Koo *et al.* used a precursor with a Se top layer and the selenization was performed under atmospheric pressure. They increased the heating ramp from 0.33 °C/s over 2 and 3 to 4 °C/s resulting in a shift of the CIGS 112 and 220/204 reflection peaks to higher angles and therefore higher Ga incorporation and reduced phase separation between  $\text{CuInSe}_2$  and  $\text{CuGaSe}_2$ . They explain their finding with the initial formation of  $\text{CuInSe}_2$ . If this  $\text{CuInSe}_2$  layer is acting as a diffusion barrier for the inter-diffusion of  $\text{CuGa}$  and Se

and the incorporation of Ga into CIGS, the  $\text{CuInSe}_2$  layer should be kept as thin as possible until a temperature regime is reached where Ga reactions take place.

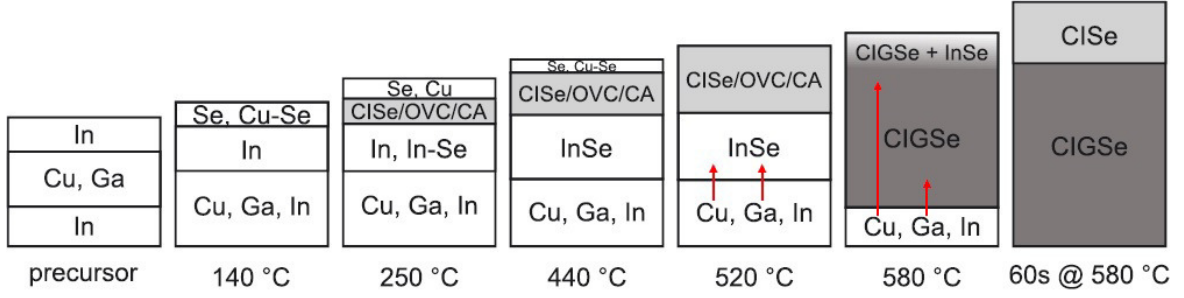


**Figure 1.11.:** Growth schematic for CIGS in relation to elemental depth distributions. Distinct movements of Cu, Ga, and In during the transitions to the next higher temperature or annealing time are denoted by red arrows, indicating the Ga movement towards the surface between 520 °C and 580 °C from [Schmidt *et al.*, 2017].

Recent *ex situ* studies [Schmidt *et al.*, 2017] with a tool for fast atmospheric selenization and elemental Se (see Sec. 2.1.2) resulted in an increased Ga concentration towards the film surface with selenization of only a few minutes. The proposed schematic of CIGS growth is shown in Fig. 1.11. Indications are found by Ga depth distribution from GDOES measurements, the observation of only one CIGS 112 diffraction peak instead of two as well as a shift of the inflection point between 1000 nm and 1300 nm in the EQE, which corresponds to a higher  $E_g$ . The authors suggest that the key was to reduce the Se supply. In contrast to the previous schematics (Fig. 110 in [Purwins, 2010] and Fig. 4 in [Mainz *et al.*, 2015b]), an ordered vacancy compound (OVC) as well as  $\text{CuInSe}_2$  in Cu-Au (CA) cation order was observed. A strong Ga diffusion is suggested to occur between 520 °C and 580 °C in their selenization. This is in agreement with observations reported in [Huang *et al.*, 2017]. Huang *et al.* observed a slight peak shift of the diffraction signal of CIGS 112 between 500 °C and 550 °C and an abrupt peak shift between 550 °C and 580 °C.

## Comparison and summary of sequential growth

Comparing the Ga free and the Ga containing growth of CIGS shows, that in a Ga free precursor, typically In and  $\text{Cu}_{11}\text{In}_9$  are identified. While with addition of Ga, the presence of In and  $\text{Cu}_{16}(\text{In},\text{Ga})_9$  are characteristic. Additionally, by increasing the Ga content, an increasing amount of  $\text{Cu}_9(\text{In},\text{Ga})_4$  is present. The further phase development exhibits some similarities. Especially  $\text{In}_4\text{Se}_3$  and InSe were found in both cases. Tentatively, this also holds for  $\text{CuSe}$  and  $\text{Cu}_{2-x}\text{Se}$  but the identification is in this case less certain and their role in the growth mechanism therefore under discussion. A participation of  $\text{Cu}_{2-x}(\text{S},\text{Se})$  (and  $\text{Cu}(\text{In},\text{Ga})_3(\text{S},\text{Se})_5$ ) at the reactive growth interface in

the formation of  $\text{Cu}(\text{In}, \text{Ga})(\text{S}, \text{Se})_2$  has been found by [Vieweg, 2007, Tuttle *et al.*, 1991, Schmid *et al.*, 1993, Kessler *et al.*, 1993, Marín *et al.*, 1998].  $\text{Ga}_2\text{Se}_3$  is found in In-free processes and therefore possible to form and to react very quickly to  $\text{CuGaSe}_2$  during growth of CIGS and thus difficult to detect.

The explanations for Ga segregation are summarized in the following with aid of Fig. 1.12. The typical initial state is a precursor, which can be prepared with several elemental depth distributions. Nonetheless, the melting temperature of In is  $157^\circ\text{C}$  [Ancsin, 1985] and thus, liquid In is very mobile during processing and is getting to the surface where it can react with Se vapor. In the next step, Cu diffuses in direction of the surface and reacts directly or via a binary Cu-Se with an In-Se to  $\text{CuInSe}_2$ . It might be that either In preferentially reacts with Se or Ga diffusion is lower than In diffusion with the consequence, that  $\text{CuInSe}_2$  formation occurs before  $\text{Ga}_x\text{Se}_y$  and  $\text{CuGaSe}_2$  formation. This can be summarized in two parts of growth. The first growth part exhibits Cu and In diffusion towards the surface. The second part is discussed by the fact, that  $\text{CuGaSe}_2$  forms last and at the back contact. For this, Se need to diffuse through the already formed  $\text{CuInSe}_2$  to the remaining metallic compounds of mainly Cu and Ga. Therefore the Se diffusion in the second part is higher than the metallic diffusion. The resulting Ga segregation suggests also, that Ga could not diffuse in direction of the surface. On the one hand there are explanations with equilibrium properties, like the formation enthalpy. The published values for the formation enthalpy  $H_{298}$  of  $\text{CuInSe}_2$  span a range from  $-280\text{ kJ/mol}$  up to  $-190\text{ kJ/mol}$  [Purwins, 2010, Ider *et al.*, 2014] which demonstrates the lack of thermodynamic data. The value might be smaller than the one for  $\text{CuGaSe}_2$  ( $H_{298} = -251\text{ kJ/mol}$  [Jäger-Waldau *et al.*, 1998]). On the other hand, this process is possibly far away from thermal equilibrium due to a fast heating rate and therefore strongly influenced or even dominated by kinetics. The surface film of In is such a kinetic growth condition. Additionally, it was found that  $\text{CuInSe}_2$  forms faster even at lower temperature than  $\text{CuGaSe}_2$  [Marudachalam *et al.*, 1997, Dittrich *et al.*, 1989].

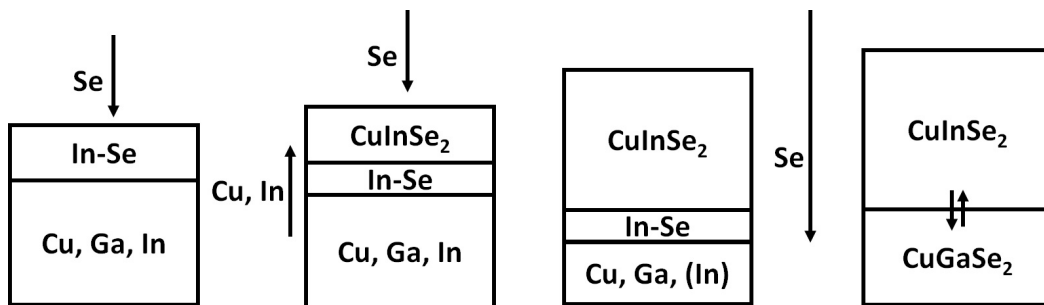


**Figure 1.12.:** Schematic of CIGS growth with Ga segregation. The first part exhibits a high diffusion of Cu and In to the surface, while in the second part, Se diffusion is higher than the diffusion of metals. At the end, inter-diffusion of In and Ga can occur under certain conditions.

Therefore  $CuInSe_2$  seems to be thermodynamically preferred. Another assumption is that Ga cannot easily diffuse through a formed layer like InSe [Huang *et al.*, 2017] or  $CuInSe_2$  [Koo *et al.*, 2013]. At least, the Ga diffusion is much smaller than the Se diffusion. This leads to another process value, the Se partial pressure which determines the diffusion coefficient of Se in CIGS (Fig. A.1b). From the CuIn-2Se phase diagram (Fig. 1.7) with its two differences for a high and a low Se supply, one can conclude, that  $P_{Se}$  might critically influence the CIGS growth and elemental diffusion processes. Unfortunately, it is difficult to measure  $P_{Se}$  due to the corrosivity of Se vapor and the temperature exceeds the electromechanic resistance of available measurement tools.

## 2. Experimental and analytical methods

The main focus of this work is the understanding of the reactive annealing of Cu-In-Ga precursor layers in Se vapor (selenization). The objective is to identify phases which are present at certain process times and assess depth distributions to understand the process route. A number of elemental, binary and ternary phases are present before CIGS is formed. A simple approach is to interrupt a process at specific stages and to analyze the quenched samples. Disadvantages of this approach are that some fast reactions might be missed and that the state of the sample at the interruption time might change during cool down and is not easily correlated with a specific temperature. These disadvantages can be avoided by *in situ* analysis of the crystal structures and depth distribution by energy dispersive X-Ray diffraction (EDXRD) and fluorescence (EDXRF). The diffraction peaks allow a phase identification. The fluorescence intensities allow to draw conclusions about the elemental depth distribution.

This chapter starts with the description of the sample preparation of the substrate and precursor as well as the different tools for annealing and selenization. The characterization of CIGS growth by EDXRD, EDXRF and the method for calculating EDXRF intensities are explained. This chapter closes with a short overview of the further characterization methods utilized for the present work.

### 2.1. Cu(In,Ga)Se<sub>2</sub> absorber preparation

#### 2.1.1. Cu-In-Ga metal precursor deposition

The substrate consists of 3.1 mm thick soda lime glass, coated with a sequence of SiO<sub>x</sub>N<sub>y</sub>/Mo/Mo:Na/Mo or SiO<sub>x</sub>N<sub>y</sub>/Mo on top of which the precursor stack is deposited. All layers are magnetron sputtered using a Leybold Optics Dresden A600V7 DC. SiO<sub>x</sub>N<sub>y</sub> acts as a diffusion barrier for Na from the substrate and is about 150 nm thick. The Mo/Mo:Na/Mo layer with a total thickness of 850 nm contains a 70 nm thick middle layer of Mo:Na (with 5 wt.% Na). It is applied to provide a laterally homogeneous and

defined amount of Na for CIGS growth since it influences grain growth and doping. Na-free Mo with 800 nm thickness is used throughout all presented *in situ* measurements in Ch. 4 and for the study of Na influence on the morphology of a precursor during thermal treatment in Ch. 3.3. A Cu-Ga (75 % Cu) and an In sputter target are utilized for the 700 nm thick precursor stacks. Different precursors were prepared for this study: i) In/CuGa and ii) CuGa/In bilayers, iii) triple layer precursor consisting of one In/CuGa/In stack and iv) multilayer precursors containing 22 In/CuGa/In triple layers. The total thickness of all precursors was kept constant and all exhibit an integral  $[\text{Cu}]/([\text{Ga}]+[\text{In}])$  (CGI) ratio of about 0.87 and a  $[\text{Ga}]/([\text{Ga}]+[\text{In}])$  (GGI) ratio of about 0.27, monitored by X-ray fluorescence (XRF) in a WD-XRF ZSX Primus II from Rigaku.

### 2.1.2. Selenization of metallic precursor layers

The setup for EDXRD and additional experiments in this work are i) a vacuum chamber with a closed reaction box inside (extended by an external Se source during this work) which can be set up at a synchrotron and ii) an industrial selenization tool working at atmospheric pressure. Further, iii) a vacuum chamber is utilized, which is normally used for thermal co-evaporation.

#### i) Vacuum based RTA/RTP tool

A reaction box in a vacuum chamber, free of selenium and sulfur, was used for the annealing of metallic Cu-In-Ga precursors in vacuum (Ch. 3). The principle was described earlier in [Rodriguez-Alvarez *et al.*, 2008]. The cylindrical reaction chamber consists of a graphite ring and quartz bottom and top to allow heating by lamps, see Fig. 2.1b. The base pressure was about  $10^{-7}$  mbar at RT. Heating experiments were performed up to a maximum substrate temperature of 600 °C and heating rates of up to 1 °C/s were applied. After heating, the lamps were switched off and the sample cooled down passively with an initial cooling rate of 1.9 °C/s. A temperature of 400 °C was reached after 3.9 min; 300 °C was reached after 13 min.

The tool was extended by an in-house built external Se source as shown in Fig. 2.1b. The reaction chamber can be closed via the chamber valve to enable a Se vapor pressure controlled by the Se crucible temperature. The setup can be used at the synchrotron to measure *in situ* EDXRD and EDXRF. The *in situ* measurement setup is sketched in Fig. 2.3. The vacuum chamber exhibits two windows with 50 µm thick Kapton foil and the reaction chamber exhibits two graphite windows of 1 mm thickness for the beamline.

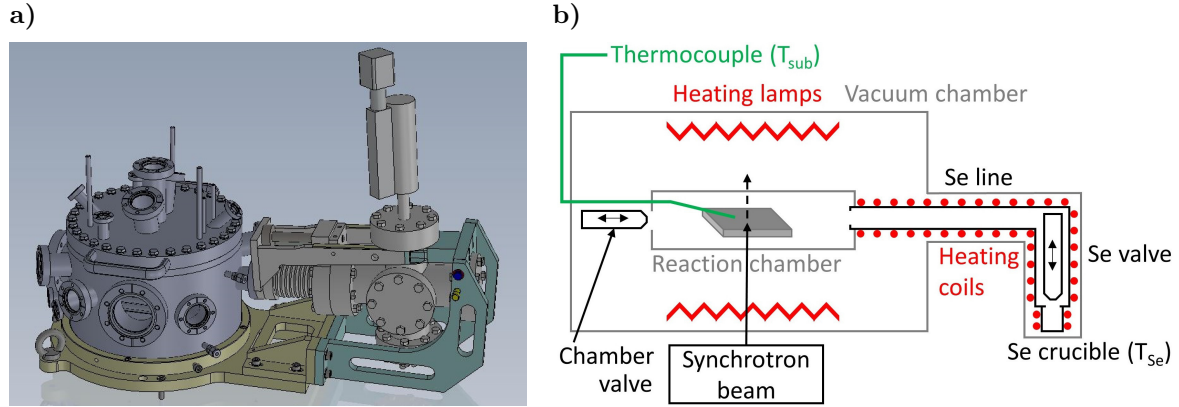


**Figure 2.1.:** Vacuum selenization tool with external Se source as a) construction drawing and b) schematic cross view. The vacuum chamber is pumped to an initial pressure below  $1 \times 10^{-5}$  mbar. The reaction chamber can be decoupled from the vacuum chamber by the chamber valve. The substrate temperature ( $T_{sub}$ ) is measured by a thermocouple for a temperature control, which is positioned approximately 2 mm above the sample. The reaction box has a graphite wall and quartz top and bottom, to enable heating of the sample by infrared light. The selenium source has three heating coils (around Se line, Se valve and Se crucible), which are controlled by thermocouples. The temperature of the Se crucible is defined as Se source temperature ( $T_{Se}$ ). The other two heating coils prevent a condensation of the Se vapor and are set to  $20^\circ\text{C}$  above  $T_{Se}$ . A synchrotron beam is indicated, because this setup can be applied to a synchrotron, see details in Fig. 2.3.

It was found during this work, that the Se crucible valve (Se valve) does not close perfectly and there is always Se condensation in the Se line from the cool down of the previous experiment. To mitigate these circumstances and to assure that the Se vapor pressure is controlled by the crucible rather than the Se line, bake out processes were carried out before each new experiment without heating the crucible directly. The Se source is attached to the graphite reaction chamber, which is at a lower temperature than the Se source during warm up of the source. Therefore the reaction chamber is cooling the opening of the attached Se line. To avoid a cold spot of the opening and therefore condensation of Se with clogging of the Se line, the standard procedure includes heating the substrate to  $T_{Sub} = 170^\circ\text{C}$  before heating the Se source. During a second annealing step at  $220^\circ\text{C}$ , the Se crucible is heated to processing temperature  $T_{Se}$ . The Se vapor gets sucked out of the reaction chamber by the surrounding vacuum chamber. Then, the valve of the reaction chamber is closed and the rapid thermal processing with selenization is started.

Another important difference to earlier setups is a thinner graphite window in the beamline for a decreased absorption loss. This enables the measurement of the Cu fluorescence for the first time.

The thermocouple for measuring the substrate temperature is placed 5 mm over the sample. This leads to a systematic error, which is concluded from the fact, that the thermally induced shift of diffraction peaks (e.g. Mo 110) due to heating of a sample to 170 °C continues during a following constant temperature. Further evidence is indicated by the melting of In during this 170 °C plateau, although the melting point of In is at 157 °C [Ancsin, 1985]. The temperature deviation is at least 14 °C.

Some preliminary remarks about Se during process preparation should be made. During warm-up of the Se source, Se condensates on the sample leading to appearing and increasing signals of Se from X-ray fluorescence and diffraction (compare Se fluorescence and reflection signals at  $t_{Se1}$  in Fig. 4.3). The warm-up of the Se line also indirectly heats the sample. Hence, for reproducibility and comparability reasons, the following heating steps were performed in every process: During warm-up of the Se source, the sample is kept at a constant temperature of 170 °C by the heating lamps. Then the precursor gets heated to 220 °C to evaporate the condensed Se for an initial state previous to the RTP step.

## ii) Atmospheric RTP tool

Atmospheric selenization is done in an in-line RTP selenization tool from Smit Thermal Solutions which allows a sample size of up to 30×30 cm<sup>2</sup>. Three hot wall chambers are equipped with external Se sources (a forth one with S) and are used for a typical selenization process, shown in Fig. 2.2.

All chambers and sources are heated to a specific temperature before the process to reach equilibrium state. The Se vapor is transported with an adjustable N<sub>2</sub> flow via an array of inlets into the reaction chamber. The process starts after purging with pump and flush cycles in the load-lock. The temperature of the chambers are  $T_{ch1} = 300$  °C,  $T_{ch2} = 710$  °C and  $T_{ch3} = 580$  °C. The temperatures of the Se sources  $T_{Se2}$  and  $T_{Se3}$  are both at 390 °C (or 420 °C, respectively) while the first is without Se supply at  $T_{Se1} = 90$  °C. The N<sub>2</sub> flows (measured in standard litre per minute: slm)  $F_{N_2}(2, 3)$  are at 1 slm while  $F_{N_2}(1)$  is 0 slm. For the first step the sample is transported to chamber 2, where it heats up with more than  $> 7$  °C/s to 580 °C. Then it moves to the third chamber for an annealing for  $t_{Ch3} = 6$  min. Afterwards the sample starts to cool down passively in the first chamber under a temperature of 300 °C for  $t_{Ch3} = 5:30$  min and is then actively cooled in the load-lock under N<sub>2</sub> pump and purge steps till the substrate temperature is beneath  $T_{sub} \approx 90$  °C.

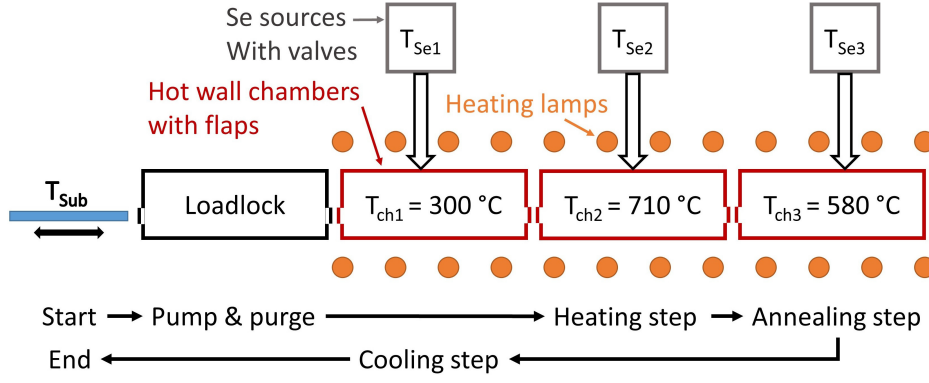


**Figure 2.2.:** Schematic of the atmospheric selenization tool and process steps indicated underneath. The chambers are at fixed temperatures  $T_{ch1,2,3}$ . The temperatures of the Se sources  $T_{Se2}$  and  $T_{Se3}$  are both at 390 or 420 °C while the first is without Se supply at  $T_{Se1} = 90\text{ °C}$ . The sample is transported via a pulley system. The process starts by purging with  $N_2$  pump and flush cycles in the load lock. Then the substrate is heated in the second chamber to reach  $T_{Sub} = 580\text{ °C}$ . This is followed by an annealing step for  $t_{Ch3} = 6\text{ min}$ . At last, the substrate cools down passively in the first chamber for  $t_{Ch3} = 5:30\text{ min}$  and is finished with an actively cooling by  $N_2$  pump and flush in the load lock to reach a temperature beneath  $T_{sub} \approx 90\text{ °C}$ .

### iii) Tool for physical vapor deposition (PVD)

This chamber is used for *in situ* EDXRD/EDXRF of Se free annealing of a Cu-Ga-In precursor (Sec. 4.1) as well as selenization of a Cu-Ga-In precursor.

The chamber holds the sample face down and there is one heater above the substrate. A Se source for thermal evaporation is mounted at the bottom of the chamber and the deposition rate is adjusted by its temperature and measured with a quartz thickness monitor. The chamber can be mounted at the EDDI beamline at BESSY II for *in situ* EDXRD. The sample holder was cleaned by bake out for a Se free annealing of the precursor for Sec. 4.1. The actual sample temperature deviates from the set point by up to 20 K. A schematic and further experimental details can be found in [Stange *et al.*, 2016, Mainz *et al.*, 2015a, Rodriguez-Alvarez *et al.*, 2013].

### 2.1.3. Preparation of solar cells

The preparation of solar cells vary by two different combinations of buffer and window materials on the absorber: 1) CdS/i-ZnO/Al:ZnO and 2) Zn(O,S)/i-ZnO followed by ZnO:Al by 2a) sputtering or by 2b) atomic layer deposition (ALD). For 1) a 60 nm thick CdS layer is applied by chemical bath deposition (CBD). For this purpose, the mixed solutions of a 2 mM Cadmiumacetate dissolved in 1 M Ammonia and a 8 mM Thiourea solved in water were heated to 65 °C. The following intrinsic ZnO

(i-ZnO) with 130 nm thickness was RF-magnetron sputtered by use of a Von Ardenne Anlagentechnik VISS 300 (VISS 300) system. For 2) Zn(O,S) as a Cd free buffer is deposited. In case 2a) Zn(O,S)/i-ZnO was sputtered by a VISS 300 with thicknesses of 60/130 nm. In case 2b) Zn(O,S)/i-ZnO were deposited by ALD in a Beneq TFS 500 at 130 °C with 60 nm Zn(O,S) (9:1 cycle ratio of ZnO:ZnS corresponding to a  $[S]/([S]+[O])$  of about 25%) and 75 nm i-ZnO as protection from sputter damage [Merdes *et al.*, 2014, Merdes *et al.*, 2015]. In all cases, 240 nm ZnO:Al was sputtered (by VISS 300) as transparent front contact and finally a Ni/Al contact grid was deposited by electron beam evaporation in a Creamet®400 by Creavac.

## 2.2. Main characterization methods

The aim of this work is to understand the growth of CIGS during thermally activated and fast reaction of a sputtered Cu-In-Ga precursor in elemental Se vapor (selenization). This investigation is mainly based on the analysis of *in situ* energy dispersive X-ray diffraction (EDXRD) and fluorescence (EDXRF) spectra. Observed diffraction peaks are used to identify crystalline phases and are analyzed<sup>1</sup> with regard to e.g. integral intensity, energetic position *etc.* and their evolution over time. The major setup for the measurement consists of the vacuum selenization tool, presented in Fig. 2.1, which is applied to the EDDI beamline at BESSY II, see Fig. 2.3.

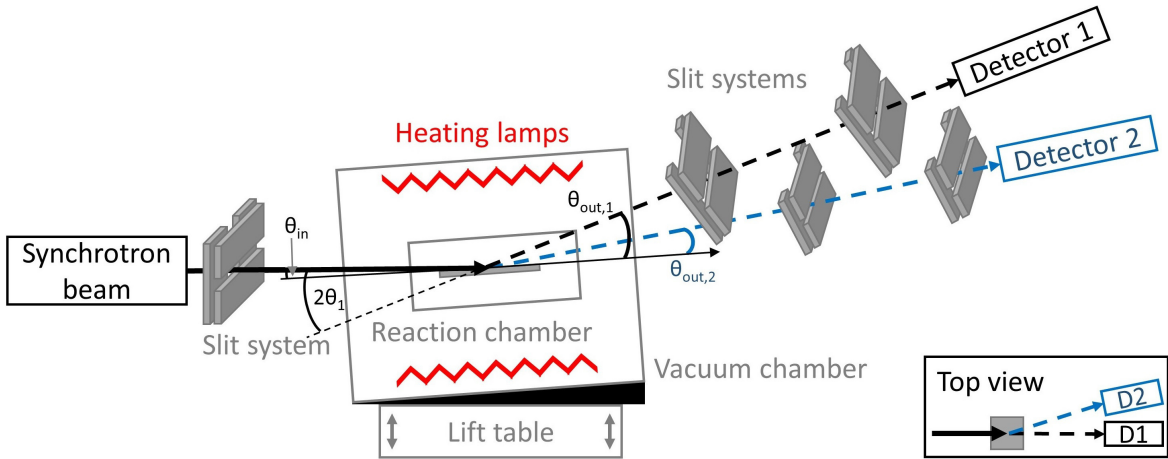


**Figure 2.3.:** Application of the vacuum selenization tool from Sec. 2.1.2 for the EDXRD/EDXRF measurement at a synchrotron, shown in side and top view. Several slit systems are needed to reduce the beam cross-section. The synchrotron beam enters (and leaves) via Kapton (0.05 mm thick) and graphite (0.5 mm thick) windows. In between, it interacts with the sample. Outgoing photons are collected with two detectors. The sample height position is adjusted with the lift table.

<sup>1</sup>Sources of errors are explained in the sup. Ch. B.

During a thermal treatment, the sample thickness can thermally change by up to 200  $\mu\text{m}$ , which is compensated by adjusting the sample height position with the lift table, which is software controlled by adjusting to the maximum Mo- $K\alpha$  intensity (see Sec. B).

For the calculation of fluorescence intensities, both angles between the sample and the incident beam as well as the reflecting beam to the detector are needed. The angle  $\theta_{in}$  was measured with photo paper by making a point with the beam at different sample height positions.  $\theta_{1,2}$  are determined by an angle calibration, as it is explained in Sec. B. The reflection angle  $\theta_{out,1}$  is calculated for detector 1 with the equation  $2\theta = \theta_{in} + \theta_{out,1}$ . While detector 1 is placed in line with the beam direction, detector 2 is rotated out of plane. The resulting angle between the sample and detector 2 is defined as  $\theta_{out,2}$ . With the position of the active volume, the  $\theta_{out,2}$  can be calculated as following:  $\cos(90^\circ - \theta_{out,2}) = \frac{-y \sin(\theta_{in}) + z \cos(\theta_{in})}{\sqrt{x^2 + y^2 + z^2}}$ . The Euclidean distance of the detector (d) to the active volume (a) is given by  $\sqrt{x^2 + y^2 + z^2} = \sqrt{(x_d - x_a)^2 + (y_d - y_a)^2 + (z_d - z_a)^2}$ , which is measured manually.

The setup of the PVD tool at the EDDI beamline exhibited the angles  $2\theta_1 = 6.275^\circ \pm 0.002^\circ$  and  $2\theta_2 = 9.696^\circ \pm 0.002^\circ$  (see [Stange *et al.*, 2016]), as applied in Sec. 4.1. The angle of the sample surface with the incident synchrotron beam was  $\theta_{in} = 2.83^\circ \pm 0.01^\circ$  and with the outgoing beams  $\theta_{out,1} = 3.43^\circ \pm 0.15^\circ$  and  $\theta_{out,2} = 1.20^\circ$ .

The setup of the vacuum RTP tool at the EDDI beamline exhibited the angles  $2\theta_1 = 5.975^\circ \pm 0.002^\circ$  and  $2\theta_2 = 9.940^\circ \pm 0.002^\circ$ , as applied in Secs. 4.2 and 4.3. The angle of the sample surface with the incident synchrotron beam was  $\theta_{in} = 3.61^\circ \pm 0.01^\circ$  and with the outgoing beams  $\theta_{out,1} = 2.37^\circ \pm 0.15^\circ$  and  $\theta_{out,2} = 0.93^\circ$ .

A special feature is, that the data of EDXRD and EDXRF is collected within a single spectrum, as shown with an exemplary spectrum in Fig. 2.4. The applied angle  $2\theta_1$  leads to a distribution of the fluorescence and diffraction peaks with only little overlap. Above the fluorescence with the highest energy, which is In- $K\beta_2$  with 27.863 keV, only diffraction peaks are observed. Below that energy, only few diffraction peaks occur. These spectra are obtained every 3 s and the presentation over time is exemplarily shown in Fig. 2.4b).

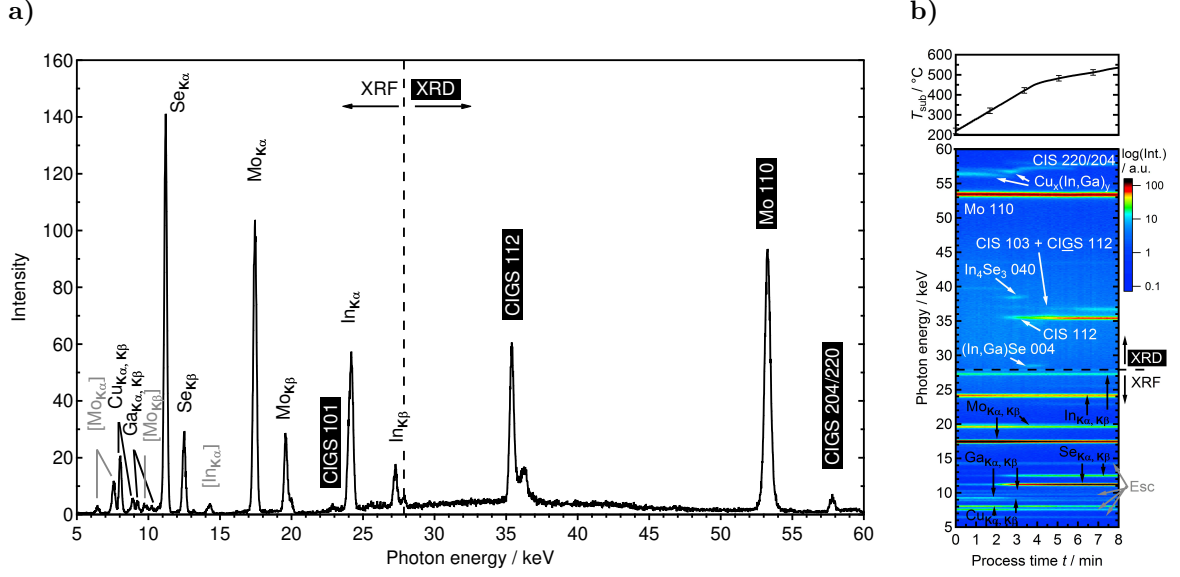


**Figure 2.4.:** Exemplary a) single spectrum and b) series of spectra over time (and substrate temperature on top), observed from EDXRD/EDXRF measurement. Diffraction (white) and fluorescence (black) peaks are indicated. The intensity in b) is color coded, as indicated on the right hand side. The indications in gray and with square brackets are photons, that are reduced by an energy of 9.875 keV, resulting from an ionization of Ge in the detector. These peaks are so called escape peaks. Their intensity decreases towards higher energies and are nearly not measurable above 30 keV [Buras and Gerward, 1989].

### 2.2.1. Energy dispersive X-ray diffraction (EDXRD)

The measurement of diffracted X-rays is used to identify crystalline phases. Continuous and real time measurements are performed and analyzed to exhibit the evolution of the crystalline phases regarding their intensity and composition.

The difference of the incoming and outgoing wave-vectors  $\vec{k}$  and  $\vec{k}'$  gives the lattice vector  $\vec{G}_{hkl}$ , which is perpendicular to the diffracting lattice plane. The equation,  $\vec{G}_{hkl} = \vec{k} - \vec{k}'$  (with  $|\vec{k}| = |\vec{k}'|$ ) is called Bragg's law. The lattice plane of atoms contributing to the reflection is defined with Miller's indices hkl. The perpendicular distance between the successive planes is  $d_{hkl}$ . It is correlated to the lattice vector via the equation  $d_{hkl} = 2\pi/|\vec{G}_{hkl}|$ . Together with  $k/2\pi = E_{Photon}/hc$ , the energy dependence of the lattice plane distance can be expressed with  $d_{hkl}(E_{Photon}) = nhc/2E_{Photon}\sin\theta$ .  $n$  is an integer representing the order of the reflection.  $\theta$  is the angle of the incident radiation as well as the reflected beam to the lattice plane.  $h$  is Planck's constant and  $c$  is the speed of light.

A polychromatic synchrotron beam is used here. As a consequence, various lattice

planes fulfill the Bragg's law with the appropriate photons. An energy dispersive detector can collect all of them for a single spectrum.

More details about the reflection of photons and the Bragg condition can be found in many books like [Kittel, 2006, Hunklinger, 2009].

The EDXRD spectra are used to determine the crystal phases. A Gaussian curve is fitted to the signals to determine the energy of the peak. Crystal phases are identified by comparing the analyzed reflections to reference patterns from the database of the International Center for Diffraction Data (ICDD). In case of a temperature above RT, thermal expansion coefficients are used to calculate the temperature dependent pattern positions. The references of used patterns and thermal expansion coefficients are listed in sup. Tabs. E.2 and E.3.

The applied spectrum at the EDDI beamline (Energy Dispersive Diffraction) is shown in [Genzel *et al.*, 2006]. It is generated by electrons, which get accelerated to a circular movement with a velocity close to the speed of light. The transverse acceleration by magnetic forces by e.g. a wiggler magnet leads to tangential radiation of synchrotron light. The electron bunch is permanently filled in top-up mode to a ring current of 300 mA. A 7 T multipole wiggler supplies the beamline EDDI with a high energy white photon beam for diffraction, which is described elsewhere in detail [Berger *et al.*, 2002]. The energy dispersive setup includes two Germanium solid state detectors (Canberra) with a resolution of 160 eV (at 10 keV) and 420 eV (at 100 keV). The advantage is a fast measurement with a time resolution down to 3 s. The usable energy range of X-rays starts at around 5 keV and goes up to  $\approx 100$  keV. Further, it is possible to get depth information, as explained in 2.2.2. A calibration for the energy and the diffraction angle is done with the fluorescence and diffraction lines of gold. The beam-area on the sample surface is approximately 1 mm $\times$ 2 mm.

### 2.2.2. Energy dispersive X-ray fluorescence (EDXRF)

The evolution of the relative intensity of X-ray fluorescence signals were evaluated to get indications for a change in the elemental depth distribution. By calculating the fluorescence intensities of specific elemental depth distributions, it is often possible to select depth distributions which may actually be present in the sample from the wider range of distributions which might in principle be present. The calculation is based on the fundamentals and resulting applied equations described in this section. Further details can be found in [Mainz, 2008]. The general working principle is outlined in Fig. 2.5.

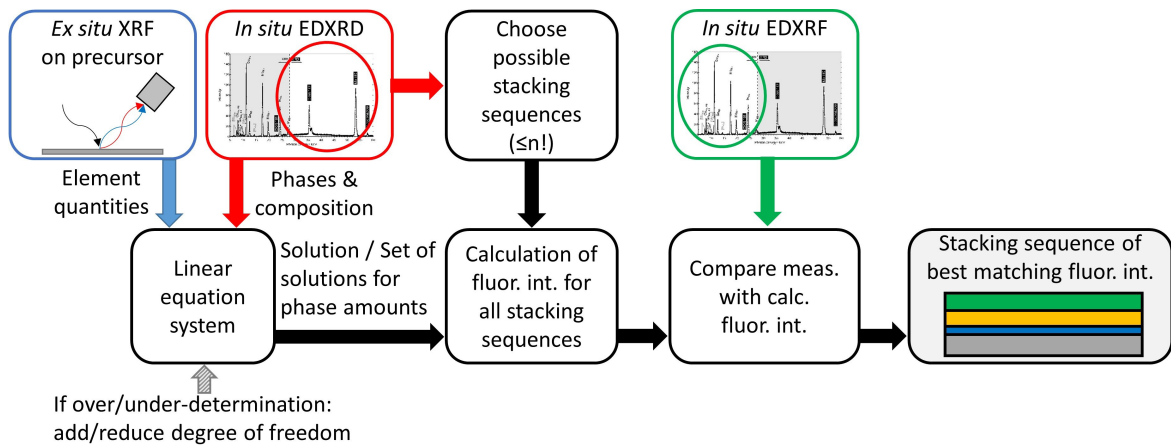


**Figure 2.5.:** Schematic of the working principle for the deduction of a phase depth distribution (stacking sequence) by use of the software EDXRFfit. An *ex situ* XRF measurement of the precursor defines the projected number of Cu, In and Ga atoms per  $\text{nm}^2$  (element quantity per area). Phases and their composition are deduced from *in situ* EDXRD at a specific point in time  $t_i$ . A linear equation system is built with the known phase compositions and known total element quantities and the unknown phase amounts. The linear equation system determines the phase amounts. The thickness of each phase is determined by its atomic density. The calculated densities are listed in sup. Tab. E.1. This results in an elemental stacking sequence, with which the fluorescence intensities are calculated, see Sec. 2.2.2.2. In general, the  $n$  phases have  $n!$  variations of a possible stacking sequence. Then, the calculated fluorescence intensities of all stacking sequences are compared with the *in situ* obtained fluorescence intensities at  $t_i$ . In the ideal case, there is only one stacking sequence, whose calculated fluorescence intensities are matching the experimental values. This is then repeated for different points in time to obtain an evolution of the phase depth profile. Difficulties can occur, for example, in an under-determined linear equation system with too many free parameters, e.g. number of phases. Then, additional parameters need to be fixed, see Sec. 2.2.2.3.

Energy dispersive X-ray fluorescence (EDXRF) is mainly dependent on the elements, their amounts and the attenuation by the sample itself. Intensity is attenuated by the traveling length through the sample as well as the density of the elements. A decreasing intensity of an element is correlated with a deeper depth position, as long as it is not evaporating. The traveling length is dependent on the incoming and outgoing beam angles to the surface,  $\theta_{in}$  and  $\theta_{out}$ . Thus the fluorescence signals from a lower angle are more surface sensitive. With the two detectors at different outgoing angles, both are compared with each other and with the calculated fluorescence intensities. Due to the simultaneous measurement (in the same detectors) of EDXRD and EDXRF their results can be correlated. Fluorescence calculation is based on the material,  $\theta_{in}$ ,  $\theta_{out}$  as well as to the detector and on defining a depth distribution function. The depth distribution function will be expressed by only a few free parameters. These parameters

are the identified phases, their densities and an assumed layered stack. The fluorescence signal intensities are calculated numerically. The result is compared with the intensities from experiment and the depth distribution is adjusted to find an adequate accuracy. This procedure allows to identify depth distributions which contradict the experiment and hence can be excluded from the possible distributions. EDXRFfit is the program used to calculate the fluorescence intensities [Mainz, 2008, Mainz and Klenk, 2011]. Some parameters from the experimental setup are considered by the program such as slight absorptions for example by air and setup windows. In case of the incident beam, a sequence of Al window/air/KAPTON (polyimide foil)/graphite with thicknesses of 0.3/200/0.05/0.5 mm is taken into account. From the sample to the detector, the outgoing beam travels through the sequence of graphite/KAPTON/air with thicknesses of 0.5/0.15/400 mm. For example, the attenuation of the radiation by the polyimide foils is calculated from its composition ( $C_{22}H_{10}N_2O_5$ ), density ( $1.43 \text{ g/cm}^3$ ) and the atomic cross sections of its elements as described by [Henke *et al.*, 1993]. The absorption of the beam in air is very small. Used densities of phases for the calculation of the layer thicknesses are listed in the sup. Tab. E.1.

### 2.2.2.1. X-ray fluorescence

X-ray fluorescence is the emission of an X-ray from an electron relaxing in an atom. The electron relaxes from an outer shell to an inner free level. E.g., the transition from an  $L_x$  shell to the  $K$  shell is called  $K\alpha_x$  and from  $M_x$  or  $N_x$  to  $K$  as  $K\beta_x$ . The energy of the emitted X-ray is characteristic for each element. Here, the free electron level is created by an inner electron which absorbs an X-ray with enough energy to eject the electron from the atom to the vacuum level (ionization). Due to the close energies of  $K\alpha_1$  and  $K\alpha_2$ , only their sum is analyzed as  $K\alpha$ . The same is done for  $K\beta_x$ .

### 2.2.2.2. Calculation of the fluorescence intensities and multiple fluorescence

The following is a short description of the calculation of the fluorescence intensities, as developed in [Mainz, 2008]. A complete derivation of the calculation equation and further details can be found in the references [Mainz, 2008, Mainz and Klenk, 2011]. The process described so far, is the absorption of a synchrotron photon and the emission of a fluorescence photon of a specific element. If this primary fluorescence photon has an energy high enough to ionize another element, it can lead to a secondary fluorescence. With the five elements here, a five-time fluorescence might be possible starting with a fluorescence photon from In which might lead to a secondary fluorescence of Mo. In turn, the fluorescence photon from Mo can lead to further ionization and fluorescing of

Se, followed by Ga and finally Cu (compare Tab. 2.1). Generally, the total fluorescence intensity is a sum of all single and multiple fluorescences. A maximum of 5% of primary fluorescence lead to secondary fluorescence as shown in [Mainz and Klenk, 2011] for Mo/CIGS and a layer thickness of about 1.7  $\mu\text{m}$ . Only the primary and secondary fluorescence are used for the calculation and every further fluorescence is neglected.

**Table 2.1.:** This table shows the fluorescence energies  $E_{K\alpha_1}$  and  $E_{K\beta_1}$  and the elements with a lower ionization energy with the possibility for a secondary fluorescence. [Thompson *et al.*, 2009]

Element 1	$E_{K\alpha_1}/\text{keV}$	$E_{K\beta_1}/\text{keV}$	Element 2	$E_K/\text{keV}$
Ga	9.25	10.26	Cu	8.98
Se	11.22	12.50	Cu	8.98
			Ga	10.37
Mo	17.48	19.61	Cu	8.98
			Ga	10.37
			Se	12.66
In	24.21	27.28	Cu	8.98
			Ga	10.37
			Se	12.66
			Mo	20.00

The attenuation of both the incidence and the fluorescence radiation is dependent on the spacial distribution of sample elements. The longer the distance of an atom from/to the surface, the smaller the probability for a incidence photon to reach the atom as well as for a fluorescence photon to leave the sample. So, the changing elemental depth distribution is the only influence on the fluorescence intensities as long as the total amount of elements is constant. In this case, the fluorescence intensities give information about the elemental depth distribution. It should be noted, that Se condensation and incorporation occur and that an evaporation of  $\text{In}_x\text{Se}_y$  is possible.

The total fluorescence intensity is the sum of primary and secondary fluorescence. The calculation is performed numerically. For this, the film is subdivided into homogeneous plane parallel layers, in this case 200. Fluorescence intensities are calculated with the probability of absorption of an incoming photon after traveling through the  $\Delta z_i$  thick layers under the angle  $\theta_{in}$  for each layer, together with the probability for creating a fluorescence photon and the probability of this fluorescence photon to exit the film under  $\theta_{out}$ . The secondary fluorescence is extended by its additional probabilities of being absorbed from another element and emitted as a fluorescence photon.

### 2.2.2.3. Parametrization

An arbitrary depth distribution may need a large number of parameters for an exact description of its various changes. For the calculation, however, the distribution needs to be described by a limited number of parameters. This is done with the phase information from EDXRD. The final calculation of the elemental depth distribution in EDXRFfit is performed by assuming parallel planes of homogeneous layers. An influence on the calculation of the fluorescence intensities by roughness of the interface was investigated in [Mainz, 2008]. It was shown, that the model with a corrugated interface was indistinguishable from a model with linear mixing.

The degree of freedom can be written for  $n$  layers and  $m$  elements as [Mainz, 2008]

$$f_{m,n} = n - m. \quad (2.1)$$

The atomic areal density is assumed as being constant for every phase. The result is, that for the simulation an input of the amount of elements is necessary. In general, for every layer in the calculation of the film, the amount of exactly one element is needed to solve the equations, for example for 5 phases, 5 element amounts are needed. Since there are 5 elements (Mo, Cu, Ga, In, Se) a maximum of 5 phases (layers, respectively) can be defined with a possible solution. For every additional layer, another degree of freedom needs to be eliminated, which is possible by fixing the atomic fraction of a layer with respect to the total amount of atoms.

The *in situ* EDXRF measurement data is not calibrated to directly calculate the element amounts. To determine the element amounts laboratory XRF measurements are performed with a calibrated determination of elements. XRF measurement on the precursor / absorber-beam-spot is performed with a spot of a diameter of 30 / 1 mm and are used as initial / resulting conditions. These are extracted by fitting a range / time frame with constant conditions (constant fluorescence intensities) with a horizontal line.

### 2.2.2.4. Correcting factor for fluorescence signal calculation

In Ch. 4, calculated fluorescence intensities will be shown and compared with the measurement. However, the detector for energy dispersive analysis has an energy dependent response. Further, intensity deviations due to the neglected influences of the vacuum and non-vacuum beam paths as well as systematic errors of the elemental amounts can occur. For example, Se might condense at the beam windows. To allow correct data interpretation and cancel out the described errors, a correcting factor is determined for each detector. For a highest precision of the correcting factor, it needs to be determined for every measurement. This is done by calculating the fluorescence

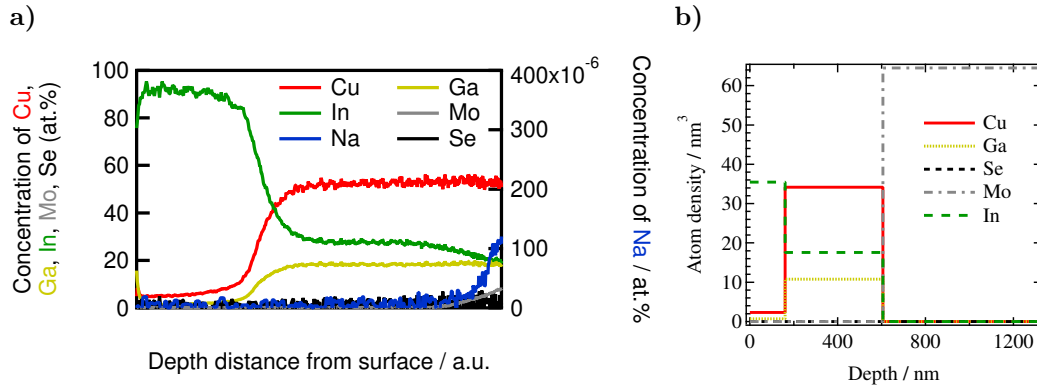


**Figure 2.6.:** a) Elemental depth distribution by GDOES of the multilayer precursor. The scale of the depth can not be evaluated due to the varying density. b) Approximated depth distribution in EDXRFfit for calculating the fluorescence intensities.

intensities of a precursor with its elemental depth distribution. The elemental depth distribution is analyzed by GDOES (see Fig. 2.6a). This measurement shows two main layers on the back contact, one mainly In and underneath one with Cu, Ga and In. The sputter-crater, created by the GDOES setup, is funnel-shaped. This shape and the sample roughness limit the depth resolution, which can be as poor as 100 nm. The transition between the two described layers is assumed to be abrupt rather than the gradual transition seen in GDOES. Further, the compositions of the two layers are approximated as being constant and fitted. The density of these layers can not be determined exactly, since only In and  $\text{Cu}_{16}(\text{In,Ga})_9$  are known as compounds, but small additional amounts of amorphous components need to be present to reach the atomic composition from XRF. Especially in the deeper layer more Cu and Ga are present than possible compared with the In content and the maximum Ga content in  $\text{Cu}_{16}(\text{In,Ga})_9$ . The density does not affect the primary fluorescence intensities. Since only 5% of the total fluorescence intensity originates from the secondary fluorescence, the influence of the density is very small.

The total elemental quantities (also referred to as projected number of atoms per nm<sup>2</sup>) in the film are defined with XRF measurement, since it achieves a higher precision than GDOES. The quantities are 15606 Cu atoms/nm<sup>2</sup>, 4908 Ga atoms/nm<sup>2</sup> and 13515 In atoms/nm<sup>2</sup>. The distribution of the element quantities into the two layers leads to a difference in the total elemental amounts of XRF and the atomic percentage of the two assumed layers from the GDOES elemental depth profile. When dividing the In and Ga amounts from XRF and attributing them to the two layers according to GDOES, a discrepancy of around 10% concerning the Cu content arises. Since the error in GDOES is the highest, the extra Cu is added to the two layers by increasing their Cu content by the same factor. The result is a top layer of 6.00 at.% Cu, 1.85 at.% Ga and 92.60 at.% In while the second layer exhibits 56.09 at.% Cu, 17.65 at.% Ga and

**Table 2.2.:** Calculated correcting factors for the investigated experiments.

Chapter	Detector	Elemental correcting factor				
		Cu	Ga	Se	Mo	In
4.2	1	1.63	1.45	1.06	1.43	1.34
4.2	2	3.37	2.23	1.03	1.37	1.31
4.3	1	2.30	2.05	1.00	1.66	1.44
4.3	2	3.93	2.51	1.00	1.69	0.74

28.83 at.% In. The measurement of the multilayer precursor and the formulated model in EDXRFfit are shown in Fig. 2.6. With this, the fluorescence intensities are calculated and the difference to the values, measured by EDXRF, results in the proportional correction factors. The factor for each element is the quotient of the calculated intensity divided by the measured intensity of the precursor. The calculated correcting factors for each experiment (described in the following chapters) and detector are shown in Tab. 2.2. The amount of Mo for the calculations is selected to equal the thickness from the Mo thickness from XRF measurement with 707 nm.

### 2.2.2.5. Calculated fluorescence intensities for exemplary stacking sequences

Calculated fluorescence intensities are presented in the following. The calculation is performed as described in Fig. 2.5.

It is useful for the considerations and the discussion presented in Ch. 4 to establish a feeling for the change of fluorescence intensities as consequence of different elemental depth profiles. Therefore, the fluorescence intensities of a chosen set of stacking sequences are calculated, see Fig. 2.7. The calculation is performed with EDXRFfit, as described in Fig. 2.5. The used element quantities correspond to the reference as applied in Ch. 4. The Se quantity is chosen as the sum of those of Cu, Ga and In.

An emitted fluorescence photon can be absorbed by another atom as described above and presented in Tab. 2.1. The probability for an absorption process is correlated to the total absorption cross-section  $\sigma_A$  (see Fig. B.2). This proportionality can be seen in the calculated elemental fluorescence intensities ( $I_{Element-K\alpha}$ ). The different thicknesses of Cu, Ga and In layers rather enhances the following findings and does not disagree (not shown). Some important findings are:

The highest  $\sigma_A$  at the photon energy of Cu- $K\alpha$  is  $\sigma_A$  of In. This is represented by the larger decrease of  $I_{Cu-K\alpha}$  when an In layer is on top of Cu (compare stacks C and E) than for a Ga layer on top of Cu (compare stacks A and B), as indicated with the red arrows.

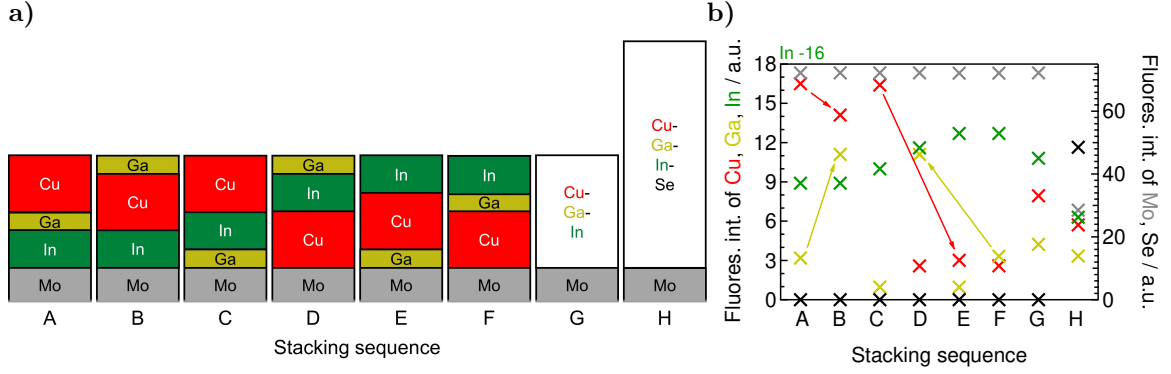


**Figure 2.7.:** a) Exemplary stacking sequences and b) calculated fluorescence intensities. G and H exhibit a homogeneous mixture. The colors correspond to the element species as indicated at the left and right axis. All  $I_{In-K\alpha}$  values are reduced by 16 for a better visibility of the differences in the fluorescence intensities. Arrows are explained in the text.

At  $Ga-K\alpha$ ,  $\sigma_A$  of Cu is only slightly smaller than that of In. Therefore the difference in  $I_{Ga-K\alpha}$  is similar when switching the Ga top layer with either In or Cu, compare A with B and D with F, as indicated with the yellow arrows.

At  $In-K\alpha$ ,  $\sigma_A$  of Cu, Ga and Se exhibit the lowest values compared with the values at the other  $K\alpha$  lines. Therefore, a different depth position has the smallest effect on  $I_{In-K\alpha}$ .

Se exhibits the highest  $\sigma_A$  at the photon energy of  $Mo-K\alpha$ . Hence, Se has the highest effect on  $I_{Mo-K\alpha}$ , compare stack G with H, assuming the error in the height alignment has a much smaller influence on  $I_{Mo-K\alpha}$ . A decrease of  $I_{Mo-K\alpha}$  suggests an incorporation of Se into the film.

The highest relative change of the intensities is found for Ga (x11.48) and Cu (x6.40), in contrast to In (x1.15). Therefore, the calculated intensities of Cu and Ga represent the most significant measure for the deduction of stacking sequences in this work.

The layer of Mo is always at the same depth position within the sample. Assuming constant element quantities and a properly adjusted height position of the sample (Sec. B), the primary fluorescence intensity of Mo is constant. In that case,  $I_{Mo-K\alpha}$  can only change by a changing stacking sequence on top, altering the contribution of the secondary fluorescence, which is described above. In case of Mo, the contribution of secondary fluorescence to the total fluorescence intensity results in a maximum factor for the difference within the stacks A to F to be a factor of 1.001. The contribution of secondary fluorescence is considered in the calculation but does not contribute significantly to the total intensity.

## 2.3. Standard characterization methods

This section describes the further utilized characterization methods and their measurement conditions.

X-Ray diffraction (**XRD**) measurement in Fig. 3.3 was performed in Bragg-Brentano geometry by use of a Panalytical X'pert MRD equipped with a goniometer PW3050/60 using the Cu  $K_\alpha$  line and a scan rate of  $0.016^\circ\text{s}^{-1}$ . The lateral element distribution was analyzed in a scanning electron microscope (**SEM**) LEO GEMINI 1530 from ZEISS equipped with an Energy Dispersive X-Ray (EDX) detector from Thermo Fisher Scientific. Measurements on precursors (see Ch. 3) were performed in top view configuration. For the cross sectional view in Fig. 3.6, an SEM S4100 from HITACHI equipped with an EDX system from AMETEK EDAX was used with an acceleration voltage of 10 keV. For a quantification of the domain sizes in Sec. 3.2, the Cu  $L\alpha$  or Mo  $L\alpha$  net counts were measured by **EDX** and escape peaks were recognized and eliminated by the ZEISS software. The net counts were transformed to binary images by use of the threshold criterion by N. Otsu [Otsu, 1979] in DipImage [Hendriks *et al.*, 1999], an extension for MATLAB. Pixels with value 1 (or 0) correspond to net count values above (below) the threshold. Connecting pixels of value 1 (or 0) within each line and each row were identified as a domain with size  $x = \text{number of connecting pixels}$ . The number of domains with various sizes  $x > 0$  were determined. The number of occurrence of each domain size  $x$  was weighted by multiplication with  $x$  to obtain a quantity that gives the fraction of domains with size  $x$  with respect to the total number of pixels with value 1 in the image.

The analysis of elemental composition was performed by wavelength dispersive X-ray fluorescence (**XRF**) using a WD-XRF ZSX Primus II from Rigaku. In general, a spot with 30 mm diameter was measured. For a measurement of the composition at a position of the EDDI beam spot, this position is measured with an aperture of 1 mm. Glow discharge optical emission spectroscopy (**GDOES**) was used for determining the elemental depth distributions. Measurements are performed within a  $5\text{ mm}^2$  spot with a Spectruma GDA 650 spectrometer. A uniform reference sample with known composition was used for quantification. The resulting GGI is used to calculate the related depth distribution of the band gap energy ( $E_g$ ). The  $E_g$  was calculated by the method from Ishizuka:  $E_g = 1 + 0.564 \times \text{GGI} + 0.116 \times \text{GGI}^2$  [Ishizuka *et al.*, 2005]. For the calculation of the depth distribution, every point of measurement with its GGI is taken into account due to a density dependence of the ratio of  $\text{CuInSe}_2$  to  $\text{CuGaSe}_2$ . The error is specified by the manufacturer to be 5% of the total depth, which is around 70 nm for the performed measurements, but the surface roughness has an additional influences on the evaluated composition and depth resolution of the measurement, as discussed in [Shimizu *et al.*, 1999]. The first 1-2 nm of an analysis are omitted due to

measurement initialization. A smoothing of factor 10 is performed.

**Standard current-voltage analysis** was conducted at 25 °C and 100 mW/cm<sup>2</sup> illumination of a AAA WACOM Dual Light source solar simulator. For statistic reasons, a 5 (10) cm<sup>2</sup> sample contains 15 (49) solar cells with 1.35 cm<sup>2</sup> active area. External quantum efficiency (**EQE**) was measured with the two beam spectral responsivity method using a grating monochromator, a quartz halogen bias light and short circuit current condition. The wavelength range was 300 to 1400 nm with an increment of 10 nm as described in [Hänel, 2008].

Measurements of the root mean square (**RMS**) roughness were either performed by use of an atomic force microscope (**AFM**) XE70 from Park Systems or an **optical confocal microscope** VK-X200 from KEYENCE. The RMS roughness from AFM is measured on a region of interest on the precursor and the absorber with an area of 100 μm<sup>2</sup> and 900 μm<sup>2</sup>, respectively. A parabolic background was removed using the software Gwyddion [Nečas and Klapetek, 2012]. The RMS roughness analyzed by an optical confocal microscope is measured with a magnification of 150 on an area of 71.50×95.35 (≅ 6800) μm<sup>2</sup>. The data is tilted to a horizontal reference plane and a weak height cut level is applied.

### 3. Lateral element redistribution during annealing of metal precursors

The ternary Cu-In-Ga phase diagram (see Fig. 1.5a) shows a mixture of possible phases present in a precursor, including  $\text{Cu}_{16}(\text{In,Ga})_9$ ,  $\text{Cu}_9(\text{In,Ga})_4$  and an In-rich liquid phase or pure solid In. Phase formation thereby strongly depends on the temperature, see Fig. 1.5. On the one hand, lateral phase separation and dewetting can occur during precursor annealing being enhanced by a melt of In above 157 °C [Ancsin, 1985]. Such a separation of elements, dewetting and coarsening in Cu-In-Ga precursor films can lead to solar cells with low shunt resistance due to pinhole formation and to a locally varying stoichiometry and in-depth distribution, leading to a deterioration of the electronic properties [Werner *et al.*, 2005]. On the other hand, the intermixing of  $\text{Cu}_{16}(\text{In,Ga})_9$  and  $\text{Cu}_9(\text{In,Ga})_4$  as well as the solubility of In in these phases increase with increasing temperature, as reported in [Hölzing *et al.*, 2011]. An increased solubility may decrease the amount of liquid In and thus counteract a possible phase separation. The possibility to reach temperatures of up to 600 °C in an annealing step prior to the chalcogenization without phase separation and dewetting, would widen the parameter space for selenization. With this, some reactions might start only when Se is supplied. Such a delay might be of high interest, since  $\text{CuInSe}_2$  formation is typically observed at a lower temperature than  $\text{CuGaSe}_2$  formation, leading to vertical phase separation (see Sec. 1.4). Overall, a delayed Se supply at a higher temperature can lead to a different phase formation during selenization and possibly enable process designs leading to optimized Ga depth profiles.

A further topic is the addition of alkali metals, which is known to have an effect on the growth and properties of  $\text{Cu}(\text{In,Ga})\text{Se}_2$  (CIGS): Na can influence the grain size [Bodegård *et al.*, 1994] and crystal orientation [Contreras *et al.*, 1997]. Furthermore, Na may impede the In/Ga-interdiffusion in CIGS films [Lundberg *et al.*, 2003]. Nonetheless, the influence of Na on a chalcogen-free annealing step, where phase separation may occur, has not been studied previously.

The influence of the precursor stacking sequence is investigated with regard to i) the film roughness by atomic force microscopy (AFM), ii) the homogeneity of lateral element distribution by energy dispersive X-ray spectroscopy (EDX) and iii) electrical and morphological properties as well as the Ga in-depth profile by glow-discharge optical emission spectroscopy (GDOES) in Sec. 3.1. The annealing of precursors with different layer stacks and the influences of heating rate and temperature on the lateral phase separation and dewetting are presented in Sec. 3.2. Dewetting is characterized by areas with exposed Mo in EDX mappings. The role of Na therein is shown in Sec. 3.3 and the effect of phase separation in the precursor on the lateral homogeneity of selenized films is studied in the last Sec. 3.4.

Parts of this chapter were published in [Bäcker *et al.*, 2017] and [Schmidt *et al.*, 2017].

Four sputtering sequences for the four precursors were investigated, see below. The two simplest bilayer structures, possible by the two sputter targets, were selected, because Ga is known to oxidize faster compared with In [Lehmann, 2010]. The triple layer and the multilayer precursor were studied because they exhibit a smoother surface and a more homogeneous Ga in-depth distribution that may affect the Ga distribution in the final absorber layer.

- Prec. 1: In/CuGa
- Prec. 2: CuGa/In
- Prec. 3: In/CuGa/In (triple layer)
- Prec. 4: 22 layers of In/CuGa/In (multilayer)

Annealing experiments are performed in a vacuum RTP tool (see Sec. 2.1.2) and were stopped at  $T_{\max} = 170, 350$  or  $580$  °C. Heating rates of 1, 0.1 and 0.01 °C/s were applied. The precursors were passively cooled down after heating. Some of the samples were subsequently selenized in an atmospheric pressure inline chalcogenization tool using sources with elemental Se (see Sec. 2.1.2). Atmospheric selenization is done by a baseline selenization sequence, as described in details in [Schmidt *et al.*, 2017, Bäcker *et al.*, 2015]. For an independent assessment of the influence of sodium fluoride (NaF) in Sec. 3.3, an 800 nm Na free molybdenum back contact on top of an Na diffusion barrier ( $\text{SiO}_x\text{N}_y$ ) was used. This enables a controlled addition of Na for homogenous and industry-compatible production in opposition to soda lime glass as Na source because the Na content may vary with the glass batch as well as locally on every glass. NaF was deposited by thermal evaporation in a high vacuum chamber with amounts of 0, 10, 20 or 30 nm before or after the precursor deposition. An In layer (around 40 nm) was deposited by evaporation prior to the precursor sputtering. This layer was used as sputtering protection of the NaF and to avoid NaF contamination of the sputtering system. The layer was deposited on all samples for reasons of comparability.

### 3.1. Influence of precursor stacking sequence on film roughness and homogeneity

Before performing annealing experiments with metal precursor layers, it is useful to analyze their initial properties, such as morphology, element distribution, etc. Fig. 3.1 shows SEM images of two precursor layers with a different architecture: Fig. 3.1a shows the triple layer precursor (see Sec. 2.1.1) which exhibits droplet like structures at the surface. Fig. 3.1b shows the multilayer precursor, which does not, or to a much lesser extent, exhibit such droplets. The RMS roughness of the precursor surfaces in case of the triple layer is 221 nm and for the multilayer 80 nm. Additionally, the multilayer precursor exhibits less dewetting after annealing e.g. with 0.1 °C/s up to 580 °C (sup. Fig. C.1). The smoother surface and a smaller tendency for dewetting during annealing in comparison to the triple layer precursor is the reason the focus is set on the multilayer precursor for the following investigations<sup>1</sup>.

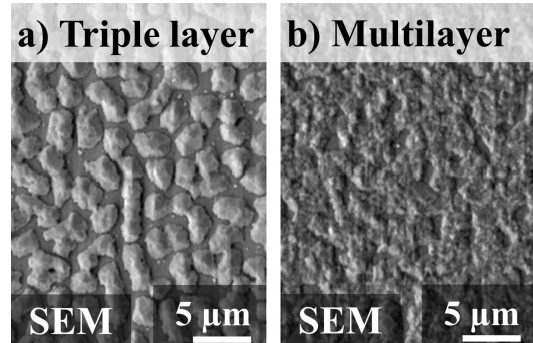


**Figure 3.1.:** SEM images observed by an acceleration voltage of 12 keV on the a) triple layer (In/CuGa/In) and b) multilayer precursor (see Sec. 2.1.1).

For studying the effect of the four different metal precursor architectures on the morphological absorber properties<sup>2</sup>, the selenization procedure was kept the same. Tab. 3.1 summarizes the RMS roughness as well as the maximum difference in surface amplitude measured by use of AFM on an absorber area of  $30 \times 30 \mu\text{m}^2$ . Both the RMS roughness and the maximum amplitude are more than 10% smaller for Prec. 3 and Prec. 4 compared with the bilayer architectures.

**Table 3.1.:** Roughness of the absorber layers fabricated with the four different metal precursor stacks measured on a  $30 \times 30 \mu\text{m}^2$  sample area.

Roughness / nm	Prec. 1	Prec. 2	Prec. 3	Prec. 4
Root mean square	392	446	342	338
Max amplitude	3100	3140	2280	2740

<sup>1</sup>Details about the electrical properties can be found in [Schmidt *et al.*, 2017]. In summary, the best  $V_{oc}$ , FF and efficiency ( $\eta$ ) are found for Prec. 4.

<sup>2</sup>For the further context in Ch. 4, it should be noted, that the Ga in-depth profiles are similar for all samples, which was even true, when all Ga was contained in the top layer of the Prec. 1.

## 3.2. Effect of heating rate and temperature on lateral element redistribution

This section is dedicated to the influence of the heating rate and maximum temperature  $T_{max}$  on the element redistribution and dewetting during annealing of the multilayer precursor.

Heating rates of 1, 0.1 and 0.01 °C/s and maximum annealing temperatures of up to  $T_{max}=170$ , 350 and 580 °C were applied. SEM as well as elemental distribution images of selected annealed samples are shown in Fig. 3.2. Cu elemental distributions measured on all samples as well as the extracted binary images are shown in the supplementary (see Figs. C.2 and C.3).

The development of the elemental distribution images (Fig. 3.2a-c) of the multilayer precursor with increasing annealing temperature  $T_{max}$  and constant heating rate of 0.01 °C/s is the following: The Mo intensity is in the order of the noise level and hence only noise is observed below  $T_{max}=580$  °C. As a result of the elemental distribution after heating up to  $T_{max}=580$  °C, which exhibits areas that show a high Mo signal and no other elements (like Fig. 3.2c and d), one can conclude that these are dewetted regions. The number and fraction of these dewetted areas decrease with increasing heating rates. An even faster heating rate may reduce them further. After annealing up to  $T_{max}=170$  °C the element distribution remains unchanged (compare Fig. 3.1b with Fig. 3.2a) within the experimental resolution of the EDX measurements. When heating up to 350 °C a different distribution of elements appears in the elemental distribution images (Fig. 3.2b). For  $T_{max}=580$  °C, larger domains in the order of several  $\mu\text{m}$  with different compositions are clearly visible (Fig. 3.2c). In Fig. 3.2c four identified domains with different elemental compositions are marked and listed in Tab. 3.2.

Point 1 in Fig. 3.2c corresponds to a lower In amount of 11 at% (see Tab. 3.2) in comparison to point 2 with an In amount of 25 at%. The highest In content observed can be as high as 100 at%, as marked in point 3. Point 4 is representative for the regions where dewetting has occurred and mainly Mo is detected. Increasing the heating rate from 0.01 °C/s to 1 °C/s reduces the area of relative dewetting from 12% to 1% (compare Fig. 3.2c, d and sup. Fig. C.4).

**Table 3.2.:** The compositions of the four marked points in Fig. 3.2c, measured by EDX. The measurement error is estimated to 1-2 at%.

No. of point	1	2	3	4
Cu (at%)	72	66	0	0
Ga (at%)	17	9	0	3
In (at%)	11	25	100	2
Mo (at%)	0	0	0	95

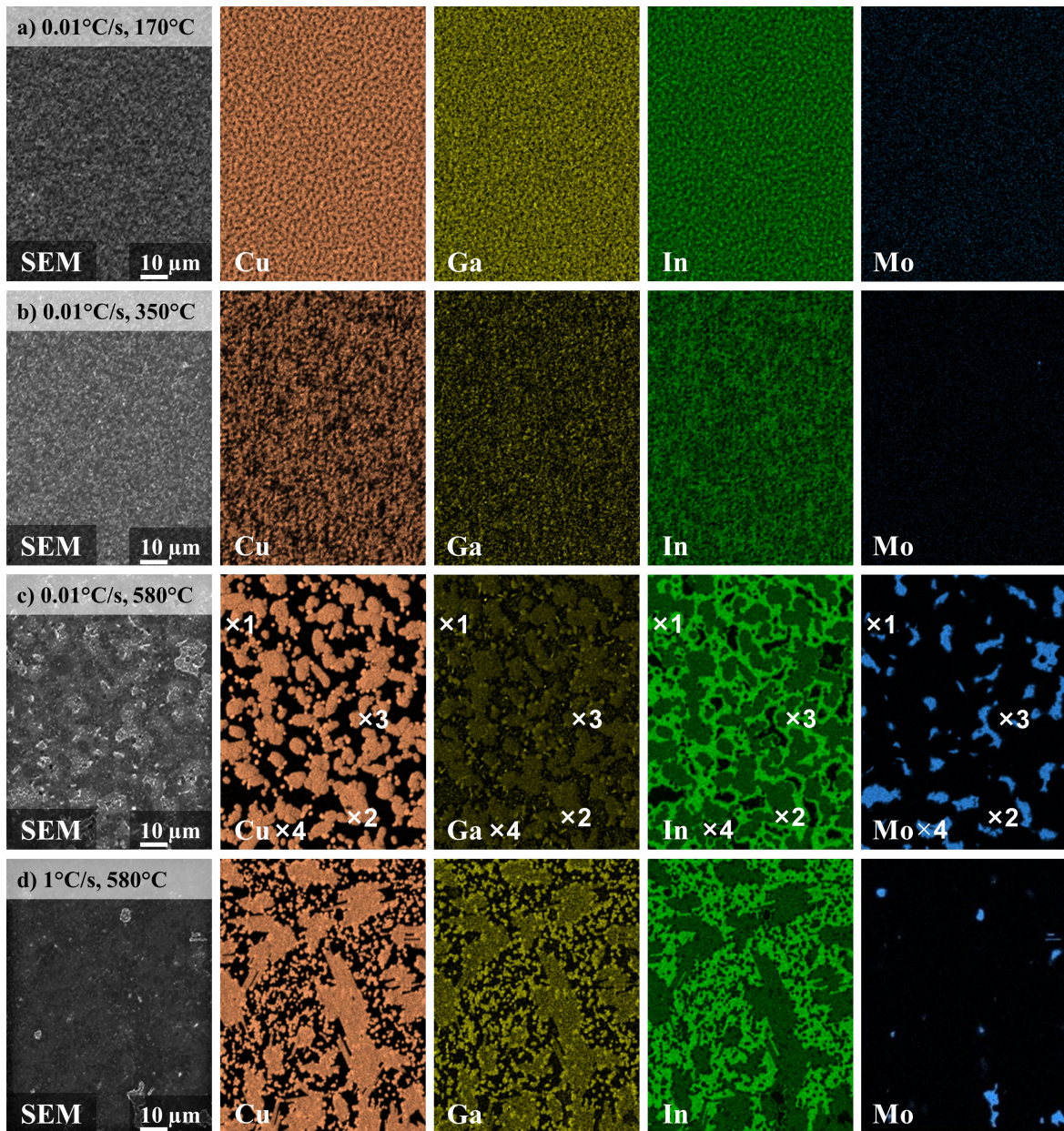


**Figure 3.2.:** SEM and elemental distribution images (net counts) of Cu, Ga, In and Mo measured by EDX and an acceleration voltage of 12 keV on the multilayer precursors at RT after heating with a) 0.01 °C/s up to 170 °C, b) 0.01 °C/s up to 350 °C, c) 0.01 °C/s up to 580 °C and d) with 1 °C/s up to 580 °C. The heating rate (°C/s) and  $T_{max}$  (°C) are indicated on the SEM images. On sample c) four different compositions (see Tab. 3.2) were identified and exemplary points are marked as 1-4.

Phase analysis was performed by use of room temperature X-ray diffraction. The result is shown for the multilayer precursor after annealing with  $0.01\text{ }^\circ\text{C/s}$  up to  $580\text{ }^\circ\text{C}$  (Fig. 3.3), for which elemental distributions are shown in Fig. 3.2c. Mo (ICDD-No. 00-042-1120), In (ICDD-No. 00-005-0642) and  $\text{Cu}_9\text{Ga}_4$  (ICDD-No. 01-071-0458) were identified in the room temperature diffractogram in Fig. 3.3. Additionally, a strong peak at around  $43^\circ$ , to the right of the position of  $\text{Cu}_{16}\text{In}_9$  102/110 (ICDD-No. 00-042-1475), can be seen (In the database the phase is denoted as  $\text{Cu}_2\text{In}$ ). In accordance with Purwins *et al.* this peak can be attributed to the solid solution of  $\text{Cu}_{16}(\text{In,Ga})_9$  [Purwins *et al.*, 2007].

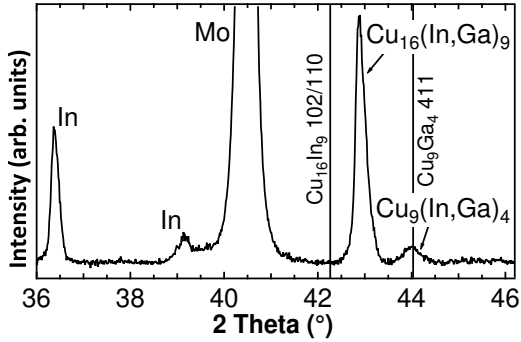


**Figure 3.3.:** The room temperature diffractogram shows the identified phases: Mo, In,  $\text{Cu}_{16}(\text{In,Ga})_9$  and  $\text{Cu}_9\text{Ga}_4$  of the multilayer precursor after annealing with  $0.01\text{ }^\circ\text{C/s}$  up to  $580\text{ }^\circ\text{C}$  (see Fig. 3.2c). The reference lines of  $\text{Cu}_{16}\text{In}_9$  102/110 (ICDD-No. 00-042-1475) and  $\text{Cu}_9\text{Ga}_4$  411 (ICDD-No. 01-071-0458) are shown.

The composition at the 4 marked points may be explained by: The pure In phase matches the composition measured at point 3. The composition at point 2 can be associated with  $\text{Cu}_{16}(\text{In,Ga})_9$ . The composition at point 1 may be explained by the presence of  $\text{Cu}_9(\text{In,Ga})_4$ . The co-existence of two  $\text{Cu}_x(\text{In,Ga})_y$  phases and In is consistent with the Cu-In-Ga phase diagram (sup. Fig. E.4) [Muzzillo *et al.*, 2015] and experimental observations [Purwins *et al.*, 2007]. From the Cu distribution images for all heating rates and all  $T_{max}$ , the area-weighted domain sizes of Cu agglomeration were quantified as introduced in the experimental section. These are shown as boxplots in Fig. 3.4. With higher  $T_{max}$  the median increases and the distribution of domain sizes extends to bigger values. The boxplots show no substantial dependency on the heating rate for  $T_{max}=170$  and  $350\text{ }^\circ\text{C}$ . The median domain size for  $T_{max}=580\text{ }^\circ\text{C}$  (red boxes) decreases slightly towards lower heating rates. Additionally, the distribution range, i.e. the range of domain sizes between the whiskers as well as within the box, gets narrower towards lower heating rates. It is remarkable that for the sample heated with  $1\text{ }^\circ\text{C/s}$ , the upper and lower whiskers are higher and lower respectively compared with lower heating rates. Only the latter might be expected, since the domain sizes in the as grown precursors are even smaller and when giving the system less time to equilibrate, the domain sizes should be closer to the initial values. One reason could be an altered composition of the four identified domains (see Fig. 3.2d) with respect to those identified in Fig. 3.2c (Tab. 3.2). However no significant differences for the respective domains are detected. Another explanation could be that the relative dewetted area increases from 1% to 12% for the sample annealed with the fastest to

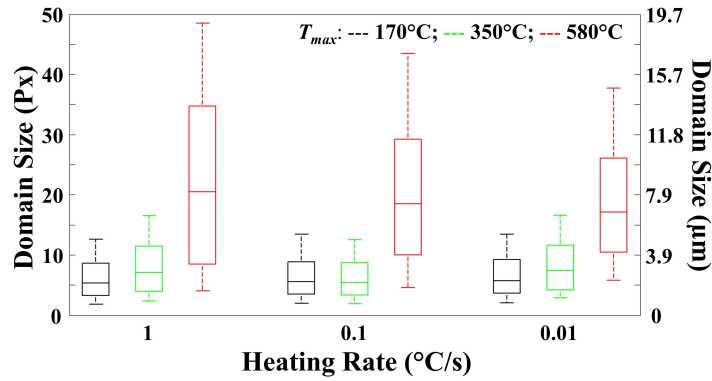


**Figure 3.4.:** Boxplots of area weighted domain sizes (as described in the experimental section) identified in the binary elemental distribution images of Cu for multilayer precursors annealed with heating rates 1, 0.1 and 0.01 °C/s up to  $T_{max}=170$ , 350 and 580 °C (see sup. Figs. C.2 and C.3). 1 Px is equal to 0.393  $\mu\text{m}$ . The median (line in the boxes) indicates that about half of the total image size (number of pixels) consists of domain sizes smaller, and about half of the total image consists of domain sizes larger than this value. The upper/lower box values (upper and lower whisker), indicate that about 75% /25% (90% /10%) of the image area consists of domain sizes smaller than the respective value.

the one annealed with the slowest heating rate. This suggests that the same amount of material is now distributed over a smaller area and hence the domains between the dewetted areas exhibit reduced lateral dimensions and an increased thickness. This effect might explain why larger domain sizes in the sample with the fastest heating rate and the least dewetted area are detected. It should be mentioned, that phase separation might also continue during cool down, which lasts around 10 min from 580 to 350 °C and might have a more relevant influence on the final state in case of a shorter heating time. Overall, the elemental distribution images (Fig. 3.2) show an increasingly strong redistribution of elements with increasing  $T_{max}$ , leading to an increasing area weighted domain size. This dependence is much less distinct with decreasing heating rate (see Fig. 3.4).

### 3.3. Impact of evaporated NaF on dewetting

Different amounts of NaF have been added on top or under the precursor by thermal evaporation before annealing in order to study the influence of NaF on the dewetting of the multilayer precursor during annealing. Na diffusion from glass is prevented by use of a diffusion barrier ( $\text{SiO}_x\text{N}_y$ ) underneath the Mo back contact and there was no Na used as dopant in the Mo back-contact. The precursors were annealed by heating with 0.01 °C/s up to 580 °C. Fig. 3.5a-c show SEM images of annealed precursors with different NaF amounts and positions. It can be seen that droplet

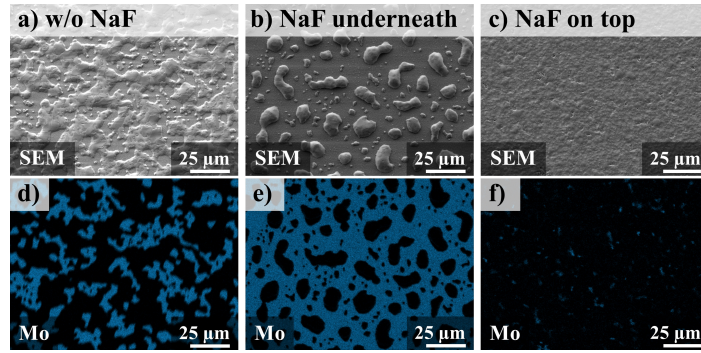


**Figure 3.5.:** SEM images at an acceleration voltage of 12 keV after heating with 0.01 °C/s up to 580 °C of a multilayer precursor a) without NaF, b) with 30 nm NaF underneath the precursor, c) with 30 nm NaF on top of the precursor. (d-f) EDX Mo intensity distributions corresponding to the SEM images in (a-c) (blue value represents Mo intensity, the binary images processed from d-f are shown in sup. Fig. C.5).

formation is enhanced for the annealed precursor with 30 nm NaF underneath the precursor (Fig. 3.5b) compared with the precursor without NaF (Fig. 3.5a). In contrast, droplet formation during annealing is significantly reduced for the sample with 30 nm NaF on top of the precursor (Fig. 3.5c). Fig. 3.5d, e and f show the Mo distribution intensity belonging to Fig. 3.5a, b and c, respectively. The Mo distribution images are further processed to binary images and analyzed by the percentage of relative dewetted area, calculated as number of red (Mo) pixels/all pixels (1024·768) (from sup. Fig. C.5). The relative dewetted areas are shown for all prepared NaF amounts in Tab. 3.3. Precursors with NaF underneath the precursor lead to an increase in percentage of relative dewetted area from 30% (without NaF) to over 60% (with 30 nm NaF underneath), see Tab. 3.3. Only for the smallest NaF thickness of about 10 nm, a slight decrease to 23% is observed. If NaF is deposited on top of the precursor (Fig. 3.5c, f) the percentage of Mo area is decreased to below 5% (Tab 3.3) for all amounts of NaF. These results show that NaF has a different influence on the precursor dewetting during annealing, depending on the initial location underneath or on top of the precursor. In Sections 3.2 and 3.2, the relative dewetted area of the sample after the same treatment ( $T_{max}=580$  °C, heating rate of 0.01 °C/s) differs. The difference is, that the sample in Sec. 3.2 (sup. Fig. C.5c, f) has a back contact consisting of a stacking of Mo/Mo:Na/Mo (as described in the Experimental section), and for the investigations on the influence of NaF addition in Sec. 3.3 (Tab. 3.3 and Fig. 3.5d), the back contact consists of Mo only. The relative dewetted area for the first sample, with Na-doped back contact, is 12% and the sample without Na is 30%.

This can either be explained by the different sputtering resulting in different surface properties or by Na diffusion from the back contact to the precursor.

**Table 3.3.:** Percentage of relative dewetted area, calculated as number of red (Mo) pixels/all pixels (1024·768) (compare sup. Fig. C.5).

NaF thickness / nm	Relative dewetted area / %	
	NaF underneath precursor	NaF on top of precursor
0	30	30
10	23	2
20	63	5
30	65	4

### 3.4. Non-reversibility of lateral phase separation with selenization

A phase separation as observed here in the metal precursors during annealing without chalcogens could, in principle, be (partly) reversible during chalcogenization by interdiffusion and lead to laterally uniform layers despite the initial phase separation. Therefore CIGS absorbers are compared after selenization of an as grown multilayer precursor (Fig. 3.6a) and a pre-annealed multilayer precursor (Fig. 3.6b). The pre-annealed precursor was heated with 0.01 °C/s up to 580 °C and exhibited a clear lateral phase separation before selenization as in Fig. 3.2c. The SEM cross section image of the selenized precursor in Fig. 3.6a shows a uniform morphology and thickness. In contrast, the pre-annealed absorber layer in Fig. 3.6b illustrates a strong variance in thickness with bumps. SEM (Fig. 3.6c) and elemental distribution images of Ga (Fig. 3.6d) and In (Fig. 3.6e) measured on the cross section view of a bump shows that the bottom part of the bump consists of CIGS with high GGI and the top and thin parts of CIGS with small GGI. This result shows that the phase separation during annealing was not reversed during selenization and demonstrates the importance of preventing lateral phase separation during precursor heating.

## 3.5. Discussion

### Influence of NaF on dewetting

Fig. 3.5 and Tab. 3.3 show that NaF affects the dewetting of precursor metals on Mo during annealing up to 580 °C differently, depending on whether the NaF layer was deposited on top or underneath the precursor stack. This suggests that the effect of NaF on the precursor during annealing is more than simply entering the solution of In or  $\text{Cu}_x(\text{In,Ga})_y$  and changing the respective chemical and physical properties, since the

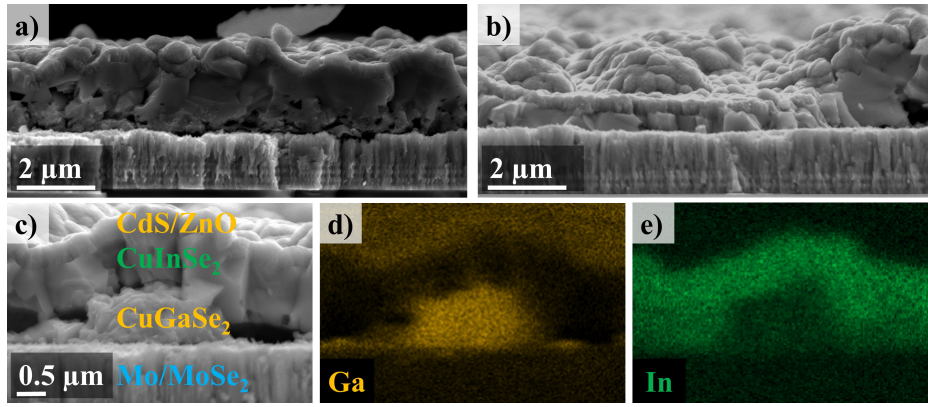


**Figure 3.6.:** Cross-section SEM images of CIGS absorber layers (on Mo and a Cd-S/ZnO top layer) fabricated by use of a) a multilayer precursor, b) an annealed multilayer precursor (with  $0.01\text{ }^{\circ}\text{C/s}$  up to  $580\text{ }^{\circ}\text{C}$ ) exhibiting phase separation as in Fig. 3.2c. c) Magnified image from sample b) with elemental image of d) Ga and e) In. Analysis was performed with an acceleration voltage of 10 keV.

effect should be similar if NaF is deposited on top or underneath the precursor. The following effects are proposed in addition:

- i) NaF underneath increases dewetting: A small amount of Na increases the melting point of elemental In, as it is reported in literature [Larose and Pelton, 1991]. Due to the NaF layer under In, either NaF with its melting point of around  $992\text{ }^{\circ}\text{C}$  [Kojima *et al.*, 1968] or a formation of  $\text{In}_8\text{Na}_5$  [Larose and Pelton, 1991] with its melting point at  $441\text{ }^{\circ}\text{C}$  might create a solid layer under the precursor. Such a solid layer could also be the reason for the increase of dewetting fraction from around 30 to over 60 %, since the Young contact angle could be different (higher) if NaF or  $\text{In}_8\text{Na}_5$  is used as substrate instead of Mo. Another possibility is that in this case, a part of the NaF is entering the solution with another phase and changes the solid-liquid interfacial energy and therefore the contact angle. In contrast to NaF on top of the precursor (see below), there is no structural confinement for the Cu-In-Ga phases on top.

The evaporation of the small NaF amount aimed for 10 nm under the precursor might have led to an inhomogeneous deposition like a non-closed layer, or this NaF amount is too small to affect the increasing dewetting during annealing (compare Tab. 3.3).

- ii) NaF on top prevents dewetting: An NaF or formed  $\text{In}_8\text{Na}_5$  layer might act as a solid top layer which might be more stable during annealing than an In top layer with its melting point at  $157\text{ }^{\circ}\text{C}$ . A closed solid top layer could indeed prevent dewetting through structural confinement of fluid phases underneath and is, e.g., utilized in so called thin film vapor-liquid-solid growth (TF-VLS)

for InP [Kapadia *et al.*, 2013]. Here a solid SiO<sub>x</sub> layer on top of an elemental In precursor thin-film is used as a dewetting prevention during processing. This effect might explain the decrease from 30 to under 5% relative dewetted area with NaF on top of the precursor. In addition solid SiO<sub>x</sub> is permeable for phosphorous vapor in TF-VLS. Similarly, NaF may be permeable for Se vapor, since precursor layers with NaF on top have been successfully selenized (not shown here).

It is still not fully clear if the phase separation observed after cool down is also present during annealing since Hölzing *et al.* showed that more In is soluble in Cu<sub>x</sub>(In,Ga)<sub>y</sub> [Hölzing *et al.*, 2011]. However if even small amounts of pure liquid In are present, the results show that phase separation is plausible to occur and has to be avoided in order to achieve uniform absorber layers. A multilayer architecture, a faster heating rate and NaF on top of precursor layers could be effective measures to avoid phase separation and dewetting.

### 3.6. Conclusion

Lateral phase separation and dewetting during selenization of Cu-In-Ga precursors is an unwanted effect for CIGS production and may become significant, if the Se supply during selenization is adjusted such that the precursor is in part or fully heated up without Se. This work studies the impact of heating rate and maximum temperature during annealing of metal precursors in Se free environment. A suitable starting point was a smoother and more homogeneous multilayer precursor in comparison with a triple layer architecture. The multilayer precursor as well as the fastest heating rate of 1 °C/s and an NaF layer on top of the precursor led to a reduced dewetting of the annealed precursor along with a different phase separation after annealing of the sample. This beneficial effect from NaF only occurred when NaF was deposited on top and was not significantly dependent on the NaF amount (between 10 and 30 nm thick layer). The necessity of a prevention of lateral phase separation during thermal processing of Cu-In-Ga precursors to CIGS absorbers was demonstrated by selenizing a precursor that exhibited distinct phase separation prior to selenization. After this selenization, an inhomogeneous lateral Ga/In distribution in the chalcopyrite phase was found.

The results above showed how to enable and widen the parameter space for selenization with a prior annealing step of up to 580 °C, even with low heating rates of 0.01 °C/s. Fast heating rates as well as NaF addition on top enable a delayed Se-addition during selenization and possibly enable process designs leading to optimized Ga depth profiles.



## 4. Evolution of crystallographic phases and vertical elemental redistribution during selenization of Cu-In-Ga precursors to CIGS

The following results aim at the understanding of the growth of CIGS layers during thermally activated reaction of a sputtered Cu-In-Ga multilayer precursor<sup>1</sup> in elemental Se vapor (“selenization”). The selenization is performed within a few minutes.

The possibilities for a direct control of the phase formation and evolution during selenization are limited. The substrate temperature ( $T_{\text{sub}}$ ) can be controlled well. A possibility for an additional control is the Se partial pressure ( $P_{\text{Se}}$ ) (see Sec. 1.3). However, the most common approach is based on placing surplus Se in the reaction chamber as pellets next to or as a layer onto the precursor film. In this way, the properties of the Se supply are coupled to the substrate temperature. This approach of processing typically results in a segregation of Ga at the Mo back contact, see Sec. 1.4.2.

In this work, Se is supplied by an external Se source to decouple the Se supply from  $T_{\text{sub}}$  (see Sec. 2.1.2). Only then, the Se source temperature ( $T_{\text{Se}}$ ) enables an additional control during CIGS formation.  $T_{\text{Se}}$  (and thus  $P_{\text{Se}}$ ) can be kept at a specific and constant value. Using the vacuum selenization tool (see Sec. 2.1.2), two different growth paths were identified, possibly correlated to a different  $P_{\text{Se}}$ . The first one led to a strong Ga segregation without Ga at the surface. The second one led to a final Ga depth profile without Ga segregation and a minimum  $[\text{Ga}]/([\text{Ga}]+[\text{In}])$  (GGI) of 0.26 (also referred to as Ga homogenization). This type of growth is studied by *in situ* analysis for the first time. The different Ga profiles could be reproduced with the atmospheric selenization tool (see Sec. 2.1.2). The results allow a direct correlation of the Ga profile with increased homogenization to a lower  $T_{\text{Se}}$ .

---

<sup>1</sup>The multilayer precursor was selected from results in Ch. 3.

Thermodynamically driven Ga segregation fundamentally limits an adjustment of the Ga depth profile. However, the Ga depth profile is important, because the GGI determines the band gap energy ( $E_g$ , see Eq. 1.2). The  $E_g$  of the absorber needs to be increased above the  $E_g$  of pure CuInSe<sub>2</sub> to achieve a higher conversion efficiency of CIGS solar cells (see Sec. 1.1.2). With a decoupled Se supply, an adjustment of the Ga depth profile during selenization to some extent is feasible. Initial experiments already led to the highest efficiency of 15.5% for a sequentially produced solar cell using elemental Se vapor [Schmidt *et al.*, 2017, Song *et al.*, 2018].

The chemical reactions during selenization are fast, so that some intermediate phases are only present within one minute. In addition, the material is complex with its large number of elements and various possible phases. For these reasons, an *in situ* measurement was applied: Information about phases present in the film were obtained by energy dispersive X-ray diffraction (EDXRD) and complemented by the information about the elemental depth profile obtained by energy dispersive X-ray fluorescence (EDXRF) at BESSY II. The measurements are performed simultaneously and thus can be correlated. The identified phases from EDXRD are used to calculate fluorescence intensities. The specific fluorescence intensities are then used to deduce the phase-depth distribution during growth of CIGS (as explained in Sec. 2.2.2). So far, this method has only been applied to the ternary Cu-In-S system. The method is applied here with higher accuracy and complexity. The possibilities and limits for an application to the growth of the more complex quaternary compound CIGS are discussed.

The following investigation is based on three experiments: i) An EDXRD/EDXRF measurement during thermal treatment of a precursor without Se has been performed to identify phases in the Se free system as basis for investigating the selenization process (Sec. 4.1). ii) The growth of CIGS during fast selenization with strong Ga segregation is analyzed (Sec. 4.2). iii) The growth of CIGS during fast selenization without a final Ga segregation is presented in Sec. 4.3.

The comprehensive phase identification and accurate determination of the composition of each phase (Secs. 4.2.1 and 4.3.1) is important for the fluorescence calculations conducted later in Secs. 4.2.2 and 4.3.2, to deduce the one-dimensional (1D) stacking order of the phases present at a given time. It is further important for the understanding of the general phase evolution of the film. A comparison of the two *in situ* investigations and deduced growth paths are shown in Sec. 4.5. An *ex situ* investigation in Sec. 4.6 supports the finding, that a more homogeneous Ga grading can be triggered via a lower Se supply. The results are used to propose a model of growth in Sec. 4.7.

## 4.1. Thermal treatment of the Cu-In-Ga multilayer precursor without Se

### 4.1.1. Analysis of the *in situ* EDXRD/EDXRF measurement

An *in situ* EDXRD/EDXRF measurement during thermal treatment of a multilayer precursor without Se was performed. First, the crystalline phases present at 34 °C and 550 °C will be identified on the basis of the EDXRD spectra. Afterwards, the evolution of reflection and fluorescence peak intensities during heating will be correlated. Phase identification on the basis of reflections is difficult since in certain temperature regimes there exist several phases with similar reflections. This is the case for  $\eta$ -Cu<sub>16</sub>(In,Ga)<sub>9</sub> and  $\gamma$ -Cu<sub>9</sub>(In,Ga)<sub>4</sub>. The energies of the diffraction peaks of both phases depend on their composition, see Sec. 1.2.1 and the reflections of the two phases can overlap. Nevertheless, the presence of  $\eta$ -Cu<sub>16</sub>(In,Ga)<sub>9</sub> is differentiated from  $\gamma$ -Cu<sub>9</sub>(In,Ga)<sub>4</sub> by a few unique low intensity reflections of  $\gamma$ -Cu<sub>9</sub>(In,Ga)<sub>4</sub>.

In the following,  $\eta$ -Cu<sub>16</sub>(In,Ga)<sub>9</sub> is referred to as Cu<sub>16</sub>(In,Ga)<sub>9</sub> or  $\eta$ -phase and  $\gamma$ -Cu<sub>9</sub>(In,Ga)<sub>4</sub> is also denoted as the  $\gamma$ -phase.

Assigning reflection peaks in the precursor helps to distinguish those from reflections of Se containing phases in Sec. 4.2 and 4.3.

#### Phase identification before heating and at 550 °C

Fig. 4.1 shows spectra measured at  $T_{\text{sub}}=34$  °C and 550 °C, which are measured for 2.48 min and 15.36 min, respectively. At 34 °C, some of the peaks can be correlated to the known reflections of crystalline In [Smith and Schneider, 1964]. The remaining peaks could in principle be attributed to either a  $\eta$ - or a  $\gamma$ -phase. No clearly assignable reflection of  $\gamma$ -Cu<sub>9</sub>(In,Ga)<sub>4</sub> is found, suggesting that only Cu<sub>16</sub>(In,Ga)<sub>9</sub> is present. The  $\eta$ -phase has no additional unique reflections in contrast to the  $\gamma$ -phase. Assuming the assigned Cu<sub>16</sub>(In,Ga)<sub>9</sub> 110/102 reflection to correspond to a  $\gamma$ -Cu<sub>9</sub>(In,Ga)<sub>4</sub> 330 reflection instead, the corresponding composition would exhibit a GGI of  $0.25\pm 0.03$ , which is in discrepancy to the Cu-In-Ga phase diagram (Fig. 1.5a), which shows a minimum GGI of 0.75 at  $T\leq 150$  °C.

An evaluation of the composition of Cu<sub>16</sub>(In,Ga)<sub>9</sub> is not strictly possible, because there is only a reference diffraction pattern available for Cu<sub>16</sub>In<sub>9</sub>. Purwins *et al.* performed a study [Purwins *et al.*, 2007] about precursors with similar elemental (GGI between 0.15 and 0.31) and phase composition as reported here. With increasing GGI of the film, the 110/102 reflection of Cu<sub>16</sub>(In<sub>1-x</sub>Ga<sub>x</sub>)<sub>9</sub> shifted until reaching 42.85°, for which they estimated a maximum Ga content of  $x = 0.29$ . This angle corresponds to 34.58 keV in the EDXRD measurement here (Fig. 4.1). The position of the 110/102 reflection

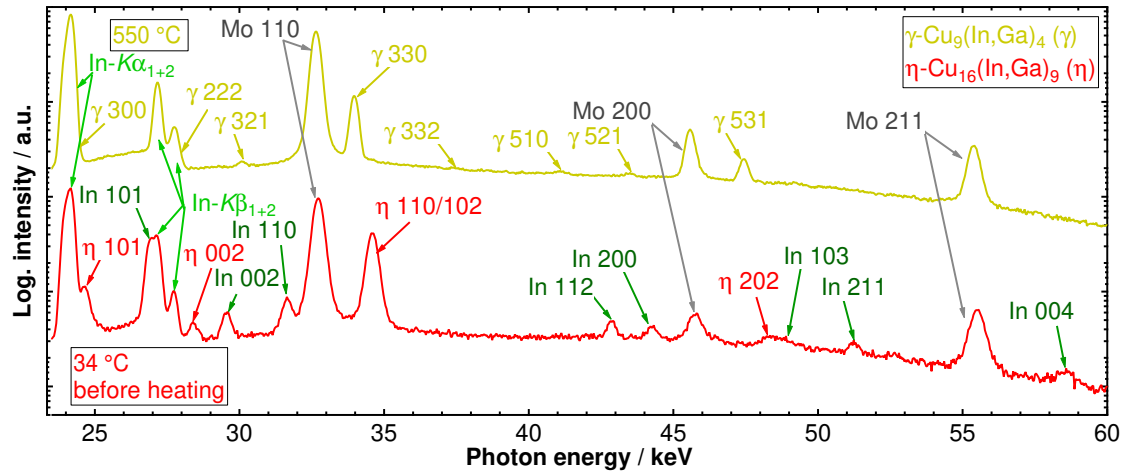


**Figure 4.1.:** EDXRD spectra of a multilayer precursor before the start of the heating process ( $T_{\text{sub}}=34\text{ }^{\circ}\text{C}$ ) and at the maximum temperature of  $550\text{ }^{\circ}\text{C}$ . The EDXRD spectra are shifted vertically for better separation. The arrows indicate assigned peaks and Miller indices of the phases Mo, In,  $\eta\text{-Cu}_{16}(\text{In,Ga})_9$  ( $\eta$ ) and  $\gamma\text{-Cu}_9(\text{In,Ga})_4$  ( $\gamma$ ) as well as the peaks from the In- $K\alpha_{1,2}$  and In- $K\beta_{1,2}$  fluorescence (partly overlapping with reflection peaks).

of the  $\eta$ -phase here is at  $34.60 \pm 0.14\text{ keV}^2$ , which is at the same position within the uncertainty. Therefore, a GGI of  $x=0.29$  in  $\text{Cu}_{16}(\text{In}_{1-x}\text{Ga}_x)_9$  is assumed for the following investigations.

At  $T_{\text{sub}}=550\text{ }^{\circ}\text{C}$ , the presence of  $\gamma\text{-Cu}_9(\text{In,Ga})_4$  is identified by means of its unique diffraction peaks 321 and 332 (see Fig. 4.1), which cannot be assigned to the  $\eta$ -phase. In principle, a small 110/102 reflection of the  $\eta$ -phase might be present within the 330 reflection of the  $\gamma$ -phase in the unlikely case of a similar change in position. Therefore, and due to a corresponding small phase amount, this is assumed to be negligible. No other phase was observed at  $550\text{ }^{\circ}\text{C}$ .

The presence of In and solid solutions of the  $\eta$ - and  $\gamma$ -phases are in agreement with the ternary Cu-In-Ga phase diagrams [Kim *et al.*, 2012b, Muzzillo *et al.*, 2015, Purwins *et al.*, 2007] and with an *in situ* study by [Mainz *et al.*, 2015b].

### Phase evolution during thermal treatment

The transformation of the phases is studied by the evolution of the main reflections of both  $\text{Cu}_x(\text{In,Ga})_y$  phases during heating. These are shown in Fig. 4.2.

The 101 reflection of In decreases with increasing  $T_{\text{sub}}$  and vanishes at the melting temperature of In of approximately  $157\text{ }^{\circ}\text{C}$  (see Fig. 4.2c)). After In has melted, the

<sup>2</sup>The 110 and 102 reflections from the reference of  $\text{Cu}_{16}\text{In}_9$  (ICDD 03-065-0704, see Tab. E.2) are in average (and weighted by intensity) at  $34.22\text{ keV}$ .

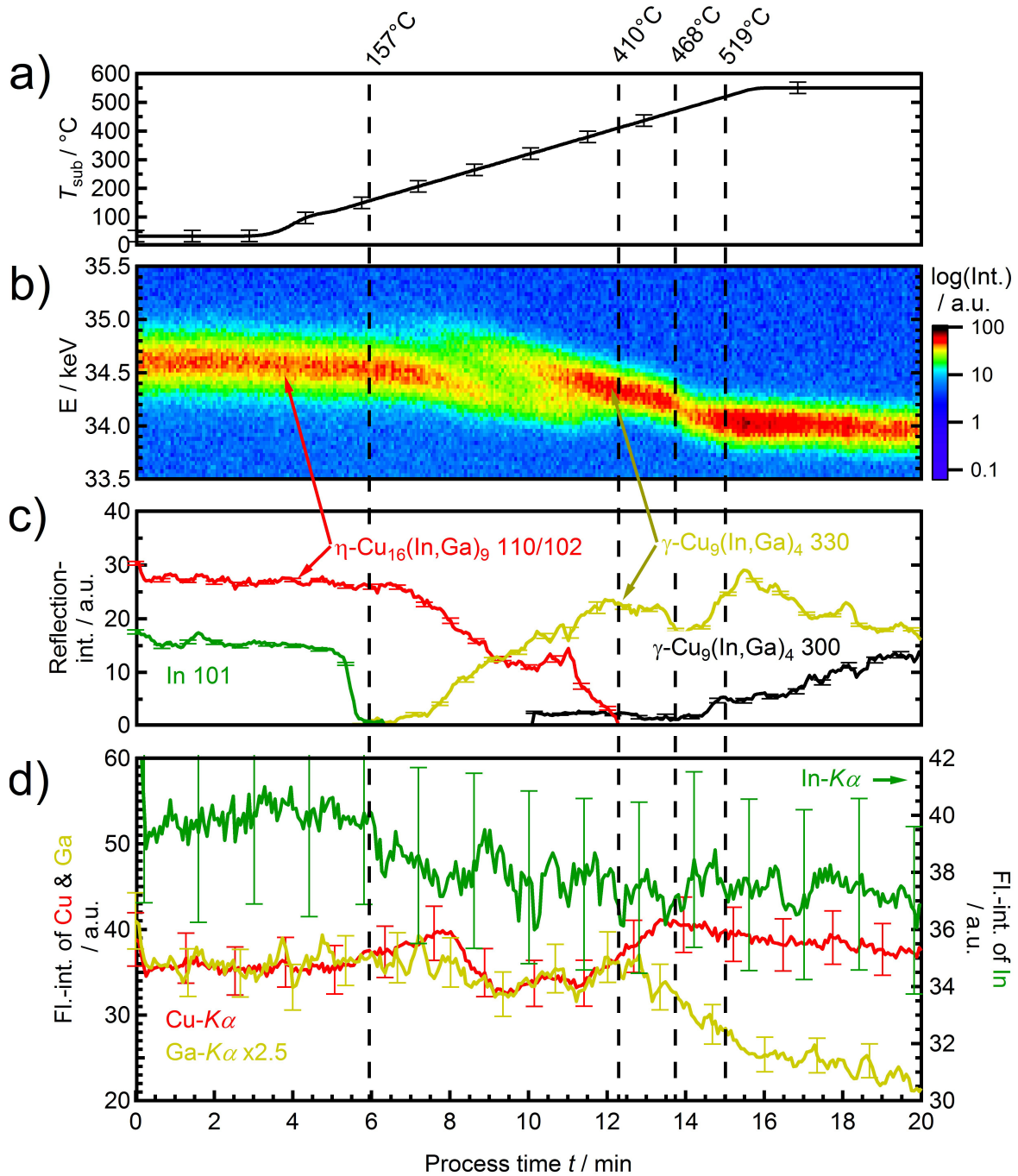


**Figure 4.2.:** Evolution of temperature and intensities of phase reflection and fluorescence peaks over process time during heating of a Cu-In-Ga multilayer precursor. a) Substrate temperature, b) Real-time EDXRD with indicated reflections  $\eta\text{-Cu}_{16}(\text{In,Ga})_9$  110/102 and  $\gamma\text{-Cu}_9(\text{In,Ga})_4$  330, which is a magnified part of the full measurement as shown in Fig. D.1c). The intensity is color coded (as indicated on the right side). c) Integral intensity of reflections and d) integral intensity of fluorescence peaks, fitted with Gaussian curves. Error bars are given in the plot as derived in Sec. B. Dashed vertical lines indicate specific temperatures, that correlate with certain changes in peak properties, for details see text.

reflection intensity of  $\text{Cu}_{16}(\text{In,Ga})_9$  110/102 starts to decrease. At the same time,  $\gamma\text{-Cu}_9(\text{In,Ga})_4$  330 appears and increases until  $\text{Cu}_{16}(\text{In,Ga})_9$  110/102 disappears at 410 °C. This suggests the formation of  $\gamma\text{-Cu}_9(\text{In,Ga})_4$  from  $\text{Cu}_{16}(\text{In,Ga})_9$ . During the initial and strongest change of the  $\text{Cu}_x(\text{In,Ga})_y$  phases between 240 and 320 °C (8 to 10 min), the intensity of In- $K\alpha$  increases while the intensities of Cu- $K\alpha$  and Ga- $K\alpha$  decrease. In the interesting temperature range between 150 °C and 350 °C, the possible Cu and Ga concentrations in  $\gamma\text{-Cu}_9(\text{In,Ga})_4$  are higher than in  $\text{Cu}_{16}(\text{In,Ga})_9$  (compare Cu-In-Ga phase diagrams for 150 °C and 350 °C in Fig. 1.5a and sup. Fig. E.4). Higher Cu and Ga concentrations in  $\gamma\text{-Cu}_9(\text{In,Ga})_4$  are also in agreement with the lattice plane distance of  $\gamma\text{-Cu}_9(\text{In,Ga})_4$  (see sup. Fig. D.2), which is closer to the reference of  $\gamma_i\text{-Cu}_9\text{Ga}_4$  than  $\gamma\text{-Cu}_9\text{In}_4$  and thus exhibits a GGI > 0.5 (using Vegard's law). Liquid In is assumed to remain on top of the film, because the as-grown multilayer exhibited a top layer with 92.6 at.% In (Fig. 2.6a) and is known to form In droplets on top during heating [Gupta and Isomura, 1998, Song *et al.*, 2003]. Therefore, the evolution of the fluorescence intensities indicates, that  $\gamma\text{-Cu}_9(\text{In,Ga})_4$ , which contains higher fractions of Cu and Ga (or less In) forms underneath  $\text{Cu}_{16}(\text{In,Ga})_9$ .

Between 468 °C and 519 °C, the  $\gamma\text{-Cu}_9(\text{In,Ga})_4$  330 reflection exhibits an increase of its integral intensity (Fig. 4.2c) and an increased change of the energetic position over time (Fig. 4.2b) (lattice plane distance, respectively). Furthermore, the reflection intensity of  $\gamma\text{-Cu}_9(\text{In,Ga})_4$  300 increases. The  $\gamma\text{-Cu}_9(\text{In,Ga})_4$  phase can be regarded as a solid solution of  $\gamma\text{-Cu}_9\text{In}_4$  and one of the four different  $\gamma_i\text{-Cu}_9\text{Ga}_4$  phases (i=0,1,2,3), which are shown in the Cu-Ga phase diagram (sup. Fig. E.1). Each of those exhibits a range of allowed Cu to Ga ratios and a corresponding varying lattice constant (sup. Fig. E.2). In principle, they can be differentiated by different intensities of some weak diffraction lines [Predel, 1994]. Unfortunately, no further details about the relative diffraction intensities were found in the literature. Regarding the  $\gamma$ -phase, it is therefore proposed, that the increasing intensity of the 330 reflection, the decreasing position of the 330 reflection and the appearing 300 reflection, indicate a phase change from one  $\gamma_i\text{-Cu}_9\text{Ga}_4$  to another  $\gamma_i\text{-Cu}_9\text{Ga}_4$ .

### 4.1.2. Summary

The metallic phases In,  $\eta\text{-Cu}_{16}(\text{In,Ga})_9$  and  $\gamma\text{-Cu}_9(\text{In,Ga})_4$  were identified. At 157 °C, complete melting of In was observed. From this temperature on, the reflection intensity of  $\eta\text{-Cu}_{16}(\text{In,Ga})_9$  110/102 decreases while the reflection intensity of  $\gamma\text{-Cu}_9(\text{In,Ga})_4$  330 increases. It is supposed, that  $\gamma\text{-Cu}_9(\text{In,Ga})_4$  forms from  $\eta\text{-Cu}_{16}(\text{In,Ga})_9$ . The formation of  $\gamma\text{-Cu}_9(\text{In,Ga})_4$  was concluded to be beneath  $\eta\text{-Cu}_{16}(\text{In,Ga})_9$  due to a decrease of the Cu- $K\alpha$ , Ga- $K\alpha$  and an increase of the In- $K\alpha$  fluorescence intensities (between 8 to 10 min).

## 4.2. Fast absorber growth with strong vertical Ga segregation

This section presents the phase evolution and the depth distribution of phases during a fast selenization of a precursor in Se vapor, which led to a vertical segregation of two CIGS phases with significantly different GGI. Most of the Ga and thus the highest GGI is found at the back contact. This typically observed Ga segregation is studied by means of the evolution of the most dominant diffraction peaks of all identified phases. Their properties, regarding integral intensity, energetic position and corresponding lattice plane distance will be evaluated considering also a correlation with the intensities of fluorescence peaks. An overview of the complete time-resolved EDXRD/EDXRF signals measured is shown in Fig. 4.3. The observed evolutions of diffraction ( $I_{hkl}^{Phase}$ ) and fluorescence peak intensities ( $I_{Element-K\alpha}$ ) during the fast heating between time  $t=0$  min ( $t_0$ ) and  $t=8$  min are shown in Fig. 4.4. The reflection intensities are not evaluated to quantify the phase amounts. However, changes in the intensity of more than the uncertainty are assumed to mainly correlate to a changing crystal amount. The lattice plane distance of a phase is denoted as  $d_{hkl}^{Phase}$ .

Due to a variety of identified CIGS phases with different compositions, the following acronyms are defined:

- CIGS: CIGS phase with a GGI above 0.35
- CIGS: CIGS phase with a GGI between 0.25 and 0.35
- CIGS: CIGS phase with a GGI between 0.1 and 0.25
- CIS: CIGS phase with a GGI below 0.1

### 4.2.1. Analysis of the *in situ* EDXRD/EDXRF measurement

A multilayer Cu-In-Ga precursor (see Sec. 2.1.1) was heated from RT to 580 °C and Se vapor was supplied in the vacuum selenization tool. The starting point of the fast selenization step at  $t_0=0$  min is prepared from  $t=-65$  min until  $t_0$ . The preparation includes the preheating of the Se source and sample for comparability reasons, as described in Sec. 2.1.2. During this preconditioning, Se fluorescence peaks and Se related reflections are detected, which are marked in Fig. 4.3. Thus, condensation and crystallization of Se occurs on the sample surface. Se then evaporates from the surface during a period of 15 min at  $T_{sub}=220$  °C. The Se vapor is pumped through the open reaction chamber valve into the surrounding vacuum chamber. A small Se fluorescence intensity remains

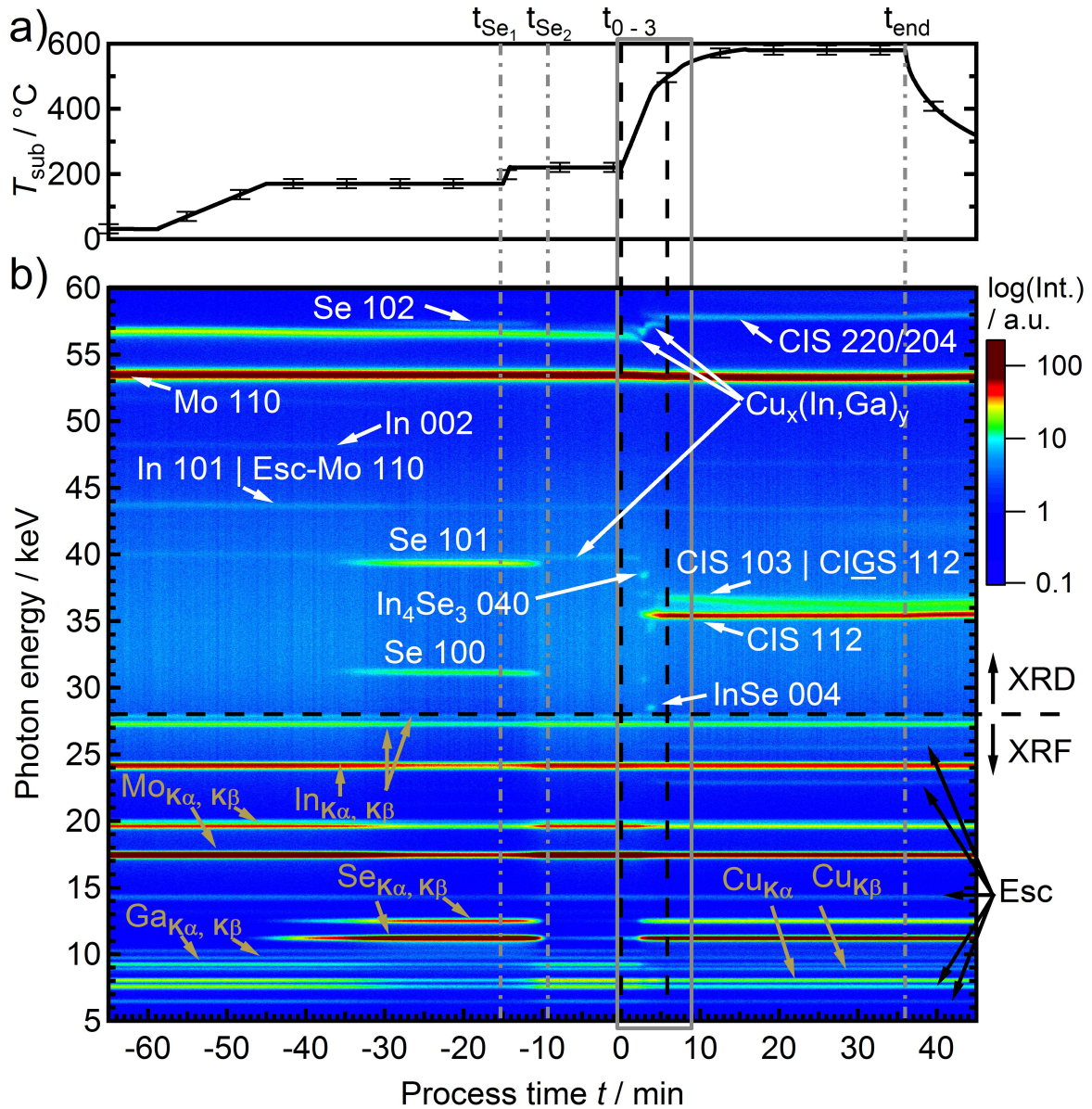


**Figure 4.3.:** Evolution of temperature, intensities of phase reflections and fluorescence peaks over process time during selenization of a Cu-In-Ga multilayer precursor. a) Substrate temperature  $T_{\text{sub}}$  and b) time-resolved EDXRD/EDXRF signals over time. The intensity is color coded (as indicated on the right side). The fluorescence peak with the highest energy is In- $\text{K}\beta_2$  (close to the horizontal dashed line). At lower energies, mainly XRF peaks are present and at higher energies only XRD peaks were found. XRF peaks are assigned in brown and XRD peaks in white. The corresponding ICDD numbers and references are listed in sup. Tab. E.2. Points in time with characteristic diffraction intensities or changes are marked with vertical dashed lines defined as  $t_i$  and  $t_0$  defines the start of the selenization process. Negative times indicate the process preparation before  $t_0$ . The measurement results between 0 and 8 min (gray rectangle) are plotted in an extended scale in Fig. 4.4.

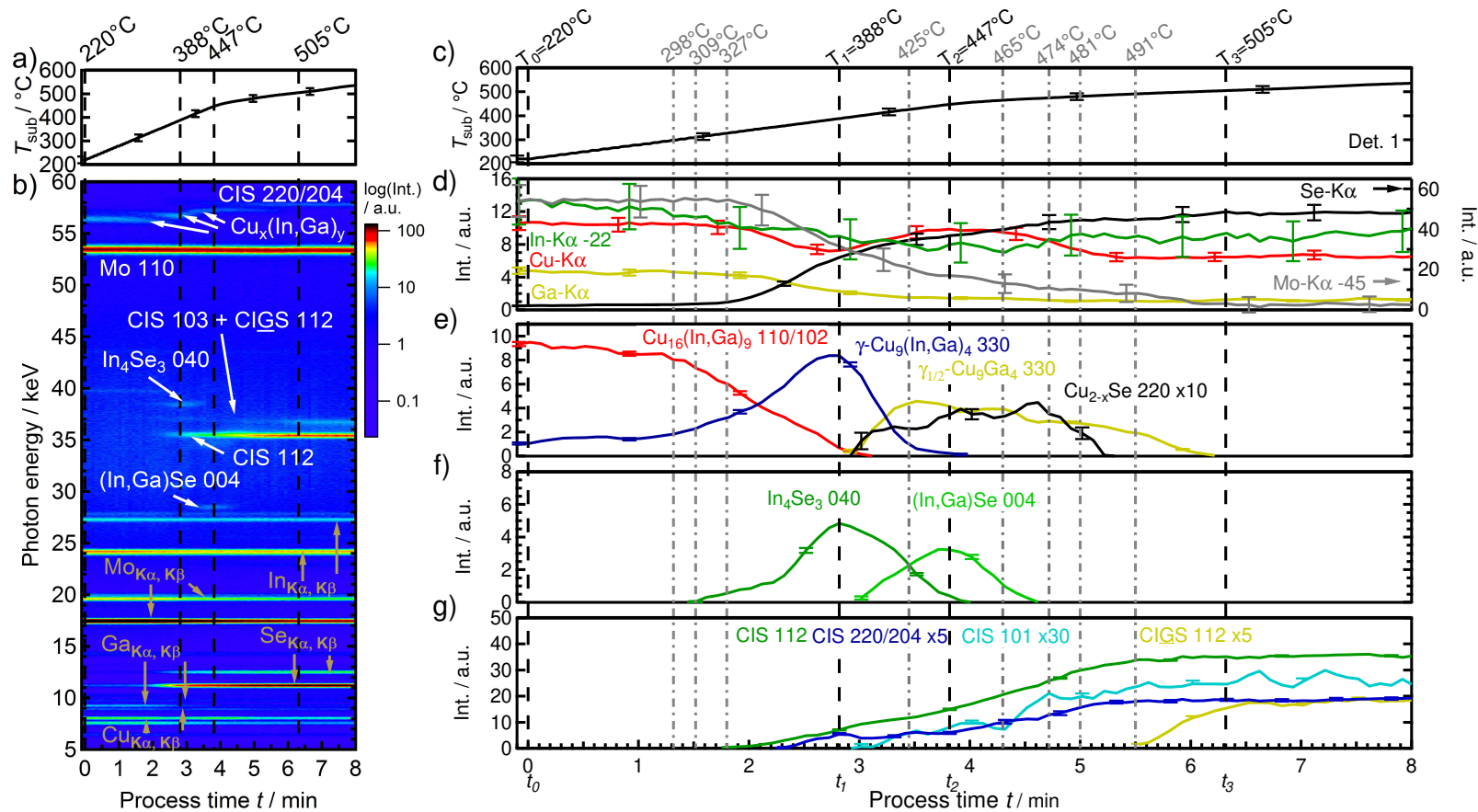


**Figure 4.4.:** Evolution of temperature and intensities of phase reflections and fluorescence peaks over process time during selenization of a Cu-In-Ga multilayer precursor. a) and c) substrate temperature  $T_{\text{sub}}$  with b) magnified region of the time-resolved EDXRD/EDXRF data in Fig. 4.3. Element fluorescence peaks and identified phases are marked. Corresponding ICDD numbers and references are listed in sup. Tab. E.2. Evolution of integral intensities of d) fluorescence peaks and diffraction peaks of e) metallic alloys, f) binary selenides and g) chalcopyrites, for the same time period as in b). Significant peak intensities are highlighted by dashed lines labeled with  $T_i$  and  $t_i$ , at which the phase depth distribution will be deduced in Sec. 4.2.2.

at  $t_{\text{Se}_2}$ . This is probably due to a small amount of Se dissolved in liquid In, which is in accordance with the In-Se phase diagram (sup. Fig. E.6). The chamber valve was then closed at the beginning of the fast heating at  $t_0$ , such that the  $P_{\text{Se}}$  is ideally determined by the Se source in the following.

At the start of the measurement at  $t=-65$  min,  $\eta\text{-Cu}_{16}(\text{In,Ga})_9$  is present with its most dominant 110/102 reflection. Until  $t_0=0$  min, its intensity ( $I_{110/102}^\eta$ ) decreases to about half the initial value. During this period, In melts and  $\gamma\text{-Cu}_9(\text{In,Ga})_4$  appears. Its most dominant reflection intensity ( $I_{330}^\gamma$ ) increases. The decline of  $I_{110/102}^\eta$  correlates with the increase of  $I_{330}^\gamma$ , which is similar to the Se free process presented in Sec. 4.1<sup>3</sup>.

### Evolution of signals between $T_0=220^\circ\text{C}$ and $T_3=505^\circ\text{C}$

Evolutions of integral signal intensities from  $T_0$  onwards are shown in Fig. 4.4. The deduction of the stacking sequence in the following section is performed at the indicated temperatures ( $T_1$ - $T_3$ ) with characteristic signal intensities and a preferably small number of phases.

Between  $T_{\text{sub}}=220^\circ\text{C}$  and  $327^\circ\text{C}$ , Fig. 4.4 shows an increasing transformation rate of the  $\eta$ - to the  $\gamma$ -phase. It also shows the formation of  $\text{In}_4\text{Se}_3$  with its most dominant 040 reflection intensity ( $I_{040}^{\text{In}_4\text{Se}_3}$ ). First reflections assigned to  $\text{In}_4\text{Se}_3$  (e.g. 040, 011, 330, 510) appear at  $T_{\text{sub}}=309^\circ\text{C}$ . Simultaneous with the increase of  $I_{040}^{\text{In}_4\text{Se}_3}$ , the Se fluorescence intensity ( $I_{\text{Se}-K\alpha}$ ) increases, which in turn correlates with the decrease of  $I_{\text{Mo}-K\alpha}$  (see Fig. 4.4d).

$I_{040}^{\text{In}_4\text{Se}_3}$  reaches a maximum at  $T_1=388^\circ\text{C}$ . This maximum occurs at the same time as the maximum of the reflection intensity of  $\gamma\text{-Cu}_9(\text{In,Ga})_4$  330 at  $388^\circ\text{C}$  (see Fig. 4.4e, f)), while  $I_{110/102}^\eta$  decreased to nearly zero. While  $I_{040}^{\text{In}_4\text{Se}_3}$  decreases, reflections of  $(\text{In,Ga})\text{Se}$  appear (004, 110, 002<sup>4</sup>) and increase in intensity ( $I_{004}^{(\text{In,Ga})\text{Se}}$ ). Initially, its composition<sup>5</sup> is close to the reference of InSe (compare sup. Fig. D.4). Over time,  $d_{004}^{(\text{In,Ga})\text{Se}}$  decreases, corresponding to an increasing Ga to In ratio. At  $T_2=447^\circ\text{C}$ , its composition is  $(\text{In}_{0.94}\text{Ga}_{0.06})\text{Se}$ .

At  $T_{\text{sub}}=327^\circ\text{C}$  the first chalcopyrite reflection appears, in the following referred to as CIS 112. Initially, its lattice plane distance  $d_{112}^{\text{CIS}}$  is slightly below the literature value of  $\text{CuInSe}_2$  112 and shifts closer to the reference at  $447^\circ\text{C}$  (see Fig. D.5 for details).

---

<sup>3</sup>The current setup is a different one as used in the previous Sec. 4.1. A different processing tool and different detection angles were used for the setups and hence peak intensities and energetic positions differ. Further experimental details can be found in Sec. 2.1.2.

<sup>4</sup>The peak corresponding to  $(\text{In,Ga})\text{Se}$  002 is overlapping with the escape peak of  $\text{In-K}\alpha$ .

<sup>5</sup> $\text{InSe}$  and  $\text{GaSe}$  can form a solid solution  $(\text{In}_{1-x}\text{Ga}_x)\text{Se}$  with  $x<0.2$  and  $x>0.8$ , as shown in the  $\text{InSe-GaSe}$  phase diagram in sup. Fig. E.7. By use of Vegard's law (Eq. 1.1),  $d_{004}^{\text{GaSe}}$  and  $d_{004}^{\text{InSe}}$ , its composition is calculated.

Between 388 °C and 481 °C, the 330 reflection of  $\gamma$ -Cu<sub>9</sub>(In,Ga)<sub>4</sub> decreases and vanishes (see Fig. 4.4). This evolution correlates with the appearance and increase of reflections assigned to  $\gamma_{1/2}$ -Cu<sub>9</sub>Ga<sub>4</sub> 330 and Cu<sub>2-x</sub>Se 220. The composition of the latter is deduced to be Cu<sub>1.72</sub>Se by use of Vegard's law and literature values from [Tonejc *et al.*, 1975, Tonejc, 1980]. (see P. 160 for further details to Cu<sub>1.72</sub>Se 220 and 111). The  $\gamma_{1/2}$ -Cu<sub>9</sub>Ga<sub>4</sub> phase exhibits a smaller  $d_{330}$  than  $\gamma$ -Cu<sub>9</sub>(In,Ga)<sub>4</sub> (see details in sup. Fig. D.3). The  $d_{330}$  corresponds to the phase composition. The applied procedure to evaluate the composition of the  $\gamma$ -Cu<sub>9</sub>(In<sub>1-x</sub>Ga<sub>x</sub>)<sub>4±y</sub> phases as accurate as possible is explained in sup. Sec. D.1. The transformation of  $\gamma$ -Cu<sub>9</sub>(In,Ga)<sub>4</sub> to In-free  $\gamma_{1/2}$ -Cu<sub>9</sub>Ga<sub>4</sub> was not observed in the Se-free experiment in Sec. 2.1.2 (compare the energetic position with Fig. 4.2b)). Here, the latter phase exhibits no (or nearly no) In anymore. It is therefore very likely, that the released In reacted with Se possibly to an In-Se phase.

At T<sub>1</sub>=388 °C, the composition of  $\gamma$ -Cu<sub>9</sub>(In,Ga)<sub>4</sub> (blue line) is estimated to be within a Cu concentration of 68±1 at.% Cu and a GGI of 0.743±0.007, which is a reasonable composition regarding the ternary phase diagram (sup. Fig. E.4). The GGI of the  $\eta$ -phase is 0.29, as estimated in Sec.4.1. Consequentially, the  $\gamma$ -phase exhibits a higher Ga concentration compared with the  $\eta$ -phase.

At T<sub>2</sub>=447 °C, the possible composition of  $\gamma_{1/2}$ -Cu<sub>9</sub>Ga<sub>4</sub> is 64±4 at.% Cu, within the uncertainty of the measurement.

Due to the release of In from  $\gamma$ -Cu<sub>9</sub>(In,Ga)<sub>4</sub> between T<sub>1</sub> and T<sub>2</sub>, also Cu needs to be released, such that the phase decreases its amount and remains in its phase existence range without a phase transition. The maximum intensity of the  $\gamma_{1/2}$ -Cu<sub>9</sub>Ga<sub>4</sub> phase is smaller than for  $\gamma$ -Cu<sub>9</sub>(In,Ga)<sub>4</sub>, also indicating a smaller total amount of  $\gamma_{1/2}$ -Cu<sub>9</sub>Ga<sub>4</sub>. The release of Cu from  $\gamma$ -Cu<sub>9</sub>(In,Ga)<sub>4</sub> coincides with the formation of Cu<sub>1.72</sub>Se.

Between 388 °C and 491 °C, the intensity of Cu<sub>1.72</sub>Se 220 exhibits a similar evolution as the Cu fluorescence intensity ( $I_{Cu-K\alpha}$ ). The relative increase in  $I_{Cu-K\alpha}$  is even more pronounced in detector 2 (Sup. Fig. D.8). This points to an increasing concentration of Cu towards the surface. The maximum  $I_{Cu-K\alpha}$  at T<sub>2</sub>=447 °C is an important point in time for an evaluation of the phase depth distribution later. The maximum  $I_{Cu-K\alpha}$  can be explained with the presence of the Cu<sub>2-x</sub>Se phase at the surface with its higher Cu content than that in CIS.

During the heating from 447 °C to 481 °C, decreasing intensities of Cu-K $\alpha$ , (In,Ga)Se 004 and Cu<sub>2-x</sub>Se 220 are observed, while all CIS related reflection intensities increase.

$I_{112}^{CIS}$  increases until 491 °C (Fig. D.5b)). Only then, an additional reflection appears, corresponding to CIGS 112 with a GGI of 0.88 and is therefore referred to as CIGS 112. The increasing  $I_{112}^{CIGS}$  correlates with a decreasing intensity of the  $\gamma_{1/2}$ -Cu<sub>9</sub>Ga<sub>4</sub> 330 reflection (Fig. D.3a)) and  $I_{112}^{CIGS}$  reaches its maximum at about 505 °C.

### Interdiffusion of In and Ga after $T_3=505^\circ\text{C}$

The final temperature interval includes the heating from  $505^\circ\text{C}$  to  $580^\circ\text{C}$  and subsequent annealing for 20 min ( $t_3 - t_{\text{end}}$ ). The phases CIS and CIGS change as follows: At  $505^\circ\text{C}$  and during the annealing at  $580^\circ\text{C}$ ,  $d_{112}^{\text{CIGS}}$ ,  $I_{112}^{\text{CIGS}}$  as well as  $d_{220/204}^{\text{CIGS}}$  and  $I_{220/204}^{\text{CIGS}}$  increase. The increase of  $d_{112}^{\text{CIGS}}$  and  $d_{220/204}^{\text{CIGS}}$  is higher than the expected increase by thermal expansion. Hence, it must be correlated with a decreasing GGI (see Fig. D.5e)). The GGI of CIGS decreases from 0.88 at  $505^\circ\text{C}$  to 0.56 until the end of the annealing period with  $580^\circ\text{C}$  ( $t=36$  min). Simultaneously,  $I_{112}^{\text{CIS}}$ ,  $d_{112}^{\text{CIS}}$  as well as  $d_{220/204}^{\text{CIS}}$  and  $I_{220/204}^{\text{CIS}}$  decrease, but relatively smaller in comparison with CIGS. An explanation for this behavior is interdiffusion of In and Ga, while a top part of the film remains Ga-free, as confirmed by the elemental depth profile (Fig. 4.5).

### Final CIGS film composition after cool down

A SEM image of the final CIGS layer is shown in a cross sectional view in Fig. 4.5a). The film was also analyzed with regard to the elemental depth profile by GDOES (see Fig. 4.5b)) and integral film composition by WDXRF (see Tab. 4.1). The GDOES measurement shows a top layer with a CGI over 1 and Se concentration above 0.5. Both are higher than expected for stoichiometric  $\text{Cu}(\text{In,Ga})\text{Se}_2$ . This is perhaps correlated with a CuSe layer, which is often found to be present at the surface, but no CuSe reflections were observed by EDXRD. The CGI of the rest of the absorber layer is about 0.9. This is in good agreement with the integral film composition which exhibits a CGI of 0.96 according to WDXRF.

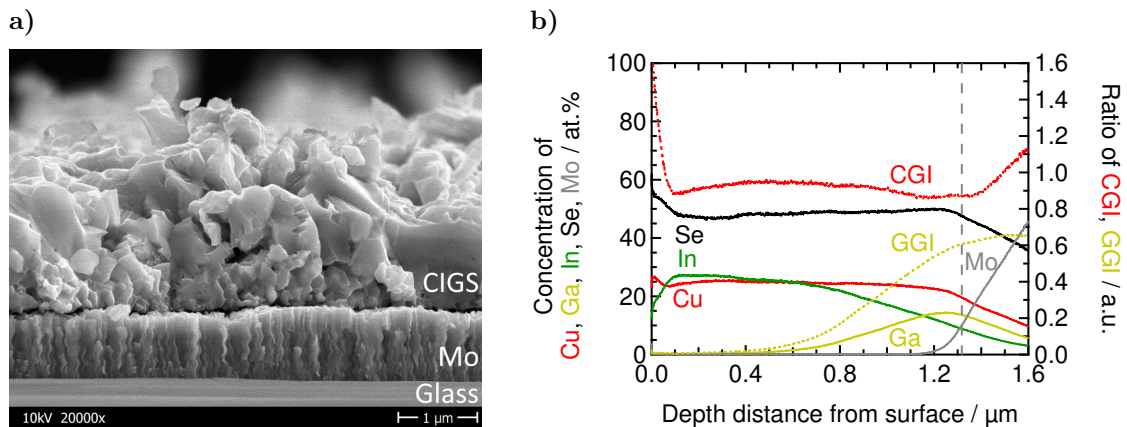


**Figure 4.5.:** a) SEM image of the cross section of the final CIGS film. b) Quantified elemental depth profile measured by GDOES on the final CIGS layer. The in-depth uncertainty is in the order of 100 nm. The back contact is assumed to start at a molar fraction of Mo at 0.1, indicated by the vertical dashed line.

**Table 4.1.:** Elemental compositions of the precursor and absorber, analyzed by WDXRF. In the latter case, the measurement position was aligned to be on the same position as the *in situ* EDXRD/EDXRF measurement.

Element / %	Cu	In	Ga	Se	CGI	GGI	Thickness
Precursor	45.9	39.7	14.4	0	0.87	0.27	610 nm
Absorber	23.2	17.9	6.1	52.8	0.96	0.26	1532 nm

The GDOES measurement shows no relevant Ga content in the top 0.4  $\mu\text{m}$  of the film. Below that, the Ga content increases towards the back contact with a GGI of about 0.6. In comparison, the composition of the two chalcopyrites from their reflections CIS 112 and CIGS 112 at the end of the EDXRD measurement at 108  $^{\circ}\text{C}$  were  $\text{Cu}(\text{In}_{0.98}\text{Ga}_{0.02})\text{Se}_2$  and  $\text{Cu}(\text{In}_{0.45}\text{Ga}_{0.55})\text{Se}_2$ , corresponding to the lattice plane distances of  $0.335 \pm 0.001$  nm and  $0.328 \pm 0.001$  nm. The elemental depth profile determined by GDOES of the absorber film and the final EDXRD signal are in agreement, indicating that two chalcopyrite phases are present, one without and one with Ga. In conclusion, this selenization led to vertical Ga segregation at the back contact.

### Summary of the *in situ* analysis and the deduced phase evolution

The most important results are listed in the following and an overview of the presence of phases observed during process time is provided in Fig. 4.6. The observed phases, their compositions and the listed relevant values at characteristic points in time  $t_i$  are the basis for deducing a growth schematic of stacking sequences in the next section. For this, the complexity of the growth process is reduced to a simple 1D model. The reflection intensities are not evaluated to quantify phase amounts. Therefore, only the presence of a reflection is correlated with the presence of the corresponding phase.

- $\gamma\text{-Cu}_9(\text{In,Ga})_4$  (Cu and Ga richer) grows while  $\text{Cu}_{16}(\text{In,Ga})_9$  reduces until  $T_1$
- $\text{In}_4\text{Se}_3$  appears at  $T_{\text{sub}}=309^{\circ}\text{C}$
- CIS formation starts at  $T_{\text{sub}}=327^{\circ}\text{C}$
- $\gamma\text{-Cu}_9(\text{In,Ga})_4$  and  $I_{\text{Cu-K}\alpha}$  are at maximum at  $T_1=388^{\circ}\text{C}$
- $\gamma\text{-Cu}_9(\text{In,Ga})_4$  transforms to  $\gamma_{1/2}\text{-Cu}_9\text{Ga}_4$  from  $388^{\circ}\text{C}$  onwards until  $T_2=447^{\circ}\text{C}$
- $(\text{In,Ga})\text{Se}$  appears at  $388^{\circ}\text{C}$ , being fed by the  $\text{In}_4\text{Se}_3$  phase
- $(\text{In,Ga})\text{Se}$ ,  $\text{Cu}_{1.72}\text{Se}$  and  $I_{\text{Cu-K}\alpha}$  are at maximum at  $447^{\circ}\text{C}$   
Afterwards,  $(\text{In,Ga})\text{Se}$ ,  $\text{Cu}_{1.72}\text{Se}$  and  $I_{\text{Cu-K}\alpha}$  decrease
- CIGS appears at  $491^{\circ}\text{C}$ , being fed by the  $\gamma_{1/2}\text{-Cu}_9\text{Ga}_4$  phase

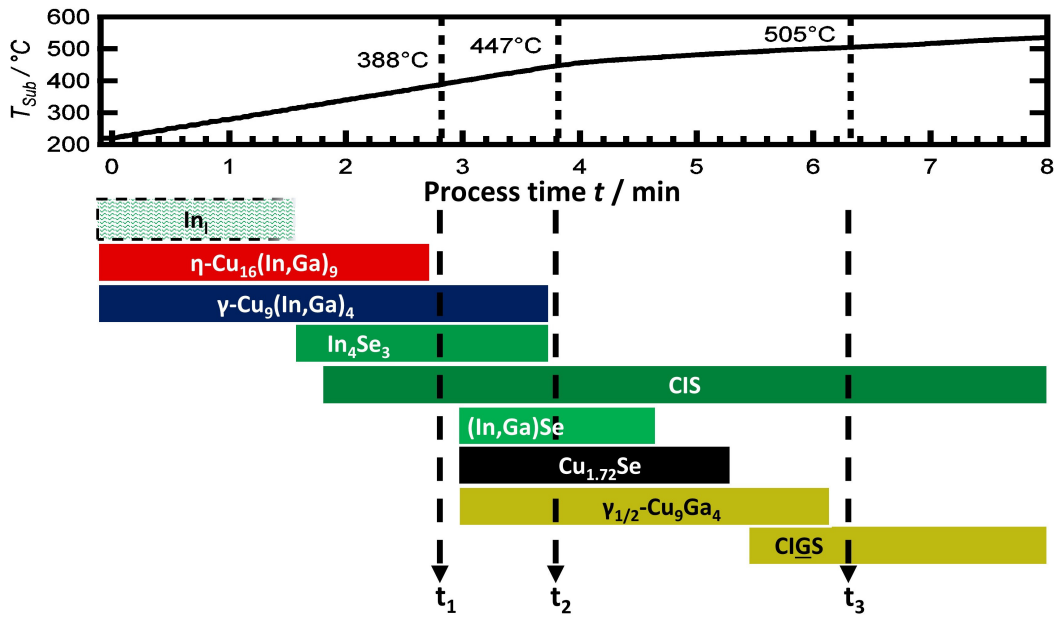


**Figure 4.6.:** Simplified overview of phases present over process time and as function of temperature. Characteristic points in time for deducing a growth schematic with specific stacking sequences are at  $T_{\text{sub}}$  of  $T_1=388^\circ\text{C}$  ( $t_1$ ),  $T_2=447^\circ\text{C}$  ( $t_2$ ) and  $T_3=505^\circ\text{C}$  ( $t_3$ ) in the next section.

- Limited inter-diffusion of Ga and In occurred, leading to a decreasing GGI of the CIGS phase from 0.88 at  $T_3=505^\circ\text{C}$  to 0.56 at end of  $T_{\text{sub}}=580^\circ\text{C}$  ( $t=36.0$  min)
- Final chalcopyrite compositions from EDXRD are  $\text{Cu}(\text{In}_{0.98}\text{Ga}_{0.02})\text{Se}_2$  (CIS) and  $\text{Cu}(\text{In}_{0.45}\text{Ga}_{0.55})\text{Se}_2$  (CIGS) and the elemental depth profile from GDOES showing CIS on top of CIGS

#### 4.2.2. Deduced 1D growth schematic

The aim of this section is to investigate the vertical phase distribution and its evolution in time during the described selenization in Sec. 4.2.1. A simplified one-dimensional growth schematic is proposed at the end of the section. In the following, the individual stacking sequences at characteristic points in time are deduced by comparing the measured fluorescence intensities with calculated fluorescence intensities. Fluorescence intensities were numerically calculated for a set of stacking sequences of the identified phases. This procedure is described in general in Sec. 2.2.2. Finally, the evolution in time of the calculated fluorescence intensities of the deduced stacking sequences are compared with the measured evolution.

The first deduction of the depth distribution of phases at  $T_1=388^\circ\text{C}$  (Sec. 4.2.2.1) is discussed in great detail to demonstrate the variety of reasons for the deduction and

the consistency of the proposed stacking sequence. Subsequent phases at higher  $T_{\text{sub}}$  are deduced analogously in Secs. 4.2.2.2 and 4.2.2.3 and described in less detail.

#### 4.2.2.1. Depth distribution of phases at $T_1=388^\circ\text{C}$

For the deduction of the phase depth distribution (stacking sequence), as described in Fig. 2.5, a linear equation system is used. Input parameters to this linear equation system are the element quantities from an *ex situ* XRF measurement of the precursor (see Sec. 2.2.2.4), number of phases and their composition determined by *in situ* EDXRD at  $388^\circ\text{C}$ . Using the linear equation system, the fraction of phase amounts are determined. If necessary, additional free parameters will be introduced or fixed to be able to solve the linear equation system (see Sec. 2.2.2.3). The thickness of each phase is then determined by its atomic density (see sup. Tab. E.1 for densities). In general,  $n$  phases exhibit  $n!$  possible stacking sequences. The fluorescence intensities were calculated for the  $n!$  stacking sequences (see Sec. 2.2.2.2). Then, the calculated fluorescence intensities of all stacking sequences are compared with the *in situ* obtained fluorescence intensities at  $388^\circ\text{C}$ .

Phases detected at  $388^\circ\text{C}$  are  $\gamma\text{-Cu}_9(\text{In,Ga})_4$ ,  $\text{In}_4\text{Se}_3$ , CIS and  $\text{Cu}_{16}(\text{In,Ga})_9$  (see summary above). The intensity of  $\text{Cu}_{16}(\text{In,Ga})_9$  110/102 is at 0.04 times the initial value. Therefore this phase is neglected here to simplify the model. Thus, the linear equation system to calculate the amounts of the three phases is explicitly solvable based on the amounts of the three elements Cu, Ga and In.

The phase composition of the  $\gamma$ -phase was determined to lie within a possible range of  $68\pm 1$  at.% Cu, as described in Sec. 4.2.1. When changing the composition of  $\gamma\text{-Cu}_9(\text{In,Ga})_4$ , the consequence is that the relative amounts of all phases change, solving the linear equation system, see Tab. 4.2. A lower Cu content in  $\gamma\text{-Cu}_9(\text{In,Ga})_4$  leads primarily to a higher share of CIS, since this is the only other Cu containing phase. A higher phase amount of CIS requires more In and results in a smaller phase amount of  $\text{In}_4\text{Se}_3$ .

**Table 4.2.:** Layer thicknesses of  $\gamma\text{-Cu}_9(\text{In,Ga})_4$ ,  $\text{In}_4\text{Se}_3$  and CIS resulting from the composition of  $\gamma\text{-Cu}_9(\text{In,Ga})_4$  for representation with markers in Fig. 4.7.

Marker for at.% Cu in $\gamma\text{-Cu}_9(\text{In,Ga})_4$	composition of $\gamma\text{-Cu}_9(\text{In}_{1-x}\text{Ga}_x)_{4\pm y}$	Thickness in nm of		
		$\gamma\text{-Cu}_9(\text{In,Ga})_4$	$\text{In}_4\text{Se}_3$	CIS
x: 67 at.% Cu	$\text{Cu}_9(\text{In}_{0.253}\text{Ga}_{0.747})_{4.43}$	258	481	221
+: 68 at.% Cu	$\text{Cu}_9(\text{In}_{0.257}\text{Ga}_{0.743})_{4.24}$	270	504	153
o: 69 at.% Cu	$\text{Cu}_9(\text{In}_{0.264}\text{Ga}_{0.736})_{4.04}$	285	529	74

The Cu concentration in CIS can not be evaluated during growth and was assumed to be stoichiometric (CGI = 1). At  $T_1=388^\circ\text{C}$ , a decrease of the CGI in CIS to 0.9 (integral CGI of the film) would influence the depth distribution only slightly by increasing the Se and In amount in CIS since the total Cu amount in CIS remains. Only about 2% of the In amount in  $\text{In}_4\text{Se}_3$  is then assigned to CIS. The influence is small in comparison with the change of the observed influence of the Cu content in  $\gamma\text{-Cu}_9(\text{In,Ga})_4$  and it is very small in comparison with the impact of a changing stacking order, as shown in the following.

Assuming that each of the three present phases exists as one layer, six permutations as stacking sequence are possible, see A-F in Fig. 4.7a). Fig. 4.7b) shows the corresponding fluorescence intensities calculated for all permutations (marker) with respect to the observed intensities at  $T_1=388^\circ\text{C}$ , marked as dashed lines.

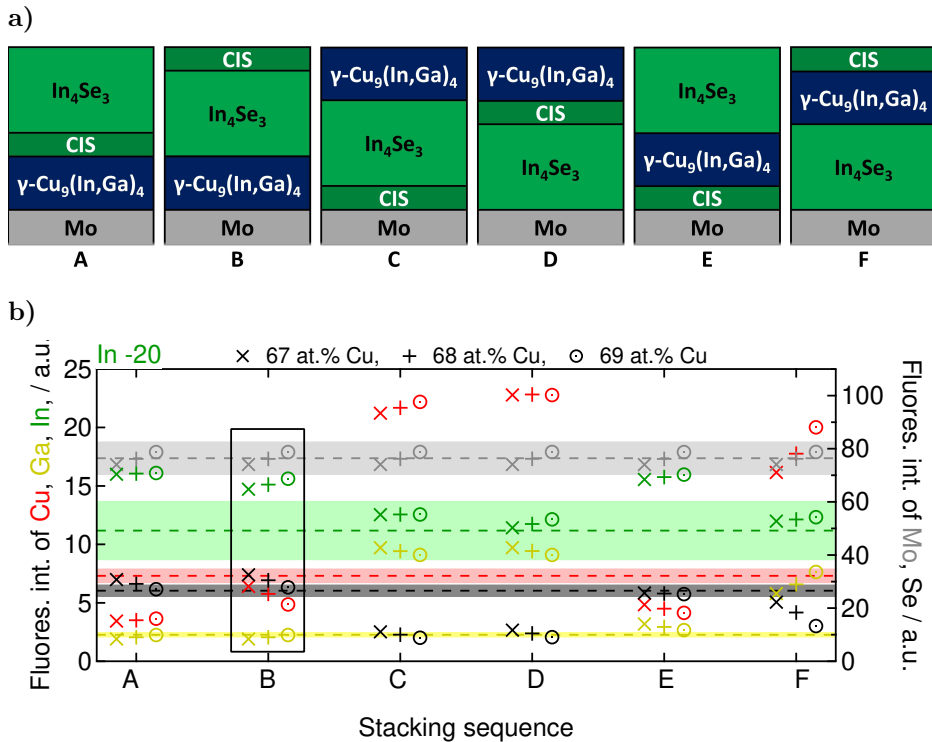


**Figure 4.7.:** a) Stacking sequences of all possible permutations of the three phases at  $T_1=388^\circ\text{C}$  and b) corresponding calculated fluorescence intensities. The colors correspond to the element species as indicated at the left and right axis. The markers (x, +, o) indicate the calculated values for different compositions of  $\gamma\text{-Cu}_9(\text{In,Ga})_4$ , see Tab. 4.2. The calculation method and general parameters are described in Sec. 2.2.2. Further parameters for the calculation and their references are listed in Sec. E. Dashed horizontal lines illustrate the experimental values. The colored background ranges indicate the maximum uncertainty of the experimental values ( $\pm 8\%$ ). The black frame encloses the best matching fluorescence intensities, as described in the text.

All phases comprise the element In. The maximum difference in  $I_{In-K\alpha}$  for the different stacking sequences is low in comparison with differences regarding the fluorescence intensities of other elements. It can not be utilized as distinct indicator to deduce the most likely stacking sequence. Changing the position of the only Ga containing phase within the stack, results in a significant difference between the calculated and the measured fluorescence intensities for stacks C, D and F. For this reason, stacking sequences C, D and F are unlikely and disregarded in the following. Significant differences of the measured and calculated  $I_{Cu-K\alpha}$  are observed for stacking sequences A, C, D, E and F. The stacking sequence, that exhibits an  $I_{Cu-K\alpha}$  fitting the experimental value best (as well as accurate intensities for all other elements) is stacking sequence B.

However, the calculated  $I_{Cu-K\alpha}$  at  $T_1=388^\circ\text{C}$  is lower than measured and not within the uncertainty, but  $I_{Cu-K\alpha}$  is assumed to be an important measure. To explain this deviation, a higher Cu concentration needs to be present in the top layers. Due to the deduction of the subsequent stacking sequence at  $T_2=447^\circ\text{C}$  with  $\text{Cu}_{1.72}\text{Se}$  on top of the film, there are two possible reasons for this discrepancy: i)  $\text{In}_4\text{Se}_3$  was Cu free in the model for calculation of the fluorescence intensities. For the formation of  $\text{Cu}_{1.72}\text{Se}$  after  $388^\circ\text{C}$  (see Fig. 4.9a, Sec.4.2.1 and following section), Cu diffusion to the surface is necessary. The only Cu containing component here is  $\gamma\text{-Cu}_9(\text{In,Ga})_4$ , from where Cu need to diffuse through the  $\text{In}_4\text{Se}_3$  layer. ii) Another possibility is, that a CuSe formation might have occurred prior to  $\text{Cu}_{1.72}\text{Se}$  formation, which was not observed by EDXRD and is not considered in the model. CuSe was found to form during growth of CIGS by others [Purwins, 2010] and to transform to  $\text{Cu}_{2-x}\text{Se}$  starting at  $377^\circ\text{C}$ . The temperature of formation of  $\text{Cu}_{2-x}\text{Se}$  found at  $377^\circ\text{C}$  coincides with the Cu-Se phase diagram (sup. Fig. E.5) showing the transformation of CuSe to  $\text{Cu}_2\text{Se}$  at  $377^\circ\text{C}$  and the difference to the observed temperature of formation of  $\text{Cu}_{1.72}\text{Se}$  here of  $388^\circ\text{C}$ , is within the error of the measurement.

The deduction by comparison of fluorescence intensities, is reviewed by the following plausibility considerations:

i) Se can react exothermically with Cu, Ga and In to form different selenides at temperatures below the temperature here of  $388^\circ\text{C}$ . There is no indication for an energetic beneficially possibility for Se to move through a part of the metallic layer and react preferably deeper in the film. A Se free layer above a Se containing layer is unlikely. A similar growth of CIGS was observed in an *ex situ* study by Mainz *et al.*. They presented a decreasing Se concentration towards Mo for all investigated elemental depth profiles during growth (Fig. 4d in [Mainz *et al.*, 2015b]). Thus, Se was likely to be incorporated into the film from top to bottom and no indication for a Se free phase on top of a Se containing phase was found. Their depth profiles also showed a double Cu gradient. This suggests that the Cu-free phase should be in between the two Cu containing phases.

ii) With lift off a film, the  $\gamma$ -phase was also found at the back contact by others [Hanket *et al.*, 2007].

iii) The position of  $\gamma$ -Cu<sub>9</sub>(In,Ga)<sub>4</sub> at the back contact is also plausible with regard to the presence of  $\gamma_{1/2}$ -Cu<sub>9</sub>Ga<sub>4</sub> at T<sub>2</sub>=447 °C, which is likely to be at the back contact where the final Ga richer CIGS layer forms at T<sub>3</sub>=505 °C (in agreement with the final elemental depth profile in Fig. 4.5b)).

These arguments support the deduction of stacking sequence B from comparison of fluorescence intensities.

The intensities of the six possible permutations confirm that the different stacking sequences lead to distinct differences in fluorescence intensities which are significant. The selection of the most likely stacking order on the basis of the best agreement of measured and calculated fluorescence intensities of all elements is in accordance with plausibility. This justifies the application of the method.

#### 4.2.2.2. Depth distribution of phases at T<sub>2</sub>=447 °C

Phases detected by EDXRD at T<sub>sub</sub>=447 °C are (In<sub>0.94</sub>Ga<sub>0.06</sub>)Se,  $\gamma_{1/2}$ -Cu<sub>9</sub>Ga<sub>4</sub>, CIS and Cu<sub>1.72</sub>Se. With four present phases, there are 4!=24 possible permutations for a stacking sequence. The total number of phases ( $\gamma_{1/2}$ -Cu<sub>9</sub>Ga<sub>4</sub>, (In,Ga)Se, CIS, Cu<sub>1.72</sub>Se) exceed the number of known element quantities (Cu, Ga, In). Hence, the system of linear equations to calculate the phase amounts exhibits a set of solutions. The set is limited as follows: CuInSe<sub>2</sub> has the lowest standard formation enthalpy, thus the amount of CIS is expected to increase over process time. The CIS amount must be higher than calculated by the previous stacking sequence at T<sub>1</sub>=388 °C, for which the linear equation system could be solved explicitly. If a constant texture of the CIS layer is assumed at states 388 °C and 447 °C, it can be approximated that the CIS amount has doubled, since the diffraction intensity increased by a factor of two from 388 °C to 447 °C, see Fig. 4.4g).

The position of  $\gamma_{1/2}$ -Cu<sub>9</sub>Ga<sub>4</sub> is concluded to be at the back contact for the self-consistent reasons as follows: i) The deduced stacking sequence at 388 °C exhibits the  $\gamma$ -phase at the back contact. ii) Later, at 491 °C, the only binary phase left is  $\gamma_{1/2}$ -Cu<sub>9</sub>Ga<sub>4</sub>, which decreased its amount while the Ga rich CIGS appeared and is located at the back contact. iii) The phase exhibits 92 % of the total Ga amount. The main difference to all other phases is the high share of Ga. As consequence of the  $\gamma_{1/2}$ -Cu<sub>9</sub>Ga<sub>4</sub> phase not being at the back contact would be an intermediate increased  $I_{Ga-K\alpha}$  during selenization, until it decreases to the final value. Such an intermediate increase of  $I_{Ga-K\alpha}$  was not observed. iv) The position is consistent with calculated fluorescence intensities for exemplary stacking sequences (sup. Fig. D.7). v) This is also in agreement with the elemental depth profiles, found for a selenization with Ga segregation in literature for

a similar growth and setup (Fig. 4c-e in [Mainz *et al.*, 2015b]).

The position of  $\gamma_{1/2}$ -Cu<sub>9</sub>Ga<sub>4</sub> at the back contact decreases the number of possible permutations from generally 24 to 6.

### Evaluation of stacking sequence with $\gamma_{1/2}$ -Cu<sub>9</sub>Ga<sub>4</sub> at the back contact

In the following, the fluorescence intensities are calculated as function of a free parameter. The amount of CIS is chosen as free parameter. More CIS leads mainly to less Cu<sub>1.72</sub>Se. The lower limit of the CIS amount is assumed as the double amount from 388 °C. The composition of  $\gamma_{1/2}$ -Cu<sub>9</sub>Ga<sub>4</sub> is set to the average value of 64 at.% Cu, for the moment. An increasing amount of CIS results in an evolution with decreasing amounts of Cu<sub>1.72</sub>Se and (In,Ga)Se. This is similar to the experimental phase evolution at 447 °C onwards in Fig. 4.4. Thus, the evolution of the calculated fluorescence intensities (Fig. 4.8a)) should also be similar to the experimental evolution. In particular, a decreasing amount of Cu<sub>1.72</sub>Se can be correlated to a decreasing  $I_{Cu-K\alpha}$ , as observed. That means a decrease of  $I_{Cu-K\alpha}$ ,  $I_{Ga-K\alpha}$  (slightly), an increase of  $I_{Se-K\alpha}$  and a slightly increase of  $I_{In-K\alpha}$ , see Fig. 4.4d) with respect to T<sub>1</sub> is expected.

(In,Ga)Se as the top layer is unlikely, since a Cu containing phase is necessary close to the surface to explain the intermediate increased  $I_{Cu-K\alpha}$  between 388 °C and 491 °C.

The measured evolution of  $I_{Cu-K\alpha}$  from T<sub>2</sub>=447 °C onwards (maximum of  $I_{Cu-K\alpha}$  at T<sub>2</sub>, see Fig. 4.4d)) until Cu<sub>1.72</sub>Se vanished (decreased  $I_{Cu-K\alpha}$ ) may be compared with the calculated evolution of  $I_{Cu-K\alpha}$  for an increasing amount of CIS (resulting in a decreasing amount of Cu<sub>1.72</sub>Se) as in Fig. 4.8a). At the rightmost value for each stack, no Cu<sub>1.72</sub>Se is left. The relative evolution of all fluorescence intensities fit better to sequence A than to D.

The exemplary stacking sequences A and D are shown to deduce the position of (In,Ga)Se and CIS within the stack, ignoring Cu<sub>1.72</sub>Se at the moment (Fig. 4.8a). Due to the slight Ga amount in (In,Ga)Se, (In,Ga)Se above CIS as in stacking sequence D would correspond to an intermediate increase of  $I_{Ga-K\alpha}$ , contrary to the observation. A formation of (In,Ga)Se fed by In<sub>4</sub>Se<sub>3</sub> is most plausible. Assuming In<sub>4</sub>Se<sub>3</sub> as the educt for (In,Ga)Se, it is likely that (In,Ga)Se is located close to the only other Ga containing phase  $\gamma_{1/2}$ -Cu<sub>9</sub>Ga<sub>4</sub>, from where it must have incorporated its Ga content. Therefore (In,Ga)Se is concluded to be below CIS and at the  $\gamma_{1/2}$ -Cu<sub>9</sub>Ga<sub>4</sub> phase.

In the following, the deduction of the position of Cu<sub>1.72</sub>Se is presented. The depth position of Cu<sub>1.72</sub>Se directly above  $\gamma_{1/2}$ -Cu<sub>9</sub>Ga<sub>4</sub> is presented as stacking sequence C. In this case,  $I_{Cu-K\alpha}$  increases with a decreasing amount of Cu<sub>1.72</sub>Se. This is in contrast to the evolution of the measured value between T<sub>2</sub> and T<sub>3</sub>.  $I_{Cu-K\alpha}$  is highest for a vanished Cu<sub>1.72</sub>Se phase. Especially the highest  $I_{Cu-K\alpha}$  is below a possible intensity to match the experimental value. Stacking sequence C is therefore ruled out.

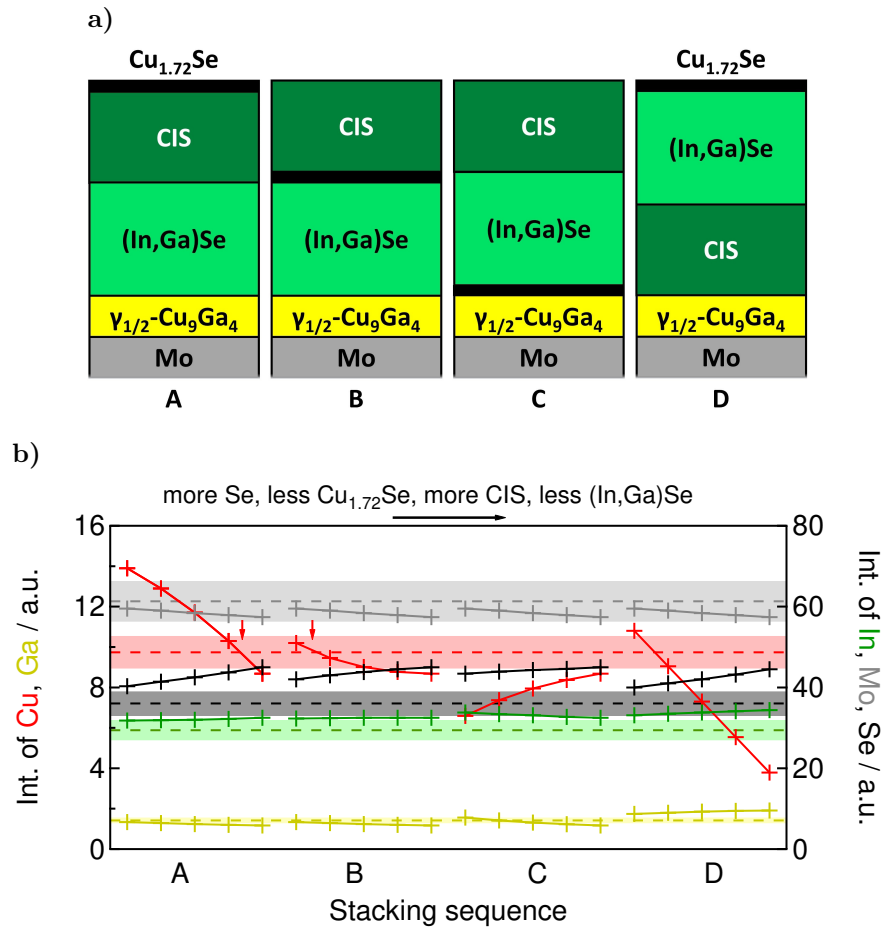


**Figure 4.8.:** a) Stacking sequences with different positioning of the three phases above  $\gamma_{1/2}$ - $\text{Cu}_9\text{Ga}_4$  and b) corresponding calculated fluorescence intensities for each stack as function of an increasing CIS thickness. The colors correspond to the element species as indicated at the left and right axis. Dashed lines indicate the experimental values at  $T_2=447^\circ\text{C}$ . The colored background ranges indicate the maximum uncertainty of the experimental values ( $\pm 8\%$ ). The arrows indicate the reasonably matching  $I_{\text{Cu}-K\alpha}$ .

The remaining stacking sequences A and B exhibit an overlap of the calculated with the measured  $I_{\text{Cu}-K\alpha}$  (red arrows in Fig. 4.8b)) and similar evolutions of the fluorescence intensities with the CIS thickness. The fluorescence intensities do not allow to distinguish between stacking sequences A and B. The studies in literature, in which presence of  $\text{Cu}_{2-x}\text{Se}$  was detected, a presence of  $\text{Cu}_{2-x}\text{Se}$  at the surface is typically concluded [Liu *et al.*, 2014, Purwins, 2010, Lei *et al.*, 2006]. Recent results also found  $\text{Cu}_{2-x}\text{Se}$  as platelets at grain boundaries and within grains [Sanli *et al.*, 2017]. This is in agreement with the results here. However, the degree of intermixing can not be investigated here. The important result is, that the phase  $\text{Cu}_{2-x}\text{Se}$  is most likely to be found on top of the film, possibly also within the CIS layer and the modeled fluorescence intensities are appropriate to describe the measured fluorescence evolutions, especially of  $I_{\text{Cu}-K\alpha}$ .

As the last step, the effect of all possible phase compositions applied to stacking sequence A is studied to test the plausibility. The influence of the Cu concentration in  $\gamma_{1/2}$ - $\text{Cu}_9\text{Ga}_4$  and the evolution of the calculated and the observed fluorescence intensities are presented in Fig. 4.9. A decreasing amount of Cu in  $\gamma_{1/2}$ - $\text{Cu}_9\text{Ga}_4$  results in an increasing amount of  $\text{Cu}_{1.72}\text{Se}$ . This mainly increases  $I_{\text{Cu}-K\alpha}$ . An evaluation of the exact amount of Cu in  $\gamma_{1/2}$ - $\text{Cu}_9\text{Ga}_4$  is not possible by comparison of the fluorescence intensities and is not necessary here. The important result remains, that the phase  $\text{Cu}_{2-x}\text{Se}$  is most likely to be found on top of the film and the range of the Cu concentration in  $\gamma_{1/2}$ - $\text{Cu}_9\text{Ga}_4$  still leads to the same stacking sequence. Stacking sequence A is selected as being representative.

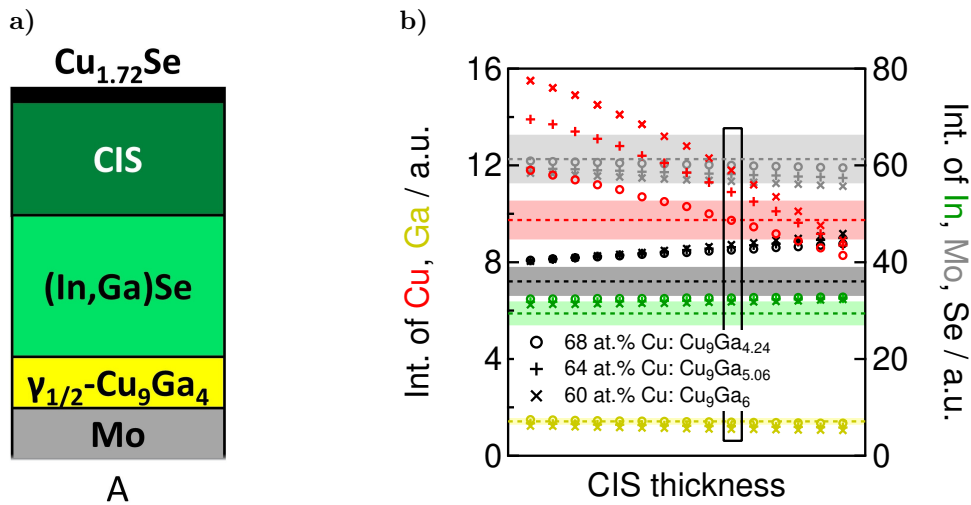


**Figure 4.9.:** a) Most probable stacking sequence at  $T_2=447^\circ\text{C}$  and b) corresponding calculated fluorescence intensities as function of an increasing CIS thickness (between the limits as described in the text). The colors correspond to the element species as indicated at the left and right axis. The dashed lines indicate the experimental values observed at  $447^\circ\text{C}$ . The colored background ranges indicate the maximum uncertainty of the experimental values ( $\pm 8\%$ ). x, +, o indicate the resulting fluorescence intensities for 60, 64, 68 at.% Cu in  $\gamma_{1/2}\text{-Cu}_9\text{Ga}_4$ . The black frame encloses the best matching fluorescence intensities, as described in the text.

#### 4.2.2.3. Depth distribution of phases at $T_3=505^\circ\text{C}$

The diffraction and fluorescence peaks at  $T_3$  are nearly at the same final values as in the end of the selenization. It is likely, that the precursor has completely transformed during thermal treatment with supplied Se vapor to the two detected chalcopyrite phases CIS and CIGS. The depth distribution of the two CIGS phases is determined by the Ga segregation at the back contact, confirmed e.g. by the absorber elemental

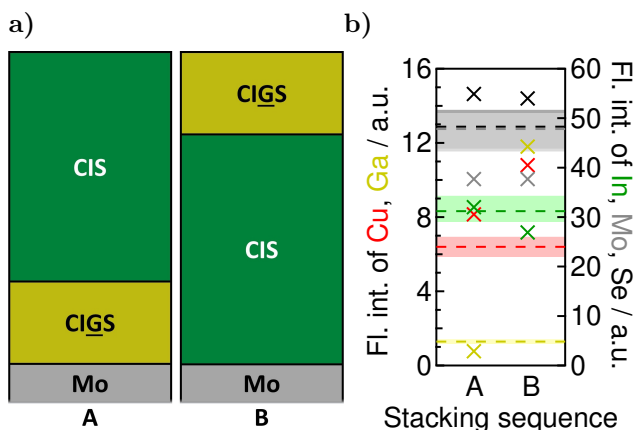


**Figure 4.10.:** a) Stacking sequences A, B and b) corresponding calculated fluorescence intensities. The colors correspond to the element species as indicated at the left and right axis. Dashed horizontal lines indicate the fluorescence intensities observed at  $T_3=505^\circ\text{C}$ . The colored background ranges indicate the maximum uncertainty of the experimental values ( $\pm 8\%$ ).

depth profile measured by GDOES (see Fig. 4.5b)). The linear equation system is overdetermined due to two phases and three element quantities. It can be solved, with leaving the Cu concentration in the CIGS phases as a free parameter. The Cu depth profile is approximated as constant over both phases. The calculated fluorescence intensities are shown in Fig. 4.10 for the two stacking sequences with either CIS (A) or CIGS (B) on top. The stacking order with CIGS on top shows significantly higher deviations of the calculated with respect to the measured fluorescence intensities for In, Ga and additionally for Cu. The depth profile of Cu is the same for both stacks and the different values demonstrate the higher attenuation of  $I_{Cu-K\alpha}$  by In than Ga. The most probable stacking sequence A is in agreement with the observed elemental depth profile by GDOES. The resulting layer thicknesses are shown in Tab. 4.3. The result validates the method used for the evaluation of the elemental depth profile by calculating fluorescence intensities for specific elemental depth profiles. However, not all calculated fluorescence intensities are within the uncertainty of the measured values. A more detailed depth profile comprising depth gradings within the phases could improve the agreement of the  $I_{Cu-K\alpha}$  and  $I_{Ga-K\alpha}$ .

**Table 4.3.:** Phases and their layer thicknesses, as deduced above for  $t_1-t_3$ .

$T_{\text{sub}} (T_i)$	$T_1=388^\circ\text{C}$	$T_2=447^\circ\text{C}$	$T_3=505^\circ\text{C}$
Phase / nm	CIS / 221 nm $\text{In}_4\text{Se}_3$ / 481 nm $\gamma\text{-Cu}_9(\text{In,Ga})_4$ / 258 nm	$\text{Cu}_{1.72}\text{Se}$ / 31 nm CIS / 493 nm $(\text{In,Ga})\text{Se}$ / 517 nm $\gamma_{1/2}\text{-Cu}_9\text{Ga}_4$ / 199 nm	CIS / 1202 nm CIGS / 462 nm

#### 4.2.2.4. Comparison between time dependence of measured and calculated fluorescence intensities

Various stacking sequences were investigated above to deduce the most likely ones at given times during selenization. Now, the concluded stacking sequences with their corresponding fluorescence intensities are shown in context to the evolution of the fluorescence intensities from *in situ* EDXRF (Fig. 4.11) for comparison and investigation of the relative evolution throughout the whole process.

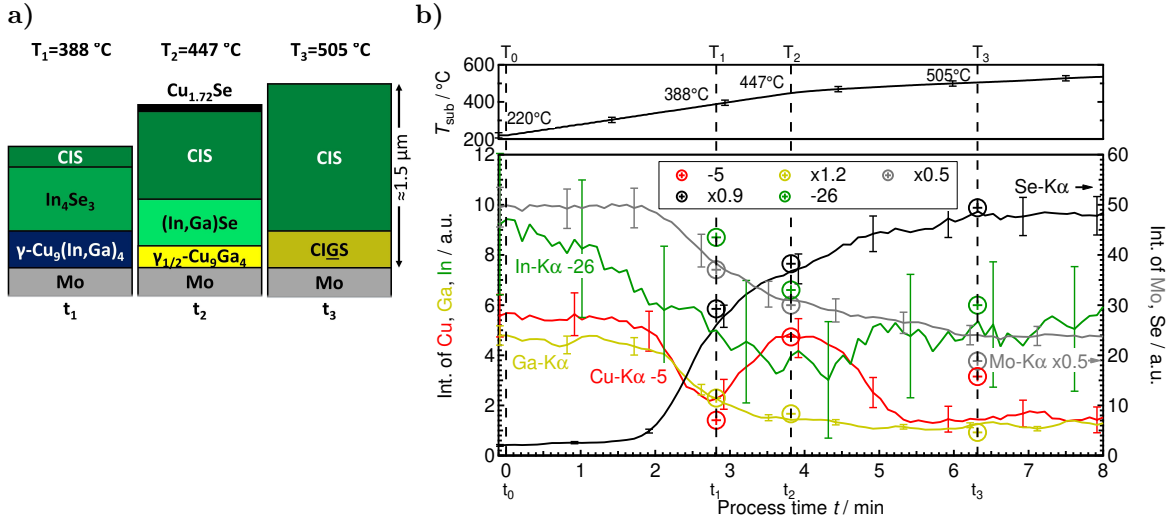


**Figure 4.11.:** a) Proposed growth schematic and b) calculated fluorescence intensities for the respective stacking sequences at  $T_{\text{sub}}$  of  $T_1=388^\circ\text{C}$  ( $t_1$ ),  $T_2=447^\circ\text{C}$  ( $t_2$ ) and  $T_3=505^\circ\text{C}$  ( $t_3$ ). The colors correspond to the element species as indicated at the left and right axis. The Ga fluorescence intensity increased until the heating lamps are turned off and the Ga rich CIGS 112 reflection shifts to lower  $d$  with lower Ga concentration. The results regarding the second detector can be found in sup. Fig. D.8.

The relative evolution is basically similar to the measured one, which is the key aspect for the proposed growth schematic. In case of individual calculated fluorescence intensities, which are outside the uncertainty of the measurement, possible reasons for this were given for each distinct deviation and discussed in the subsections above. A general and small deviation of all fluorescence intensities of a distinct element can result from a systematic error. A systematic error can result from the calibration of the correcting factor. For the calculation of this factor, a stack comprising two layers with a constant elemental composition were assumed. The top layer was approximated by an average Cu content of 6 at.%, although the elemental depth profile by GDOES in Fig. 2.6a) shows a slight gradient, which could not be determined in more detail due to the depth resolution of the GDOES setup.

Assuming this systematic error to be present, an additional factor for the fluorescence

intensities decreases this mismatch retrospectively<sup>6</sup>. With this, the matching evolution is highlighted. In detail, the calculated  $I_{Se-K\alpha}$  and  $I_{In-K\alpha}$  were slightly higher than the measured intensities during each deduction of a stacking sequence. Furthermore,  $I_{Ga-K\alpha}$  was slightly lower. Using these factors does not change the deduced stacking sequences and the good agreement of the relative change of calculated and measured fluorescence intensities.

In case of  $I_{In-K\alpha}$ , a further explanation for the generally slightly higher calculated than measured fluorescence intensities might be a slight In-loss during selenization. An evaporation of an In-Se is likely [Greenberg *et al.*, 1973, Chatillon, 1993].

A second detector was applied in a smaller angle to the substrate (see Sec. 2.2.1) and the fluorescence intensities were also calculated for detector 2, based on the deduced stacking sequences. Interestingly, the relative evolution is also similar in detector 2 (see sup. Fig. D.8), although the deduction was only based on the experimental results from detector 1.

The general discussion of the applied EDXRD/EDXRF method for the deduction of a growth schematic can be found in Sec. 4.4.

Overall, the presented resulting evolutions of the calculated fluorescence intensities of all elements are in good agreement with the observed fluorescence intensities. This strongly supports the proposed growth schematic. Such a detailed growth model in regard to phase compositions has not been presented before.

This is the first time that the method of calculating fluorescence intensities is applied to a whole Cu(In,Ga)Se<sub>2</sub> growth process. The results approve the applicability to such a complex system.

In literature, there are two accepted schematic presentations for the growth of CIGS with strong Ga segregation concerning the elemental depth distributions and phases during growth from Mainz *et al.* and Purwins:

i) Mainz *et al.* proposed a simplified 1D growth model (Fig. 4 in [Mainz *et al.*, 2015b]), based on *in situ* EDXRD and *ex situ* elemental depth profiles. The final elemental depth profile and the general evolution of phases from Mainz *et al.* (Fig. 1.10) is similar to the observations presented in Fig. 4.4. Their schematic of the evolution starts with melting of In and the presence of Cu<sub>x</sub>(In,Ga)<sub>y</sub> phases (suggested as Cu<sub>16</sub>(In,Ga)<sub>9</sub> and Cu<sub>9</sub>(In,Ga)<sub>4</sub>), which vanished during Se incorporation. Selenides like In<sub>4</sub>Se<sub>3</sub> and afterwards InSe were forming as well as the growth of CIGSe/CIGSe and CGSe/CIGSe (denoted here as CIS and CIGS, respectively) were observed. Here, the Cu<sub>x</sub>(In,Ga)<sub>y</sub> phases were differentiated as Cu<sub>16</sub>(In,Ga)<sub>9</sub>,  $\gamma$ -Cu<sub>9</sub>(In,Ga)<sub>4</sub> and  $\gamma_{1/2}$ -Cu<sub>9</sub>Ga<sub>4</sub>, with the latter two phases growing below the first one. Mainz *et al.* found indications for In-Se beneath Cu-Se, which was identified here as Cu<sub>1.72</sub>Se. They could not distinguish

---

<sup>6</sup>The factors were determined for Ga and Se (see Fig. 4.11b)) by use of the average proportionality of all three calculated points to the measured values.

the phases  $\text{In}_4\text{Se}_3$  and  $\text{InSe}$  in their elemental depth profiles by EDX and denoted a layer as In-Se. This assumption is confirmed with the results here, showing that  $\text{InSe}$  formed at the same position as  $\text{In}_4\text{Se}_3$ . It also agrees to be below  $\text{Cu-Se}$  and  $\text{CuInSe}_2$ . While they showed a replacement of  $\text{Cu-Se}$  by  $\text{CuInSe}_2$  and  $\text{In-Se}$  present beneath these phases, here,  $\text{InSe}$  vanished before  $\text{Cu}_{1.72}\text{Se}$  vanished. Their stacking order of  $\text{In-Se}$  below  $\text{CuInSe}_2$  is in agreement with the stacking sequence deduced here.

ii) Purwins proposed a 2D model (Fig. 110 in [Purwins, 2010]) of the growth of CIGS with excess chalcogen supply, based on calorimetric and *in situ* as well as *ex situ* XRD investigations. This schematic of consecutive stacking sequences explains the initial formation of some phases and further growth by use of partly lateral distributed crystals instead of only closed layers. For example, the stacking sequences b)  $\text{Mo/Cu}_9\text{Ga}_4/\text{In}_4\text{Se}_3/\text{InSe}/\text{CuInSe}_2/\text{CuSe}$ , c)  $\text{Mo/Cu}_9\text{Ga}_4/\text{InSe}/\text{CuInSe}_2/\text{Cu}_2\text{Se}$  and g) of  $\text{Mo/CuGaSe}_2/\text{CuInSe}_2$  are in agreement with the deduced stacks at  $T_1$ ,  $T_2$  and  $T_3$ . A formation of  $\text{CuInSe}_2$  is shown to be fed by  $\text{InSe}$ , in contrast to the formation observed in the present work, where the formation of  $\text{CuInSe}_2$  is starting already with the appearance of  $\text{In}_4\text{Se}_3$ . He suggested the presence of  $\text{CuSe}$  on top of the film before  $\text{Cu}_2\text{Se}$  appears. This is also possible here, based on the too low  $\text{Cu}$  fluorescence intensity calculated for  $T_1$ .

The results here are in good agreement with the literature.

### 4.2.3. Summary

A selenization process with final Ga segregation was investigated. The present phases were determined by *in situ* EDXRD. A 1D growth schematic with the position of the phases within the film was deduced by comparing the evolution of the *in situ* EDXRF results with calculated fluorescence intensities. The method of calculating the elemental fluorescence intensities on the basis of a 1D layer stack of identified phases was applied. This is the first time that the method of calculating fluorescence intensities has been applied to a complete selenization process of a  $\text{Cu-In-Ga}$  precursor to CIGS. This growth path with Ga segregation is well documented in literature. A good agreement of the obtained results with the literature was achieved. The utilization of this method to a system with such a high complexity and the good agreement of the deduced 1D growth schematic with the measurement results demonstrate the applicability and limits of the method. The growth schematic is more detailed in regard to phases, phase composition and depth distribution as it was previously proposed using other methods. It could be shown, that  $\text{Cu}$  movement towards the surface occurs, when it occurs and that it is correlated to the formation of  $\text{Cu}_{2-x}\text{Se}$ .

### 4.3. Fast absorber growth without final vertical Ga segregation

The following results reveal the phase evolution and phase depth distribution during the selenization with a finally homogenized Ga depth profile which exhibits a minimum GGI of 0.26. This is the first report of an *in situ* observation of such a process. The following results are in contrast to the results presented before in Sec. 4.2, where nearly no Ga was in the top part of the final CIGS film. Both processes were performed with the same temperature profile and with precursors, which were prepared in the same sputter run. Again, the results obtained during selenization with the *in situ* EDXRD/EDXRF method are presented first (Sec. 4.3.1). Then, the stacking sequence of the present phases is deduced by comparison of the obtained EDXRF intensities to calculated fluorescence intensities. This is repeated for specific points in time  $t_i$  to propose an evolution of the phase depth distribution during selenization (Sec. 4.3.2).

#### 4.3.1. Analysis of the *in situ* EDXRD/EDXRF measurement

The multilayer precursor was heated with 1 °C/s in supplied Se vapor in the vacuum selenization tool. Fig. 4.12 presents the applied temperature profile ( $T_{\text{sub}}$ ) together with the time-resolved EDXRD/EDXRF signal during the heat up. Significant reflection intensity maxima or changes are marked with dashed lines at specific temperatures  $T_i$  (points in time  $t_i$ , respectively) starting with  $T_0=220$  °C and  $t_0=0$  min.

#### Evolution until the first appearance of a CIGS related reflection

$$T_0=220 \text{ °C} \leq T_{\text{sub}} \leq T_1=388 \text{ °C} \quad (t_0 \leq t \leq t_1)$$

At the start of the fast heating step at  $T_0=220$  °C, the sample contains the  $\eta$ - and  $\gamma$ -phases. Their most dominant reflections are  $\eta$ -Cu<sub>16</sub>(In,Ga)<sub>9</sub> 110/102 and  $\gamma$ -Cu<sub>9</sub>(In,Ga)<sub>4</sub> 330. The corresponding intensities are denoted as  $I_{110/102}^\eta$  and  $I_{330}^\gamma$ . At  $T_0$ ,  $I_{110/102}^\eta$  exhibits only half the value compared with the beginning of the measurement (not shown, compare Fig. D.9). The decline of  $I_{110/102}^\eta$  correlates with the occurrence and increase in intensity of  $I_{330}^\gamma$  (Fig. 4.12e)). These trends become more significant above  $T_{\text{sub}}=310$  °C. The same general evolution was found by detector 2 (dashed lines in Fig. 4.12e)). The relative intensities of the alloys differ between the two detectors. While  $I_{330}^\gamma$  reaches nearly the same height as the  $I_{110/102}^\eta$  reflection in detector 1, in detector 2  $I_{330}^\gamma$  increases only to half the height of the  $I_{110/102}^\eta$  reflection.

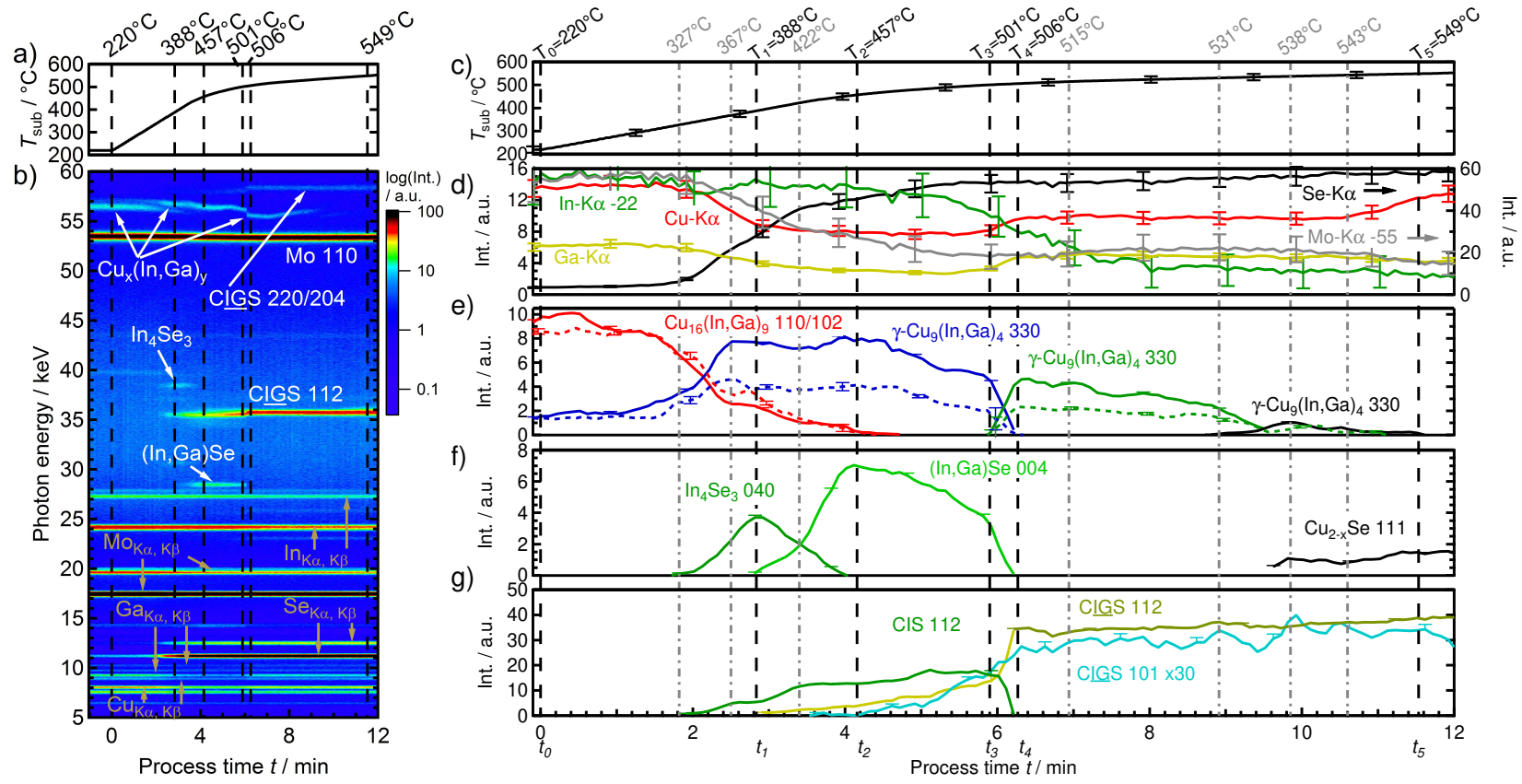


**Figure 4.12.:** Evolution of temperature and intensities of phase reflections and fluorescence peaks over process time during selenization of a Cu-In-Ga multilayer precursor. a) and c) substrate temperature profile with b) magnified area from time-resolved EDXRD/EDXRF data of detector 1. The complete measurement data is appended as Fig. D.9. Element fluorescence peaks and identified phases are marked. Corresponding ICDD numbers and references are listed in sup. Tab. E.2. Evolution of integral intensities of d) fluorescence peaks and diffraction peaks of e) metallic alloys (dashed lines for the same reflections of detector 2), f) binary selenides and g) chalcopyrites. Significant peak intensities are highlighted by dashed lines labeled with  $T_i$  and  $t_i$ , at which the phase depth distribution will be deduced in Sec. 4.3.2.

Detector 2 is more surface sensitive. Thus, the lower relative intensity of  $\gamma$ -Cu<sub>9</sub>(In,Ga)<sub>4</sub> 330 in detector 2 points to a growth of  $\gamma$ -Cu<sub>9</sub>(In,Ga)<sub>4</sub> below Cu<sub>16</sub>(In,Ga)<sub>9</sub>. This is in agreement with the results from the Se free treatment in Sec. 4.1, where the same conclusion was drawn, based on the decreasing  $I_{Cu-K\alpha}$  and  $I_{Ga-K\alpha}$  together with the increasing  $I_{In-K\alpha}$  fluorescence intensities.

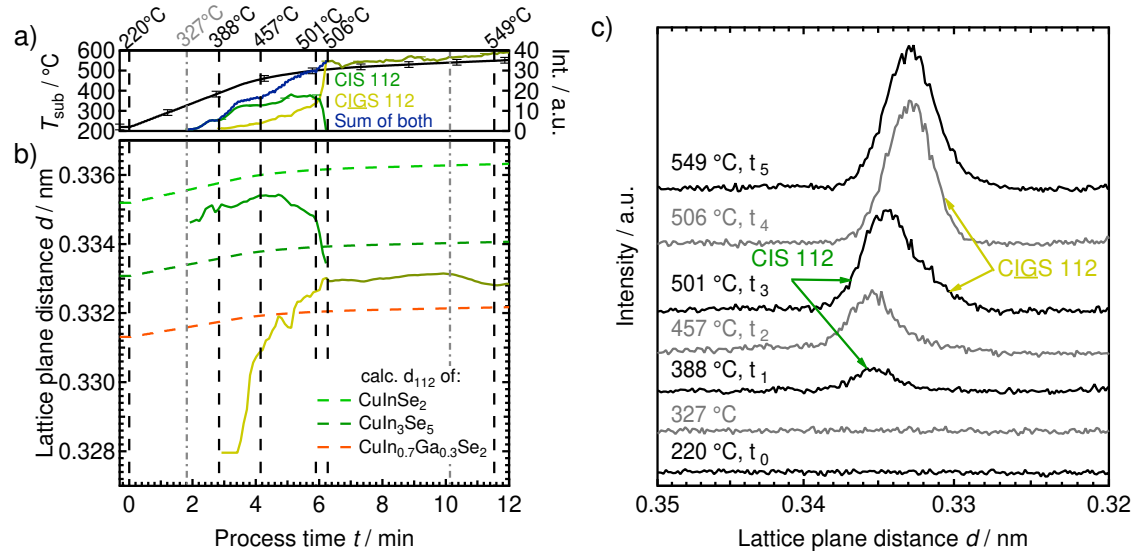


**Figure 4.13.:** Evolution of temperature and chalcopyrite 112 reflection over process time, extracted from the EDXRD/EDXRF data in Fig. 4.12. a)  $T_{\text{sub}}$  (black line),  $I_{112}^{\text{CIS}}$  and  $I_{112}^{\text{CIGS}}$  (colored lines) of the occurring chalcopyrite 112 diffraction peaks and b) corresponding lattice plane distances  $d_{112}$ . The dashed lines in b) represent the  $d_{112}$  of the phases CuInSe<sub>2</sub>, CuIn<sub>3</sub>Se<sub>5</sub> and CuGaSe<sub>2</sub>, calculated as function of  $T_{\text{sub}}$ , based on their value at RT and thermal expansion coefficient, given in literature (see sup. Tabs. E.2 and E.3). c) EDXRD spectra at different temperatures vs. lattice plane distance.

The  $I_{330}$  of the  $\gamma$ -phase reaches its maximum at 367 °C, where the decrease of  $I_{110/102}$  of the  $\eta$ -phase changes to a slower rate.

No increase of Cu fluorescence was observed here as an indicator for Cu<sub>2-x</sub>Se. Reflections of In<sub>4</sub>Se<sub>3</sub> (001, 011, 330, 040) occur at 327 °C and increase (see Fig. 4.12f)). Together with In<sub>4</sub>Se<sub>3</sub>, also a chalcopyrite 112 reflection appears (see CIS in Fig. 4.12g)). Its lattice plane distance (Fig. 4.13b) at  $T_1=388$  °C corresponds to Cu(In<sub>0.95</sub>Ga<sub>0.05</sub>)Se<sub>2</sub> and it is therefore referred to CIS.

**Transformation of CIS and intermediate phases to CIGS****T<sub>1</sub>=388 °C - T<sub>4</sub>=506 °C (t<sub>1</sub> - t<sub>4</sub>)**

The decrease of  $I_{040}^{\text{In}_4\text{Se}_3}$  after T<sub>1</sub>=388 °C correlates to an appearance and increase of (In,Ga)Se reflections (004, 100/101 and 002<sup>7</sup>). The composition is evaluated by use of Vegard's law and its dominant 004 reflection, which evolution is shown in the sup. Fig. D.12. Its composition is (In<sub>0.95</sub>Ga<sub>0.05</sub>)Se at the maximum of  $I_{004}^{(\text{In,Ga})\text{Se}}$  at T<sub>2</sub>=457 °C as well as afterwards at T<sub>3</sub>=501 °C.

At about 422 °C, an additional reflection occurs in the EDXRD signal, which is overlapped by the CIS 112 reflection (see spectra in Figs. 4.13 and 4.14). Between T<sub>2</sub>=457 °C and T<sub>3</sub>=501 °C, both 112 reflections are shifting towards each other. The signal evolves to a single 112 reflection at T<sub>4</sub>=506 °C, referred to as CIGS 112 (see Figs. 4.13b) and 4.14). Its  $d_{112}^{\text{CIGS}}$  is smaller than the simulated values of CuInSe<sub>2</sub> and CuIn<sub>3</sub>Se<sub>5</sub>. Hence, it needs to be correlated to a Ga containing phase like Cu(In<sub>0.72</sub>Ga<sub>0.28</sub>)Se<sub>2</sub> or Cu(In<sub>0.70</sub>Ga<sub>0.30</sub>)<sub>3</sub>Se<sub>5</sub>. No unique reflection of an C(IG)<sub>3</sub>S<sub>5</sub> (like 002 or 102) was found, but could be hidden by the background signal due to typically low reflection intensities. Therefore, CIGS instead of C(IG)<sub>3</sub>S<sub>5</sub> was assumed at this point.

Characteristic changes occur between T<sub>3</sub>=501 °C and T<sub>4</sub>=506 °C in all present phases and the Cu-K $\alpha$  and Ga-K $\alpha$  fluorescence intensities. This period lasts 22 s.

For example,  $\gamma$ -Cu<sub>9</sub>(In,Ga)<sub>4</sub> 330 vanishes (blue line in Fig. 4.12e) and sup. Fig. D.11)

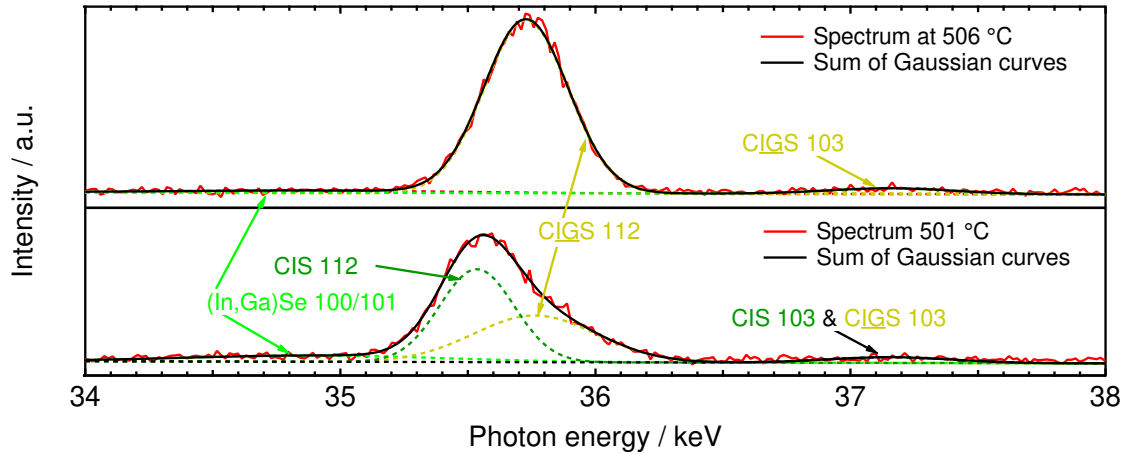


**Figure 4.14.:** EDXRD spectra at 501 °C (t<sub>3</sub>), 506 °C (t<sub>4</sub>) and description of the signal with Gaussian curves.

and another 330 reflection of a  $\gamma$ -phase (green line) with a higher lattice plane distance occurs. The difference in  $d_{330}$  can be either due to i) a phase transition, ii) a decreasing Cu concentration and/or iii) a decreasing Ga concentration. The Cu-Ga

<sup>7</sup>The (In,Ga)Se 002 reflection is overlapping with the escape peak (ESC) of In-K $\alpha$  fluorescence.

phase diagram in sup. Fig. E.2b) shows a transition from  $\gamma_1$ -Cu<sub>9</sub>Ga<sub>4</sub> to  $\gamma_0$ -Cu<sub>9</sub>Ga<sub>4</sub> at 67.87 at.% Cu and the corresponding lattice constant  $d_{330}^I$ . Their difference is about  $\Delta d_{330}=0.00054 \text{ nm}^8$  between both phases. This  $\Delta d_{330}$  is only a fourth of the observed difference  $\Delta d_{330}=0.00198 \text{ nm}$  at 503 °C. Hence, another or an additional effect by a change of the composition must be present. A necessity of a lower Cu concentration according to ii) will be evaluated in Sec. 4.3.2.5, while regarding iii), the GGI will remain constant.

Remarkably, the reflections of (In,Ga)Se show a strongly enhanced decrease from 501 °C until they disappear at 506 °C<sup>9</sup> (see Fig. 4.12f)). They disappear either due to melting and/or due to a reaction to e.g. chalcopyrite. This will be discussed in Sec. 4.3.2.

This Ga depth homogenization is in accordance with the results by use of the atmospheric selenization tool (as reported in [Schmidt *et al.*, 2017]), where the homogenization occurred above 520 °C, whereas it is observed here until 506 °C. However, the actual  $T_{\text{sub}}$  in the atmospheric selenization tool is estimated rather than measured.

#### Evolution after $T_4=506 \text{ °C}$ and final film composition after cool down

From  $T_4=506 \text{ °C}$  on, the 330 reflection intensities of the  $\gamma$ -Cu<sub>9</sub>(In,Ga)<sub>4</sub> phases (green and black lines in Fig. 4.12e)) decrease while  $I_{112}^{\text{CGS}}$  and  $I_{\text{Se-K}\alpha}$  increase slightly. Furthermore, at 537 °C a Cu<sub>2-x</sub>Se phase occurs, possibly correlated to an increase of  $I_{\text{Cu-K}\alpha}$ . It is supposed, that the  $\gamma$ -phase releases the same quantity of Cu and (In+Ga) to react with Se to chalcopyrite. In this way, the Cu concentration in  $\gamma$ -Cu<sub>9</sub>(In,Ga)<sub>4</sub> increases, shifting the  $d_{330}$ . When the  $\gamma$ -phase reaches its upper limit of Cu content, Cu<sub>2-x</sub>Se starts to form.

During cool down, Cu<sub>2-x</sub>Se disappeared and CuSe (102 and 006 reflections) occurred around 260 °C (not shown). The presence of Cu<sub>2-x</sub>Se and CuSe in the finalizing process are typically observed in Cu rich films. This is in agreement with the composition analysis by XRF measurement of the final film which shows an increased CGI to 1.1 and increased GGI to 0.32 (see Tab. 4.4). Hence, the initial composition for Cu-poor absorbers (CGI<1) has changed to a Cu-rich (CGI>1) composition, which can be explained by In-loss.

A selenization in the atmospheric tool with  $T_{\text{Se}}=390 \text{ °C}$  led also to an increased Ga concentration towards the surface (Fig. 4.26b)). Its final film composition exhibited a Cu-poor ratio (“Absorber (at.)” in Tab. 4.4). It is concluded, that the In-loss is not the cause for the smoothed Ga grading profile. Some literature suggests, that Cu-Se

<sup>8</sup>Respectively  $\Delta a=0.0023 \text{ nm}$  with  $d_{330}=a/(3^2 + 3^2 + 0^2)$

<sup>9</sup>In the experiment with the lower heating rate of 0.5 °C/s, (In,Ga)Se 004 vanished also until 506 °C (see Fig. D.10).

**Table 4.4.:** Elemental compositions of the precursor and absorber films, analyzed by WDXRF. The absorber processed in the vacuum tool (vac.) was analyzed with the measurement position aligned to be on the same position as the *in situ* EDXRD/EDXRF measurement. The absorber from Fig. 4.26c was processed in the atmospheric tool, denoted with (at.).

Element / %	Cu	In	Ga	Se	CGI	GGI	Thickness
Precursor	45.86	39.72	14.42	0	0.87	0.27	610 nm
Absorber (vac.)	25.06	15.16	7.25	52.53	1.12	0.32	1462 nm
Precursor	47.04	38.04	14.93	0	0.89	0.28	597 nm
Absorber (at.)	20.11	16.52	6.01	57.36	0.89	0.27	1852 nm

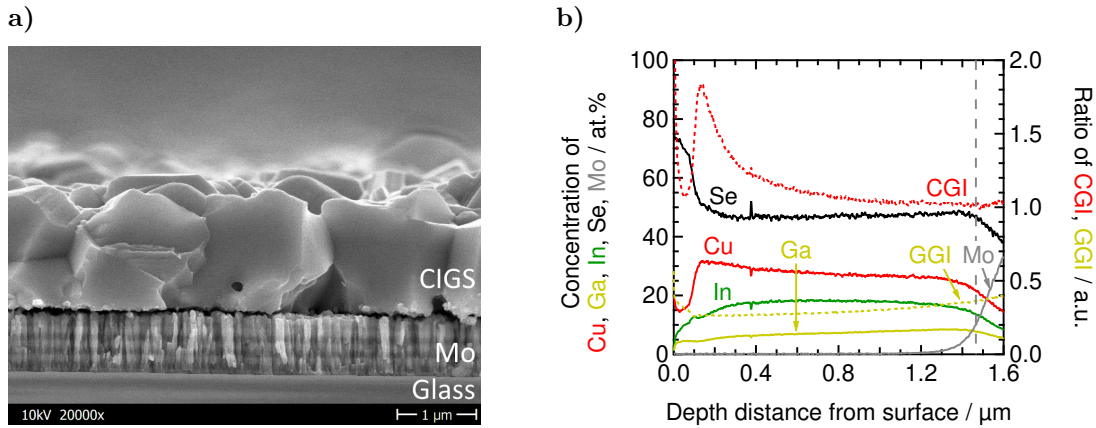


**Figure 4.15.:** a) SEM image of the cross section of the final CIGS film. b) Quantified elemental depth profile measured by GDOES on the final layer. The in-depth uncertainty is in the order of 100 nm. CGI and GGI are on the left axis. The back contact is assumed to start at a molar fraction of Mo at 0.1, indicated by the vertical dashed line.

binary compounds like  $\text{Cu}_{2-x}\text{Se}$  are related to an increased interdiffusion of In and Ga [Tuttle *et al.*, 1994, Walter and Schock, 1993]. This correlation is not found here, since the formation of CIGS occurred before the observation of Cu-Se compounds.

A SEM image of the final CIGS layer is shown in cross sectional view in Fig. 4.15a). The SEM image presents grains larger than  $1\ \mu\text{m}$ . This is in contrast to [Kaelin *et al.*, 2003, Wang *et al.*, 2012], who found smaller CIGS crystals for a low  $P_{\text{Se}}$ .

The film was also analyzed by GDOES (see Fig. 4.15b)) and WDXRF (see “Absorber (vac.)” in Tab. 4.4). The elemental depth distribution shows an increased Se concentration in the top 100 nm. This is likely to be the CuSe, which was found via EDXRD. Beneath, the Cu concentration steps up while In increases continuously and Ga stays nearly constant. The Cu concentration falls rapidly to a stoichiometric composition at the rear side. The Se concentration is at a stoichiometric level.

The EDXRD spectrum at the end of the measurement (at  $T_{\text{sub}}=149\text{ }^{\circ}\text{C}$ ) shows a  $d_{112}^{\text{CIGS}}$  of 0.3309 nm corresponding to  $\text{Cu}(\text{In}_{0.68}\text{Ga}_{0.32})\text{Se}_2$ . This is in accordance to the GGI of 0.32 from XRF. Fig. 4.15b) shows a minimum GGI of 0.26 at 0.1  $\mu\text{m}$ . According to Eq. 1.2, this corresponds to an  $E_g$  of 1.15 eV.

### Summary of the *in situ* analysis and the deduced phase evolution

A summary of the most important results is listed in the following. A time corresponding presence of observed phases is provided by Fig. 4.16. The observed phases and the listed relevant values for characteristic points in time are the basis for proposing a growth schematic of stacking sequences.

- $\gamma\text{-Cu}_9(\text{In,Ga})_4$  (Cu and Ga richer) grows while  $\text{Cu}_{16}(\text{In,Ga})_9$  reduces
- $\text{In}_4\text{Se}_3$  appears at  $T_{\text{sub}}=327\text{ }^{\circ}\text{C}$  and subsequently CIS appears
- $\text{CIGS}/\text{C}(\text{IG})_3\text{S}_5$  appears at  $T_1=388\text{ }^{\circ}\text{C}$
- $I_{\text{Cu-K}\alpha}$  reaches minimum at  $388\text{ }^{\circ}\text{C}$
- $(\text{In}_{0.95}\text{Ga}_{0.05})\text{Se}$  appears at  $388\text{ }^{\circ}\text{C}$  and is fed by  $\text{In}_4\text{Se}_3$
- $\text{Cu}_{16}(\text{In,Ga})_9$  vanishes until  $T_2=457\text{ }^{\circ}\text{C}$
- Significant transformations occur within a small temperature interval between  $T_3=501\text{ }^{\circ}\text{C}$  and  $T_4=506\text{ }^{\circ}\text{C}$  lasting only 22 s
  - Transformation to a single chalcopyrite phase  $\text{CIGS}$  until  $506\text{ }^{\circ}\text{C}$
  - $(\text{In,Ga})\text{Se}$  vanishes
  - $I_{\text{Cu-K}\alpha}$  and  $I_{\text{Ga-K}\alpha}$  increase
  - $\gamma\text{-Cu}_9(\text{In,Ga})_4$  transforms to a similar phase with higher lattice plane distance
- A second transformation of  $\gamma\text{-Cu}_9(\text{In,Ga})_4$  occurs, again to a higher lattice plane distance and evolves to a lower  $d_{330}$  again
- $\gamma\text{-Cu}_9(\text{In,Ga})_4$  330 vanishes until  $T_5=549\text{ }^{\circ}\text{C}$
- $\text{Cu}_{2-x}\text{Se}$  forms at  $549\text{ }^{\circ}\text{C}$  and transforms to  $\text{CuSe}$  during cool down
- Final film properties:
  - Increased CGI from 0.87 to 1.12 and increased GGI from 0.27 to 0.32 by XRF

- CIGS composition from EDXRD is  $\text{Cu}(\text{In}_{0.68}\text{Ga}_{0.32})\text{Se}_2$
- SEM shows a homogeneous and closed film with grains in size of film thickness

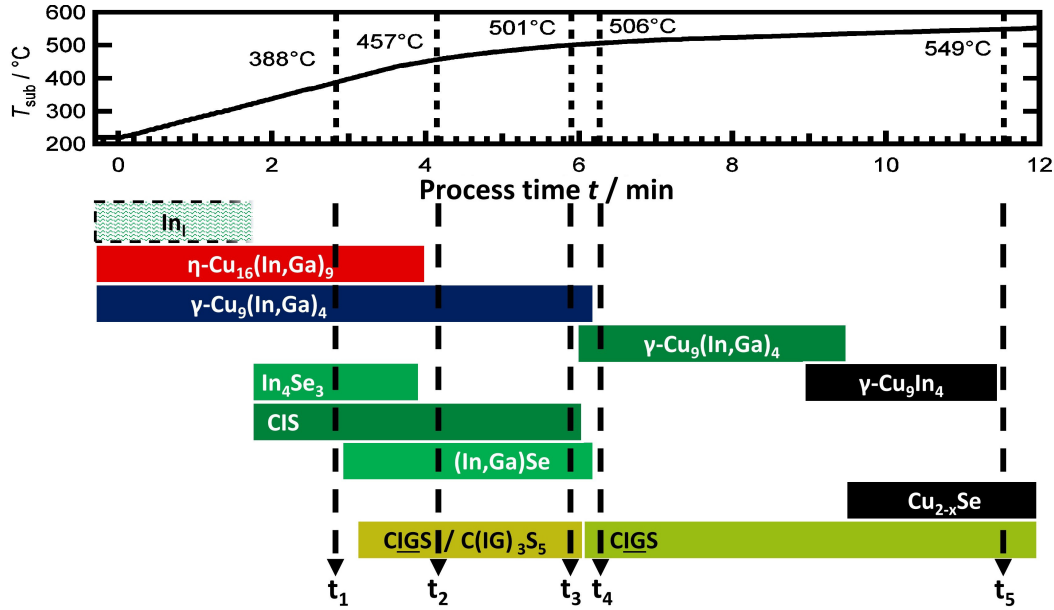


**Figure 4.16.:** Simplified overview of phases present over process time and as function of temperature. Characteristic points in time for deducing a growth schematic with specific stacking sequences are at  $T_{\text{sub}}$  of  $T_1=388^\circ\text{C}$  ( $t_1$ ),  $T_2=457^\circ\text{C}$  ( $t_2$ ),  $T_3=501^\circ\text{C}$  ( $t_3$ ),  $T_4=506^\circ\text{C}$  ( $t_4$ ) and  $T_5=549^\circ\text{C}$  ( $t_5$ ) in the next section.

### 4.3.2. Deduced 1D growth schematic

The aim of this section is to investigate the vertical phase distribution and its evolution in time during the selenization described in Sec. 4.3.1. Stacking sequences for characteristic points in time during the investigated selenization are deduced and are combined to a simplified one-dimensional growth schematic. The evaluation of stacking sequences is based on the phases identified in the previous section in combination with numerically calculated fluorescence intensities as well as the time evolution of the measured fluorescence intensities. This procedure is described in general in Sec. 2.2.2 and is similar to the previous application in Sec. 4.2.2. The approximation of the actual elemental depth profile by a 1D model with phases defined as parallel layers without intermixing results in deviations of the calculated to the experimental fluorescence intensities. First, the deduction is performed for specific points in time. Second, it is very important, that stringing together the single findings result in an evolution, that reproduces the experimental evolution. The focus here is on the change in fluorescence intensities indicating a change in the elemental depth profile. It will be shown, that

the observed changes can be reproduced using the suggested model. Therefore, the evolution in time of the individually calculated fluorescence intensities are compared with the evolution of the experimental values, resulting in a proposed model of stacking sequences. The detailed deduction of each stacking sequence is presented in the following.

#### 4.3.2.1. Depth distribution of phases at $T_1=388^\circ\text{C}$

Phases detected at  $T_1=388^\circ\text{C}$  are  $\gamma\text{-Cu}_9(\text{In,Ga})_4$ ,  $\text{Cu}_{16}(\text{In,Ga})_9$ ,  $\text{In}_4\text{Se}_3$  and CIS ( $\text{Cu}(\text{In}_{0.95}\text{Ga}_{0.05})\text{Se}_2$ ). Besides, liquid In was concluded to be present at  $T_0=220^\circ\text{C}$  and may still be present in the sample at  $388^\circ\text{C}$ . Since a liquid cannot be detected by EDXRD, the point in time, at which the liquid In vanishes due to a complete reaction to other phases is unknown. As a first assumption, the In is assumed to be completely transformed to other phases like  $\text{In}_4\text{Se}_3$  (as it was the case in Sec. 4.2.2 at  $T_{\text{sub}}=388^\circ\text{C}$ ). The composition of  $\gamma\text{-Cu}_9(\text{In,Ga})_4$  is deduced to exhibit a Cu concentration of  $67.5\pm 1.5\text{ at.}\%$  Cu, regarding the Cu-In-Ga phase diagram (Fig. 1.5a). The exact composition of the  $\gamma$ -phase is calculated in regard to its  $d_{330}$  and possible Cu concentration range, as described in sup. Sec. D.1. The calculated composition range can be found in sup. Tab. D.1. The table contains the possible compositions of the  $\gamma$ -phase for all investigated points in time.

Due to the presence of four phases, the linear equation system is under-determined (see Eq. 2.1). A set of solutions must therefore be considered. The CIS thickness is chosen to be the free parameter. There is an interdependence of the CIS thickness and the Cu concentration in the  $\gamma$ -phase. The upper limit of the CIS thickness, for which the linear equation system is solvable, depends on the allowed Cu concentration in the  $\gamma$ -phase.

In general, four phases allow  $4!$  stacking sequences. The number of possible stacking sequences can be reduced, since CIS and  $\text{In}_4\text{Se}_3$  are the only Se containing components. They are assumed to lie closest to the supplied Se vapor. Hence, the two metallic phases are assumed to be located at the back contact. In the previous *ex situ* study to the similar growth, an incorporation of Se from the film surface continuously towards the back contact was found [Schmidt *et al.*, 2017].

$\text{Cu}_{16}(\text{In,Ga})_9$  is only a thin layer (58 nm will be deduced below). Furthermore, the  $\eta$ - and  $\gamma$ -phases exhibit the same elements and a similar composition. As a consequence, flipping these two layers results in no significant change in the calculated fluorescence intensities (not shown). Hence, their stacking order cannot be determined from calculated fluorescence intensities. From the precursor annealing experiment in Sec. 4.1, it was concluded, that  $\gamma\text{-Cu}_9(\text{In,Ga})_4$  forms below  $\text{Cu}_{16}(\text{In,Ga})_9$ . This is also assumed

to be the case here. In consequence of this assumption, two different stacking sequences with either  $\text{In}_4\text{Se}_3$  or CIS on top are likely, see Figs. 4.17a) and d).

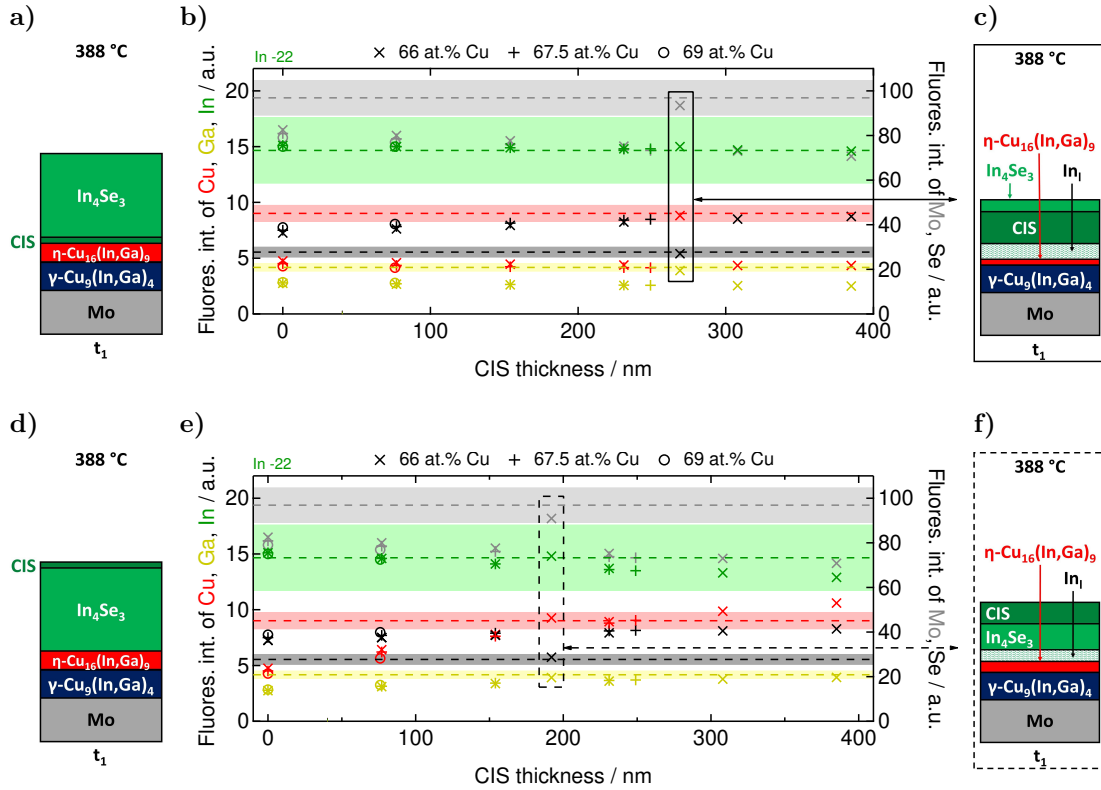


**Figure 4.17.:** Possible stacking sequences in a) and d) and corresponding calculated fluorescence intensities with the CIS thickness as parameter in b) and e). The colors correspond to the element species as indicated at the left and right axis. Dashed horizontal lines illustrate the experimental values at  $T_1=388$  °C. The colored background ranges indicate the maximum uncertainty of the experimental values ( $\pm 8\%$ ). x, +, o indicate the results for 66, 67.5, 69 at.% Cu in  $\gamma\text{-Cu}_9(\text{In,Ga})_4$ . The values in the rectangles in b) and d) present matching values, achieved with the modified stacking sequences in c) and f) with liquid In present. These could only be achieved for the lower limit of the Cu concentration in  $\gamma\text{-Cu}_9(\text{In,Ga})_4$ . Further explanations can be found in the text. All  $I_{\text{In}-K\alpha}$  values are reduced by 22 for a better visibility of the deviations.

For the two stacking sequences in Figs. 4.17a) and d), the fluorescence intensities are calculated as a function of the CIS thickness, see Figs. 4.17b) and e). Independent of the CIS thickness, the values of  $I_{\text{Se}-K\alpha}$  are too high and the  $I_{\text{Mo}-K\alpha}$  values are too low for both stacking sequences. The  $I_{\text{Se}-K\alpha}$  is concluded to be too high, because the linear equation system results in too much Se. This amount of Se attenuates  $I_{\text{Mo}-K\alpha}$ , so that the calculated  $I_{\text{Mo}-K\alpha}$  is below the experimental value. Better matching fluorescence intensities can be achieved by assuming liquid In to be present. As a consequence of

an additional phase, the linear equation system is under-determined. Therefore, the thickness of the  $\text{In}_4\text{Se}_3$  is selected as the additional free parameter to exhibit a set of solutions. Reducing its thickness results in an increase of the thickness of the liquid In layer. This can compensate the divergence of the  $I_{\text{Se}-K\alpha}$  and  $I_{\text{Mo}-K\alpha}$ . The precursor exhibited most In in the top part of the film and liquid In is assumed to be present as a layer between the other Se free and the Se containing phases. The  $\text{In}_4\text{Se}_3$  thickness is adjusted to achieve a matching  $I_{\text{Se}-K\alpha}$  and the CIS thickness is adjusted to achieve a matching  $I_{\text{Cu}-K\alpha}$ . For a Cu concentration  $\geq 67.5$  at.% Cu in the  $\gamma$ -phase, there is no matching  $I_{\text{Cu}-K\alpha}$  for the whole range of CIS thickness. For 66 at.% Cu (lower limit) in the  $\gamma$ -phase, matching fluorescences were found for both stacking sequences, see Figs. 4.17c) and f), and highlighted with a black frame in Figs. 4.17b) and e). In case of  $\text{In}_4\text{Se}_3$  on top, the CIS thickness needs to be higher than for the inverse sequence. For both sequences, the fluorescence intensities are matching similarly well. To distinguish between these two stacking sequences, a result from below is taken into account. At the following points in time with  $T_2=457^\circ\text{C}$  and  $T_3=501^\circ\text{C}$ , InSe is deduced to be on top of the film. A transformation of  $\text{In}_4\text{Se}_3$  to InSe is likely (and was similarly observed in Sec. 4.2). Thus, the stacking sequence with  $\text{In}_4\text{Se}_3$  on top (Fig. 4.17c)) is assumed at  $388^\circ\text{C}$ . The corresponding layer thicknesses are listed in Tab. 4.5 on page 101.

#### 4.3.2.2. Depth distribution of phases at $T_2=457^\circ\text{C}$

Phases detected at  $T_{\text{sub}}=457^\circ\text{C}$  are  $\gamma\text{-Cu}_9(\text{In,Ga})_4$ ,  $(\text{In,Ga})\text{Se}$  ( $(\text{In}_{0.95}\text{Ga}_{0.05})\text{Se}$ ), CIS ( $\text{Cu}(\text{In}_{0.96}\text{Ga}_{0.04})\text{Se}_2$ ) and a second tetragonal phase (see Fig. 4.14). The latter was labeled as CIGS in Sec. 4.3.1. It is noted in advance, that the calculation of fluorescence intensities with a CIGS phase as the second tetragonal phase at  $457^\circ\text{C}$  and  $501^\circ\text{C}$  resulted in no matching fluorescence intensities (compare sup. Sec. D.4.1). Instead, the presence of a  $\text{C}(\text{IG})_3\text{S}_5$  phase is proposed here.  $\text{C}(\text{IG})_3\text{S}_5$  exhibits the same reflections as CIGS with additional reflections. None of such an additional reflection could be uniquely attributed to a  $\text{C}(\text{IG})_3\text{S}_5$  phase. However, a unique reflection could be small and hidden within the background. Assuming the presence of a  $\text{C}(\text{IG})_3\text{S}_5$  phase, the position of the 112 reflection corresponds to a composition of  $\text{Cu}(\text{In}_{0.58}\text{Ga}_{0.42})_3\text{Se}_5$ , compare Fig. 4.13. The composition of the  $\gamma$ -phase is limited to a Cu concentration of  $68\pm 2$  at.% Cu by the Cu-In-Ga phase diagram (Fig. 1.5b)), see sup. Tab. D.1 for the detailed composition.

Again, the linear equation system is under-determined. The CIS amount is selected as the free parameter of the set of solutions. With an increasing amount of CIS, the amount of the  $\text{C}(\text{IG})_3\text{S}_5$  increases while the amounts of  $(\text{In,Ga})\text{Se}$  and  $\gamma\text{-Cu}_9(\text{In,Ga})_4$  decrease. The respective Cu concentration in  $\gamma\text{-Cu}_9(\text{In,Ga})_4$  defines the lower and upper limit of the CIS amount in the set of solutions of the linear equation system,

as marked with arrows in Fig. 4.18b). The lower limits are reached when either the  $C(IG)_3S_5$  or the CIS thickness reaches 0 nm. All upper limits of the CIS thickness are determined by a disappearance of the  $(In,Ga)Se$  phase. Hence, matching fluorescence intensities must be found between these limits.

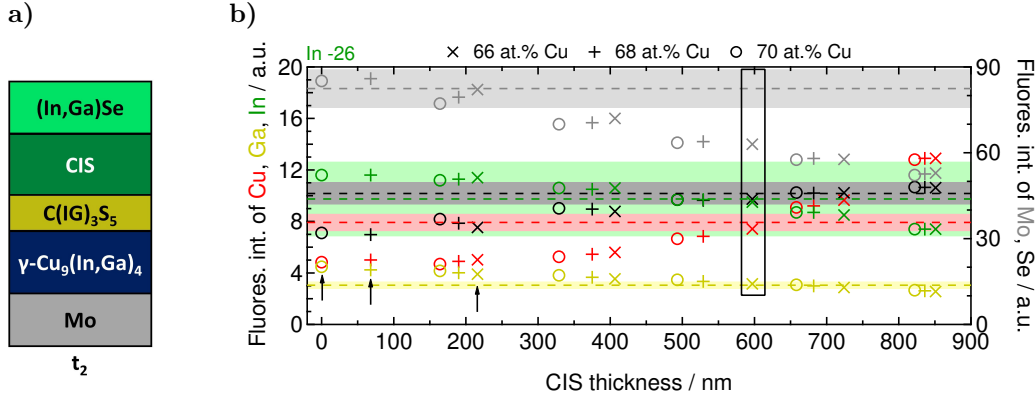


**Figure 4.18.:** a) Proposed stacking sequence at  $T_{sub}=457^\circ C$  ( $t_2$ ) and b) corresponding calculated fluorescence intensities. The colors correspond to the element species as indicated at the left and right axis. x, +, o indicate the results for different Cu concentrations in  $\gamma-Cu_9(In,Ga)_4$ . Dashed lines illustrate the observed intensities from experiment at  $T_{sub}=457^\circ C$ . The colored background ranges indicate the maximum uncertainty of the experimental values ( $\pm 8\%$ ). Arrows indicate the lower limits of the set of solutions. The limits of the CIS amount are 216 nm and 851 nm for 66 at.% Cu, 68 nm and 836 nm for 68 at.% Cu and between 0 nm and 822 nm for 70 at.% Cu in  $\gamma-Cu_9(In,Ga)_4$ . All  $I_{In-K\alpha}$  values are reduced by 26 for a better visibility of the deviations.

The  $\gamma-Cu_9(In,Ga)_4$  phase is the only Se free phase and supposed to be located below all Se containing phases at the back contact. Then, there are six possible permutations for the stacking sequence of the other layers.

All stacking sequences, except for sequence D, are unlikely due to very large differences between the calculated and the observed intensities of e.g. either  $I_{Cu-K\alpha}$  or  $I_{Ga-K\alpha}$  or both (compare sup. Fig. D.13). For Cu concentrations of 68 and 70 at.% Cu in the  $\gamma$ -phase, there are similarly well matching fluorescence intensities at a similar CIS amount (see the area around the black frame in Fig. 4.18b)). However, the values for 66 at.% Cu are selected (see black frame in Fig. 4.18b)) due to the best matching  $I_{In-K\alpha}$  and highest  $\gamma$ -phase thickness. The  $I_{330}^\gamma$  at  $457^\circ C$  is similar to the value at  $388^\circ C$  and decreases to  $501^\circ C$ . The corresponding layer thicknesses are listed in Tab. 4.5 on page 101.

As a result of the stacking sequences for increasing the  $T_{sub}$  from  $388^\circ C$  to  $457^\circ C$ , the CIS phase was growing, the  $C(IG)_3S_5$  phase appeared,  $Cu_{16}(In,Ga)_9$  vanished and the thickness of  $\gamma-Cu_9(In,Ga)_4$  decreased. This is in agreement with the observed evolution

of corresponding reflection intensities, except for the  $\gamma$ -phase, which was observed to be similar.

#### 4.3.2.3. Depth distribution of phases at $T_3=501^\circ\text{C}$

Phases detected at  $T_{\text{sub}}=501^\circ\text{C}$  are the same as at  $457^\circ\text{C}$ :  $\gamma\text{-Cu}_9(\text{In,Ga})_4$ ,  $(\text{In,Ga})\text{Se}$  ( $(\text{In}_{0.95}\text{Ga}_{0.05})\text{Se}$ ), CIS ( $\text{Cu}(\text{In}_{0.9}\text{Ga}_{0.1})\text{Se}_2$ ) and  $\text{C}(\text{IG})_3\text{S}_5$  ( $\text{Cu}(\text{In}_{0.76}\text{Ga}_{0.24})_3\text{Se}_5$ ). In comparison with  $T_{\text{sub}}=457^\circ\text{C}$ , the Ga concentration in CIS doubled and in  $\text{C}(\text{IG})_3\text{S}_5$  halved. The composition of the  $\gamma$ -phase is limited to a Cu concentration of  $68\pm 2\text{at.}\%$  Cu by the Cu-In-Ga phase diagram (Fig. 1.5b)) again, see sup. Tab. D.1 for the detailed composition.

A loss of In by evaporation of a volatile In compound during this selenization process was concluded in Sec. 4.3.1 based on the different initial and final film compositions measured by *ex situ* XRF. A decreasing amount of In during selenization is expected to result in a decreasing experimental value of  $I_{\text{In-K}\alpha}$  and a correlated increase of  $I_{\text{Mo-K}\alpha}$ . Both changes occurred between  $457^\circ\text{C}$  ( $t_2$ ) and  $515^\circ\text{C}$  (Fig. 4.12d)). The decrease of  $I_{\text{In-K}\alpha}$  towards  $515^\circ\text{C}$  is bigger than it could result from attenuation caused alone by Se incorporation into the film after a complete transformation to CIGS (compare Fig. 4.4d)), nor by another stacking sequence. Hence, a loss of In between  $457^\circ\text{C}$  and  $515^\circ\text{C}$  is likely. Regarding the linear equation system, a decrease of the In quantity mainly decreases the thickness of  $(\text{In,Ga})\text{Se}$ . The result is less Se effecting a lower  $I_{\text{Se-K}\alpha}$  and a higher  $I_{\text{Cu-K}\alpha}$  (due to a decreased attenuation). The In loss is assumed to be mainly responsible for the decrease of  $I_{\text{In-K}\alpha}$ . Regarding the  $I_{\text{In-K}\alpha}$  at  $501^\circ\text{C}$ , this is about 1/4 of the total difference in the evolution of  $I_{\text{In-K}\alpha}$ . The total In loss is estimated by the initial and final In quantities from *ex situ* XRF ( $13515\text{ atoms/nm}^2$ - $9440\text{ atoms/nm}^2$ ) as a maximum loss. One fourth of the total In loss is an absolute loss of about 7.5% less In. The reference In quantity of  $13515\text{ atoms/nm}^2$  is reduced to  $12496\text{ atoms/nm}^2$  and used for the following calculation of fluorescence intensities.

The linear equation system is under-determined and the CIS thickness is selected as the free parameter of the set of solutions. The Cu concentration in the  $\gamma$ -phase again defines the range of CIS thicknesses for which the linear equation system is solvable (see arrows in Fig. 4.19b)). All lower limits are determined by a disappearance of either the  $\text{C}(\text{IG})_3\text{S}_5$  or the CIS phase. All upper limits of the CIS thickness are determined by a disappearance of the  $(\text{In,Ga})\text{Se}$  phase. Hence, a matching fluorescence intensity must be within these limits.

Again, assuming the position of the only Se free phase,  $\gamma\text{-Cu}_9(\text{In,Ga})_4$ , to be furthest from Se supply, *i.e.* at the back contact, there are six possible permutations regarding

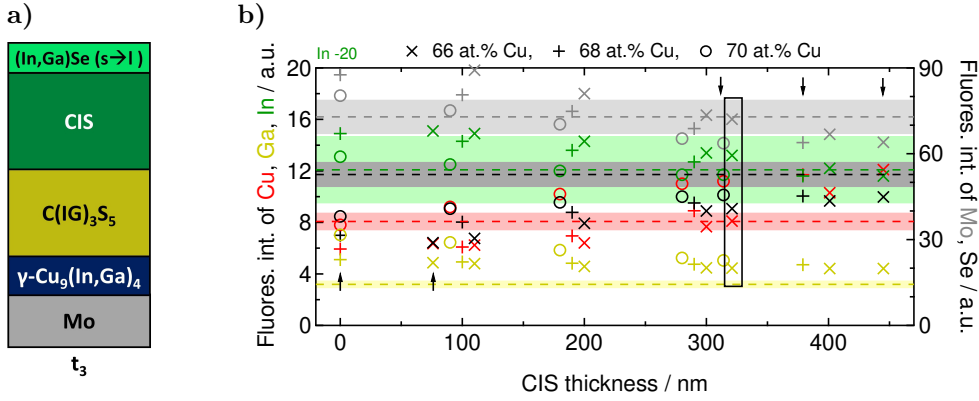


**Figure 4.19.:** a) Proposed stacking sequence and b) corresponding calculated fluorescence intensities. The colors correspond to the element species as indicated at the left and right axis. Dashed lines illustrate the experimental intensities at  $T_{\text{sub}}=501^\circ\text{C}$  ( $t_3$ ). The colored background ranges indicate the maximum uncertainty of the experimental values ( $\pm 8\%$ ). x, +, o indicate the results for 66, 68, 70 at.% Cu in the  $\gamma$ -phase. Arrows pointing upwards (downwards) indicate the lower (upper) limits of the CIS thickness for each set of solutions. All  $I_{\text{In-K}\alpha}$  values are reduced by 20 for a better visibility of the deviations. The black frame encloses the best matching fluorescence intensities (312 nm CIS and 66 at.% Cu).

the stacking sequence (Fig. D.13b)). The calculated fluorescence intensities of the whole set of solutions for all six stacking sequences can be found in Fig. D.13d). The calculated fluorescence intensities, that are matching best to the experiment are found for the stacking sequence D while A, B, C, E and F are unlikely again (Fig. 4.19a)). This is consistent with the stacking order proposed at  $T_{\text{sub}}=457^\circ\text{C}$  ( $t_2$ ).

The best matching fluorescence intensities were identified for 66 at.% Cu in the  $\gamma$ -phase. For a Cu concentration of 68 at.% Cu, there are similar fluorescence intensities at about 250 nm CIS (extrapolated). Comparing the CIS 112 reflection at  $457^\circ\text{C}$  and  $501^\circ\text{C}$ , its intensity is similar. Whereas all CIS thicknesses here are below the one deduced at  $457^\circ\text{C}$ . Thus, the one with the highest CIS thickness and slightly better matching  $I_{\text{In-K}\alpha}$  was selected. The best matching values are found for 321 nm CIS (66 at.% Cu), see values in the rectangle in Fig. 4.19b). The corresponding layer thicknesses are listed in Tab. 4.5 on page 101.

As a result when evaluating the stacking sequences at  $457^\circ\text{C}$  and  $501^\circ\text{C}$ , it can be seen, that the thickness of (In,Ga)Se decreased and that of C(IG)<sub>3</sub>S<sub>5</sub> increased. Unfortunately, the thickness of CIS decreased, but is still higher than at  $388^\circ\text{C}$ . The thickness of  $\gamma$ -Cu<sub>9</sub>(In,Ga)<sub>4</sub> increased, which seems to be in contrast to the decreased reflection intensity from  $457^\circ\text{C}$  to  $501^\circ\text{C}$ .

However, there is still a noticeable difference between the calculated and the measured  $I_{Se-K\alpha}$  (dashed rectangle in Fig. 4.19b)). This deviation will be discussed after presenting the complete evolution of the fluorescence intensities.

#### 4.3.2.4. Depth distribution of phases at $T_4=506\text{ }^\circ\text{C}$

This point in time is after a short period of remarkable changes, occurring within only 20 s and a change in  $T_{\text{sub}}$  of only  $5\text{ }^\circ\text{C}$ . The most important change is, that the 112 reflections of CIS and  $\text{C(IG)}_3\text{S}_5$  merge to a single reflection assigned to the CIGS phase.

Phases detected at  $T_{\text{sub}}=506\text{ }^\circ\text{C}$  are CIGS,  $\gamma\text{-Cu}_9(\text{In,Ga})_4$  and possibly liquid  $(\text{In,Ga})\text{Se}$ . The composition of CIGS is determined to be  $\text{Cu}(\text{In}_{0.77}\text{Ga}_{0.23})\text{Se}_2$ . At this temperature, the Ga containing part ( $\gamma_i\text{-Cu}_9\text{Ga}_4$ ) of the solid solution can be  $\gamma_0$  or  $\gamma_1$ . For  $\gamma_0$ , there is no information regarding the relation between the Cu concentration and the lattice constant. In consequence, the composition of the  $\gamma$ -phase cannot be deduced as before. An increase in the Cu concentration towards the surface is concluded from the phase transformation of  $\text{C(IG)}_3\text{S}_5$  to CIGS. The only phase that can be the source of Cu for this transformation is the  $\gamma$ -phase. Since the 330 reflection intensity is similar at  $501\text{ }^\circ\text{C}$  and  $506\text{ }^\circ\text{C}$ , the crystal amount of the phase is concluded to be similar with one difference: For this case, the Cu concentration in the  $\gamma$ -phase is concluded to decrease. The Cu concentration in the  $\gamma$ -phase is estimated at the lower limit of 61 at.% Cu<sup>10</sup>. Its position in the stacking sequence is again assumed to be at the back contact. It is unlikely to change the position with the phases on top.

The composition of CIGS is assumed to exhibit a nearly stoichiometric Cu concentration of 0.9, since the film is in the transition to a  $\text{CGI} > 1$  until  $549\text{ }^\circ\text{C}$  ( $t_5$ ).

The In loss has continued and increased to 14.9% regarding the relative decrease of  $I_{\text{In}-K\alpha}$  as calculated at  $501\text{ }^\circ\text{C}$ . The reference In quantity of 13515 atoms/nm<sup>2</sup> is reduced to 11500 atoms/nm<sup>2</sup> and used for the following calculation of fluorescence intensities.

The reflections of  $(\text{In,Ga})\text{Se}$  disappeared from  $501\text{ }^\circ\text{C}$  to  $506\text{ }^\circ\text{C}$  either due to melting and/or due to a reaction to e.g. chalcopyrite. In the *ex situ* study, InSe was found after reaching  $580\text{ }^\circ\text{C}$  and cool down (see Fig. 7(a) in [Schmidt *et al.*, 2017]). Another aspect is, that  $I_{\text{Cu}-K\alpha}$  was much too high (1.5 times) in a calculation of fluorescence

---

<sup>10</sup>An increase with a following decrease of the lattice plane distance of  $\gamma\text{-Cu}_9(\text{In,Ga})_4$  330 was also found during the evolution of a slower selenization with a similar final Ga distribution (without Ga segregation), shown in sup. Fig. D.10. There, this time-wise increase was correlated to a decrease of the Cu concentration in  $\gamma\text{-Cu}_9(\text{In,Ga})_4$ , due to the formation of  $\text{Cu}_{2-x}\text{Se}$  on top. At the temperature of  $506\text{ }^\circ\text{C}$ , the information in the literature about  $\gamma\text{-Cu}_9(\text{In,Ga})_4$  is little. Furthermore, the linear equation system exhibits no solution when assuming the Cu concentration of 66 at.% Cu from the previous state, which was the lower limit there.

intensities for a stack without (In,Ga)Se (not shown). The presence of (In,Ga)Se is proposed.

Since the Ga concentration  $x$  in  $\gamma\text{-Cu}_9(\text{In}_{1-x}\text{Ga}_x)_{5.75}$  is unknown, this is set as the free parameter in the linear equation system. The set of solutions exhibits a decreasing phase thickness of the  $\gamma$ -phase for an increasing Ga concentration. Since the 330 reflection intensity of the  $\gamma$ -phase is similar at 501 °C and 506 °C, the thickness is expected to be the same or smaller now. Therefore, the determined thickness at 501 °C of 212 nm is expected as a limit. This value defines the lower limit of  $x$  to be 0.52. The upper limit is an In free phase ( $x=1$ ). The calculated fluorescence intensities are shown in Fig. 4.20.

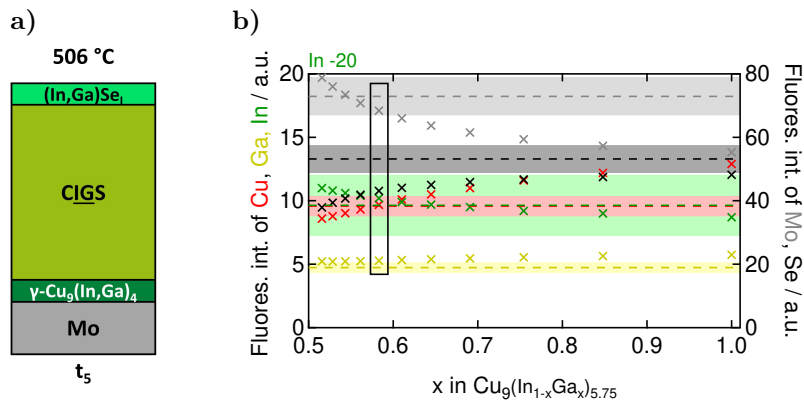


**Figure 4.20.:** a) Suggested stacking sequence at  $T_{\text{sub}}=506$  °C ( $t_4$ ) and b) corresponding calculated fluorescence intensities. The colors correspond to the element species as indicated at the left and right axis. Dashed horizontal lines illustrate the observed intensities from experiment at the according temperature. The colored background ranges indicate the maximum uncertainty of the experimental values ( $\pm 8\%$ ). All  $I_{\text{In-K}\alpha}$  values are reduced by 20 for a better visibility of the deviations.

Since the experimental values of  $I_{\text{Cu-K}\alpha}$  and  $I_{\text{Ga-K}\alpha}$  significantly increased to 506 °C, they are an important measure. The best matching fluorescences are found for  $x = 0.58$ . The corresponding layer thicknesses are listed in Tab. 4.5 on page 101. At 501 °C,  $x$  was deduced from  $d_{330}$  to be 0.57. This is a similar value and indicates, that assuming the lower limit of the Cu concentration in the  $\gamma$ -phase is reasonable. In conclusion, the shift of the 330 reflection corresponds to the lower Cu concentration in  $\gamma\text{-Cu}_9(\text{In,Ga})_4$ .

#### 4.3.2.5. Depth distribution of phases at $T_5=549$ °C

Phases detected at  $T_{\text{sub}}=549$  °C are CIGS and the high temperature phase  $\beta\text{-Cu}_{2-x}\text{Se}$ . There is not enough information available in the literature to determine the composition

of  $\beta$ -Cu<sub>2-x</sub>Se.

The Cu<sub>2-x</sub>Se 111 reflection intensity and  $I_{Cu-K\alpha}$  increased from  $T_{\text{sub}}=543^\circ\text{C}$  to  $549^\circ\text{C}$ . Simultaneously, the  $\gamma$ -phase reflection disappeared. In consequence, the  $\gamma$ -phase transformed to CIGS and Cu<sub>2-x</sub>Se.

For the calculation of fluorescence intensities, the In quantity is set as a free parameter and so the linear equation system with two phases and the Cu and Ga quantity can determine the CIGS thickness and the excess Cu for the Cu<sub>2-x</sub>Se layer. It can not determine x in Cu<sub>2-x</sub>Se.

A stoichiometric Cu concentration of 1 was assumed in CIGS. The Ga concentration y in CIGS (CuIn<sub>1-y</sub>Ga<sub>y</sub>Se<sub>2</sub>) was estimated based on  $d_{112}^{\text{CIGS}}$  to be  $y=0.25\pm 0.1$ . The uncertainty results from the maximum uncertainty in  $d_{112}^{\text{CIGS}}$  of  $\pm 0.4\%$ , as estimated for the maximum error in the height alignment. However, the linear equation system exhibits no solution for  $y < 0.315$ . A higher Ga to Cu ratio in CIGS results in a thinner layer. Since the total Cu quantity is fixed, a thinner CIGS layer results in a thicker Cu<sub>2-x</sub>Se layer. Only a value of  $y > 0.315$  leads to a present Cu<sub>2-x</sub>Se layer. Assuming the observed final composition of  $y=0.32$  for the CIGS layer, which is within the uncertainty, a solution for the linear equation system is found. The calculated fluorescence intensities are shown in Fig. 4.21b). The total amount of Cu in in Cu<sub>2-x</sub>Se is defined by the Cu reference quantity and the linear equation system. Varying x from 0.27 to 0 changes only the calculated quantity of Se from 155 to 134 projected number of Se atoms per nm<sup>2</sup>. In case of stacking sequence A, this change decreases the calculated  $I_{Se-K\alpha}$  unremarkably from 4.722 a.u. to 4.716 a.u.. Cu<sub>2</sub>Se is assumed in the following. The resuming layer thicknesses are 7 nm Cu<sub>2</sub>Se and 1437 nm CIGS (see Tab. 4.5). This film thickness is in accordance to the XRF and GDOES measurement (see Tab. 4.4 and Fig. 4.15b)).

In comparison with the previous values at  $506^\circ\text{C}$ , the increase of  $I_{Cu-K\alpha}$  and the decrease of  $I_{In-K\alpha}$  are reproduced by the calculated values. Furthermore, the In quantity (as free parameter) in the solution of the linear equation system exhibits a decrease of about 23% compared with the initial quantity. This is in agreement with the observed In loss by XRF.

An inverse stacking sequence results in no significant differences of the fluorescence intensities (see Fig. 4.21). The two stacking sequences can not be distinguished from the calculated fluorescence intensities.

A film composition with a CGI > 1 contains more Cu than it can be bound in CIGS and in consequence a Cu-Se compound forms. The formation of Cu<sub>2-x</sub>Se on top of the film is typically observed in a film with a CGI  $\geq 1$  and it is typically observed on top of a film (see Sec. 1.4). Therefore, the stacking sequence A in Fig. 4.21 is proposed. This is in agreement to the increase of  $I_{Cu-K\alpha}$ , which can indicate an increase of the

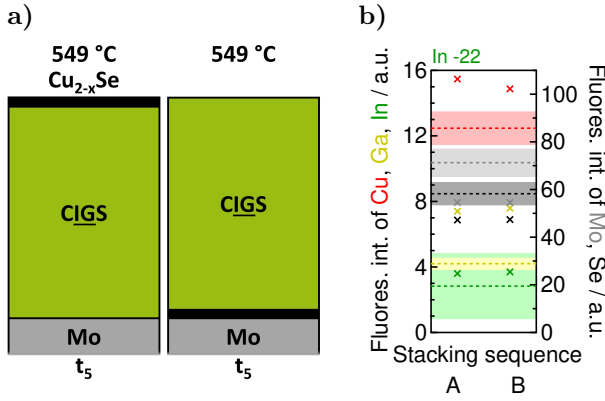


**Figure 4.21:** a) Possible stacking sequences at  $T_{\text{sub}}=549\text{ °C}$  ( $t_5$ ) and b) corresponding calculated fluorescence intensities. The colors correspond to the element species as indicated at the left and right axis. The colored background ranges indicate the maximum uncertainty of the experimental values ( $\pm 8\%$ ). All  $I_{\text{In}-K\alpha}$  values are reduced by 22 for a better visibility of the deviations.

Cu concentration towards the surface.  $\text{Cu}_{2-x}\text{Se}$  exhibits a higher Cu concentration as CIGS.

The calculated  $I_{\text{Ga}-K\alpha}$  is higher, than the experimental value. This indicates, that the model could lead to better matching fluorescence intensities, if a Ga gradient was assumed in the absorber, with a lower concentration in the top part instead of a constant composition over depth.

#### 4.3.2.6. Comparison of the temporal evolution of measured and calculated fluorescence intensities

The calculated fluorescence intensities based on the respective proposed stacking sequences for  $T_{\text{sub}}=388\text{ °C}$ ,  $457\text{ °C}$ ,  $501\text{ °C}$ ,  $506\text{ °C}$  and  $549\text{ °C}$  ( $t_0$ - $t_5$ ) are shown together with the measured fluorescence intensities in Fig. 4.22 to compare their evolutions throughout the whole selenization. The deduced layer thicknesses are presented in Tab. 4.5.

Overall, the relative evolution of the measured fluorescence intensities could be reproduced well enough to find out new details of the evolution leading to the proposed stacking sequences. However, some deviations need to be mentioned as follows.

From  $T_{\text{sub}}=501\text{ °C}$  onwards, the calculated  $I_{\text{Se}-K\alpha}$  is significantly below the experimental values. One reason can be an inaccurate Se correcting factor (for detector 1). The Se correcting factor had to be determined without a reference for calibration. In the case of a higher correcting factor, the values at  $220\text{ °C}$  and at  $388\text{ °C}$  can be deduced with a smaller Se quantity without changing the stacking sequence. Nonetheless, the value at  $457\text{ °C}$  would be too high. The thickness of the  $\gamma$ -phase at  $457\text{ °C}$  is below that at  $501\text{ °C}$ , which indicates an inaccuracy. The highest uncertainty is assumed to result from the only estimated Cu concentration in CIS and the uncertainty in  $\gamma\text{-Cu}_9(\text{In,Ga})_4$ , which were both present at  $457\text{ °C}$ .

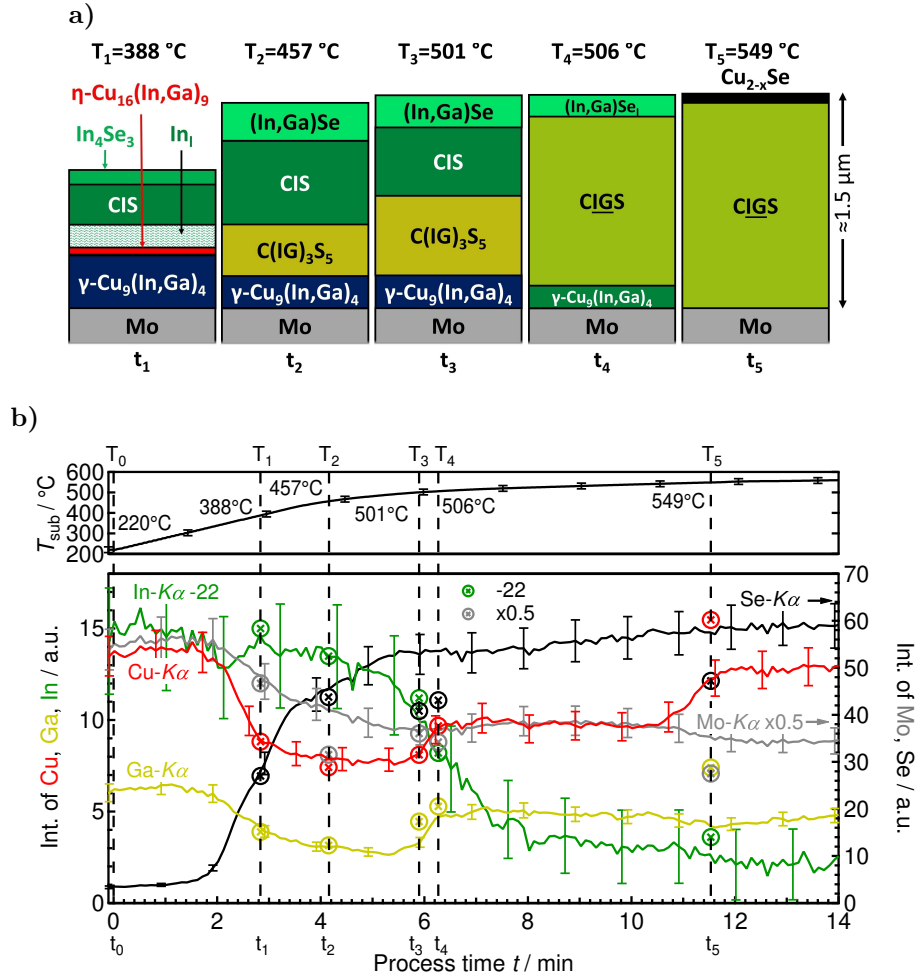


**Figure 4.22.:** a) Proposed growth schematic with b) calculated fluorescence intensities for the respective stacking sequences at  $T_{\text{sub}}$  of  $T_1=388^\circ\text{C}$  ( $t_1$ ),  $T_2=457^\circ\text{C}$  ( $t_2$ ),  $T_3=501^\circ\text{C}$  ( $t_3$ ),  $T_4=506^\circ\text{C}$  ( $t_4$ ) and  $T_5=549^\circ\text{C}$  ( $t_5$ ) are shown together with the measured fluorescence intensities. The colors correspond to the element species as indicated at the left and right axis. The results regarding the second detector can be found in sup. Fig. D.14.

At  $549^\circ\text{C}$ , also Cu and Ga deviate by a too high calculated value. The  $I_{\text{Ga}-\text{K}\alpha}$  results from a constant Ga concentration in CIGS over the depth and should be smaller, since the measured elemental depth profile shows a slight Ga gradient, decreasing towards the surface. No explanation for the deviation of  $I_{\text{Cu}-\text{K}\alpha}$  was found.

The *in situ* measurement setup included a second detector. The data detected by this more surface sensitive detector shows a similarly matching evolution of the fluorescence intensity with deviations for the same values mentioned above (Fig. D.14). The evolution of  $I_{\text{Se}-\text{K}\alpha}$  matches slightly better than presented above.  $I_{\text{Ga}-\text{K}\alpha}$  must be decreased by 0.5, possibly due to the higher sensitivity of the correcting factor by the

Ga concentration in the top layer of the precursor, which exhibited a slight gradient in the depth profile from GDOES, but was approximated as a constant.

**Table 4.5.:** Phases and their layer thicknesses, as deduced above for the different points in time.

$T_{\text{sub}} (T_i)$	$T_1=388\text{ }^\circ\text{C}$	$T_2=457\text{ }^\circ\text{C}$	$T_3=501\text{ }^\circ\text{C}$	$T_4=506\text{ }^\circ\text{C}$	$T_5=549\text{ }^\circ\text{C}$
Phase (nm)	$\text{In}_4\text{Se}_3$ (264 nm)	(In,Ga)Se (215 nm)	(In,Ga)Se (174 nm)	(In,Ga)Se (132 nm)	$\text{Cu}_2\text{Se}$ (7 nm)
	CIS (192 nm)	CIS (597 nm)	CIS (321 nm)	CIGS (901 nm)	CIGS (1437 nm)
	In(l) (143 nm)	$\text{C(IG)}_3\text{S}_5$ (317 nm)	$\text{C(IG)}_3\text{S}_5$ (412 nm)	$\gamma$ -phase (155 nm)	
	$\eta$ -phase (58 nm)	$\gamma$ -phase (162 nm)	$\gamma$ -phase (212 nm)		
	$\gamma$ -phase (227 nm)				

A very similar evolution of phases and fluorescence intensities was observed when applying a lower heating rate as well as in another selenization chamber with external Se source, the PVD tool (Sec. 2.1.2). All these experiments had in common, that an independent operated Se evaporation source was used to supply Se vapor, instead of placing Se pellets next to the sample and heating these together with the sample. Thus, it is a reproducible selenization process.

In case of the independently operated Se source, the Se supply can be reduced below a critical value, that changes the growth evolution and the resulting final film from exhibiting strong Ga segregation to a prevention of Ga segregation. The external Se supply also maintains sufficient Se for a complete selenization of the precursor film. A further explanation is depicted in Sec. 4.5 and the following sections.

An increasing Ga incorporation into CIGS with an increasing heating rate from  $0.33\text{ }^\circ\text{C/s}$  to  $4\text{ }^\circ\text{C/s}$  was reported in [Koo *et al.*, 2013]. This is contrary to the observation here, because a high incorporation of Ga was also observed with a lower heating rate of 1 and  $0.5\text{ }^\circ\text{C/s}$ . This might result from the different experimental setups.

A closed film with grains reaching from surface to the back contact were observed. This might be correlated to the melting of (In,Ga)Se and the formation of single phase CIGS. A liquid might act as an effective fluxing agent leading to a densification and bigger grain sizes. A significant increase of grain size was observed during fast growth of  $\text{CuInSe}_2$  assisted by liquid Se [Uhl *et al.*, 2015].

Another point is the composition of the last  $\gamma$ -phase during selenization without Ga

segregation, which is much closer to the composition of the chalcopyrite above (CIGS), to which it got slowly incorporated. In contrast, the composition of the  $\gamma_{1/2}$ -Cu<sub>9</sub>Ga<sub>4</sub> phase during selenization with Ga segregation leads to a different growth of CIGS with more differently lattice constants. Hence, the closer composition lead to a more similar chalcopyrite crystal constant of the growing CIGS at the rear side and thus preventing the formation of voids.

In the already published *ex situ* study on the growth of single phase CIGS with the atmospheric selenization tool [Schmidt *et al.*, 2017], different Raman peaks were found for the phases InSe and CIGS. An additional peak was found at around 151 cm<sup>-1</sup> at 250 °C and 520 °C, before Ga distributed towards the surface. This peak was suggested to correspond to a C(IG)<sub>3</sub>S<sub>5</sub> phase. This is in agreement with the results obtained here. Furthermore, a CIGS phase in the CuAu order was suggested to possibly be present during growth of CuInSe<sub>2</sub>, due to a Raman peak (184 cm<sup>-1</sup>) at the same position as it could be observed for CuGaSe<sub>2</sub>, but no CuGaSe<sub>2</sub> should be present at this state of growth. In the present thesis, it is put in more concrete terms, that at least a C(IG)<sub>3</sub>S<sub>5</sub> is definitely present. The stacking sequence here with the C(IG)<sub>3</sub>S<sub>5</sub> within the film, is partly in agreement with the earlier observed Cu minimum (double gradient in GDOES profile, Fig. 5 in [Schmidt *et al.*, 2017]) within the film, which showed a stacking of CIS (stoichiometric)/C(IG)<sub>3</sub>S<sub>5</sub> (Cu-poorer)/ $\gamma$ -Cu<sub>9</sub>(In,Ga)<sub>4</sub> (Cu-richer). In contrast, the (In,Ga)Se was assumed to be below the C(IG)<sub>3</sub>S<sub>5</sub>, while here it is found to be on top, although there was only an observations of a Cu decrease and In increase at the surface at the sample after 580 °C in the earlier elemental depth profiles from GDOES measurements.

Regarding the observed *ex situ* evolution of the elemental depth profile, there was a segregation of Cu and Ga at the back contact until it distributed towards the surface. It was concluded, that both originate from the  $\gamma$ -phase at the back contact. The *in situ* results showed an increase of the Cu and Ga fluorescence intensities and thus the same distribution of Cu and Ga towards the surface. In comparison of the *ex situ* results to the stacking sequences here, the change can be distinguished in more detail: The  $\gamma$ -phase exhibits a decreased Cu concentration and the same Ga to In ratio after the homogenization. This means, that the Ga atoms, which distribute towards the surface originate especially from the C(IG)<sub>3</sub>S<sub>5</sub> phase and only the Cu atoms, that distribute towards the surface, originate from the  $\gamma$ -phase.

A more profound understanding of the growth is still needed. In the following, the complex and detailed results are reduced to obtain the key facts by comparing both selenizations (Sec. 4.5). On this basis, a model of growth is suggested.

### 4.3.3. Summary

A CIGS film with an increased GGI towards the surface has been achieved within a few minutes. Furthermore, a first *in situ* measurement of such a growth could be performed. The results from the *in situ* measurement show a phase evolution as well as a phase depth distribution during selenization, which are generally different to a process with Ga segregation. In detail, a long presence of the intermediate phases  $\gamma\text{-Cu}_9(\text{In,Ga})_4$  and  $(\text{In,Ga})\text{Se}$  as well as the presence of a  $\text{C}(\text{IG})_3\text{S}_5$  phase were observed. The Cu motion towards the surface was initially impeded and both In-Se phases were concluded to be on top of the film. Due to the assumed low  $P_{\text{Se}}$ , the reaction rates were decreased and  $(\text{In,Ga})\text{Se}$  was still present at a temperature of 501 °C and for the same reason, it melted at this temperature. This is the moment, when Cu from  $\gamma\text{-Cu}_9(\text{In,Ga})_4$  and Ga from  $\text{C}(\text{IG})_3\text{S}_5$  suddenly moved towards the surface, forming a single phase CIGS. The knowledge about reaching the important  $T_{\text{sub}}$  of 501 °C is assumed to be important for a more precise production in the future. The needed minimum temperature is known and too high temperatures, like 550 °C with formation of  $\text{MoSe}_2$  can be avoided or applied afterwards for a particular thickness of  $\text{MoSe}_2$ .

## 4.4. Discussion of the applied EDXRD/EDXRF method and assumptions

On the one hand, the aim of this thesis was to deduce a simplified 1D model of the growth of CIGS for a fundamental understanding of the different growth paths. On the other hand, the deduced model was tested by taking possible uncertainties of the assumptions made into consideration.

The calculated fluorescence intensities of the deduced growth schematics (Figs. 4.11 and 4.22) were not always within the uncertainty of the measured fluorescence intensities. Therefore, the limits of the applied EDXRD/EDXRF method and the applied assumptions are discussed in the following.

Possible reasons for the deviation between the calculated and the measured fluorescence intensities are i) the uncertainty of the measured fluorescence intensities is higher than expected, ii) an uncertainty of exact phase compositions, iii) phases that can not be detected or distinguished from other phases by EDXRD and iv) an oversimplification of the model.

i) Uncertainties in the measured fluorescence intensities were estimated to be  $\pm 8\%$ . This estimation is based on the maximum estimated height misalignment of the applied measurement program routine when compensating the thermal expansion of the setup. The uncertainty of the measured fluorescence intensities is not higher than expected.

Calculated fluorescence intensities of deduced the stacking sequences outside of the uncertainty are not a consequence of the uncertainty of the measured fluorescence intensities.

ii) It was not possible to determine the exact phase composition for all observed phases. Therefore, the largest possible range of composition (according to phase diagrams) was considered to test the deduced stacking sequences by means of the corresponding calculated range of fluorescence intensities. A range of composition was considered for the  $\gamma$ -phases ( $\gamma_i$ -Cu<sub>9</sub>(In<sub>1-x</sub>Ga<sub>x</sub>)<sub>4±y</sub>), e.g. with the largest range for  $\gamma_{1/2}$ Cu<sub>9</sub>Ga<sub>4</sub>-phase with 64±4 at.% Cu. This composition range was found to influence the calculated  $I_{Cu-K\alpha}$  at T<sub>1</sub> and T<sub>2</sub> in Sec. 4.2.2. However, the differences in calculated fluorescence intensities were small. The uncertainty with respect to the CGI of the  $\gamma$ -phases did still enable a deduction of the stacking sequence by calculated fluorescence intensities. The stacking sequence deduced in Sec. 4.2 was in agreement with literature.

In case of CIGS and C(IG)<sub>3</sub>S<sub>5</sub>, the Cu concentration cannot be determined based on the EDXRD/EDXRF measurement. The phase diagram of In<sub>2</sub>Se<sub>3</sub>-Cu<sub>2</sub>Se shows a range of Cu composition in CIGS of 23±2 at.% Cu (Fig. 1.6b without Na). In case of T<sub>2</sub> in Sec. 4.2.2, the integral film composition (23 at.% Cu) and the maximum Cu content possible in CIGS (25 at.% Cu) were assumed (CGI of 0.9 and 1 in CIGS, respectively) and resulted in a difference of the fluorescence intensities much smaller compared with the difference with respect to the Cu concentration in the  $\gamma$ -phase. Therefore, a range of possible Cu compositions in the tetragonal compounds was disregarded.

The uncertainty of the lattice plane distance  $d$  was estimated to be  $\Delta d = 0.4\%$ . The GGI identified for the  $\gamma$ -phase, (In,Ga)Se, CIGS and C(IG)<sub>3</sub>S<sub>5</sub> was estimated based on  $d$  and Vegard's law. In case of Cu(In<sub>1-x</sub>Ga<sub>x</sub>)Se<sub>2</sub>,  $\Delta d = 0.4\%$  corresponds to an uncertainty in the GGI of  $\Delta x = 0.1$ , which is the highest for the compounds. This error is likely to be an overestimation as explained in the following based on the example of the growth of CIGS with Ga segregation in Sec. 4.2: The final position of the CIS 112 reflection – and CIS was determined to be at the film surface by GDOES – is in accordance with the literature value of CuInSe<sub>2</sub>. The maximum difference between the CIS 112 reflection and the literature value for CuInSe<sub>2</sub> was observed at 327 °C, corresponding to  $\Delta x = 0.01$ . This is much smaller than the uncertainty above. It is concluded, that the maximum uncertainty of the GGI of  $\pm 0.1$  is likely an overestimation when determining the composition of CIGS and C(IG)<sub>3</sub>S<sub>5</sub>.

In summary, the uncertainty of the phase compositions did not justify the deduction of a different stacking sequence.

iii) The limit of the phase identification by EDXRD is reached, if a set of reflections match several crystal structures possibly present that cannot be distinguished e.g. by additional reflections, or if the intensity of reflections is too small or not present, e.g. due to a liquid phase. Here, the information of EDXRF was supporting the EDXRD

analysis, e.g. the identification of the  $\text{Cu}_{2-x}\text{Se}$  phase or additional phases which did not lead to signals in the EDXRD spectrum.  $\text{Cu}_{2-x}\text{Se}$  was one of the phases whose presence has been reported regarding the growth of CIGS with Ga segregation. It exhibits a wide range of possible peak positions (e.g. a range of 2.1 keV between the reflections of  $\text{Cu}_2\text{Se}$  220 and  $\text{Cu}_{1.72}\text{Se}$  220 at 474 °C, see Fig. D.6) for each reflection due to the composition range of  $x=0-0.28$  and the corresponding lattice constant. The reflections can also overlap with reflections of (In,Ga)Se and CIGS. Furthermore, the relevant publications are inconsistent. For instance, considerable differences were reported for the lattice constant of  $\text{Cu}_{1.8}\text{Se}$  (cubic) at RT, ranging from  $a=5.564 \text{ \AA}$  to  $5.781 \text{ \AA}$  in [Yamamoto and Kashida, 1991, Heyding and Murray, 1976, Tonejc, 1980, Tonejc *et al.*, 1975, Murray and Heyding, 1975]. Additionally, the composition can change during the measurement.

By combining EDXRD with the EDXRF analysis, the presence of  $\text{Cu}_{2-x}\text{Se}$  was supported by the similar evolution of the Cu- $K\alpha$  fluorescence intensity and a small reflection intensity of  $\text{Cu}_{2-x}\text{Se}$  220 in Sec. 4.2. The only explanation found for the evolution of  $I_{\text{Cu}-K\alpha}$  was the presence of  $\text{Cu}_{2-x}\text{Se}$  at  $T_2$  in the top part of the film.

Large deviations between the measured fluorescence intensities and all calculated fluorescence intensities of the initially possible stacking sequences were observed at  $T_1$  in Sec. 4.3.2. The deviation was eliminated by combining the EDXRD and EDXRF signals. The combination led to the assumption of the presence of an additional and reasonable phase, which can not be observed by EDXRD due to low reflection intensities or due to being a liquid phase. The latter was the case for  $T_1$ .

iv) In the model, a distinct number of phases is assumed and each phase is approximated as a layer with a constant composition. However, due to the kinetics, concentration gradients (between and in the layers) and diffusion, composition gradients can be expected to exist within the allowed composition ranges<sup>11</sup>.

The case of a higher number of layers than number of observable quantities led to an under-determined linear equation system. If an under-determination occurred at a specific  $t_i$ , an additional boundary parameter had to be chosen. By choosing an additional free parameter, e.g. the CIS thickness, a set of fluorescence intensities with a solution matching to the experimental values was calculated.

The applied method might be further improved with a more accurate determination of the phase composition other depth. However, considering additional gradients for the calculation of fluorescence intensities, would increase the number of free parameters with possibly giving solutions indistinguishable with respect to the deduction of the stacking sequence.

---

<sup>11</sup>The gradient in CIGS can be estimated from XRD only in certain cases [Neisser *et al.*, 2003, Neisser, 2002].

v) The amount of material may change during the process (e.g. In evaporates), as it was the case in Sec. 4.3. However, the identification of the period of evaporation was possible by a simultaneously decrease of  $I_{In-K\alpha}$  and increase of  $I_{Mo-K\alpha}$ . The loss of In did not lead to indistinguishable solutions and the estimation of the amount of In lost at the specific points in time was possible.

### **Deduction of the growth schematic**

In general, an objective and quantitative evaluation of each stacking sequence, based on the overall deviation between calculated and measured fluorescence intensities for all elements (e.g. by a method of least squares) was not strictly possible.

The limitations of the method and necessary assumptions were discussed in i) - v) above. In addition some stacking sequences may have very similar calculated fluorescence intensities and/or a similar overall deviation to the measured values. Therefore, the proposed stacking sequences were deduced not only on the basis of the minimum deviation at the distinct points in time  $t_i$ , whereby the Cu and Ga fluorescence intensities were weighted higher. They were also deduced by judging the plausibility with respect to the overall evolution of the fluorescence and reflection intensities as well as corresponding (calculated) phase thicknesses and data available in literature. This led to a series of stacking sequences whose evolution of calculated fluorescence intensities are consistently in accordance with the measured fluorescence intensities throughout the process for both cases with and without Ga segregation (Secs. 4.2 and 4.3). They are consistent in terms of the stacking order, which does not change arbitrarily, e.g. by permutations of two phases with respect to the stacking sequences before and afterwards. They are also consistent in terms of the position of each phase at time  $t_i$ , which is plausible with respect to possible reactions and stacking sequences deduced for  $t_{i-1}$  and  $t_{i+1}$ .

In these terms, two consistent and reasonable series of stacking sequences (growth schematics) were deduced with the applied simplified model. In case that two or more stacking sequences, could not be distinguished by their calculated fluorescence intensities, the use of an additional parameter or plausibility reasons allowed a deduction.

## 4.5. Comparison of the two distinct growth paths from *in situ* investigation

First, the main identified differences of the two growth paths with and without Ga segregation from *in situ* experiments are presented in the following. Afterwards, the influence of  $T_{Se}$  on the growth path is discussed on the basis of a series of *ex situ* experiments carried out in the atmospheric selenization tool (Sec. 4.6). Finally, a growth model is presented (Sec. 4.7).

The comparison of the two *in situ* investigations from Secs. 4.2 and 4.3 is shown in regard to the evolution of the deduced stacking sequences (Fig. 4.23) as well as the fluorescence and reflection peak intensities (Fig. 4.24). It should be noted, that the fluorescence intensities (Fig. 4.24b-f) during the selenization without final Ga segregation were higher than for the measurement with strong Ga segregation. This results from different processing days leading to slightly different initial signal intensities. The fluorescence intensities of both measurements are normalized to the initial value at the beginning of each measurement, for which the elemental depth profiles of the precursors are assumed to be identical. The normalization is not possible in case of Se, since there was no Se in the precursor and thus no reference  $I_{Se-K\alpha}$ . The value of  $I_{Se-K\alpha}$  was higher during growth without Ga segregation than during growth with Ga segregation, but should be smaller instead due to the following two reasons: In the period before In loss occurs (0-5 min), the evolution of the normalized  $I_{Mo-K\alpha}$  of the process with Ga segregation exhibits a lower value due to the attenuation by a higher rate of Se incorporation. This is also in agreement with the deduced difference in the stacking sequences at 388 °C in Fig. 4.23.

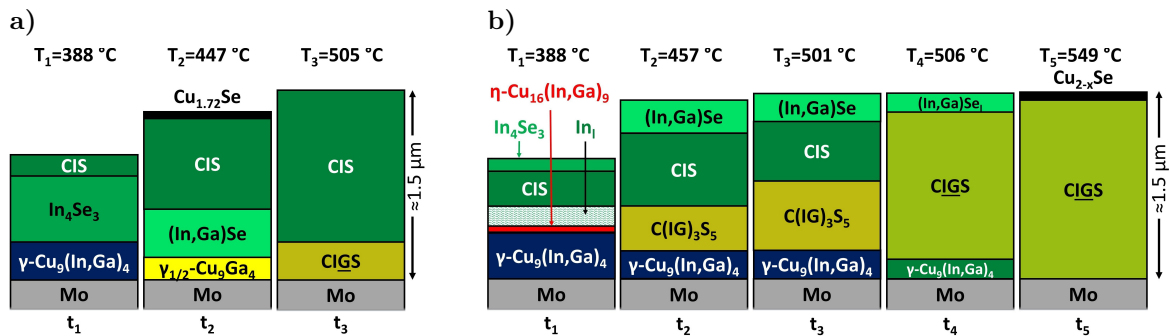


**Figure 4.23.:** Proposed growth schematics for growth of CIGS a) with Ga segregation and b) with Ga homogenization from Secs. 4.2 and 4.3 for a direct comparison.

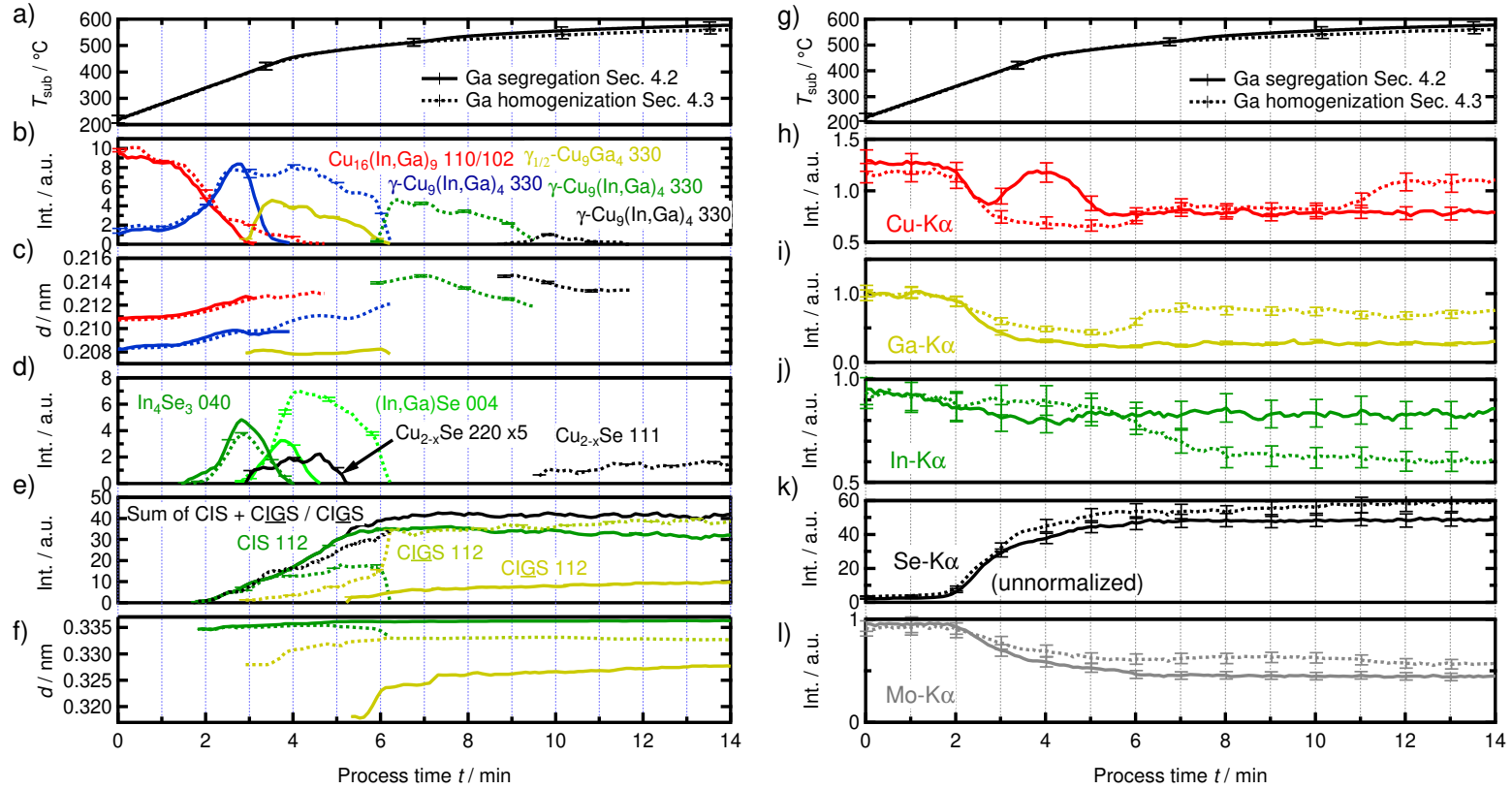


**Figure 4.24.:** Evolution of integral fluorescence and reflection intensities from selenization with (Fig. 4.4) (line) and without (Fig. 4.12) (dotted line) Ga segregation for qualitative comparison. a)  $T_{\text{sub}}$ .  $K\alpha$ -Fluorescence intensities of b) Cu, c) Ga, d) In, e) Se and f) Mo. All fluorescence intensities are normalized to the initial value at the begin of the measurement, except for Se. g)  $T_{\text{sub}}$ . Reflection intensities of the denoted phases in h) - l).

The comparison of the growth paths with Ga segregation (S) and Ga homogenization (H) is summarized to the following list of identified key points. These either have been similarly observed earlier in literature and references are added, or, in case they are observed in this work for the first time, they are highlighted with bold text.

1. S: CuInSe<sub>2</sub> forms before Ga participation in reactions with Se [Mainz *et al.*, 2015b, Moon *et al.*, 2012]  
     CuInSe<sub>2</sub> forms above In-Se  
     H: **CuInSe<sub>2</sub> forms also as first tetragonal phase, but below In-Se**
  
2. S: Cu<sub>2-x</sub>Se is present during growth [Hergert *et al.*, 2005]  
     H: **Cu<sub>2-x</sub>Se formation as an intermediate phase can be prevented**
  
3. S: **Cu moves towards the surface and Cu<sub>2-x</sub>Se forms on top of the film**  
     H: **The initial motion of Cu upwards is reduced, see stacking sequence at 457 °C**
  
4. S: Se moves downwards more quickly than Ga moves upwards, throughout the whole selenization. Finally, Se moves through CuInSe<sub>2</sub> to react with Ga at the rear side [Mainz *et al.*, 2015b, Purwins, 2010]  
     H: **In moves to the surface.** Se still moves downwards through the already formed phases, **but Se motion is slower and Ga motion is enhanced.**  $D_{\text{Se}}$  in CuInSe<sub>2</sub> is smaller due to a smaller  $P_{\text{Se}}$ , according to [von Bardeleben, 1984].
  
5. S: InSe acts as diffusion barrier for Ga [Huang *et al.*, 2017, Mainz *et al.*, 2015b]  
     H: **Due to its location on top of the stack,** InSe cannot locally separate the Ga containing  $\gamma$ -phase from the growing C(IG)<sub>3</sub>S<sub>5</sub> phase.
  
6. S: After the formation of CuInSe<sub>2</sub> and CuGaSe<sub>2</sub> as separate phases, there is not sufficient inter-diffusion to increase the minimum Ga concentration at the surface within the applied processing time of minutes [Mainz *et al.*, 2015b, Marudachalam *et al.*, 1997]  
     H: **InSe present at a lower melting temperature of 501 °C for low  $P_{\text{Se}}$ .** **The melt of InSe possibly enhances the observed strong inter-diffusion.** **Further simultaneous changes are: single CIGS phase formation,  $\gamma$ -phase composition changes, increase of  $I_{\text{Cu-K}\alpha}$  and  $I_{\text{Ga-K}\alpha}$ .**

These key points may be characteristic for the respective growth paths. They are assumed to be interesting possibilities for an application as process control in the future.

## 4.6. Comparison of the two distinct growth paths from *ex situ* investigation

From the experiments described in Secs. 4.2 and 4.3, there are clear indications, that Se supply determines which of the two growth paths occur in the system. It is difficult to unambiguously confirm this with the vacuum selenization tool alone. Despite the external Se source introduced for this work, the control-ability of the Se partial pressure was not precise enough for that purpose. The experience gathered, indicated that the results are influenced by the preceding process, due to different amounts of residual Se in the selenization tool.

The atmospheric selenization tool (Fig. 2.2), however, is equipped with external Se sources, that are controlled well via their Se source temperatures and the results are reproducible. Furthermore, Se is transported via a N<sub>2</sub> flux, which can be defined with a specific profile during processing.

Therefore, the atmospheric tool was used to test the hypothesis concerning Se supply and growth paths. For this, it was mandatory to confirm that the back ground pressure is not by itself a significant parameter. Indeed, only slight differences were observed when *in situ* EDXRD/EDXRF experiments were carried out at low (vacuum of  $\approx 10^{-5}$  mbar) and at atmospheric background pressure, respectively (see sup. Sec. D.5).

The correlation between Se supply, growth path and Ga depth profile was then studied using the atmospheric tool. Two approaches were investigated:

- i.) Investigation of the influence of  $T_{\text{Se}}$  on the incorporation of Se by a variation of  $T_{\text{Se}}$  and a process which consisted of a heating step only to a  $T_{\text{sub}}=580^\circ\text{C}$  with subsequent cool down.
- ii.) Investigation of the final film morphology, Ga depth distribution and electrical properties after a complete processing with heating and annealing using low and high Se supply.

### i.) Influence of $T_{\text{Se}}$ on the incorporation of Se

A series of films were prepared by a selenization of the multilayer precursor within only a heating step and subsequent cool down<sup>12</sup>. The  $T_{\text{Se}}$  was varied between 300 °C and 420 °C while the processing time was kept the same to reach a  $T_{\text{sub}}=580^\circ\text{C}$ . The influences of  $T_{\text{Se}}$  on the formation of CIGS were analyzed by *ex situ* XRD regarding

---

<sup>12</sup>A heating rate of about 6 °C/s was applied by keeping the samples in the 710 °C hot wall chamber for 103 s, during which the substrate temperature ( $T_{\text{sub}}$ ) reached 580 °C, see Fig. 2.2. Se was transported in a N<sub>2</sub> flow from an external Se source with controlled temperature  $T_{\text{Se}}$ . Se supply was varied by different  $T_{\text{Se}}$  while the N<sub>2</sub> flux was held constant at 1 slm (standard litre per minute). All Mo layers were 800 nm thick (compare Experimental).

the 112 reflections (see Fig. 4.25a)). The amount of Se incorporation was analyzed with *ex situ* XRF (see Fig. 4.25b)).

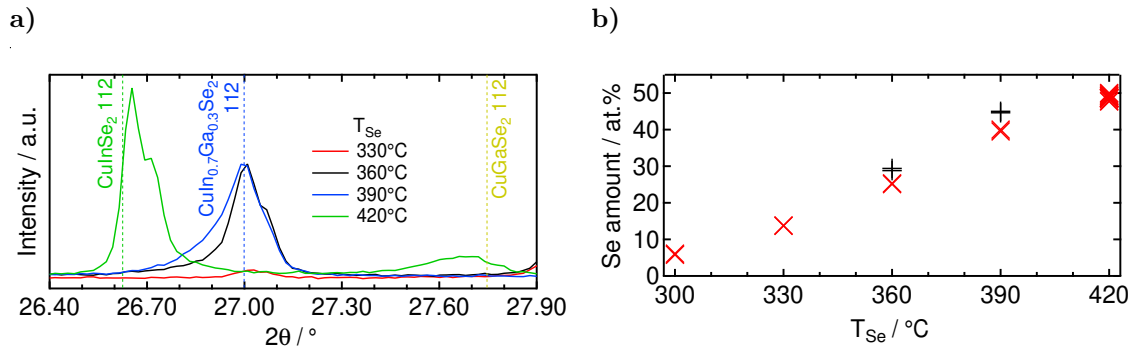


**Figure 4.25.:** Influence of  $T_{Se}$  on the CIGS 112 reflections and amount of Se incorporation. a) The diffractograms show the intensity of the chalcopyrite 112 reflections, measured at RT. Dashed vertical lines indicate the position of the 112 reflections from reference pattern for  $CuInSe_2$  and  $CuGaSe_2$  (see sup. Tab. E.2). Reflections in between exhibit a solid solution of both. The position of  $CuIn_{0.7}Ga_{0.3}Se_2$  112 is exemplarily calculated with Vegard’s law from the references. The precursor and the sample for  $T_{Se}=300^\circ C$  exhibit no chalcopyrite related reflection intensity and are therefore not shown. b) Se source temperature vs. Se amount from XRF analysis with an aperture of 30 mm, measured on the samples from a).  $\times$  indicates the first experiment series and  $+$  indicates experiments repeated later.

The position of a CIGS 112 reflection can be correlated to the composition by a linear interpolation between the reference positions of  $CuInSe_2$  and  $CuGaSe_2$  using Vegard’s law (see Sec. 1.1.1). No diffraction of a chalcopyrite was found for  $T_{Se} = 300^\circ C$  with formation of only binary selenides (not shown). Remarkably, for  $T_{Se}$  between  $330^\circ C$  and  $390^\circ C$  only one CIGS 112 reflection appeared which indicates  $Cu(In_{0.7}Ga_{0.3})Se_2$  is formed, which is similar to the integral GGI of the film. A  $T_{Se}$  of  $420^\circ C$  leads to two CIGS 112 reflections with one close to  $CuInSe_2$  and the other one close to  $CuGaSe_2$ . This finding corresponds to Ga segregation, as it was also found via *in situ* investigation in the vacuum selenization tool, presented in Sec. 4.2. It is concluded, that there is a critical value of the Se partial pressure (between  $T_{Se}$  of  $390^\circ C$  and  $420^\circ C$ ), at which the growth path switches. Above the critical  $P_{Se}$  Ga segregation occurs and below it a formation of a single phase CIGS with  $Cu(In_{0.7}Ga_{0.3})Se_2$  is enabled throughout the absorber depth.

The Se amount in the film increases with increasing  $T_{Se}$  and reaches the stoichiometric value of 50% at  $420^\circ C$ . The rate of Se incorporation during the fast heating seems shows a linear dependence of  $T_{Se}$  between  $T_{Se}=300-420^\circ C$ . Therefore, Se incorporation into the precursor film is limited by the Se supply rather than the reaction kinetics at

the surface or in the bulk (at least below a  $T_{\text{Se}}$  of 420 °C). That confirms a control of the film formation by Se supply.

## ii.) Final film morphology, Ga depth distribution and correlation with electrical properties after a complete processing at low and high Se supply

In contrast to the previous experiment, the selenization here was extended by an annealing period (with unchanged  $T_{\text{Se}}$ ) at constant  $T_{\text{sub}}=580$  °C. Experiments were performed with  $T_{\text{Se}}$  of 390 °C and 420 °C. The temperatures of the two Se sources were the same for the heating and the annealing process steps (see  $T_{\text{Se}1}$  and  $T_{\text{Se}2}$  in Fig. 2.2). Two samples were selenized with 1 slm of  $\text{N}_2$  flux for Se transport during heating up to 580 °C and a subsequent annealing at constant temperature. The subsequent annealing was performed in Se atmosphere for 3 min with 0.5 slm  $\text{N}_2$  flux and 3 min with 0.2 slm of  $\text{N}_2$  flux. The comparison of the CIGS 112 reflections between Fig. 4.25a) and Fig. 4.26a) shows, that the Ga distribution in the CIGS phases remains unchanged during the subsequent annealing. Only the case of the lower  $T_{\text{Se}}=390$  °C led to an additional intensity of the reflection signal towards a smaller angle, a CIGS phase with smaller GGI respectively. The different Ga distribution in the CIGS phases is shown by the Ga depth profiles in Fig. 4.26b), which shows an increased Ga concentration towards the surface for a lower Se supply. SEM images of the two samples in Fig. 4.26c) and Fig. 4.26d) show different morphologies. The latter film ( $T_{\text{Se}}=420$  °C) exhibits two parts, with a fine-grained layer at the Mo back contact and a closed layer with big grains on top. This is known to form in CIGS layers or complete films with high Ga concentration [Probst *et al.*, 2001, Abou-Ras *et al.*, 2008, Eisenbarth *et al.*, 2009]. The lower  $T_{\text{Se}}=390$  °C resulted in a homogeneous and closed layer with big grains, nearly without voids. This is in contrast to [Kaelin *et al.*, 2003, Wang *et al.*, 2012], who found smaller CIGS crystals for a low  $P_{\text{Se}}$ .

An increasing Ga concentration and a corresponding increase of the minimum  $E_g$  should increase the  $V_{oc}$  (as described in Sec. 1.1.2 and by [DIAGNE *et al.*, 2016]). In case of the lower  $T_{\text{Se}}$ , the Ga concentration was increased towards the surface (Fig. 4.26b)) and thus should be reflected by a higher  $E_g$  and higher  $V_{oc}$ . Indeed, the  $V_{oc}$  of the absorber without Ga segregation was 479.6 mV and hence higher as the one with Ga segregation and a  $V_{oc}$  of 445.8 mV, shown in Fig. 4.26e). The same is observed for the  $E_g$  by EQE measurement with an  $E_g$  of 1.03 eV compared with 1.01 eV, respectively, shown in Fig. 4.26f). A further investigation of the selenization parameters is necessary to adjust the minimum GGI closer to the predicted optimum at 0.25 for an  $E_g=1.15$  eV.

### Best solar cell with low Se supply

The best solar cell produced in this work has a conversion efficiency of  $\eta = 15.5\%$  (Fig. 4.27) (active area of 1.35 cm<sup>2</sup>, without anti reflective coating), while the median of

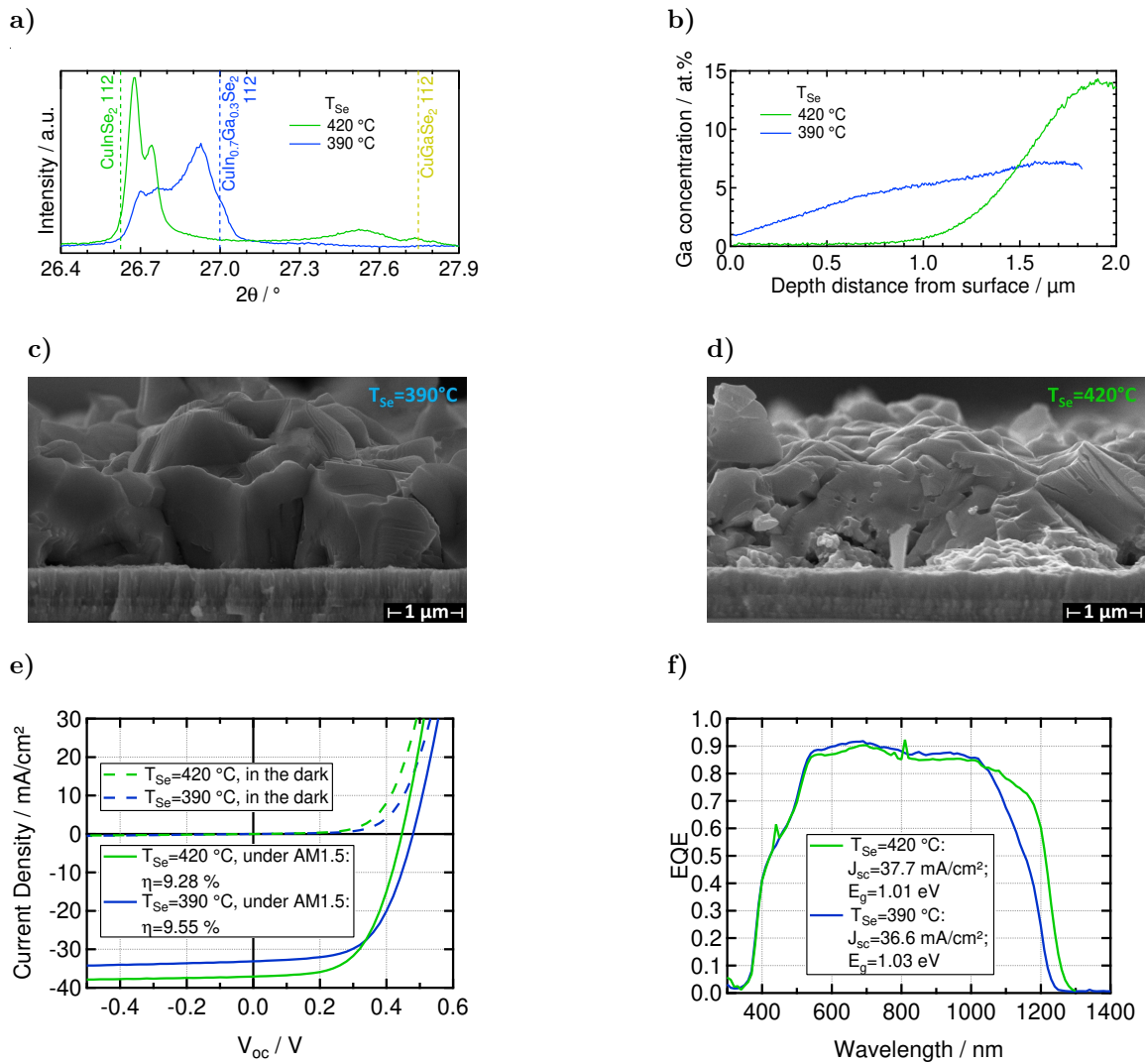


**Figure 4.26.:** Properties of final CIGS films, selenized with low and high Se supply. The temperatures indicate  $T_{\text{Se}}$  of 390 °C and 420 °C. a) The diffractograms show the intensity of the CIGS 112 reflections, measured at RT. Dashed vertical lines indicate the position of the 112 reflections from reference pattern for  $\text{CuInSe}_2$  and  $\text{CuGaSe}_2$ . Peaks in between exhibit a solid solution of both. The position of  $\text{CuIn}_{0.7}\text{Ga}_{0.3}\text{Se}_2$  112 is exemplarily calculated with Vegard’s law from the references. b) Ga depth profiles from GDOES of the same films. The GDOES measurement is assumed to reach the Mo layer at 10 at.% of Mo and the curves are cut there. SEM images of with 20k magnification for a  $T_{\text{Se}}$  of c) 390 °C and of d) 420 °C. In-house measurement of e) the current-voltage characteristics measured in the dark and under AM1.5 illumination and f) corresponding EQE. In-house measurements of e) the current-voltage characteristics measured under AM1.5 illumination (line) and in the dark (dashed line) and f) EQE measurement of the same solar cells. The estimated  $E_g$  corresponds to the inflection point of the EQE between 1000 nm and 1300 nm.

49 solar cells on the  $10 \times 10 \text{ cm}^2$  sample was 14.9%. Its  $E_g$  is around 1.03 eV, which is calculated from the inflection point between 1000 nm and 1300 nm shown in Fig. 4.27b. This is similar to the value of 1.02 eV regarding Eq. 1.2 and using the minimum GGI of 0.04 in the GDOES depth profile at 0.04  $\mu\text{m}$ . The selenization was performed without sulfur and at atmospheric pressure in the order of a few minutes. A multilayer precursor

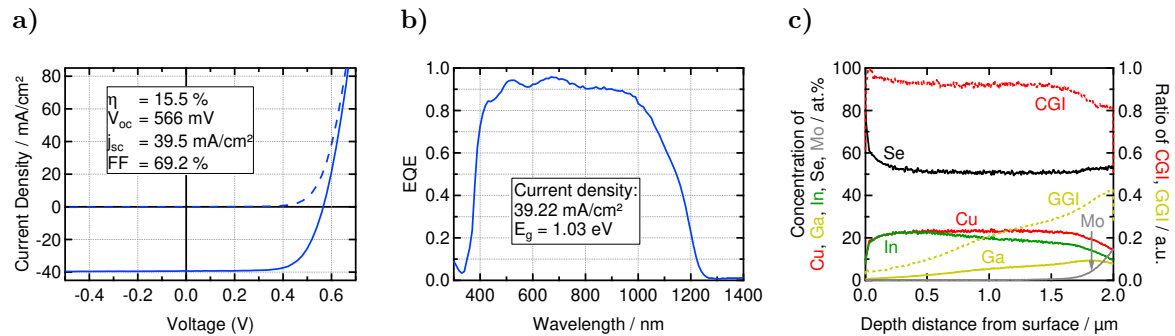


**Figure 4.27.:** Best solar cell with its a) current-voltage, b) EQE-wavelength characteristics and c) elemental depth profile. In-house measurements of a) the current-voltage characteristics measured under AM1.5 illumination (line) and in the dark (dashed) and b) EQE measurement of the best solar cell whose elemental depth distribution exhibited a Ga gradient in c). The estimated  $E_g$  corresponds to the inflection point of the EQE between 1000 nm and 1300 nm. c) Elemental depth profile from GDOES measurement on the final absorber with highest efficiency presented in this section. The back contact is assumed to be at 10 at.% Mo. The electrical characteristics were already published in [Schmidt *et al.*, 2017].

is selenized with the baseline sequence (see Experimental and [Schmidt *et al.*, 2017]) and a Zn(O,S) buffer layer was used. The elemental depth distribution in Fig. 4.27c shows an absorber with increased Ga concentration towards the surface. This is more similar to the elemental depth profile with Ga homogenization in Fig. 4.15b) than with Ga segregation in Fig. 4.5b).

In summary, the *ex situ* investigation by use of the atmospheric selenization tool confirmed, that the growth of CIGS can be controlled by the Se supply. The growth path with resulting Ga segregation or Ga homogenization depend on choosing a high or a low Se supply, respectively. The two different growth paths with final films, similar according to morphology, CIGS phases and elemental depth profiles, are observed independently of the background pressure.

By utilizing the respective CIGS formation with a higher GGI close to the absorber surface and optimizing the precursor architecture towards a multilayer precursor consisting of 22 In/CuGa/In layers, solar cells with a conversion efficiency of up to 15.5% were achieved (active area, in-house measured, no anti reflective coating). According to a recent review paper, this is the highest reported efficiency for sulfur

free CIGS -based solar cells utilizing fast (few minutes) atmospheric processes and elemental Se [Song *et al.*, 2018].

## 4.7. CIGS growth model and correlation with the Se supply

First, the key points from Sec. 4.5 for the cases of high and low Se supply are now correlated to the effects of the Se supply. In this matter, the key points can be combined/condensed to two topics, the stacking sequence and the intermediate phases. The focused results of this work are illustrated by a proposed schematic of a model of growth in Fig. 4.28. The phases  $\text{In}_4\text{Se}_3$  and  $(\text{In,Ga})\text{Se}$  are referred to as In-Se, while the metallic phases are summarized as Cu-In-Ga.

### 1. Stacking sequences:

A high/low Se supply is correlated to a high/low  $P_{\text{Se}}$ , which in turn influences the elemental diffusion, especially of Se (high/low  $D_{\text{Se}}$  known for  $\text{CuInSe}_2$ ). The consequences for this are:

In case of a high  $P_{\text{Se}}$  and  $D_{\text{Se}}$ , Se moves quickly deep into the film and reacts faster with the preferred element In<sup>13</sup>. This leads to a reaction of all initial excess In to In-Se and afterwards In leaves the  $\gamma\text{-Cu}_9(\text{In,Ga})_4$  phase to react with Se. This leads to excess Cu in the  $\gamma_{1/2}\text{-Cu}_9\text{Ga}_4$  phase that is also released. Due to the generally high mobility of Cu, Cu reaches the surface to react with Se. The presence of  $\text{Cu}_{2-x}\text{Se}$  promotes the growth of CIS, because  $\text{Cu}_{2-x}\text{Se}$  is very mobile to get to the growth front and can be the base lattice for a topotaxial [Wada *et al.*, 1997] growth of CIS.

Hence, the Se supply determines the growth position of In-Se within the film. In consequence, the educts present at the growth front exchange between InSe (high Se supply) and the Ga containing  $\gamma$ -phase (low Se supply).

In case of a low  $P_{\text{Se}}$  and  $D_{\text{Se}}$ , liquid In is longer present and exhibits a higher mobility in CIS than Se. At first, liquid In reaches the surface, where it reacts with Se starting at 327 °C. Without liquid In present anymore, which maybe the case when  $\text{C(IG)}_3\text{S}_5$  starts to grow at 390 °C (3 min), Se needs to diffuse deeper into the film to react with the  $\gamma\text{-Cu}_9(\text{In,Ga})_4$  phase (Fig. 4.23b)). There is no phase (like InSe during Ga segregation) that locally separates the reaction front of CIS from the metallic phase. The presence of the  $\gamma$ -phase at the reaction front (between 4-6 min) leads to further selenization reactions with Ga. Nevertheless,

<sup>13</sup>Se reacts first with In, due to the smallest enthalpy of formation of -383 kJ/mol for  $\text{In}_4\text{Se}_3$  [Purwins, 2010] than  $\text{Cu}_{2-x}\text{Se}$  with -59 kJ/mol [Anderson *et al.*, 2003].

the  $C(IG)_3S_5$  phase exhibits a higher In than Ga content. Therefore, In is still slightly preferred in the selenization reactions.

2. Intermediate phases:

A high Se supply leads to the additional intermediate phases Cu-Se, besides In-Se. Cu-Se and In-Se provide already most Se as well as Cu and In atoms needed to quickly form a chalcopyrite.

A low Se supply slows down the reactions. InSe is longer present. A low Se supply also effects a lower melting point of InSe (from 611 °C to 501 °C). The liquid phase presumably distributes along the grain boundaries where it enhances the motion of all elements, especially of Ga.

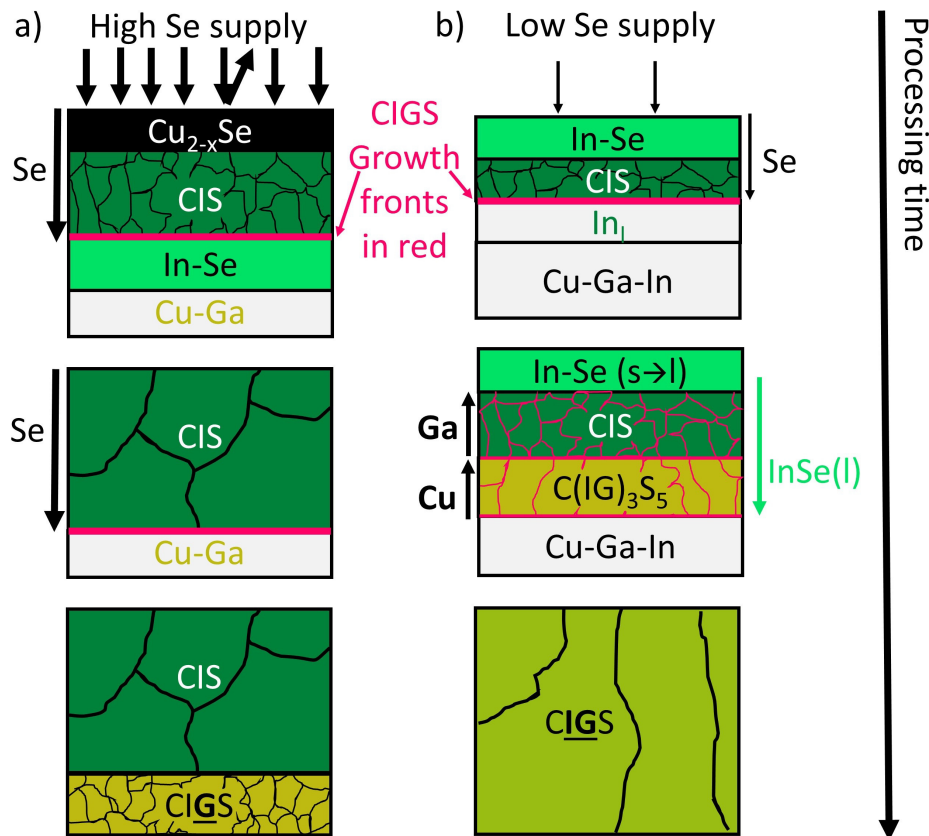


**Figure 4.28.:** Proposed schematic representation of growth models for CIGS with different Se supply and a) strong Ga segregation or b) without final Ga segregation. The vertical arrows at side of the stacks denote the distinct movement of elements. Pink colored lines indicate the growth front of the tetragonal phases. The phases  $In_4Se_3$  and  $(In,Ga)Se$  are summarized as In-Se, while the metallic phases are summarized as Cu-In-Ga.

## 5. Conclusion and outlook

In conclusion, the Se supply during selenization of Cu-In-Ga precursors is important with regard to lateral and vertical phase separation, which are unwanted effects for CIGS production.

i) Lateral phase separation and even dewetting can become significant, if the Se supply during selenization is adjusted such that the precursor is in part or fully heated up without Se. The necessity of a prevention of lateral phase separation during thermal processing of Cu-In-Ga precursors to CIGS absorbers was demonstrated by selenizing a precursor that exhibited distinct phase separation prior to selenization. After this selenization, an inhomogeneous lateral Ga/In distribution in the chalcopyrite phase was found.

The impact on lateral phase separation and dewetting were investigated regarding the heating rate and the maximum temperature during annealing of metal precursors in Se free environment. A suitable starting point was a smoother and more homogeneous multilayer precursor in comparison with a double and triple layer architecture. Slowest heating rate of 0.01 °C/s led to the highest dewetted area and most significant phase separation. Both effects were observed to be impeded with increasing heating rate, such as 1 °C/s. However, dewetted Mo areas were still found. An additional NaF layer on top of the precursor led to a reduced dewetting of the annealed precursor along with a different phase separation after annealing of the sample. This beneficial effect from NaF only occurred when NaF was deposited on top and was not significantly dependent on the NaF amount (between 10 and 30 nm thick layers). Even for the slowest heating rate of 0.01 °C/s, an effective prevention of the dewetting effect is found.

Overall, the results show how to enable and widen the parameter space for selenization with a prior annealing step of up to 580 °C, even with slow heating rates of 0.01 °C/s. Fast heating rates and NaF addition on top enable a delayed Se-addition during selenization and possibly enable process designs leading to optimized Ga depth profiles.

ii) Vertical phase separation, in particular Ga segregation at the back contact, is typically observed during the fast selenization of precursors with elemental Se. For a better understanding, the evolution of phases and their depth distribution were investigated by an *in situ* EDXRD/EDXRF method. This method was shown to be

appropriate to obtain the phase depth distribution for characteristic points in time during selenization.

A good agreement of the results with Ga segregation to the literature demonstrates the possibilities of applying the *in situ* EDXRD/EDXRF method to the highly complex system of selenization of a Cu-In-Ga precursor. However, the method is limited by solving the linear equation system with a finite number of degrees of freedom. Every additional degree of freedom increases the number of solutions. In general, adding a parameter can lead to an indistinguishable set of solutions. A further limit is reached, if two phases exhibit a too similar composition and thus a set of solutions with fluorescence intensities within the uncertainty of the measurement. This can also be the case for a layer, that is too thin for sufficient variation of the fluorescence intensities for different stacking sequences of the present phases. However, in the case of growth of CIGS layers investigated in this thesis, a deduction of stacking sequences was possible and a model of growth is proposed.

The observed Ga segregation inhibits the adjustment of the effective band gap energy to achieve more efficient solar cells. It is shown, that controlling the supply of elemental Se during selenization opens up new possibilities to adjust the Ga grading within sequentially fabricated CIGS absorber layers.

A lower Se source temperature corresponds to a lower Se supply for the CIGS formation and was the key for a prevention of Ga segregation in the absorber. For the process with a smoothed Ga in-depth profile, the results showed a new and different phase evolution in contrast to the growth with Ga segregation. The new phase evolution is referred to as Ga homogenization (to indicate the contrast to the case described by the common term segregation). The new results of this work are as follows:

- i) In case of Ga segregation, the investigation showed the presence of  $\text{Cu}_{2-x}\text{Se}$  during selenization, which was only supposed by *ex situ* investigations in previous works. Furthermore, this phase was shown here to be on top of the stacking sequence. The formation of  $\text{CuInSe}_2$  was found to be on top of the In-Se phases.
- ii) In case of Ga homogenization, this selenization process was observed *in situ* for the first time. In-Se phases were deduced to form on top of the film and thus without the possibility to act as a diffusion barrier for Ga. In contrast, in the earlier published *ex situ* study, In-Se was assumed to be between  $\text{CuInSe}_2$  and the metallic phases [Schmidt *et al.*, 2017]. The growth of a  $\text{C(IG)}_3\text{S}_5$  phase and that Ga was involved in an earlier stage of growth were concluded. A consequence of the low Se supply was a longer presence of the intermediate phases InSe and  $\gamma\text{-Cu}_9(\text{In,Ga})_4$ . The low Se partial pressure led to a melting of InSe at 501 °C. Simultaneously to the melting InSe, Cu and Ga were found to move quickly towards the surface. A CIGS film with an increase Ga concentration at the surface was achieved.

---

By utilizing the respective CIGS formation with a higher GGI close to the absorber surface and optimizing the precursor architecture towards a multilayer precursor consisting of 22 In/CuGa/In layers, solar cells with a conversion efficiency of up to 15.5% were achieved (active area, in-house measured, no anti reflective coating). This is the highest reported efficiency for sulfur free CIGS-based solar cells utilizing fast (few minutes) atmospheric processes and elemental Se [Schmidt *et al.*, 2017, Song *et al.*, 2018].

## Outlook

In the next step, the homogenization of the Ga depth distribution can be investigated to find out, if one can control the reactions in a way to achieve a specific  $E_g$  in the top part of the film and an increase towards the back contact. Such an increase can then be optimized for an electron collection in the bulk and prevention of recombination at the back contact. A second gradient with an  $E_g$  in the top part, which increases towards the surface might further enhance the efficiency, as discussed in [Witte *et al.*, 2015]. This is possible by adding a subsequent sulfurization.

The multilayer precursor was optimized within the scope of an absorber with Ga segregation. With the new processing and the Ga homogenization, the precursor can again be optimized, especially regarding the number of layers (a lower number may industrially be more attractive).

Void formation in CIGS at the back contact has been investigated intensively and has been suggested to result from the formation of the  $\gamma$ -Cu<sub>9</sub>(Ga,In)<sub>4</sub> compound at the rear interface [Kim *et al.*, 2012a]. The shown CIGS growth with Ga homogenization seems to exhibit grains over the whole film thickness and less void formation. This might be another great advantage and should be investigated in the future.

# Kurzfassung

Cu(In,Ga)Se<sub>2</sub> (CIGS) wird als Absorberschicht für die Herstellung von Dünnschicht-Solarzellen eingesetzt. Ein industriell relevanter Ansatz zur kostengünstigen und schnellen Herstellung von CIGS ist der sequentielle Prozess. Der in dieser Arbeit angewandte sequentielle Prozess basiert auf dem Sputtern einer Cu-In-Ga-Vorläuferschicht, der dann in Se-Dampf aufgeheizt wird um innerhalb von Minuten zu einer CIGS-Schicht zu reagieren (Selenisierung). Der sequentielle Prozess führt jedoch typischerweise zu einer Ga-Segregation am Rückkontakt. Die beobachtete Ga-Segregation verhindert das Einstellen der effektiven Bandlücke, um Solarzellen mit höherer Effizienz zu erreichen. Eine ausreichende Anpassung des Ga-Tiefenprofils bei der schnellen Selenisierung in Se-Dampf wurde bisher nicht erreicht. Das Ziel dieser Arbeit ist es, die physikalischen Ursachen von Ga-Segregation zu identifizieren und die starke Ga-Segregation innerhalb eines schnellen sequentiellen Prozesses zu verhindern. Der Einfluss eines i) verzögerten Se-Angebots sowie ii) des Se-Partialdruckes auf die Kinetik wurden untersucht.

Die Untersuchung ergab, dass i) ein verzögertes Se-Angebot zu lateraler Phasensegregation und Entnetzung führen kann. Die Ergebnisse zeigen die Möglichkeit und das Erweitern des Parameterraums für die verzögerte Selenisierung mit einem vorherigen Aufheizen von bis zu 580 °C durch schnelle Aufheizraten oder einer zusätzlichen NaF-Schicht auf dem Vorläufer. ii) Die Steuerung des Se-Angebots wurde durch Verdampfen von Se aus einer externen Quelle erreicht. Zum besseren Verständnis des Wachstums von CIGS wurde die Entwicklung von Phasen und deren Tiefenverteilung mit einer simultanen *in situ* EDXRD/EDXRF-Methode untersucht. Durch den Vergleich der gemessenen mit numerisch berechneten Fluoreszenzintensitäten wurde ein schematisches Modell für die Entwicklung der Phasentiefenverteilung während der Selenisierung ermittelt. Zwei verschiedene Wachstumspfade wurden analysiert, einer mit starker Ga-Segregation und einer mit Ga-Homogenisierung. Für Ersteren war es möglich, die Bildung und die Dauer der Anwesenheit von Cu<sub>2-x</sub>Se und die Position im oberflächennahen Teil des Films zum ersten Mal mit dieser Methode nachzuweisen.

Die Absenkung der Temperatur der Se-Quelle entspricht einem geringeren Se-Angebot und war der Schlüssel zur Verhinderung der Ga-Segregation im Absorber. Dieses Wachstum mit Ga-Homogenisierung wurde erstmals mit einer *in situ*-Methode beobachtet. In diesem Fall wurde eine andere Entwicklung der Phasenbildung und des Tiefenprofils beobachtet. Eine Folge des geringen Se-Angebots war eine längere Anwesenheit der Zwischenphasen InSe und  $\gamma$ -Cu<sub>9</sub>(In,Ga)<sub>4</sub>. Bei 500 °C bewegen sich Ga und Cu schnell in Richtung der Oberfläche und die minimale Bandlücke des resultierenden Absorbers wird vergrößert. Ein schematisches Wachstumsmodell wird vorgeschlagen. Dieser Herstellung wird eine wichtige Rolle für eine zukünftige industriell relevante Technologie zugeschrieben.

Die Nutzung der CIGS-Herstellung mit einer höheren Ga-Konzentration nahe der Absorberoberfläche und der Optimierung der Vorläuferherstellung hin zu einem vielschichtigen Vorläuferfilm wurden Solarzellen mit einem Wirkungsgrad von bis zu 15,5 % erreicht (aktive Fläche, intern gemessen, keine Antireflexionsbeschichtung). Dies ist der höchste berichtete Wirkungsgrad für schwefelfreie CIGS-basierte Solarzellen, die mit einem schnellen und atmosphärischen Prozess sowie elementarem Selen hergestellt wurden.

# Abstract

Cu(In,Ga)Se<sub>2</sub> (CIGS) is applied as absorber layer for thin film solar cells. An industrially relevant approach for low cost and fast preparation of CIGS is the sequential processing. The sequential process applied in this work is based on sputtering a Cu-In-Ga precursor, which is then heated in Se vapor to form a CIGS layer (selenization) within minutes. However, sequential processing typically leads to Ga segregation at the back contact. The observed Ga segregation inhibits the adjustment of the effective band gap energy to achieve more efficient solar cells. Up to now, a sufficient adjustment of the Ga in-depth profile during fast selenization in Se vapor has not been achieved. Identifying pathways to prevent strong Ga segregation within a fast sequential process is the aim of this thesis.

A possible parameter for an additional control of kinetics during growth of CIGS is the Se supply, whose influences are investigated here. This can mean a control of i) the time of starting the Se supply and ii) the Se partial pressure.

It is found, that i) a delayed Se supply can lead to lateral phase segregation and dewetting. The results show how to enable and widen the parameter space for a delayed selenization with a prior annealing step at a temperature of up to 580 °C by fast heating rates or NaF addition on top of the precursor.

ii) The control of the Se supply was achieved by evaporation of Se from an external source. For a better understanding of the growth of CIGS, the evolution of phases and their depth distributions were investigated by a simultaneous *in situ* EDXRD/EDXRF method. By comparing the measured with numerically calculated fluorescence intensities, a schematic model of the evolution of the phase depth distribution during selenization was obtained. With this approach, two different growth paths, one with strong Ga segregation and one with Ga homogenization were analyzed. For the former, it was possible to experimentally observe the formation and period of presence of Cu<sub>2-x</sub>Se with this method for the first time and to confirm the position to be near the surface of the film.

Decreasing the Se source temperature corresponds to a lower Se supply for the CIGS formation and was the key for preventing Ga segregation in the absorber. The growth without Ga segregation was observed via an *in situ* method the first time. A different evolution of the phase formation and depth profile was observed. A consequence of the low Se supply was a longer presence of the intermediate phases InSe and  $\gamma$ -Cu<sub>9</sub>(In,Ga)<sub>4</sub>. At 500 °C, Ga and Cu quickly move towards the surface and the minimum band gap of the resulting absorber film is widened. A schematic model of growth is presented. This processing is considered to play an important role for a forthcoming industrially relevant technology.

By utilizing the CIGS formation with a higher Ga concentration close to the absorber surface and optimizing the precursor architecture towards a multilayer precursor consisting of 22 In/CuGa/In layers, solar cells with a conversion efficiency of up to 15.5% were achieved (active area, in-house measured, no anti reflective coating). This is the highest reported efficiency for sulfur free CIGS-based solar cells utilizing fast atmospheric processes and elemental Se.



# Bibliography

- [Abou-Ras *et al.*, 2008] Abou-Ras, D., Caballero, R., Kaufmann, C. A., Nichterwitz, M., Sakurai, K., Schorr, S., Unold, T., and Schock, H. W. (2008). Impact of the Ga concentration on the microstructure of  $\text{CuIn}_{1-x}\text{Ga}_x\text{Se}_2$ . *PHYS STATUS SOLIDI-R*, 2(3):135–137.
- [Abou-Ras *et al.*, 2012] Abou-Ras, D., Schmidt, S. S., Caballero, R., Unold, T., Schock, H.-W., Koch, C. T., Schaffer, B., Schaffer, M., Choi, P.-P., and Cojocar-Mirédin, O. (2012). Confined and Chemically Flexible Grain Boundaries in Polycrystalline Compound Semiconductors. *Advanced Energy Materials*, 2(8):992–998.
- [Alberts, 2004] Alberts, V. (2004). Band gap engineering in polycrystalline  $\text{Cu}(\text{In,Ga})(\text{Se,S})_2$  chalcopyrite thin films . *Materials Science and Engineering: B*, 107(2):139 – 147.
- [Alberts, 2007] Alberts, V. (2007). A comparison of the material and device properties of homogeneous and compositional-graded  $\text{Cu}(\text{In,Ga})(\text{Se,S})_2$  chalcopyrite thin films. *Semiconductor Science and Technology*, 22(6):585.
- [Alberts *et al.*, 2004] Alberts, V., Nemraoui, O., Leitch, A. W. R., and Botha, J. R. (2004). Structural and optical characterization of homogeneous monophasic  $\text{Cu}(\text{In}_{1-x}\text{Ga}_x)(\text{Se}_{1-y}\text{S}_y)_2$  thin films. *PHYS STATUS SOLIDI C*, 1(9):2311–2315.
- [Alberts *et al.*, 2006] Alberts, V., Scholtz, E., Chiteme, C., Dhlamini, F., Sheppard, C., Molefe, P., and Chenene, M. (2006). CIGSSe pilot facility results dramatic demonstration of commercial success. *21st EUPVSEC*.
- [Aliev *et al.*, 1973] Aliev, N., Kerimov, I., and Kurbanov, M. (1973). Thermal Expansion and Isothermal Compressibility of In Chalcogenide Single Crystals. *Soviet Physics-Solid State*, 14(12):3106–3107.
- [Aliev *et al.*, 1972] Aliev, N., Kerimov, I., Kurbanov, M., and Mamedov, T. (1972). Anisotropy of the linear thermal expansion and isothermal compressibility of a GaSe single crystal. *FIZIKA TVERDOGO TELA*, 14(5):1522–1524.
- [Ancsin, 1985] Ancsin, J. (1985). Melting Curves and Heat of Fusion of Indium. *Metrologia*, 21(1):7.
- [Anderson *et al.*, 2003] Anderson, T., Crisalle, O., Li, S., and Holloway, P. (2003). Future CIS Manufacturing Technology Development. *Final Report, NREL*.

- [Bäcker *et al.*, 2015] Bäcker, J.-P., Rodriguez-Alvarez, H., Hartig, M., Kaufmann, C., Kavalakkatt, J., Mainz, R., Merdes, S., Schmidt, S., Wolf, C., Ziem, F., and Schlatmann, R. (2015). Kinetics of phase separation & coarsening in Cu-In-Ga precursor thin films for sequentially processed Cu(In,Ga)Se<sub>2</sub> solar cells. Talk at DPG-Frühjahrstagung 2015 Berlin, Germany.
- [Bäcker *et al.*, 2017] Bäcker, J.-P., Schmidt, S. S., Rodriguez-Alvarez, H., Wolf, C., Kaufmann, C. A., Hartig, M., Mainz, R., and Schlatmann, R. (2017). Lateral phase separation in Cu-In-Ga precursor and Cu(In,Ga)Se<sub>2</sub> absorber thin films. *SOL ENERG MAT SOL C*, 162:120 – 126.
- [Bahari *et al.*, 2003] Bahari, Z., Dichi, E., Legendre, B., and Dugué, J. (2003). The equilibrium phase diagram of the copper-indium system: a new investigation. *Thermochimica Acta*, 401(2):131 – 138.
- [Berger *et al.*, 2002] Berger, D., Wehreter, E., Mezentsev, N., and Shkaruba, V. (2002). A superconducting 7 T multipole wiggler for BESSY II: Main challenges and first field measurements. In *Proc. EPAC*, page 2595.
- [Bodegård *et al.*, 2003] Bodegård, M., Lundberg, O., Lu, J., and Stolt, L. (2003). Recrystallisation and interdiffusion in CGS/CIS bilayers. *Thin Solid Films*, 431-432:46.
- [Bodegård *et al.*, 1994] Bodegård, M., Stolt, L., and Hedström, J. (1994). The Influence on the Grain Structure of CuInSe<sub>2</sub> Films for Photovoltaic Applications. In *Proceedings of the 12th European PVSEC*, pages 1743–1746, Amsterdam.
- [Bronstein *et al.*, 1997] Bronstein, I., Semendjajew, K., Musiol, G., and Mühlig, H. (1997). *Taschenbuch der Mathematik*. Verlag Harri Deutsch, Thun und Frankfurt/M.
- [Broussillou *et al.*, 2015] Broussillou, C., Viscogliosi, C., Rogee, A., Angle, S., Grand, P. P., Bodnar, S., Debauche, C., Allary, J. L., Bertrand, B., Guillou, C., Parissi, L., and Coletti, S. (2015). Statistical Process Control for Cu(In,Ga)(S,Se)<sub>2</sub> electrodeposition-based manufacturing process of 60×120cm<sup>2</sup> modules up to 14,0% efficiency. In *IEEE 42nd PVSC*, pages 1–5.
- [Brühl *et al.*, 1981] Brühl, H.-G., Neumann, H., Pfeiffer, T., and Kühn, G. (1981). Anisotropic thermal expansion of Cu-III-VI<sub>2</sub> compounds. *PHYS STATUS SOLIDI A*, 66(2):597–600.
- [Buras and Gerward, 1989] Buras, B. and Gerward, L. (1989). Application of X-ray energy-dispersive diffraction for characterization of materials under high pressure. *Prog. Crystal Growth and Charact.*, 18:93 – 138.
- [Burgelman *et al.*, 2000] Burgelman, M., Nollet, P., and Degraeve, S. (2000). Modelling polycrystalline semiconductor solar cells. *Thin Solid Films*, 361-362:527 – 532.

- [Caballero *et al.*, 2006] Caballero, R., Guillén, C., Gutiérrez, M. T., and Kaufmann, C. A. (2006). CuIn<sub>1-x</sub>Ga<sub>x</sub>Se<sub>2</sub>-based thin-film solar cells by the selenization of sequentially evaporated metallic layers. *Prog. Photovolt.: Res. Appl.*, 14(2):145–153.
- [Cech *et al.*, 1973] Cech, F., Rieder, M., and Vrana, S. (1973). Drysdallite, MoSe<sub>2</sub>, a new mineral. *Neues Jahrb. Mineral., Monatsh.*, 10:433–442.
- [Chakrabarti and Laughlin, 1981] Chakrabarti, D. and Laughlin, D. (1981). The Cu-Se (Copper-Selenium) System. *Bulletin of Alloy Phase Diagrams*, 2(3):305–315.
- [Chatillon, 1993] Chatillon, C. (1993). Critical analysis of the thermodynamic properties of the In-Se gaseous and solid phases. *Journal of Crystal Growth*, 129(1):297 – 311.
- [Che and Ellner, 1992] Che, G. and Ellner, M. (1992). Powder Crystal Data for the High-Temperature Phases Cu<sub>4</sub>In, Cu<sub>9</sub>In<sub>4</sub>(h) and Cu<sub>2</sub>In(h). *Powder Diffraction*, 7(2):107–108.
- [Chernomordik *et al.*, 2016] Chernomordik, B. D., Ketkar, P. M., Hunter, A. K., BÅ©land, A. E., Deng, D. D., and Aydil, E. S. (2016). Microstructure Evolution During Selenization of Cu<sub>2</sub>ZnSnS<sub>4</sub> Colloidal Nanocrystal Coatings. *Chemistry of Materials*, 28(5):1266–1276.
- [Chirilă *et al.*, 2011] Chirilă, A., Buecheler, S., Pianezzi, F., Patrick Bloesch, C. G., Uhl, A. R., Fella, C., Kranz, L., Perrenoud, J., Seyrling, S., Verma, R., Nishiwaki, S., Romanyuk, Y. E., Bilger, G., and Tiwari, A. N. (2011). Highly efficient Cu(In,Ga)Se<sub>2</sub> solar cells grown on flexible polymer films. *Nature Materials*, 10:857–861.
- [Cho *et al.*, 2013] Cho, Y., Kim, D.-W., Ahn, S., Nam, D., Cheong, H., Jeong, G. Y., Gwak, J., and Yun, J. H. (2013). Recombination in Cu(In,Ga)Se<sub>2</sub> thin-film solar cells containing ordered vacancy compound phases. *Thin Solid Films*, 546:358 – 361.
- [Choi and Lee, 2007] Choi, I. and Lee, D. (2007). Preparation of CuIn<sub>1-x</sub>Ga<sub>x</sub>Se<sub>2</sub> films by metalorganic chemical vapor deposition using three precursors. *Thin Solid Films*, 515(11):4778 – 4782.
- [Colombara *et al.*, 2017] Colombara, D., Berner, U., Ciccioli, A., Malaquias, J. C., Bertram, T., Crossay, A., Schöneich, M., Meadows, H. J., Regesch, D., Delsante, S., *et al.* (2017). Deliberate and accidental gas-phase alkali doping of chalcogenide semiconductors: Cu (In, Ga) Se<sub>2</sub>. *Scientific Reports*, 7:43266.
- [Contreras *et al.*, 1997] Contreras, M. A., Egaas, B., Dippo, P., Webb, J., Granata, J., Ramanathan, K., Asher, S., Swartzlander, A., and Noufi, R. (1997). On the role of Na and modifications to Cu(In,Ga)Se<sub>2</sub> absorber materials using thin-MF (M=Na, K, Cs) precursor layers [solar cells]. In *26th IEEE PVSC*, pages 359–362.
- [Contreras *et al.*, 2012] Contreras, M. A., Mansfield, L. M., Egaas, B., Li, J., Romero, M., Noufi, R., Rudiger-Voigt, E., and Mannstadt, W. (2012). Wide bandgap Cu(In,Ga)Se<sub>2</sub> solar cells with improved energy conversion efficiency. *Prog. Photovolt.: Res. Appl.*, 20(7):843–850.

- [Coutts *et al.*, 1986] Coutts, T., Kazmerski, L., and Wagner, S. (1986). *Copper indium diselenide for photovoltaic applications*. Harwood Academic Publishers GmbH.
- [Denks and Genzel, 2007] Denks, I. and Genzel, C. (2007). Enhancement of energy dispersive residual stress analysis by consideration of detector electronic effects. *NUCL INSTRUM METH B*, 262(1):87 – 94.
- [Deslattes *et al.*, 2003] Deslattes, R. D., Kessler, E. G., Indelicato, P., de Billy, L., Lindroth, E., and Anton, J. (2003). X-ray transition energies: new approach to a comprehensive evaluation. *Rev. Mod. Phys.*, 75:35–99.
- [DIAGNE *et al.*, 2016] DIAGNE, O., EHEMBA, A. K., DIALLO, D., WADE, I., SOCE, M. M., and DIENG, M. (2016). Effect of  $[Ga]/[In+Ga]$  Atomic Ratio on Electric Parameters of  $Cu(In,Ga)Se_2$  Thin Film Solar Cells. *International Journal of Scientific Engineering and Technology*, 5:252–255.
- [Dirnstorfer *et al.*, 2000] Dirnstorfer, I., Burkhardt, W., Kriegseis, W., Österreicher, I., Alves, H., Hofmann, D., Ka, O., Polity, A., Meyer, B., and Braunger, D. (2000). Annealing studies on  $CuIn(Ga)Se_2$ : the influence of gallium. *Thin Solid Films*, 361-362:400 – 405.
- [Dittrich *et al.*, 1989] Dittrich, H., Prinz, U., Szot, J., and Schock, H. (1989). Analysis of Reaction Kinetics of Selenized  $CuInSe_2$  and  $CuGaSe_2$  Thin Films. In *Proc. 9th EC Photov. Solar Energy Conf., Freiburg*, page 163.
- [Dullweber *et al.*, 2001] Dullweber, T., Anna, G., Rau, U., and Schock, H. (2001). A new approach to high-efficiency solar cells by band gap grading in  $Cu(In,Ga)Se_2$  chalcopyrite semiconductors. *Solar Energy Materials and Solar Cells*, 67(1):145–150.
- [Dullweber *et al.*, 2000] Dullweber, T., Hanna, G., Shams-Kolahi, W., Schwartzlander, A., Contreras, M., Noufi, R., and Schock, H. (2000). Study of the effect of gallium grading in  $Cu(In,Ga)Se_2$ . *Thin Solid Films*, 361:478 – 481.
- [Eisenbarth *et al.*, 2009] Eisenbarth, T., Unold, T., Caballero, R., Kaufmann, C., Abou-Ras, D., and Schock, H.-W. (2009). Origin of defects in  $CuIn_{1-x}Ga_xSe_2$  solar cells with varied Ga content. *Thin Solid Films*, 517(7):2244 – 2247.
- [Folmer *et al.*, 1985] Folmer, J. C. W., Turner, J. A., Noufi, R., and Cohen, D. (1985). Structural and Solar Conversion Characteristics of the  $(Cu_2Se)_x(In_2Se_3)_{1-x}$  System. *Journal of The Electrochemical Society*, 132(6):1319–1327.
- [Frontier, 2015] Frontier, S. (2015). Corporate Profile. Technical report, Solar Frontier Europe GmbH.
- [Gabor *et al.*, 1994] Gabor, A. M., Tuttle, J. R., Albin, D. S., Contreras, M. A., Noufi, R., and Hermann, A. M. (1994). High-efficiency  $CuIn_xGa_{1-x}Se_2$  solar cells made from  $(In_xGa_{1-x})_2Se_3$  precursor films. *Applied Physics Letters*, 65(2):198–200.

- [Gabor *et al.*, 1996] Gabor, A. M., Tuttle, J. R., Bode, M. H., Franz, A., Tennant, A. L., Contreras, M. A., Noufi, R., Jensen, D. G., and Hermann, A. M. (1996). Band-gap engineering in Cu(In,Ga)Se<sub>2</sub> thin films grown from (In,Ga)<sub>2</sub>Se<sub>3</sub> precursors. *Solar Energy Materials and Solar Cells*, 41:247 – 260.
- [Gambino and Seiden, 1970] Gambino, R. J. and Seiden, P. E. (1970). Correlation of the Superconducting Transition Temperature with an Empirical Pseudopotential Determined from Atomic Spectra. *Phys. Rev. B*, 2:3571–3577.
- [Gartsman *et al.*, 1997] Gartsman, K., Chernyak, L., Lyahovitskaya, V., Cahen, D., Didik, V., Kozlovsky, V., Malkovich, R., Skoryatina, E., and Usacheva, V. (1997). Direct evidence for diffusion and electromigration of Cu in CuInSe<sub>2</sub>. *J APPL PHYS*, 82(9):4282–4285.
- [Genzel *et al.*, 2006] Genzel, C., Denks, I. A., and Klaus, M. (2006). The Materials Science Beamline EDDI for Energy-Dispersive Analysis of Subsurface Residual Stress Gradients. *MSF*, 524-525:193–198.
- [Gödecke *et al.*, 2000a] Gödecke, T., Haalboom, T., and Ernst, F. (2000a). Phase equilibria of Cu-In-Se. I. Stable states and nonequilibrium states of the In<sub>2</sub>Se<sub>3</sub>-Cu<sub>2</sub>Se subsystem. *Zeitschrift für Metallkunde*, 91(8):622–634.
- [Gödecke *et al.*, 2000b] Gödecke, T., Haalboom, T., and Ernst, F. (2000b). Phase equilibria of Cu-In-Se. II. Stable states and nonequilibrium states of the In<sub>2</sub>Se<sub>3</sub>-Cu<sub>2</sub>Se subsystem. *Zeitschrift für Metallkunde*, 91(8):622–634.
- [Gödecke *et al.*, 2000c] Gödecke, T., Haalboom, T., and Ernst, F. (2000c). Phase equilibria of Cu-In-Se. III. Stable states and nonequilibrium states of the In<sub>2</sub>Se<sub>3</sub>-Cu<sub>2</sub>Se subsystem. *Zeitschrift für Metallkunde*, 91(8):622–634.
- [Gödecke *et al.*, 1998] Gödecke, T., Haalboom, T., and Sommer, F. (1998). Stable and Metastable Phase Equilibria of the In-Se and System. *J PHASE EQUILIB*, 19(6):572–576.
- [Greenberg *et al.*, 1973] Greenberg, J., Borjakova, V., and Shevelkov, V. (1973). Thermodynamic properties of In<sub>2</sub>Se. *The Journal of Chemical Thermodynamics*, 5(2):233 – 237.
- [Grigorov *et al.*, 2008] Grigorov, S., Kosevich, V., Kosmachev, S., and Taran, A. (2008). Phase transformation in two-layered In<sub>2</sub>Se<sub>3</sub>-Cu film system. *PROBL AT SCI TECH*, 2:145–148.
- [Guillemoles, 2000] Guillemoles, J. (2000). Stability of Cu(In,Ga)Se<sub>2</sub> solar cells: a thermodynamic approach. *Thin Solid Films*, 361-362(Supplement C):338 – 345.
- [Gupta and Isomura, 1998] Gupta, A. and Isomura, S. (1998). Precursor modification for preparation of CIS films by selenization technique. *SOL ENERG MAT SOL C*, 53(3):385.
- [Gütay and Bauer, 2007] Gütay, L. and Bauer, G. (2007). Spectrally resolved photoluminescence studies on Cu(In,Ga)Se<sub>2</sub> solar cells with lateral submicron resolution. *Thin Solid Films*, 515(15):6212 – 6216.

- [Gütay and Bauer, 2009] Gütay, L. and Bauer, G. H. (2009). Non-uniformities of optoelectronic properties in Cu(In,Ga)Se<sub>2</sub> thin films and their influence on cell performance studied with confocal photoluminescence. In *34th IEEE PVSC*, pages 874–877.
- [Haalboom, 1998] Haalboom, T. (1998). *Mikrostruktur und Konstitution von Kupfer-Indium-Selen-Mischkristallen für Solarzellen*. PhD thesis, Universität Stuttgart.
- [Haarstrich *et al.*, 2011] Haarstrich, J., Metzner, H., Oertel, M., Ronning, C., Rissom, T., Kaufmann, C., Unold, T., Schock, H., Windeln, J., Mannstadt, W., and Rudigier-Voigt, E. (2011). Increased homogeneity and open-circuit voltage of Cu(In,Ga)Se<sub>2</sub> solar cells due to higher deposition temperature. *SOL ENERG MAT SOL C*, 95(3):1028 – 1030.
- [Hack, 2003] Hack, C. (2003). *Homoepitaxie der Verbindungshalbleiter CuInS<sub>2</sub> und CuInSe<sub>2</sub>*. PhD thesis, Friedrich-Alexander-Universität.
- [Hänel, 2008] Hänel, T. (2008). Spannungs- und intensitätsabhängige spektrale Empfindlichkeit von poly-Si Dünnschichtsolarellen. Diplomarbeit, HTW Berlin.
- [Hanket *et al.*, 2007] Hanket, G. M., Shafarman, W. N., McCandless, B. E., and Birkmire, R. W. (2007). Incongruent reaction of Cu-(InGa) intermetallic precursors in H<sub>2</sub>Se and H<sub>2</sub>S. *J APPL PHYS*, 102(7):074922.
- [Hanna *et al.*, 2001] Hanna, G., Jasenek, A., Rau, U., and Schock, H. (2001). Influence of the Ga-content on the bulk defect densities of Cu(In,Ga)Se<sub>2</sub>. *Thin Solid Films*, 387(1):71–73.
- [Heath *et al.*, 2002] Heath, J. T., Cohen, J. D., Shafarman, W. N., Liao, D. X., and Rockett, A. A. (2002). Effect of Ga content on defect states in CuIn<sub>1-x</sub>Ga<sub>x</sub>Se<sub>2</sub> photovoltaic devices. *Applied Physics Letters*, 80(24):4540–4542.
- [Hendriks *et al.*, 1999] Hendriks, C. L., van Vliet, L., Rieger, B., and van Ginkel, M. (1999). DIPimage: a scientific image processing toolbox for Matlab. *Cent. Eur. J. Phys.*
- [Henke *et al.*, 1993] Henke, B., Gullikson, E., and Davis, J. (1993). X-Ray Interactions: Photoabsorption, Scattering, Transmission, and Reflection at E = 50-30,000 eV, Z = 1-92. *Atomic Data and Nuclear Data Tables*, 54(2):181 – 342.
- [Hergert *et al.*, 2005] Hergert, F., Hock, R., Weber, A., Purwins, M., Palm, J., and Probst, V. (2005). In situ investigation of the formation of Cu(In,Ga)Se<sub>2</sub> from selenised metallic precursors by X-ray diffraction - The impact of Gallium, Sodium and Selenium excess. *J. Phys. Chem. Solids*, 66(11):1903 – 1907.
- [Hetzer *et al.*, 2005] Hetzer, M. J., Strzhemechny, Y. M., Gao, M., Contreras, M. A., Zunger, A., and Brillson, L. J. (2005). Direct observation of copper depletion and potential changes at copper indium gallium diselenide grain boundaries. *Applied Physics Letters*, 86(16):162105.
- [Heyding and Murray, 1976] Heyding, R. D. and Murray, R. M. (1976). The crystal structures of Cu<sub>1.8</sub>Se, Cu<sub>3</sub>Se<sub>2</sub>, α- and γCuSe, CuSe<sub>2</sub>, and CuSe<sub>2</sub>II. *CAN J CHEM*, 54(6):841–848.

- [Hirai *et al.*, 2014] Hirai, Y., Kurokawa, Y., and Yamada, A. (2014). Numerical study of Cu(In,Ga)Se<sub>2</sub> solar cell performance toward 23% conversion efficiency. *JPN J APPL PHYS*, 53(1):012301.
- [Hogg *et al.*, 1973] Hogg, J. H. C., Sutherland, H. H., and Williams, D. J. (1973). The crystal structure of tetraindium triselenide. *Acta Crystallogr.*, 29(8):1590–1593.
- [Hölzing, 2013] Hölzing, A. (2013). *Untersuchung des Kristallisationsmechanismus von Cu(In,Ga)(S,Se)<sub>2</sub> Dünnschichtsolarzellenmaterialien durch in-situ Röntgenbeugung während der Reaktion von Metallschichten mit Schwefel und Selen*. PhD thesis, Friedrich-Alexander-Universität.
- [Hölzing *et al.*, 2011] Hölzing, A., Schurr, R., Jost, S., Palm, J., Deseler, K., Wellmann, P., and Hock, R. (2011). The influence of gallium on phase transitions during the crystallisation of thin film absorber materials Cu(In,Ga)(S,Se)<sub>2</sub> investigated by in-situ X-ray diffraction. *Thin Solid Films*, 519:7197–7200.
- [Hsieh *et al.*, 2011] Hsieh, T.-P., Chuang, C.-C., Wu, C.-S., Chang, J.-C., Guo, J.-W., and Chen, W.-C. (2011). Effects of residual copper selenide on CuInGaSe<sub>2</sub> solar cells. *Solid-State Electronics*, 56(1):175 – 178.
- [Hsu *et al.*, 2012] Hsu, H. R., Hsu, S. C., and sheng Liu, Y. (2012). Improvement of Voc and Jsc in CuInGaSe<sub>2</sub> solar cells using a novel sandwiched CuGa/CuInGa/In precursor structure. *Applied Physics Letters*, 100(23):233903.
- [Huang, 2008] Huang, C.-H. (2008). Effects of Ga content on Cu(In,Ga)Se<sub>2</sub> solar cells studied by numerical modeling. *J. Phys. Chem. Solids*, 69(2):330 – 334.
- [Huang *et al.*, 2017] Huang, Y., Han, A., Wang, X., Liu, X., Liu, Z., and Meng, F. (2017). Role of the intermediate phases InSe and Cu<sub>9</sub>(In<sub>1-x</sub>Ga<sub>x</sub>)<sub>4</sub> in fabricating Cu(In<sub>1-x</sub>Ga<sub>x</sub>)Se<sub>2</sub> films by selenization of Cu-In-Ga precursors. *JPN J APPL PHYS*, 56(1):015503.
- [Hume-Rothery *et al.*, 1951] Hume-Rothery, W., Betterton, J., and Reynolds, J. (1951). The Equilibrium Diagram of the System Copper-Indium in the Region 25-35 At.-% Indium. *J Inst Met*, 80:637–640.
- [Hunklinger, 2009] Hunklinger, S. (2009). *Festkörperphysik*. Oldenbourg Verlag.
- [Ider *et al.*, 2014] Ider, M., Pankajavalli, R., Zhuang, W., Shen, J., and Anderson, T. (2014). Thermochemistry of the Cu<sub>2</sub>Se-In<sub>2</sub>Se<sub>3</sub> system. *J. Alloy. Compd.*, 604:363 – 372.
- [Ishizuka *et al.*, 2005] Ishizuka, S., Sakurai, K., Yamada, A., Shibata, H., Matsubara, K., Yonemura, M., Nakamura, S., Nakanishi, H., Kojima, T., and Niki, S. (2005). Progress in the Efficiency of Wide-Gap Cu(In<sub>1-x</sub>Ga<sub>x</sub>)Se<sub>2</sub> Solar Cells Using CIGSe Layers Grown in Water Vapor. *JPN J APPL PHYS*, 44(5L):L679.

- [Jäger-Waldau *et al.*, 1998] Jäger-Waldau, A., Meyer, N., Weiss, T., Fiechter, S., Lux-Steiner, M., Tempelhoff, K., and Richter, W. (1998). A New Approach to Grow Polycrystalline CuGaSe<sub>2</sub> Thin Films: Chemical Vapor Deposition with I<sub>2</sub> as Transport Agent. *JPN J APPL PHYS*, 37(3S):1617.
- [Jellinek and Hahn, 1961] Jellinek, F. and Hahn, H. (1961). Zur Polytypie des Galliummonoselenids, GaSe. *Zeitschrift für Naturforschung B*, 16(11):713–715.
- [Jungbluth *et al.*, 2008] Jungbluth, N., Tuchschnid, M., and de Wild-Scholten, M. (2008). Life Cycle Assessment of Photovoltaics: Update ofecoinvent data V2.0. *ESU-services Ltd.*
- [Kaelin *et al.*, 2003] Kaelin, M., Rudmann, D., Kurdesau, F., Meyer, T., Zogg, H., and Tiwari, A. (2003). CIS and CIGS layers from selenized nanoparticle precursors. *Thin Solid Films*, 431-432:58 – 62.
- [Kapadia *et al.*, 2013] Kapadia, R., Yu, Z., Wang, H.-H., Zheng, M., Battaglia, C., Hettick, M., Kiriya, D., Takei, K., Lobaccaro, P., Beeman, J., Ager, J., Maboudian, R., Chrzan, D., and Javey, A. (2013). A direct thin-film path towards low-cost large-area III-V photovoltaics. *Sci. Rep.*, 3:2275.
- [Kessler *et al.*, 1993] Kessler, J., Schmid, D., Schaffler, R., Schock, H. W., and Menezes, S. (1993). Electro-optical and photoelectrochemical studies of CuIn<sub>3</sub>Se<sub>5</sub> chalcopyrite films. In *23th IEEE PVSC*, pages 549–554.
- [Kim *et al.*, 2012a] Kim, K., Hanket, G. M., Huynh, T., and Shafarman, W. N. (2012a). Three-step H<sub>2</sub>Se/Ar/H<sub>2</sub>S reaction of Cu-In-Ga precursors for controlled composition and adhesion of Cu(In,Ga)(Se,S)<sub>2</sub> thin films. *J APPL PHYS*, 111(8):083710.
- [Kim *et al.*, 2012b] Kim, W. K., Shen, J., Chu, M., Jung, J. H., and Anderson, T. J. (2012b). Prediction of the CuGaIn Ternary Phase Diagram. *J NANO-ELECTRON OPTOE*, 7(5):425–429.
- [Kistaiah and Murthy, 1985] Kistaiah, P. and Murthy, K. (1985). Temperature behaviour of the tetragonal distortion and thermal expansion of Cu-III-VI<sub>2</sub> chalcopyrite semiconductors. *Journal of the Less Common Metals*, 105(1):37 – 54.
- [Kittel, 2006] Kittel, C. (2006). *Einführung in die Festkörperphysik*. Oldenbourg.
- [K.K., 20] K.K., S. F. (2017-12-20). Solar Frontier Achieves World Record Thin-Film Solar Cell Efficiency of 22.9%. Press release.
- [Kleinfeld and Wiemhöfer, 1988] Kleinfeld, M. and Wiemhöfer, H.-D. (1988). Chemical diffusion coefficients and stability of CuInS<sub>2</sub> and CuInSe<sub>2</sub> from polarization measurements with point electrodes. *Solid State Ionics*, 28:1111 – 1115.
- [Knight, 1992] Knight, K. (1992). The crystal structures of CuInSe<sub>2</sub> and CuInTe<sub>2</sub>. *MATER RES BULL*, 27(2):161 – 167.

- [Kojima *et al.*, 1968] Kojima, H., Whiteway, S., and Masson, C. (1968). Melting points of inorganic fluorides. *Can. J. Chem.*, 46:2968–2971.
- [Koo *et al.*, 2013] Koo, J., Jeon, S., Oh, M., il Cho, H., Son, C., and Kim, W. K. (2013). Optimization of Se layer thickness in Mo/CuGa/In/Se precursor for the formation of Cu(InGa)Se<sub>2</sub> by rapid thermal annealing. *Thin Solid Films*, 535:148 – 153.
- [Koo *et al.*, 2016] Koo, J., Kwon, S., Roh, Y.-S., Lee, S.-J., Jung, K.-Y., Shafarman, W. N., Park, J.-H., Kim, D. H., Myoung, J.-M., and Kim, W. K. (2016). Effect of reaction temperature and time during two-step selenization and sulfurization of Se-Coated CuGa/In precursors. *Electronic Materials Letters*, 12(4):484–493.
- [Kulkarni *et al.*, 2009] Kulkarni, S. S., Koishiyev, G. T., Moutinho, H., and Dhere, N. G. (2009). Preparation and characterization of  $CuIn_{1-x}Ga_xSe_{2-y}S_y$  thin film solar cells by rapid thermal processing. *Thin Solid Films*, 517(7):2121 – 2124.
- [Kumar and Reddy, 1997] Kumar, A. P. and Reddy, K. (1997). Lateral self-diffusion of selenium in CuInSe<sub>2</sub> thin films. *Thin Solid Films*, 304(1):365 – 370.
- [Larose and Pelton, 1991] Larose, S. and Pelton, A. (1991). The In-Na (Indium-Sodium) System. *J. Phase Equilib.*, 12:371–376.
- [Lavrenko *et al.*, 2015] Lavrenko, T., Ott, T., and Walter, T. (2015). Impact of sulfur and gallium gradients on the performance of thin film Cu(In,Ga)(Se,S)<sub>2</sub> solar cells. *Thin Solid Films*, 582:51 – 55.
- [Lehmann, 2010] Lehmann, J. (2010). *Oberflächenpräparation zur Untersuchung von elektronischen Korngrenzeigenschaften in Cu(In,Ga)Se<sub>2</sub>*. PhD thesis, Diplomarbeit, Freie Universität Berlin.
- [Lehmann *et al.*, 2014] Lehmann, J., Lehmann, S., Laueremann, I., Rissom, T., Kaufmann, C. A., Lux-Steiner, M. C., Bär, M., and Sadewasser, S. (2014). Reliable wet-chemical cleaning of natively oxidized high-efficiency Cu(In,Ga)Se<sub>2</sub> thin-film solar cell absorbers. *J APPL PHYS*, 116(23):233502.
- [Lei *et al.*, 2006] Lei, C. H., Rockett, A. A., Robertson, I. M., Papathanasiou, N., and Siebentritt, S. (2006). Interface reactions and Kirkendall voids in metal organic vapor-phase epitaxy grown Cu(In,Ga)Se<sub>2</sub> thin films on GaAs. *J APPL PHYS*, 100(11):114915.
- [Levenberg, 1944] Levenberg, K. (1944). A method for the solution of certain non-linear problems in least squares. *Quarterly of applied mathematics*, 2(2):164–168.
- [Lewerenz and Jungblut, 1995] Lewerenz, H.-J. and Jungblut, H. (1995). *Photovoltaik*. Springer-Verlag Berlin Heidelberg.
- [Lin *et al.*, 1987] Lin, Z., Xu, F., and Weaver, J. H. (1987). Surface segregation at metal-dash-III-V-compound-semiconductor interfaces. *Phys. Rev. B*, 36:5777–5783.

- [Liu *et al.*, 2014] Liu, J., ming Zhuang, D., jie Cao, M., long Li, X., Xie, M., and wei Xu, D. (2014). Cu(In,Ga)Se<sub>2</sub>-based solar cells prepared from Se-containing precursors . *Vacuum*, 102:26 – 30.
- [Logvinenko *et al.*, 1975] Logvinenko, A., Spitkovskii, I., and Stakhira, I. (1975). In<sub>x</sub>-Se<sub>y</sub> compounds. *Solid State*, 16:1774. English Transl. from Fiz. Tverd. Tela 16: 2743; Sov. Phys. 1974.
- [Ludwig, 2011] Ludwig, C. D. (2011). *Optimising thin-film solar cells by computer simulations*. PhD thesis, Johannes Gutenberg-Universität, Mainz.
- [Ludwig *et al.*, 2010] Ludwig, C. D. R., Gruhn, T., Felser, C., Schilling, T., Windeln, J., and Kratzer, P. (2010). Indium-Gallium Segregation in CuIn<sub>x</sub>Ga<sub>1-x</sub>Se<sub>2</sub>: An Ab Initio-Based Monte Carlo Study. *Phys. Rev. Lett.*, 105:025702.
- [Lundberg *et al.*, 2003] Lundberg, O., Lu, J., Rockett, A., Edoff, M., and Stolt, L. (2003). Diffusion of indium and gallium in Cu(In,Ga)Se<sub>2</sub> thin film solar cells. *J PHYS CHEM SOLIDS*, 64(9-10):1499–1504.
- [Lyubomirsky *et al.*, 1997] Lyubomirsky, I., Rabinal, M. K., and Cahen, D. (1997). Room-temperature detection of mobile impurities in compound semiconductors by transient ion drift. *J APPL PHYS*, 81(10):6684–6691.
- [Madelung *et al.*, 1998] Madelung, O., Rössler, U., and Schulz, M. (1998). *Non-Tetrahedrally Bonded Elements and Binary Compounds I*, volume 41C. Springer-Verlag Berlin Heidelberg.
- [Mainz, 2008] Mainz, R. (2008). *In-situ Analyse und Wachstum photovoltaischer Absorber mit Bandlückengradienten*. PhD thesis, Freien Universität Berlin.
- [Mainz and Klenk, 2011] Mainz, R. and Klenk, R. (2011). In situ analysis of elemental depth distributions in thin films by combined evaluation of synchrotron x-ray fluorescence and diffraction. *J APPL PHYS*, 109(12):123515.
- [Mainz *et al.*, 2015a] Mainz, R., Rodriguez-Alvarez, H., Klaus, M., Thomas, D., Lauche, J., Weber, A., Heinemann, M. D., Brunken, S., Greiner, D., Kaufmann, C. A., Unold, T., Schock, H.-W., and Genzel, C. (2015a). Sudden stress relaxation in compound semiconductor thin films triggered by secondary phase segregation. *PHYS REV B*, 92(15).
- [Mainz *et al.*, 2015b] Mainz, R., Weber, A., Rodriguez-Alvarez, H., Levchenko, S., Klaus, M., Pistor, P., Klenk, R., and Schock, H.-W. (2015b). Time-resolved investigation of Cu(In,Ga)Se<sub>2</sub> growth and Ga gradient formation during fast selenisation of metallic precursors. *Prog. Photovolt.: Res. Appl.*, 23(9):1131–1143.
- [Mandel *et al.*, 1977] Mandel, L., Tomlinson, R. D., and Hampshire, M. J. (1977). Crystal data for CuGaSe<sub>2</sub>. *Journal of Applied Crystallography*, 10(2):130–131.

- [Marín *et al.*, 1998] Marín, G., Tauleigne, S., Wasim, S., Guevara, R., Delgado, J., Rincón, C., Mora, A., and Sánchez Pérez, G. (1998). X-ray powder diffraction and optical characterization of the  $\text{Cu}(\text{In}_{1-x}\text{Ga}_x)_3\text{Se}_5$  semiconducting system. *MATER RES BULL*, 33(7):1057–1068.
- [Marquardt, 1963] Marquardt, D. W. (1963). An Algorithm for Least-Squares Estimation of Nonlinear Parameters. *J SOC IND APPL MATH*, 11(2):431–441.
- [Marudachalam *et al.*, 1994] Marudachalam, M., Birkmire, R., Schultz, J. M., and Yokimcus, T. (1994). Characterization of Cu-In-Ga precursors used to form  $\text{Cu}(\text{In,Ga})\text{Se}_2$  films. In *Proceedings of 1st WCPEC*, volume 1, pages 234–237.
- [Marudachalam *et al.*, 1997] Marudachalam, M., Birkmire, R. W., Hichri, H., Schultz, J. M., Swartzlander, A., and Al-Jassim, M. M. (1997). Phases, morphology, and diffusion in  $\text{CuIn}_x\text{Ga}_{1-x}\text{Se}_2$  thin films. *J APPL PHYS*, 82(6):2896–2905.
- [Marudachalam *et al.*, 1995] Marudachalam, M., Hichri, H., Klenk, R., Birkmire, R. W., Sharfman, W. N., and Schultz, J. M. (1995). Preparation of homogeneous  $\text{Cu}(\text{In,Ga})\text{Se}_2$  films by selenization of metal precursors in  $\text{H}_2\text{Se}$  atmosphere. *APPL PHYS LETT*, 67(26):3978.
- [Marudachalam *et al.*, 1996] Marudachalam, M., Hichri, I., Birkmire, R. W., Schultz, J. M., Swartzlander, A. B., and Al-Jassim, M. M. (1996). Diffusion of In and Ga in selenized Cu-In and Cu-Ga precursors. *25th IEEE PVSC*, page 805.
- [Matsushita and Takizawa, 1997] Matsushita, H. and Takizawa, T. (1997). Phase diagram of the CuIn-2Se system for  $\text{CuInSe}_2$  crystal growth by controlling Se contents. *Journal of Crystal Growth*, 179(3):503 – 509.
- [McMaster *et al.*, 1969] McMaster, W., Del Grande, N., Mallett, J., and Hubbell, J. (1969). *Compilation of X-Ray cross sections. Section III*. Academic Press.
- [Merdes *et al.*, 2014] Merdes, S., Malinen, V., Ziem, F., Lauermann, I., Schüle, M., Stober, F., Hergert, F., Papathanasiou, N., and Schlattmann, R. (2014). Zn(O,S) buffer prepared by atomic layer deposition for sequentially grown  $\text{Cu}(\text{In,Ga})(\text{Se,S})_2$  solar cells and modules. *Solar Energy Materials and Solar Cells*, 126:120 – 124.
- [Merdes *et al.*, 2015] Merdes, S., Ziem, F., Lavrenko, T., Walter, T., Lauermann, I., Klingsporn, M., Schmidt, S., Hergert, F., and Schlattmann, R. (2015). Above 16% efficient sequentially grown  $\text{Cu}(\text{In,Ga})(\text{Se,S})_2$ -based solar cells with atomic layer deposited Zn(O,S) buffers. *Prog. Photovolt.: Res. Appl.*, 23(11):1493–1500.
- [Merino *et al.*, 2000] Merino, J., Mahanty, S., León, M., Diaz, R., Rueda, F., and de Vidales, J. M. (2000). Structural characterization of  $\text{CuIn}_2\text{Se}_{3.5}$ ,  $\text{CuIn}_3\text{Se}_5$  and  $\text{CuIn}_5\text{Se}_8$  compounds. *Thin Solid Films*, 361:70 – 73.
- [Mikkelsen, 1981] Mikkelsen, J. C. (1981). Ternary phase relations of the chalcopyrite compound  $\text{CuGaSe}_2$ . *Journal of Electronic Materials*, 10(3):541–558.

- [Moon *et al.*, 2012] Moon, D. G., Yun, J. H., Gwak, J., Ahn, S., Cho, A., Shin, K., Yoon, K., and Ahn, S. (2012). Cu(In,Ga)Se<sub>2</sub> thin films without Ga segregation prepared by the single-step selenization of sputter deposited Cu-In-Ga-Se precursor layers. *Energy & Environmental Science*, 5(12):9914–9921.
- [Mueller *et al.*, 2016] Mueller, B., Opananont, B., Haug, V., Hergert, F., Zweigart, S., and Herr, U. (2016). Influence of selenium amount on the structural and electronic properties of Cu(In,Ga)Se<sub>2</sub> thin films and solar cells formed by the stacked elemental layer process. *Thin Solid Films*, 608:62 – 70.
- [Murray and Heyding, 1975] Murray, R. M. and Heyding, R. D. (1975). The Copper-Selenium System at Temperatures to 850 K and Pressures To 50 Kbar. *CAN J CHEM*, 53(6):878–887.
- [Muschinsky and Pawlenko, 1969] Muschinsky, W. P. and Pawlenko, N. M. (1969). Untersuchung des Systems GaSe-InSe. *Krist. Techn.*, 4(2):K5–K7.
- [Muzzillo *et al.*, 2015] Muzzillo, C. P., Campbell, C. E., and Anderson, T. J. (2015). Cu-Ga-In thermodynamics: experimental study, modeling, and implications for photovoltaics. *J Mater Sci*.
- [Nečas and Klapetek, 2012] Nečas, D. and Klapetek, P. (2012). Gwyddion: an open-source software for SPM data analysis. *Cent. Eur. J. Phys.*, 10:181–188.
- [Negami *et al.*, 1995] Negami, T., Kohara, N., Nishitani, M., Wada, T., and Hirao, T. (1995). Preparation and characterization of Cu(In<sub>1-x</sub>Ga<sub>x</sub>)<sub>3</sub>Se<sub>5</sub> thin films. *Applied Physics Letters*, 67(6):825–827.
- [Neisser, 2002] Neisser, A. (2002). *Gallium as an Isovalent Substitution in CuInS<sub>2</sub> Absorber Layers for Photovoltaic Applications*. PhD thesis, FU Berlin.
- [Neisser *et al.*, 2003] Neisser, A., Klenk, R., and Lux-Steiner, M. C. (2003). Diffusion of Ga and In in Sequentially Prepared Cu(In,Ga)S<sub>2</sub> Thin Films for Photovoltaic Applications. *MRS Proceedings*, 763.
- [Nishimura *et al.*, 2017] Nishimura, T., Toki, S., Sugiura, H., Nakada, K., and Yamada, A. (2017). Effect of Cu-deficient layer formation in Cu(In,Ga)Se<sub>2</sub> solar-cell performance. *Prog. Photovolt.: Res. Appl.*, 0(0).
- [Noufi *et al.*, 1984] Noufi, R., Axton, R., Herrington, C., and Deb, S. K. (1984). Electronic properties versus composition of thin films of CuInSe<sub>2</sub>. *APPL PHYS LETT*, 45(6):668–670.
- [Ogorelec and Čelustka, 1966] Ogorelec, Z. and Čelustka, B. (1966). Coefficient of linear expansion in different solid phases of cuprous selenide. *Acta Metallurgica*, 14(5):687.
- [Ohtani *et al.*, 1998] Ohtani, T., Tachibana, Y., Ogura, J., Miyake, T., Okada, Y., and Yokota, Y. (1998). Physical properties and phase transitions of  $\beta$  Cu<sub>2-x</sub>Se (0.20 ≤ x ≤ 0.25). *J. Alloy. Compd.*, 279(2):136 – 141.

- [Oikkonen *et al.*, 2012] Oikkonen, L. E., Ganchenkova, M. G., Seitsonen, A. P., and Nieminen, R. M. (2012). Redirecting focus in CuInSe<sub>2</sub> research towards selenium-related defects. *Phys. Rev. B*, 86:165115.
- [Oikkonen *et al.*, 2013] Oikkonen, L. E., Ganchenkova, M. G., Seitsonen, A. P., and Nieminen, R. M. (2013). Mass transport in CuInSe<sub>2</sub> from first principles. *J APPL PHYS*, 113(13):133510.
- [Oliveria *et al.*, 1988] Oliveria, M., McMullan, R., and Wuensch, B. (1988). Single crystal neutron diffraction analysis of the cation distribution in the high-temperature phases  $\alpha$ -Cu<sub>2-x</sub>S,  $\alpha$ -Cu<sub>2-x</sub>Se, and  $\alpha$ -Ag<sub>2</sub>Se. *Solid State Ionics*, 28:1332 – 1337.
- [Orlova *et al.*, 2002] Orlova, N., Bodnar, I., Kushner, T., and Kudritskaya, E. (2002). Crystal Growth and Properties of the Compounds CuGa<sub>3</sub>Se<sub>5</sub> and CuIn<sub>3</sub>Se<sub>5</sub>. *Crystal Research and Technology*, 37(6):540–550.
- [Otsu, 1979] Otsu, N. (1979). A Threshold Selection Method from Gray-Level Histograms. *IEEE Transactions on Systems, Man, and Cybernetics*, SMC-9(1):62–66.
- [Palm *et al.*, 2015] Palm, J., Karg, F., Schneider, H., Kushiya, K., Stolt, L., Tiwari, A., Niemi, E., Beck, M., Eberspacher, C., Wohlfart, P., *et al.* (2015). White paper for CIGS thin film solar cell technology. <http://cigs-pv.net/>.
- [Palm *et al.*, 2004] Palm, J., Probst, V., Stetter, W., Toelle, R., Visbeck, S., Calwer, H., Niesen, T., Vogt, H., Hernández, O., Wendl, M., and Karg, F. (2004). CIGSSe thin film PV modules: from fundamental investigations to advanced performance and stability. *Thin Solid Films*, 451-452:544 – 551.
- [Pamplin and Feigelson, 1979] Pamplin, B. and Feigelson, R. (1979). Spray pyrolysis of complex sphalerite materials. *MATER RES BULL*, 14(1):1 – 4.
- [Pearson, 2013] Pearson, W. B. (2013). *A handbook of lattice spacings and structures of metals and alloys: International series of monographs on metal physics and physical metallurgy*, volume 4. Elsevier.
- [Persson *et al.*, 2005] Persson, C., Zhao, Y.-J., Lany, S., and Zunger, A. (2005). n-type doping of CuInSe<sub>2</sub> and CuGaSe<sub>2</sub>. *Phys. Rev. B*, 72:035211.
- [Popović *et al.*, 1979] Popović, S., Tonejc, A., Gržeta-Plenković, B., Čelustka, B., and Trojko, R. (1979). Revised and new crystal data for indium selenides. *Journal of Applied Crystallography*, 12(4):416–420.
- [Predel, 1994] Predel, B. (1994). Cu-Ga (Copper-Gallium): Datasheet from Landolt-Börnstein - Group IV Physical Chemistry · Volume 5D: “Cr-Cs – Cu-Zr”.

- [Probst *et al.*, 2001] Probst, V., Stetter, W., Riedl, W., Vogt, H., Wendl, M., Calwer, H., Zweigart, S., Ufert, K.-D., Freienstein, B., Cerva, H., and Karg, F. (2001). Rapid CIS-process for high efficiency PV-modules: development towards large area processing. *Thin Solid Films*, 387(1-2):262 – 267.
- [Purwins, 2010] Purwins, M. (2010). *Phasenbildung und Reaktionskinetik bei der Herstellung des Chalkopyrit-Solarzellenmaterials Cu(In,Ga)(Se,S)<sub>2</sub>*. PhD thesis, Friedrich-Alexander-Universität Erlangen-Nürnberg (FAU).
- [Purwins *et al.*, 2007] Purwins, M., Enderle, R., Schmid, M., Berwian, P., Müller, G., Hergert, F., Jost, S., and Hock, R. (2007). Phase relations in the ternary Cu-Ga-In system. *Thin Solid Films*, 515:5895–5898.
- [Rau, 1974] Rau, H. (1974). Vapour composition and critical constants of selenium. *The Journal of Chemical Thermodynamics*, 6(6):525 – 535.
- [Rau and Werner, 2004] Rau, U. and Werner, J. H. (2004). Radiative efficiency limits of solar cells with lateral band-gap fluctuations. *Applied Physics Letters*, 84(19):3735–3737.
- [Rockett *et al.*, 1989] Rockett, A., Lommasson, T., Campos, P., Yang, L., and Talieh, H. (1989). Growth of CuInSe<sub>2</sub> by two magnetron sputtering techniques. *Thin Solid Films*, 171(1):109–123.
- [Rodriguez-Alvarez *et al.*, 2014] Rodriguez-Alvarez, H., Mainz, R., and Sadewasser, S. (2014). A one-dimensional Fickian model to predict the Ga depth profiles in three-stage Cu(In,Ga)Se<sub>2</sub>. *J APPL PHYS*, 115(20):204913.
- [Rodriguez-Alvarez *et al.*, 2008] Rodriguez-Alvarez, H., tschau, I. K., and Schock, H. (2008). Pressure-dependent real-time investigations on the rapid thermal sulfurization of Cu-In thin films. *Journal of Crystal and Growth*, 310:3638–3644.
- [Rodriguez-Alvarez *et al.*, 2013] Rodriguez-Alvarez, H., Weber, A., Lauche, J., Kaufmann, C. A., Rissom, T., Greiner, D., Klaus, M., Unold, T., Genzel, C., Schock, H.-W., and Mainz, R. (2013). Formation of CuInSe<sub>2</sub> and CuGaSe<sub>2</sub> Thin-Films Deposited by Three-Stage Thermal Co-Evaporation: A Real-Time X-Ray Diffraction and Fluorescence Study. *Advanced Energy Materials*, 3(10):1381–1387.
- [Sanli *et al.*, 2017] Sanli, E. S., Ramasse, Q. M., Mainz, R., Weber, A., Abou-Ras, D., Sigle, W., and van Aken, P. A. (2017). Evidence for Cu<sub>2-x</sub>Se platelets at grain boundaries and within grains in Cu(In,Ga)Se<sub>2</sub> thin films. *Applied Physics Letters*, 111(3):032103.
- [Scheer and Schock, 2011] Scheer, R. and Schock, H.-W. (2011). *Chalcogenide Photovoltaics*. WILEY-VCH.
- [Schmid *et al.*, 1993] Schmid, D., Ruckh, M., Grunwald, F., and Schock, H. W. (1993). Chalcopyrite/defect chalcopyrite heterojunctions on the basis of CuInSe<sub>2</sub>. *J APPL PHYS*, 73(6):2902–2909.

- [Schmidt *et al.*, 2017] Schmidt, S. S., Wolf, C., Rodriguez-Alvarez, H., Bäcker, J.-P., Kaufmann, C. A., Merdes, S., Ziem, F., Hartig, M., Cinque, S., Dorbandt, I., Köble, C., Abou-Ras, D., Mainz, R., and Schlattmann, R. (2017). Adjusting the Ga grading during fast atmospheric processing of Cu(In,Ga)Se<sub>2</sub> solar cell absorber layers using elemental selenium vapor. *Prog. Photovolt.: Res. Appl.*, 25(5):341–357.
- [Schroeder *et al.*, 1996] Schroeder, D. J., Berry, G. D., and Rockett, A. A. (1996). Gallium diffusion and diffusivity in CuInSe<sub>2</sub> epitaxial layers. *Applied Physics Letters*, 69(26):4068.
- [Shay and Wernick, 1975] Shay, J. and Wernick, J. (1975). Ternary chalcopyrite semiconductors: Growth, electronic structure and applications.
- [Shimizu *et al.*, 1999] Shimizu, K., Brown, G., Habazaki, H., Kobayashi, K., Skeldon, P., Thompson, G., and Wood, G. (1999). Influence of surface roughness on the depth resolution of GDOES depth profiling analysis. *Surface and interface analysis*, 27(3):153–156.
- [Shockley and Queisser, 1961] Shockley, W. and Queisser, H. J. (1961). Detailed Balance Limit of Efficiency of  $p - n$  Junction Solar Cells. *J APPL PHYS*, 32(3):510–519.
- [Siebentritt, 2011] Siebentritt, S. (2011). What limits the efficiency of chalcopyrite solar cells? . *Solar Energy Materials and Solar Cells*, 95(6):1471 – 1476.
- [Smith and Schneider, 1964] Smith, J. and Schneider, V. (1964). Anisotropic thermal expansion of indium. *Journal of the Less Common Metals*, 7(1):17 – 22.
- [Soltz *et al.*, 1988] Soltz, D., Dagan, G., and Cahen, D. (1988). Ionic mobility and electronic junction movement in CuInSe<sub>2</sub>. *Solid State Ionics*, 28:1105 – 1110.
- [Song *et al.*, 2003] Song, H. K., Jeong, J. K., Kim, H. J., Kim, S. K., and Yoon, K. H. (2003). Fabrication of CuIn<sub>1-x</sub>Ga<sub>x</sub>Se<sub>2</sub> thin film solar cells by sputtering and selenization process. *Thin Solid Films*, 435(1):186–192.
- [Song *et al.*, 2004] Song, J., Li, S. S., Huang, C., Crisalle, O., and Anderson, T. (2004). Device modeling and simulation of the performance of Cu(In<sub>1-x</sub>Ga<sub>x</sub>)Se<sub>2</sub> solar cells. *Solid-State Electronics*, 48(1):73 – 79.
- [Song *et al.*, 2018] Song, Y. J., Kang, J.-Y., Baek, G. Y., Bae, J. A., Yang, S. H., and Jeon, C.-W. (2018). Two-step selenization using nozzle free Se shower for Cu(In,Ga)Se<sub>2</sub> thin film solar cell. *Prog. Photovolt.: Res. Appl.*, 26(3):223–233.
- [Stange *et al.*, 2016] Stange, H., Brunken, S., Greiner, D., Heinemann, M.-D., Kaufmann, C. A., Schmidt, S. S., Bäcker, J.-P., Klaus, M., Genzel, C., and Mainz, R. (2016). Diffusion-induced grain boundary migration as mechanism for grain growth and defect annihilation in chalcopyrite thin films. *Acta Materialia*, 111:377 – 384.
- [Stokhuyzen *et al.*, 1974] Stokhuyzen, R., Brandon, J. K., Chieh, P. C., and Pearson, W. B. (1974). Copper-gallium  $\gamma_1$ -Cu<sub>9</sub>Ga<sub>4</sub>. *Acta Crystallogr.*, 30(12):2910–2911.

- [Stull, 1947] Stull, D. R. (1947). Vapor Pressure of Pure Substances. Organic and Inorganic Compounds. *Industrial & Engineering Chemistry*, 39(4):517–540.
- [Subramanian and Laughlin, 1992] Subramanian, P. and Laughlin, D. (1992). *Binary Alloy Phase Diagrams*, volume 3. ASM International, 2 edition.
- [Suri *et al.*, 1989] Suri, D. K., Nagpal, K. C., and Chadha, G. K. (1989). X-ray study of  $\text{CuGa}_x\text{In}_{1-x}\text{Se}_2$  solid solutions. *Journal of Applied Crystallography*, 22(6):578–583.
- [Swanson, 1954] Swanson, H. (1954). Natl. Bur. Stand. *Circ.*
- [Swanson and Tatge, 1953] Swanson, H. and Tatge, E. (1953). Natl. Bur. Stand. *Circ.*
- [Swanson and et al., 1955] Swanson and et al., H. (1955). Natl. Bur. Stand. (U.S.). *Circ.*, 539(54).
- [Tell and Bridenbaugh, 1977] Tell, B. and Bridenbaugh, P. M. (1977). Photovoltaic properties and junction formation in  $\text{CuInSe}_2$ . *J APPL PHYS*, 48(6):2477–2480.
- [Thompson *et al.*, 2009] Thompson, A., Lindau, I., Attwood, D., Liu, Y., Gullikson, E., Pianetta, P., Howells, M., Robinson, A., Kim, K.-J., Scofield, J., Kirz, J., Underwood, J., Kortright, J., Williams, G., and Winick, H. (2009). *X-Ray Data Booklet*. Lawrence Berkeley National Laboratory, third edition.
- [Tonejc, 1980] Tonejc, A. (1980). Phase diagram and some properties of  $\text{Cu}_{2-x}\text{Se}$  ( $2.01 \geq 2-x \geq 1.75$ ). *Journal of Materials Science*, 15(12):3090–3094.
- [Tonejc *et al.*, 1975] Tonejc, A., Ogorelec, Z., and Mestnik, B. (1975). X-ray investigation of copper selenides  $\text{Cu}_{2-x}\text{Se}$  ( $2.00 \geq 2-x \geq 1.72$ ). *J APPL CRYSTALLOGR*, 8(3):375–379.
- [Tuttle *et al.*, 1991] Tuttle, J., Albin, D., and Noufi, R. (1991). Thoughts on the microstructure of polycrystalline thin film  $\text{CuInSe}_2$  and its impact on material and device performance. *Solar Cells*, 30(1):21 – 38.
- [Tuttle *et al.*, 1994] Tuttle, J. R., Albin, D., Tennant, A., Gabor, A., Contreras, M., and Noufi, R. (1994). Characterization of variable-band-gap thin-film  $\text{Cu}(\text{In,Ga})\text{Se}_2$ : a simple model for the interdiffusion of In and Ga in alloy structures. *Solar Energy Materials and Solar Cells*, 35:193 – 201.
- [Uhl *et al.*, 2015] Uhl, A. R., Fuchs, P., Rieger, A., Pianezzi, F., Sutter-Fella, C. M., Kranz, L., Keller, D., Hagendorfer, H., Romanyuk, Y. E., LaMattina, F., Yoon, S., Karvonen, L., Magorian-Friedlmeier, T., Ahlswede, E., VanGenechten, D., Stassin, F., and Tiwari, A. N. (2015). Liquid-selenium-enhanced grain growth of nanoparticle precursor layers for  $\text{CuInSe}_2$  solar cell absorbers. *Prog. Photovolt.: Res. Appl.*, 23(9):1110–1119.
- [Vegard, 1921] Vegard, L. (1921). Die konstitution der mischkristalle und die raumfüllung der atome. *Zeitschrift für Physik*, 5(1):17–26.

- [Vieweg, 2007] Vieweg, B. (2007). Transmissionselektronenmikroskopische Untersuchungen zum Bildungsprozess des Chalkopyrits  $\text{Cu}(\text{In}_{1-x}\text{Ga}_x)(\text{Se}_{1-y}\text{S}_y)_2$  beim Stacked Elemental Layer Verfahren. Studienarbeit.
- [von Bardeleben, 1984] von Bardeleben, H. J. (1984). Selenium self-diffusion study in the 1-3-6<sub>2</sub> semiconductor:  $\text{CuInSe}_2$ . *J APPL PHYS*, 56(2):321–326.
- [Voorwinden *et al.*, 2003] Voorwinden, G., Kniese, R., and Powalla, M. (2003). In-line  $\text{Cu}(\text{In,Ga})\text{Se}_2$  co-evaporation processes with graded band gaps on large substrates. *Thin Solid Films*, 431:538 – 542.
- [Wada *et al.*, 1997] Wada, T., Kohara, N., Negami, T., and Nishitani, M. (1997). Growth of  $\text{CuInSe}_2$  crystals in Cu-rich Cu-In-Se thin films. *J MATER RES*, 12(6):1456.
- [Walter and Schock, 1993] Walter, T. and Schock, H. (1993). Crystal growth and diffusion in  $\text{Cu}(\text{In, Ga})\text{Se}_2$  chalcopyrite thin films. *Thin Solid Films*, 224(1):74 – 81.
- [Wang *et al.*, 2013] Wang, J., Zhang, Y. F., and Zhu, J. (2013). Diffusion Coefficients of Selenium and Gallium during the  $\text{Cu}(\text{In}_{1-x}\text{Ga}_x)\text{Se}_2$  Thin Films Preparation Process. In *Progress in Materials Science and Engineering: ICMSE 2013*, volume 815 of *Advanced Materials Research*, pages 448–453. Trans Tech Publications.
- [Wang *et al.*, 2012] Wang, W., Han, S.-Y., Sung, S.-J., Kim, D.-H., and Chang, C.-H. (2012). 8.01%  $\text{CuInGaSe}_2$  solar cells fabricated by air-stable low-cost inks. *Physical Chemistry Chemical Physics*, 14(31):11154–11159.
- [Wasim, 1986] Wasim, S. (1986). Transport properties of  $\text{CuInSe}_2$ . *Solar Cells*, 16:289 – 316.
- [Weber *et al.*, 2011] Weber, A., Rodriguez, H., Mainz, R., Klaer, J., Pistor, P., Klenk, R., Klaus, M., Meeder, A., Neisser, A., and Schock, H. W. (2011). Fast  $\text{Cu}(\text{In,Ga})\text{Se}_2$  formation by processing Cu-In-Ga precursors in selenium atmosphere. In *2011 37th IEEE Photovoltaic Specialists Conference*, pages 003315–003320.
- [Wei and Zunger, 1995] Wei, S.-H. and Zunger, A. (1995). Band offsets and optical bowings of chalcopyrites and Zn-based II-VI alloys. *J APPL PHYS*, 78(6):3846–3856.
- [Werner *et al.*, 1995] Werner, J. H., Brendel, R., and Queisser, H.-J. (1995). Radiative efficiency limit of terrestrial solar cells with internal carrier multiplication. *Applied Physics Letters*, 67(7):1028–1030.
- [Werner *et al.*, 2005] Werner, J. H., Mattheis, J., and Rau, U. (2005). Efficiency limitations of polycrystalline thin film solar cells: case of  $\text{Cu}(\text{In,Ga})\text{Se}_2$ . *Thin Solid Films*, 480-481:399.
- [White and Andrikidis, 1996] White, G. K. and Andrikidis, C. (1996). Thermal expansion of chromium at high temperature. *Phys. Rev. B*, 53:8145–8147.
- [Williams and Miller, 1950] Williams, D. D. and Miller, R. R. (1950). Densities of liquid and solid Indium. *J AM CHEM SOC*, 72(8):3821–3821.

- [Windeln *et al.*, 2009] Windeln, J., Schock, H.-W., Felser, C., Metzner-Fraune, H., Mannstadt, W., R. Klenk, T. G., Kaufmann, C., Rudigier-Voigt, E., Speit, B., Haag, M., Rissom, T., Kieven, D., Ludwig, C., Haarstrich, J., and Oertel, M. (2009). comCIGS - Integrative Framework of Experimental and Virtual Lab. *in Proceedings of the 24th EUPVSEC*, pages 2443–5.
- [Witte *et al.*, 2015] Witte, W., Abou-Ras, D., Albe, K., Bauer, G. H., Bertram, F., Boit, C., Brüggemann, R., Christen, J., Dietrich, J., Eicke, A., Hariskos, D., Maiberg, M., Mainz, R., Meessen, M., Müller, M., Neumann, O., Orgis, T., Paetel, S., Pohl, J., Rodriguez-Alvarez, H., Scheer, R., Schock, H.-W., Unold, T., Weber, A., and Powalla, M. (2015). Gallium gradients in Cu(In,Ga)Se<sub>2</sub> thin-film solar cells. *Prog. Photovolt.: Res. Appl.*, 23(6):717–733.
- [Wolf and Müller, 2000] Wolf, D. and Müller, G. (2000). In-situ Monitoring of Phase Formation in CuInSe<sub>2</sub> Thin Films. *JPN J APPL PHYS*, 39(S1):173.
- [Wu *et al.*, 2018] Wu, J.-L., Tai, K. F., Iwata, Y., Kato, T., Sugimoto, H., and Bermudez, V. (2018). Investigation on Alkali-treatment mechanisms for improving energy conversion efficiency of Cu(In,Ga)(Se,S)<sub>2</sub> modules.
- [Wu *et al.*, 2014] Wu, T.-T., Huang, J.-H., Hu, F., ho Chang, C., Liu, W.-L., Wang, T.-H., Shen, C.-H., Shieh, J.-M., and Chueh, Y.-L. (2014). Toward high efficiency and panel size 30x40 cm<sup>2</sup> Cu(In,Ga)Se<sub>2</sub> solar cell: Investigation of modified stacking sequences of metallic precursors and pre-annealing process without Se vapor at low temperature. *Nano Energy*, 10:28 – 36.
- [Würfel, 2000] Würfel, P. (2000). *Physik der Solarzellen*. Spektrum Akademischer Verlag.
- [Xue *et al.*, 2016] Xue, H., Tang, F., Zhang, F., Lu, W., and Feng, Y. (2016). Temperature effects on distribution and inhomogeneous degree of In-Ga atoms in CuIn<sub>1-x</sub>Ga<sub>x</sub>Se<sub>2</sub> alloys. *Materials Letters*, 164:169 – 171.
- [Yamamoto and Kashida, 1991] Yamamoto, K. and Kashida, S. (1991). X-ray study of the average structures of Cu<sub>2</sub>Se and Cu<sub>1.8</sub>S in the room temperature and the high temperature phases. *Journal of Solid State Chemistry*, 93(1):202 – 211.
- [Zhang *et al.*, 1998] Zhang, S., Wei, S.-H., Zunger, A., and Katayama-Yoshida, H. (1998). Defect physics of the CuInSe<sub>2</sub> chalcopyrite semiconductor. *Phys. Rev. B*, 57:9642–9656.
- [Zhang *et al.*, 1997] Zhang, S. B., Wei, S.-H., and Zunger, A. (1997). Stabilization of Ternary Compounds via Ordered Arrays of Defect Pairs. *Phys. Rev. Lett.*, 78:4059–4062.
- [Zhao *et al.*, 2004] Zhao, Y.-J., Persson, C., Lany, S., and Zunger, A. (2004). Why can CuInSe<sub>2</sub> be readily equilibrium-doped n-type but the wider-gap CuGaSe<sub>2</sub> cannot? *Applied Physics Letters*, 85(24):5860–5862.
- [Zunger *et al.*, 1997] Zunger, A., Zhang, S., and Wei, S.-H. (1997). Revisiting the Defect Physics in CuInSe<sub>2</sub> and CuGaSe<sub>2</sub>. In *IEEE PVSC*, volume 26, pages 313–318.

# A. Supplementary for Ch. 1

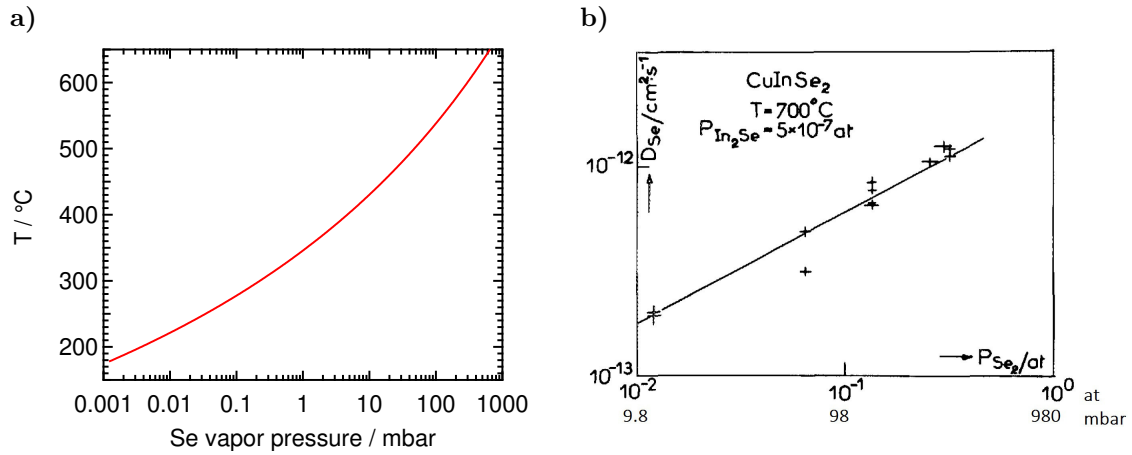


**Figure A.1.:** Dependence of Diffusion coefficient ( $D_{Se}$ ) on Se vapor pressure ( $P_{Se}$ ) and dependence of  $P_{Se}$  on  $T_{sub}$ . a)  $P_{Se}$ , calculated with the formula  $\log_{10}(P)=A-(B/(T+C))$  and constants A, B, and C from [Stull, 1947]. b)  $D_{Se}$  in CuInSe<sub>2</sub> as a function of the Se<sub>2</sub> partial pressure ( $P_{Se}$ ) at 700 °C from von Bardeleben [von Bardeleben, 1984].

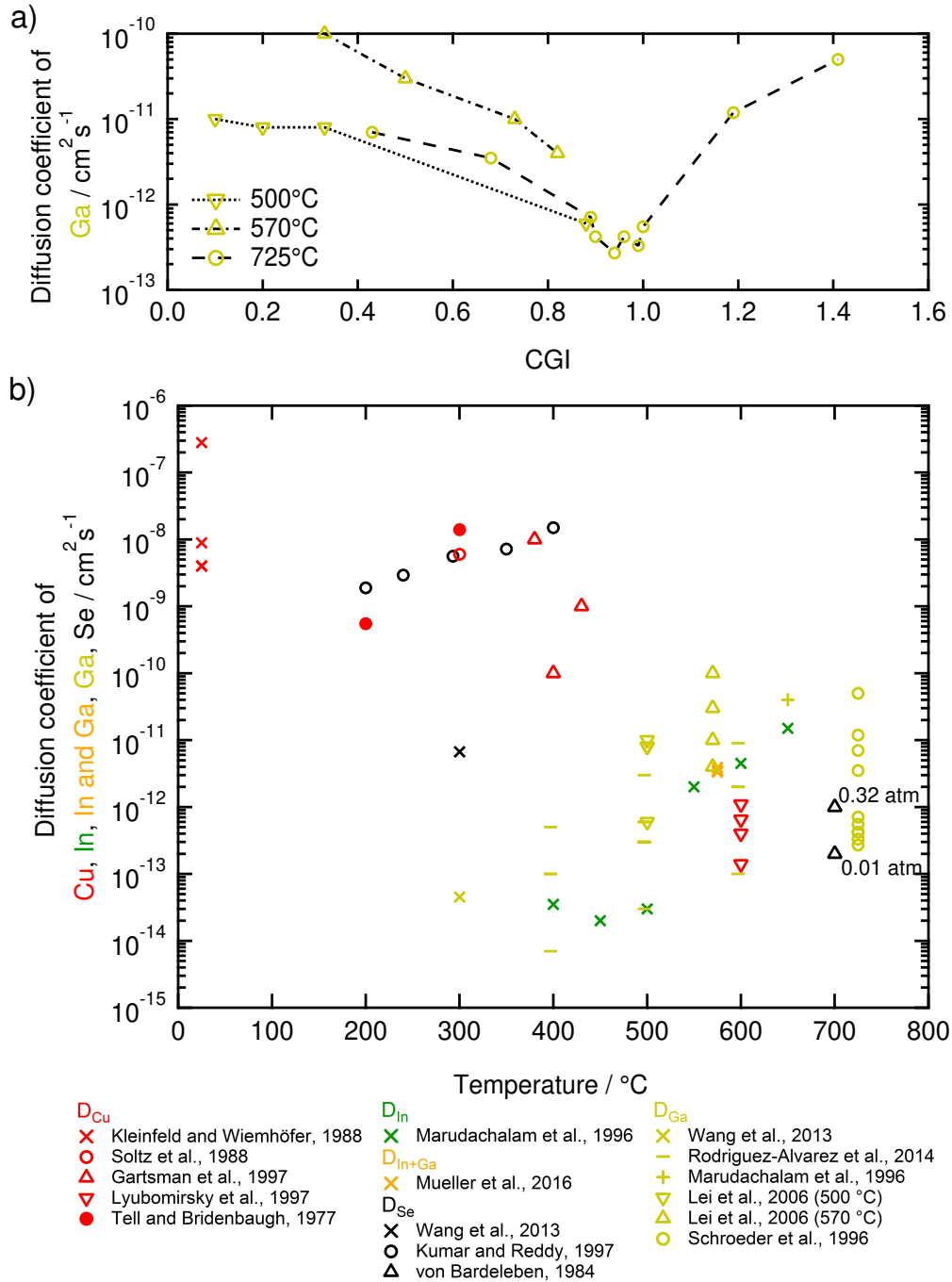


**Figure A.2.:** Elemental diffusion coefficients in CIGS. a)  $D_{\text{Ga}}$  in CIGS for various CGI film compositions at 500°C, 570°C and 725°C. The CGI for 725°C is the initial Cu/In ratio before Ga addition. b) Diffusion coefficients for Cu, In, Ga and Se in CIGS, reported in [Mueller *et al.*, 2016, Gartsman *et al.*, 1997, Soltz *et al.*, 1988, Kleinfeld and Wiemhöfer, 1988, Lyubomirsky *et al.*, 1997, Tell and Bridenbaugh, 1977, Lei *et al.*, 2006, von Bardeleben, 1984, Wang *et al.*, 2013, Kumar and Reddy, 1997, Marudachalam *et al.*, 1996, Schroeder *et al.*, 1996, Rodriguez-Alvarez *et al.*, 2014]

**Table A.1.:** SCAPS simulation parameters used for the calculation of the band diagram in Fig. 1.4. The  $\text{Cu}(\text{In}_{1-x}\text{Ga}_x)\text{Se}_2$  layer consists of  $0.6\ \mu\text{m}$   $\text{CuInSe}_2$  and below  $0.9\ \mu\text{m}$  with a linearly increasing GGI from 0 to 0.6 at the back contact. CB: conduction band, VB: valence band.

	ZnO	CdS	$\text{Cu}(\text{In}_{1-x}\text{Ga}_x)\text{Se}_2$	
Thickness / $\mu\text{m}$	0.5	0.05	1.5	
			$\text{CuInSe}_2$	$\text{CuGaSe}_2$
Bandgap energy / eV	3.3	2.4	1.0	1.6
Electron affinity / eV	4.45	4.2	4.5	3.9
Dielectric permittivity	9.0	10	13.6	13.6
Effective density of states in CB / $1/\text{cm}^3$	$2.2 \cdot 10^{18}$	$2.2 \cdot 10^{18}$	$2.2 \cdot 10^{18}$	$2.2 \cdot 10^{18}$
Effective density of states in VB / $1/\text{cm}^3$	$1.8 \cdot 10^{19}$	$1.8 \cdot 10^{19}$	$1.8 \cdot 10^{19}$	$1.8 \cdot 10^{19}$
Thermal velocity of electrons / $\text{cm/s}$	$1 \cdot 10^7$	$1 \cdot 10^7$	$1 \cdot 10^7$	$1 \cdot 10^7$
Thermal velocity of holes / $\text{cm/s}$	$1 \cdot 10^7$	$1 \cdot 10^7$	$1 \cdot 10^7$	$1 \cdot 10^7$
Electron mobility / $\text{cm}^2/\text{Vs}$	$1 \cdot 10^2$	$1 \cdot 10^2$	$1 \cdot 10^2$	$1 \cdot 10^2$
Hole mobility / $\text{cm}^2/\text{Vs}$	25	25	25	25
Shallow uniform donor density / $1/\text{cm}^3$	$1 \cdot 10^{18}$	$1 \cdot 10^{16}$	0	0
Shallow uniform acceptor density / $1/\text{cm}^3$	0	0	$1 \cdot 10^{15}$	$1 \cdot 10^{15}$
Defects:				
Capture cross section for electrons / $\text{cm}^2$	$1 \cdot 10^{-12}$	$1 \cdot 10^{-13}$	$2 \cdot 10^{-14}$	$2 \cdot 10^{-14}$
Capture cross section for holes / $\text{cm}^2$	$1 \cdot 10^{-12}$	$1 \cdot 10^{-13}$	$1 \cdot 10^{-13}$	$1 \cdot 10^{-13}$
Energy level with respect to VB / eV	1.65	1.2	0.5	0.8
Defect density / $1/\text{cm}^3$	$1.8 \cdot 10^{16}$	$1.8 \cdot 10^{17}$	$5 \cdot 10^{14}$	$5 \cdot 10^{14}$
Absorption constant A / $\text{eV}^{1/2}/\text{cm}$			$1 \cdot 10^5$	$1 \cdot 10^5$
Metallic contacts:				
	back	front		
Surface recombination velocity e / $\text{cm/s}$	$1 \cdot 10^7$	$1 \cdot 10^7$		
Surface recombination velocity h / $\text{cm/s}$	$1 \cdot 10^7$	$1 \cdot 10^7$		



## B. Supplementary for Ch. 2

### Analysis of diffraction signals and error estimation

The heating induces a thermal expansion of the setup. This expansion in the vertical  $\bar{z}$ -direction lifts the sample and hence shifts the active volume. If not corrected, the position of the diffraction peaks would change and their intensity would decrease, while the background from glass would increase [Denks and Genzel, 2007]. This setup is build for a measurement with a fixed angle. To compensate this thermal drift the measurement program includes a routine for a compensation. The Mo fluorescence intensity is the regulation parameter to ensure a constant position of the active volume by adjusting the  $z$  position.

An important size is the dead time, which is defined as  $DT(\%) = 1 - \frac{time^{collection}}{time^{real}}$ . That means a dead time of 40 % corresponds to a collection time of 40 % of the real measurement time. A normalization after measuring is implemented in the analysis part of the program, defined within the calculation of corrected areas.

For observation of such fast processes as performed here, the integration time of the detection is set as short as possible (3s in the original measurement) for a maximum possible time resolution. Longer integration times improve the signal to noise ratio and enable a higher accuracy of the measured peak properties. Instead of increasing the integration time for a higher accuracy, the spetrac can be summed up afterwards and by using the average with a definable number of previous and following spectra in the fitting procedure. The main cause of a background is the underlying glass substrate. A linear background is removed by selecting energy ranges before and after the signal. Fits of the signals are performed to extract the information about intensity and energetic position. To select an appropriate fit of the diffraction signals, knowledge about the characteristic influences on the signal profile is useful. The standard approach in regression analysis to approximate the solution with the method of least squares for  $X^2$  (see below) is performed with the Levenberg-Marquardt algorithm [Levenberg, 1944, Marquardt, 1963]. Selecting a function is guided by the specific influences on the signal profile by the sample and the measurement. A perfect crystal structure with infinite dimension would exhibit a profile of a diffraction signal like a delta function. However, defects, impurities, strain and limited grains sizes lead to

both, a Gaussian and a Lorentzian broadening. A convolution of both results in a Voigt function which can be approximated by the pseudo-Voigt function. The measurement characteristics such as the resolution capability of the detector influences the signal profile with an additional Gaussian broadening. The reflections from gold powder for the calibrations are fitted with the pseudo-Voigt function. The measurement signals during selenization are fitted with a Gaussian function, since the fit could not be improved by a pseudo-Voigt function.

Hence, to calculate the intensity of a signal, it is approximated by a function  $F_{signal}(E)$  and the integral area is calculated as intensity:  $I_{signal} = \int_{-\infty}^{\infty} F_{signal}(E) dE$ . The fitting minimizes the sum of the error square:  $X^2 = \sum_n \left( \frac{y_{n,calc} - y_{n,sign}}{w_n} \right)^2$  with a difference of the calculated value ( $y_{n,calc}$ ) and signal value ( $y_{n,sign}$ ). The data points are weighted with the standard deviation  $w_n$  of the signal values. Recording photons is a counting of events and subject to the Poisson statistic. Therefore the standard deviation can be written as  $w_n = \sqrt{y_n}$  [Bronstein *et al.*, 1997].

## Energy and angle calibration

The detected photons of every EDXRD/EDXRF measurement were assigned to the 2048 channels in an analog-to-digital converter and summed over the specified measurement time. To assign the channels to the energy of the photons, element fluorescence signals were measured. The channel with the maximum intensity of each fluorescence signal was assigned to the fluorescence energy from literature [Deslattes *et al.*, 2003]. By use of linear regression and the assignments (energy-channel), the parameters  $E_0$  and  $m$  were determined (Eq. B.1). The standard deviations  $s_{E_0}$  and  $s_m$  result from the linear regression. A Taylor expansion with the first term results in the relative deviation of the energy (Eq. B.2).

$$E_{photon}(channel) = E_0 + m \times channel \quad (\text{B.1})$$

$$s_E = s_{E_0} + \frac{s_m}{m}(E_0 - E) \quad (\text{B.2})$$

For the angle calibration, gold powder was used as reference (with 99.99% purity). The fluorescence peaks  $Au_{LI}$ ,  $Au_{Lg1}$ ,  $Au_{K\alpha2}$  and  $Au_{K\alpha1}$  were utilized for calibrating the energy axis. Then, the diffraction angle  $\theta$  was calibrated with the known energetic positions from lattice plane distances for the diffraction peaks using Au 111, Au 200 and Au 220. The energy calibration can slightly differ between each measurement, compare Tab. B.1. Therefore, the energy axis of each measurement is calibrated with the fluorescence signals  $Cu_{K\beta_1}$ ,  $Se_{K\beta_1}$ ,  $Mo_{K\beta_1}$  and  $In_{K\beta_1}$ . For example, the

values regarding detector 1 in Sec. 4.1 are:  $E_0=-0.00260$ ,  $m=0.0328$ ,  $s_{E_0}=0.0333$ ,  $s_m=0.0000500$ , resulting in  $0.0333 - 0.00152 \times E$ .

**Table B.1.:** Standard deviations of the energy in the obtained spectra after calibration with fluorescence signals.

Sec.	$s_E$	
	Detector 1	Detector 2
4.1	$0.0333 - 0.00152 \times E$	$0.0896 - 0.00401 \times E$
4.2	$0.0273 - 0.00125 \times E$	$0.0243 - 0.00098 \times E$
4.3	$0.0265 - 0.00121 \times E$	$0.0298 - 0.00137 \times E$

## Estimation of the standard deviation of the lattice plane distance

The lattice plane distance is calculated with the energy of the Bragg photon that got reflected and the fixed measurement angle. Its energy is determined by the energetic position of the Gaussian fitted peak. It is calculated by  $d(E, \theta) = \frac{hc}{2E \sin(\theta)}$ . The angle resume from a calibration with standard deviation, as described before and the energetic position is estimated by use of a Gaussian function. The uncertainty  $\sigma_d$  of the lattice plane distance can be calculated by the Gauß' error propagation and the uncertainties of  $\sigma_E$  and  $\sigma_\theta$ :

$$\begin{aligned}
 \sigma_d &= \sqrt{\left(\sigma_E \frac{\partial d(E, \theta)}{\partial E}\right)^2 + \left(\sigma_\theta \frac{\partial d(E, \theta)}{\partial \theta}\right)^2} \\
 &= \frac{hc}{2} \cdot \sqrt{\left(\frac{\sigma_E}{E^2 \sin(\theta)}\right)^2 + \left(\frac{\sigma_\theta \cos \theta}{E (\sin \theta)^2}\right)^2} \\
 &= 0.62 \text{ keV nm} \cdot \sqrt{\left(\frac{\sigma_E}{E^2 \sin(\theta)}\right)^2 + \left(\frac{\sigma_\theta \cos \theta}{E (\sin \theta)^2}\right)^2}
 \end{aligned}$$

The values, used for calculating this uncertainty, originate from EDXRD / EDXRF measurement data which were observed at a constant temperature (RT). However, there is another source of error, which results from the height alignment (see lift table in Fig. 2.3) routine due to thermal expansion and the Se incorporation. A difference in the height results in a different diffraction angle, because the synchrotron beam and the detector are at fixed positions. The sample volume from where photons are detected is defined as active volume. Its volume is formed by the intersection of the

incoming X-ray beam and the region of space seen by the detector form the active volume. The beam is shaped by slits and has a divergence. The window of the detector is also limited by slits. The maximum possible detected intensity results from an optimal position of the sample in the active volume. Therefore, the adjustment routine is initialized with a search for the z position of maximum intensity of the fluorescence signal of Mo. At this position, the measurement is started. It is known from previous experiments that the thermal expansion of the setup lifts the Mo film position in z direction. Therefore the z-position should be corrected. Hence, the software routine is continuously trying to keep the sample at a height z by adjusting the maximum intensity by comparing the actual intensity  $I_0$  at position  $z_0$  with the intensity  $I_1$  at a 10  $\mu\text{m}$  higher position  $z_1 = z_0 + 10 \mu\text{m}$ . The gradient of  $\frac{I_1 - I_0}{z_1 - z_0}$  is either negative and the position  $z_0$  is corrected to a lower position, or it is positive and the position  $z_0$  is corrected to a higher z value.

Mo yields a relative high fluorescence intensity and is used for the adjustment of the z position throughout the measurement. Its fluorescence intensity is mainly attenuated by the material on top. In the beginning of a process, this is the precursor consisting of Cu, Ga and In. As long as their amount is constant, a changing depth distribution has no strong influence on the Mo fluorescence. During processing, Se incorporation can occur which results in a lower Mo fluorescence intensity. Se has the highest absorption cross section below the emission energy of Mo-K $\alpha$  (compare Fig. 1 in [Mainz and Klenk, 2011]). In the case of fast Se incorporation and fast heating,  $I_1$  might be smaller although the sample is at the position  $z_1$  at a new/actual but lower maximum fluorescence intensity than before. Then, the correction to a lower position is executed though not correct. This is correlated to a decrease of the Bragg reflection Mo 110. To estimate the error limit of the lattice plane distance, the maximum difference in Mo 110 intensity during fast heating and Se incorporation is used. This difference is proportional to the difference of the height position. The maximum intensity of Mo 110 results from an optimal height position or optimal position of Mo in the active area. If the sample position increases or decreases, the diffraction intensity decreases proportionally. In this setup, the diffraction intensity reaches 0 after a height difference (higher or lower z-position) of about 60  $\mu\text{m}$  to the optimal position. That means, that a decrease of the intensity of 10 % results from a wrong z-position of 10 % of 60  $\mu\text{m}$ .

The maximum possible error is estimated by the percentage difference between the maximum Mo 110 reflection intensity before and after a fast Se increase, exemplarily shown in Fig. B.1 for the measurement from Sec. 4.2. The percentage of the difference to the optimum position is about 8.3 % of 60  $\mu\text{m}$  resulting in a  $\Delta z = 8.3/100 \times 60 \mu\text{m} = 4.98 \mu\text{m}$ . This results in an error limit of the angle, which is estimated by small angle approximation and the distance  $\Delta y$  between detector and sample of 2.657 m:  $\sigma_\theta = \text{atan}(\frac{\Delta z}{\Delta y})$ , compare Tab. B.2.

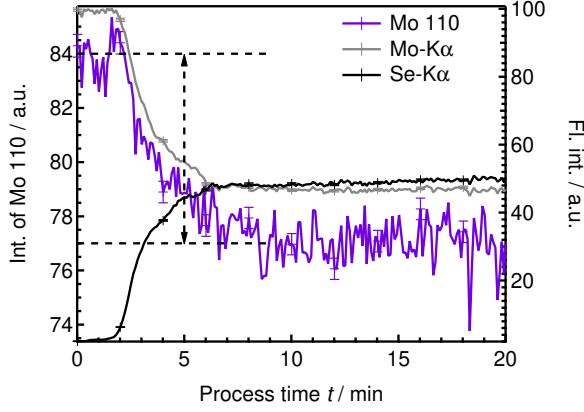


**Figure B.1:** Evolution of the integral  $K\alpha$  fluorescence intensities of Mo and Se and integral diffraction intensity of Mo 110 of the measurement in Sec. 4.2. The maximum difference of the intensity of Mo 110 is indicated with the arrow and dashed lines to be  $\Delta I=7$  a.u., which is a decrease of 8.3 %

**Table B.2.:** Uncertainties calculated for lattice plane distance of Mo 110 for the experiment from Sec. 4.2, first by subsequent fault calculation and the energetic position  $E_{Mo110}$  and second by estimation from the maximum deviation of the intensity of the Mo 110 signal during heating.

Sec. 4.2 Detector 1	
Uncertainty of d from uncertainties from calibrations of E and $\theta$	
$\theta \pm \sigma_\theta$	$2.98751640^\circ \pm 0.000227^\circ$
$E \pm \sigma_{E_{Mo110}}$	$53.279 \text{ keV} \pm 0.001 \text{ keV}$
$d \pm \sigma_{d_{Mo110}}$	$0.2233 \text{ nm} \pm 0.0010 \text{ nm} (\pm 0.4 \%)$
Uncertainty of d from misalignment $\Delta z$	
$\theta \pm \sigma_\theta$	$2.98751640^\circ \pm 0.000107^\circ$
$E \pm \sigma_{E_{Mo110}}$	$53.279 \text{ keV} \pm 0.001 \text{ keV}$
$d \pm \sigma_{d_{Mo110}}$	$0.2233 \text{ nm} \pm 0.0005 \text{ nm} (\pm 0.2 \%)$

To compare both uncertainties and to obtain the bigger one for estimating the error limit, the uncertainties are calculated for Mo.  $\sigma_d$  (from calibrations) is exemplary calculated for the Mo 110 peak in the measurement (shown in Sec. 4.2) to compare it with the estimated maximum height misalignment, see Tab. B.2. For the calculation of the standard deviation of the energetic position of Mo 110, the results from the fit at the end of the measurement in Fig. B.1 are used, since here the intensity is the lowest after Se incorporation with possibly the highest standard deviation. The highest standard deviation of the fitted energetic position ( $E_{Mo110}$ ) after 0 min is at 35.4 min with  $53.279 \text{ keV} \pm 0.001 \text{ keV}$  and  $d = 0.22325 \text{ nm}$ .

## Reasons for an asymmetric signal profile

In this work, solid solutions like  $\text{Cu}(\text{In,Ga})\text{Se}_2$  are present. Such a solid solution can exhibit an inhomogeneous composition which leads to a variation of the lattice

constants in the measured active volume. The reflection energy depends on the ratio, which is linear between both phases after Vegard's law [Vegard, 1921], as described in Sec. 1.1.1. The active volume can exhibit different lattice constants, which are closer to each other than the energy resolution of the detector allows to differentiate. The resulting signal is superimposed, typically leading to an asymmetric profile. Therefore, superimposition of several Gaussian profiles can be used as description.

## Escape peaks (Esc)

A photon with energy  $E_0$ , which is reaching the detector can be absorbed by Ge and lead to Ge specific fluorescence (e.g. Ge- $K\alpha=9.9$  keV). Consequently, two events are detected: the fluorescence photon of Ge and the initially photon energy, which is reduced by the energy of the Ge fluorescence photon. The energy of such an escape peak is then  $E_{\text{Esc}}=E_0-E_{\text{Ge-}K\alpha}$ .

## Inaccurate spectra

Some spectra in the data from detector 1 are incorrect, as indicated by a short and distinct deviation of the dead time and the height positioning. This occurred for some spectra in both *in situ* measurements for Sec. 4.2 and Sec. 4.2.1. In Fig. 4.3, the spectra between -6.75 min and -6.72 min (1169 - 1170) as well as between -5.40 min and -5.30 min (1197-1199) were deleted. In Fig. D.9, the spectra between -33.97 min and -33.92 min (637-639) were deleted.

## Uncertainty of fluorescence intensities

The maximum uncertainty of the fluorescence intensities from EDXRF is estimated as follows. The automatic height alignment routine (as described above) corrects the height position for each measurement period by comparing the intensity of Mo- $K\alpha_1$  with the value from the previous measurement period. The maximum height variation to find the maximum fluorescence intensity is  $\pm 10$   $\mu\text{m}$ . It is known from the experimental setup, that the decrease of the fluorescence intensity can be approximated by a linear dependence to the height position. The intensity decreases to 0 a.u. for a misalignment of  $\pm 60$   $\mu\text{m}$  from the optimal height position. In consequence, the maximum error that can occur during the routine is 10/60. By averaging every two

spectra of the measurement afterwards, this is decreased to its half. In conclusion, the height misalignment can be  $\pm 5/60$ , which corresponds to a maximum uncertainty for each fluorescence intensity of 8.3%.

## Total atomic cross-sections

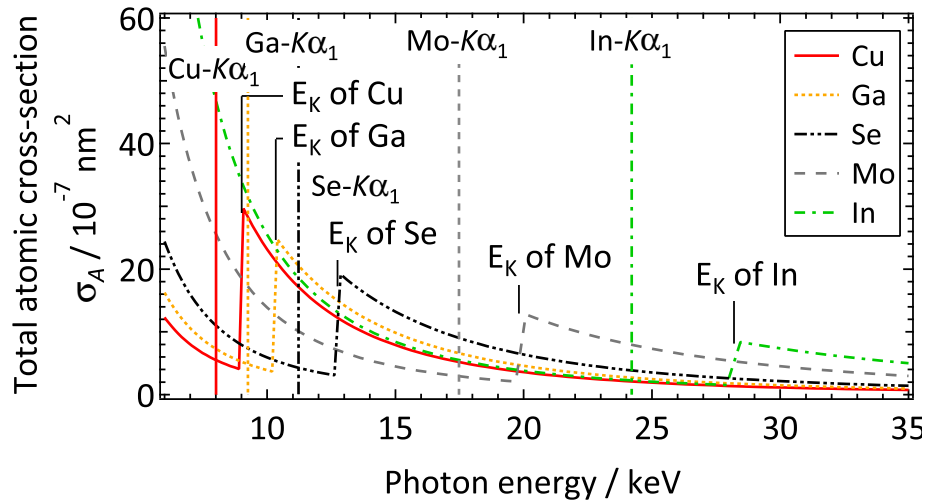


**Figure B.2.:** Total atomic cross-section  $\sigma_A(h\nu)$  for the elements Cu, Ga, In, Mo and Se from [McMaster *et al.*, 1969]. The elemental  $K\alpha_1$  lines are depicted as vertical lines. The total absorption cross-section is a measure for the probability of an absorption process and thus important for the calculation of the elemental fluorescence intensities.



## C. Supplementary for Ch. 3

The following figures have been published before in [Bäcker *et al.*, 2017].

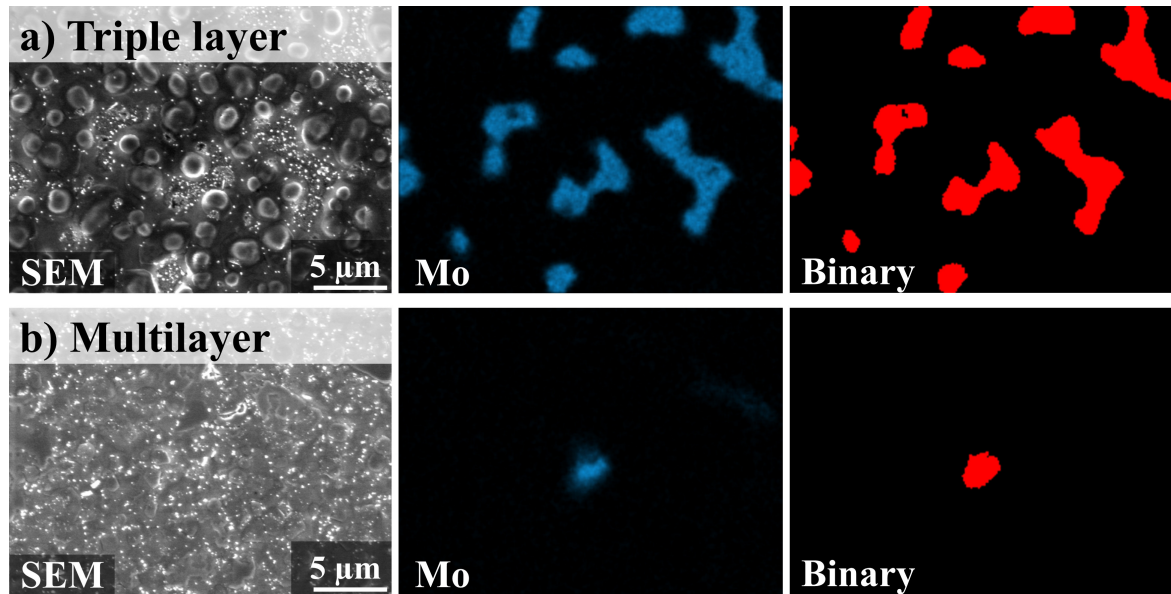


**Figure C.1.:** SEM and elemental distribution images (net counts) of Mo (measured with EDX at room temperature) and binary images on a) triple layer precursor and b) multilayer precursor after heating with 0.1°C/s up to 580 °C. Binary images show a relative dewetting of 14.3% (triple layer) and 0.8% (multilayer).

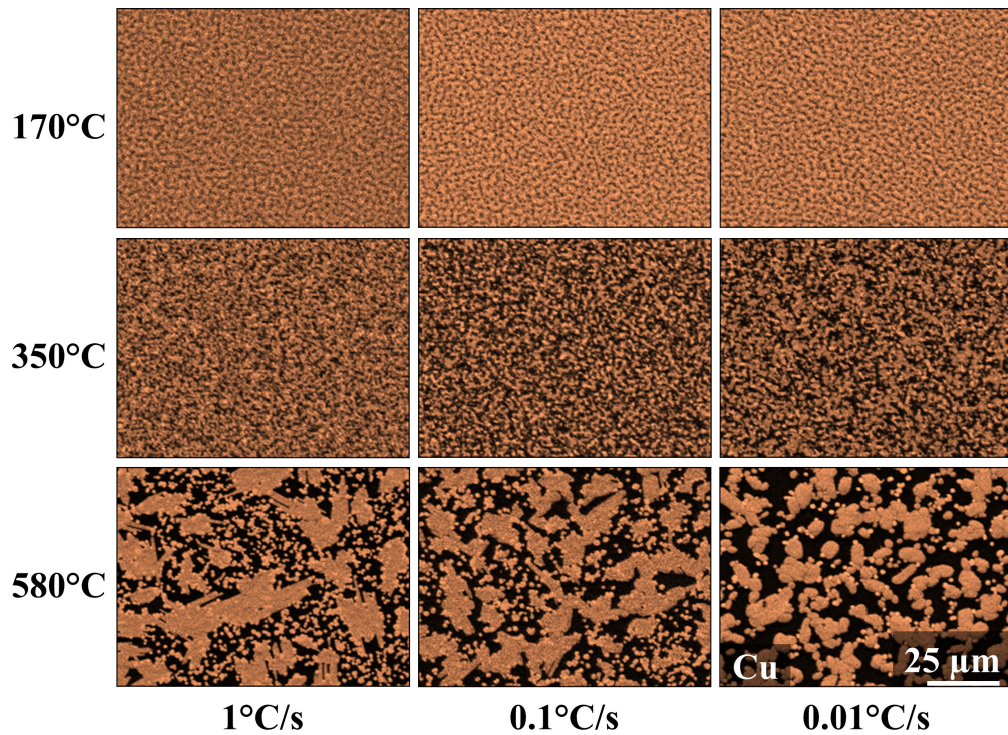


**Figure C.2.:** Cu intensity distribution images (EDX) of the multilayer precursors after annealing with 1, 0.1 and 0.01°C/s up to  $T_{\max} = 170, 350$  and 580°C. All images have the same scale.

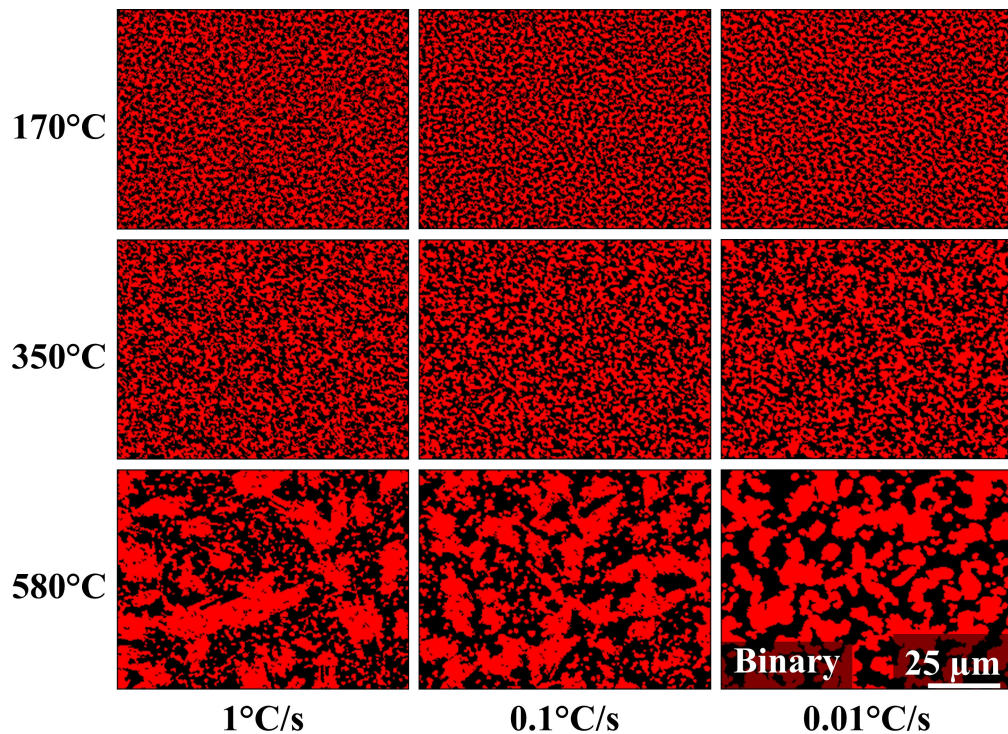


**Figure C.3.:** Binary images of the Cu Intensity elemental images from Fig. C.2. From left to right with 1, 0.1 and 0.01°C/s heating rate and from top to bottom with the annealing temperatures of  $T_{\max} = 170, 350$  and 580°C. All images have the same scale.

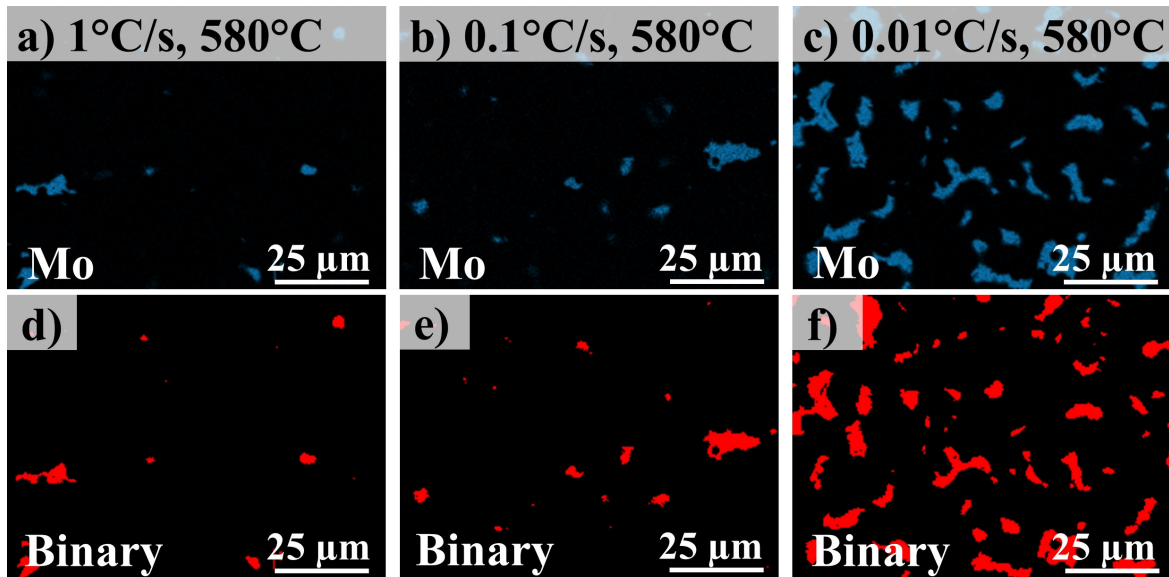


**Figure C.4.:** Elemental distribution images (net counts) of Mo (measured with EDX at room temperature) and after heating with a) 1°C/s, b) 0.1°C/s and c) 0.01°C/s up to 580 °C of a multilayer precursor.  $T_{\max}$  (°C) and the heating rates (°C/s) are indicated on the SEM images. Binary images d-f (belong to a-c) show a relative dewetting of 1% (d), 2% (e) and 12% (f).



**Figure C.5.:** Binary images after heating with 0.01°C/s up to 580°C of a multilayer precursor a) without NaF, b) with 30 nm NaF under precursor and c) with 30 nm NaF on top of precursor, processed from Mo intensity distribution images (elemental images Fig. 3.5) by method of N. Otsu (1979). Dewetting determined from the binary images is a) 30%, b) 65% and c) 4% (Tab. 3.3).



## D. Supplementary for Ch. 4

### D.1. Evaluation of the composition of the $\gamma$ -Cu<sub>9</sub>(In<sub>1-x</sub>Ga<sub>x</sub>)<sub>4±y</sub> for Sec. 4.2 and Sec. 4.3

The accurate composition of each phase may be important for the fluorescence calculations conducted in Sec. 4.2.2 and Sec. 4.3.2, to deduce the stacking order of the present phases at a given time. It may further be important for the comprehensive understanding of the general phase evolution of the film. This chapter describes the applied procedure to evaluation the composition of the Cu<sub>9</sub>(In<sub>1-x</sub>Ga<sub>x</sub>)<sub>4±y</sub> phases as accurate as possible.

The lattice plane distance  $d_{330}$  is correlated to the phase composition. Both, the CGI as well as the GGI determine  $d_{330}$ . The possible minimum and maximum of the Cu concentration are estimated at the substrate temperature by means of the Cu-Ga phase diagram in Fig. E.1. The corresponding lattice plane distance of allowed phases is calculated by use of the phase diagram showing the lattice constant (which is equal  $d_{330}$  by a proportionality factor) as function of the Cu concentration in  $\gamma_i$ -Cu<sub>9</sub>Ga<sub>4</sub> (Fig. E.2a) and by use of the thermal expansion coefficient<sup>1</sup>. In the case, that a calculated value of  $d_{330}$  of  $\gamma_i$ -Cu<sub>9</sub>Ga<sub>4</sub> (without In) is with error significantly lower than the measured  $d_{330}$ , a solid solution  $\gamma$ -Cu<sub>9</sub>(In,Ga)<sub>4</sub> of  $\gamma_i$ -Cu<sub>9</sub>Ga<sub>4</sub> ( $i=1,2,3$ ) and  $\gamma$ -Cu<sub>9</sub>In<sub>4</sub> must be assumed<sup>2</sup>. In this case, the composition limits of  $\gamma$ -Cu<sub>9</sub>(In,Ga)<sub>4</sub> are the limits from the phase existence ranges of  $\gamma$ -Cu<sub>9</sub>(In,Ga)<sub>4</sub> in the Cu-In-Ga phase diagrams in Figs. 1.5a, E.4 and 1.5b. Then, the Ga to In ratio is determined by use of Vegard's law and the difference to the observed  $d_{330}$ . Thus, the upper and lower limit of the GGI in  $\gamma$ -Cu<sub>9</sub>(In,Ga)<sub>4</sub> are calculated as a function of the upper and lower limit of the Cu concentration.

---

<sup>1</sup>Only for  $\gamma_0$  and  $\gamma_1$  a thermal expansion coefficient can be found in the literature, but not for  $\gamma_2$  nor  $\gamma_3$ . Therefore the coefficient of  $\gamma_1$  is applied to  $\gamma_{2,3}$ ., compare Tabs. E.2 and E.3

<sup>2</sup>Muzzillo *et al.* suggested  $\gamma$ -Cu<sub>9</sub>(In,Ga)<sub>4</sub> to be a solid solution of  $\gamma_1$ -Cu<sub>9</sub>Ga<sub>4</sub> and  $\gamma$ -Cu<sub>9</sub>In<sub>4</sub> [Muzzillo *et al.*, 2015], possibly for a simpler calculability. The phases  $\gamma_2$  and  $\gamma_3$  are not excluded here, since no distinct reason for that was found.

## D.2. Supplementary for Sec. 4.1

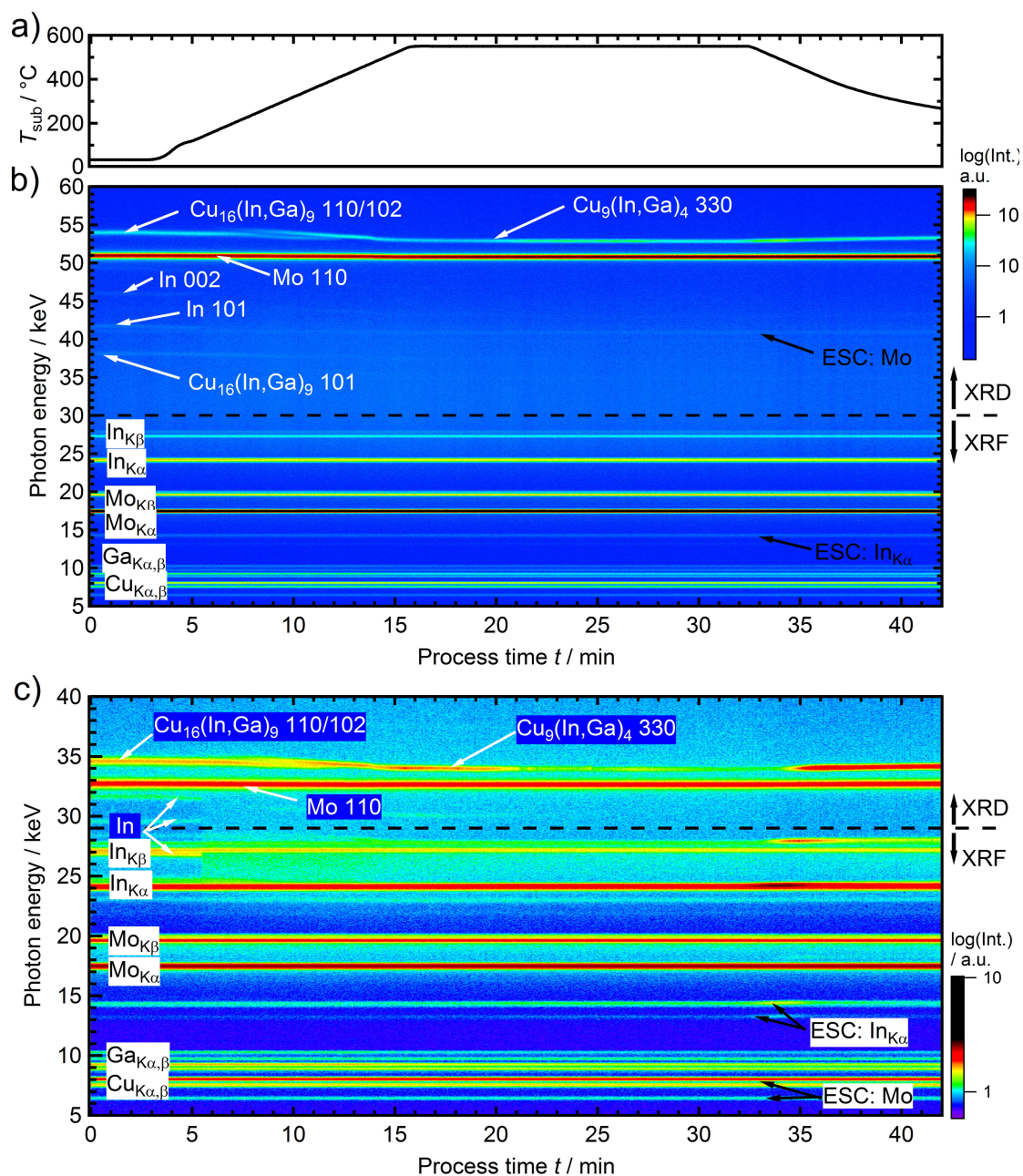


**Figure D.1.:** a) Substrate temperature ( $T_{\text{sub}}$ ) and *in situ* EDXRD/EDXRF data by b) detector 1 and by c) detector 2, observed during thermal treatment of a multilayer precursor. The EDXRD/EDXRF intensity is color coded (as indicated on the right side). The horizontal dashed line at 30 keV indicates, that the peaks above correspond to diffracted photons and the peaks below originate mainly from elemental fluorescence. Assigned EDXRD peaks are indicated with white arrows and the belonging phase and Miller indices. Escape peaks are indicated with black arrows. Further details and identification of peaks can be found in the text. A magnification of the main reflections of d) of the  $\eta$ - and  $\gamma$ -phases can be found in Fig. 4.2.

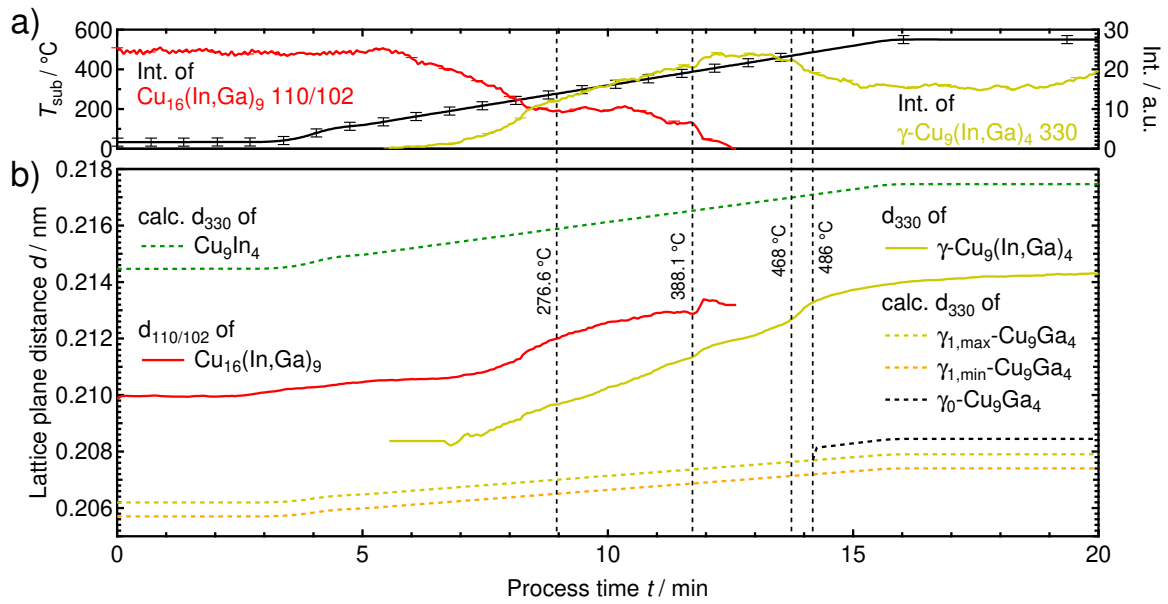


**Figure D.2.:** Magnified evolution of  $\text{Cu}_{16}(\text{In,Ga})_9$  110/102 and  $\gamma\text{-Cu}_9(\text{In,Ga})_4$  330 from Fig. D.1b). a)  $T_{\text{sub}}$  (left axis) and reflection intensities (right axis) of  $\gamma\text{-Cu}_9(\text{In,Ga})_4$  330 (and  $\text{Cu}_{16}(\text{In,Ga})_9$  110/102) b) corresponding lattice plane distances calculated from the energetic peak position, together with simulated (dashed)  $d_{330}$  of  $\text{Cu}_9\text{In}_4$ , min. and max. of  $\gamma_1$ - and  $\gamma_0\text{-Cu}_9\text{Ga}_4$  as a function of  $T_{\text{sub}}$ . With increasing temperature from 490 °C up to 645 °C, the  $\gamma_1\text{-Cu}_9\text{Ga}_4$  phase can transform to  $\gamma_0\text{-Cu}_9\text{Ga}_4$ , as it is shown in the Cu-Ga phase diagram (Fig. E.1).

### D.3. Supplementary for Sec. 4.2

#### Composition of $\gamma\text{-Cu}_9(\text{In}_{1-x}\text{Ga}_x)_{4\pm y}$

The  $d_{330}$  of the  $\gamma\text{-Cu}_9(\text{In}_{1-x}\text{Ga}_x)_{4\pm y}$  phases (sup. Fig. D.3) corresponds to the phase composition. The accurate composition of each phase is important for the fluorescence calculations conducted in Secs. 4.2.2 and 4.3.2, to deduce the stacking order of the present phases at a given time. It is further important for the understanding of the general phase evolution of the film. The applied procedure to evaluate the composition of the  $\gamma\text{-Cu}_9(\text{In}_{1-x}\text{Ga}_x)_{4\pm y}$  phases as accurate as possible is explained in sup. Sec. D.1. At 388 °C ( $t_1$ ),  $d_{330}$  of  $\gamma\text{-Cu}_9(\text{In,Ga})_4$  (blue line) is  $0.2098\pm 0.001$  nm. The composition is estimated within the possible Cu composition range of  $68\pm 1$  at.% Cu of  $\gamma_1\text{-Cu}_9\text{Ga}_4$ . This results in a GGI in  $\gamma\text{-Cu}_9(\text{In,Ga})_4$  of  $0.766\pm 0.007$  for  $\pm 1$  at.% Cu. This GGI is slightly above the maximum of 0.75 as shown in the Cu-In-Ga phase diagram (sup. Fig. E.4). Assuming the upper limit of the uncertainty of  $d_{330}$ , the GGI is about  $0.750\pm 0.007$ , and thus a reasonable composition regarding the ternary phase diagram. At 447 °C ( $t_2$ ), the  $\gamma_{1/2}\text{-Cu}_9\text{Ga}_4$  phase (yellow line in Fig. D.3) exhibits a  $d_{330}$  of  $0.2079\pm 0.001$  nm and shifts to smaller  $d_{330}$  getting closer to the reference of  $\gamma_{1,max}\text{-Cu}_9\text{Ga}_4$  with  $d=0.2076\pm 0.001$  nm (see Fig. D.3b)). The slightly higher  $d_{330}$  of  $\gamma_{1/2}\text{-Cu}_9\text{Ga}_4$ , compared with the  $\gamma_1\text{-Cu}_9\text{Ga}_4$  reference could theoretically correspond to a very small amount of In in  $\gamma_{1/2}\text{-Cu}_9\text{Ga}_4$ . However, the ternary phase diagram (sup. Fig. E.4) shows a miscibility gap in this region. Furthermore, the difference of the measured value to the reference is below the uncertainty. It is concluded, that the  $\gamma_{1/2}\text{-Cu}_9\text{Ga}_4$  phase is In free. Without In,  $d_{330}$  may determine the Cu to Ga ratio. However, it cannot be distinguished here between  $\gamma_1$ - and  $\gamma_2$ -phases (compare sup. Fig. E.2a)). Only the  $\gamma_3$ -phase is excluded, since it is not present anymore in the Cu-Ga phase diagram within the respective temperature regime (sup. Fig. E.1), before the 330 reflection vanishes at  $505\pm 14$  °C. Within the uncertainty of the measurement, the possible composition of  $\gamma_{1/2}\text{-Cu}_9\text{Ga}_4$  is  $36\pm 4$  at.% Ga.

The decreasing Ga fluorescence intensity and the transformation of  $\gamma\text{-Cu}_9(\text{In,Ga})_4$  to  $\gamma_{1/2}\text{-Cu}_9\text{Ga}_4$  (between 388 °C and 447 °C) with a lower reflection intensity are concluded to indicate a release of In (and corresponding Cu) from  $\gamma\text{-Cu}_9(\text{In,Ga})_4$ .

#### Identification and composition of $\text{Cu}_{2-x}\text{Se}$

In the following, indications for the presence of a  $\text{Cu}_{2-x}\text{Se}$  phase will be evaluated, since this phase is difficult to identify and has been found by others with *ex situ* analysis only.

At  $T_{\text{sub}}=388$  °C ( $t_1$ ), a shoulder occurs at the right side of the CIS 112 peak. This shoulder is best visible at 474 °C (Fig. D.6a)).

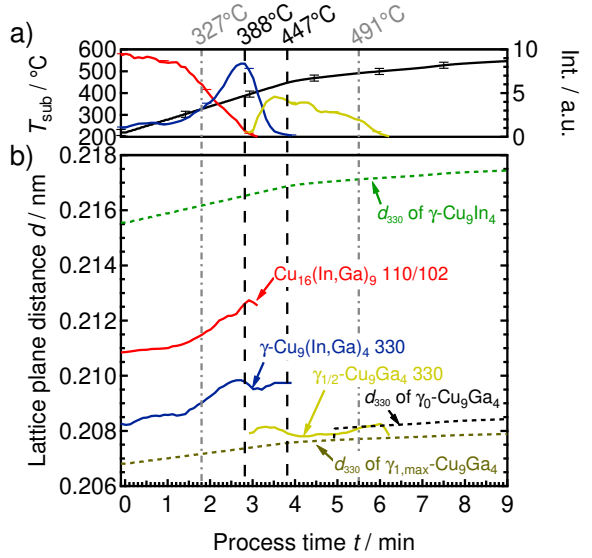


**Figure D.3.:** Evolution of the reflections of the metallic alloys over processing time, extracted from the EDXRD/EDXRF data in Fig. 4.3. a)  $T_{\text{sub}}$  and reflection intensities of  $\text{Cu}_{16}(\text{In,Ga})_9$  110/102 (red),  $\gamma$ - $\text{Cu}_9(\text{In,Ga})_4$  330 (blue),  $\gamma_{1/2}$ - $\text{Cu}_9\text{Ga}_4$  330 (yellow) and b) corresponding  $d_{hkl}$ . The dashed lines in b) represent the  $d_{330}$  of selected  $\gamma$ -phases calculated as function of  $T_{\text{sub}}$ , based on their value at RT and thermal expansion coefficient, given in literature (see sup. Tabs. E.2 and E.3).

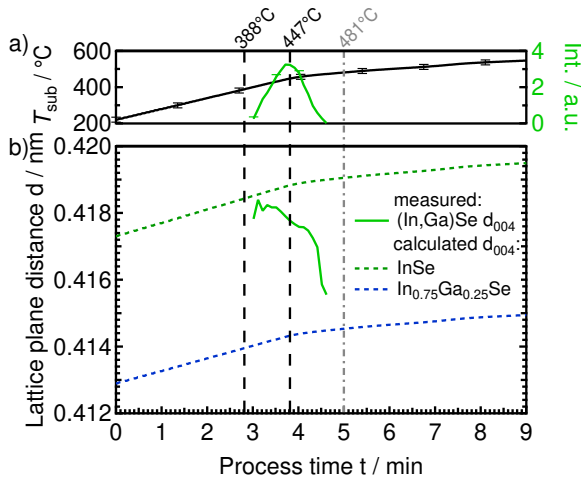


**Figure D.4:** Evolution of the (In,Ga)Se 004 reflection over process time, extracted from the EDXRD/EDXRF data in Fig. 4.3. a)  $T_{\text{sub}}$  and  $I_{004}$  of (In,Ga)Se. b) lattice plane distance of measured (In,Ga)Se 004. The dashed lines represent the  $d_{004}$  of InSe, GaSe from literature taking  $T_{\text{sub}}$  into account.  $(\text{In}_{0.75}\text{Ga}_{0.25})\text{Se}$  is linearly interpolated. The composition is estimated to  $(\text{In}_{0.94}\text{Ga}_{0.06})\text{Se}$  at 447 °C ( $t_2$ ) and a further decreasing ratio of In/Ga to higher temperatures.

A reasonable fit of this shoulder was possible at 474 °C but not throughout the respective process time. Therefore the area of the shoulder is not included when fitting the CIS 112 diffraction peak. Another diffraction peak could be observed during the same time, defined as Peak-A in Fig. D.5d). Peak-A is at the right side of the CIS 220/204 reflection. Thus, both reflections (shoulder and Peak-A) are likely to be related to the same phase. The shoulder vanishes until 481 °C, where  $d_{112}^{\text{CIS}}$  is in accordance with the Ga free reference (Fig. D.5c)). If the shoulder would have been a solid solution of CIGS, its vanishing would imply, that it diffuses into the CIS phase. In that case, the CIS phase would get Ga richer and its  $d_{112}$  must shift towards a lower value corresponding to CIGS. In contrast, it does shift to the CIS reference. Therefore, the reflections of the shoulder and Peak-A do not correlate to a Ga containing  $\text{Cu}(\text{In,Ga})\text{Se}_2$  phase. However, both shoulders can be explained by reflections of other phases, *i.e.*  $\text{CuIn}_3\text{Se}_5$  and  $\text{Cu}_{1.72}\text{Se}$ . This is demonstrated for the region close to the CIS 112 and 220/204 reflections at the instance of the spectrum acquired at 474 °C in Fig. D.6. The acquired

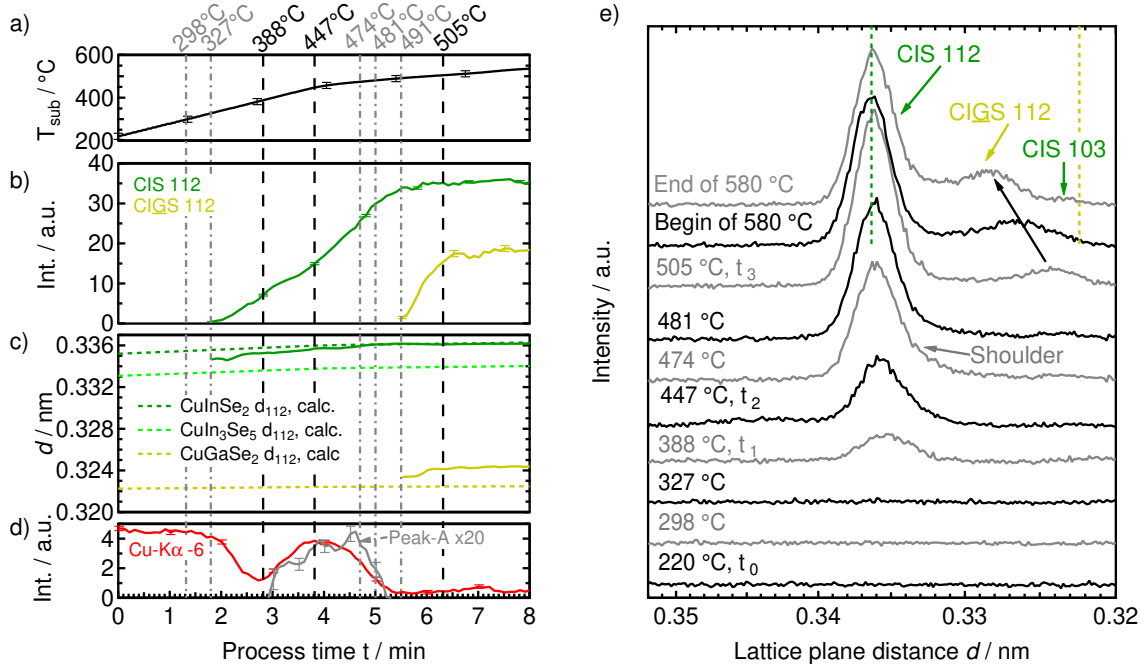


**Figure D.5.:** Evolution of reflections over process time, extracted from the EDXRD/EDXRF data in Fig. 4.3. Plotted are a)  $T_{\text{sub}}$ , b) integral intensities of CIS 112 and CIGS 112 with c) corresponding lattice plane distances  $d_{112}$ . The dashed lines in c) represent the  $d_{112}$  of the phases  $\text{CuInSe}_2$ ,  $\text{CuIn}_3\text{Se}_5$  and  $\text{CuGaSe}_2$  calculated as function of  $T_{\text{sub}}$ , based on their value at RT and thermal expansion coefficient, given in literature (see sup. Tabs. E.2 and E.3). d) Integral intensities of  $\text{Cu-K}\alpha$  fluorescence and Peak-A. e) EDXRD spectra at different temperatures vs. lattice plane distance. The vertical dashed lines indicate the  $d_{112}$  from reference pattern of  $\text{CuInSe}_2$  (green) and  $\text{CuGaSe}_2$  (yellow) at  $580^\circ\text{C}$ . The black arrow indicate the shift of the 112 reflection of CIGS. The shoulder at  $474^\circ\text{C}$  is magnified in Fig. D.6a).

spectrum can be described by a set of reflections with a Gaussian profile. Possible corresponding reflections of  $\text{CuIn}_3\text{Se}_5$  112 and  $\text{Cu}_{1.72}\text{Se}$  111 are overlapping (as well as  $\text{CuIn}_3\text{Se}_5$  204 and  $\text{Cu}_{1.72}\text{Se}$  220 overlap at Peak-A). The reflections of  $\text{Cu}_{2-x}\text{Se}$  were found to shift linearly with the composition ( $x = 0 - 0.28$ ) [Tonejc *et al.*, 1975, Tonejc, 1980, Ohtani *et al.*, 1998, Murray and Heyding, 1975] and can be overlapping with other reflections, e.g.  $\text{Cu}_{2-x}\text{Se}$  111 with  $(\text{In,Ga})\text{Se}$  101,  $\text{CuIn}_{1-x}\text{Ga}_x\text{Se}_2$  112 or  $\text{Cu}(\text{In}_{1-x}\text{Ga}_x)_3\text{Se}_5$  112. This made the assignment of Peak-A and the shoulder to a specific phase difficult.

Earlier studies with a similar *in situ* EDXRD setup could not identify a Cu-Se binary, but their *ex situ* Raman measurements on quenched samples showed a vibrational mode possibly explained by  $\text{Cu}_{2-x}\text{Se}$  [Mainz *et al.*, 2015b].  $\text{Cu}_{2-x}\text{Se}$  can transform to  $\text{CuSe}$  below  $377^\circ\text{C}$ .  $\text{CuSe}$  crystals were found on top of a film by SEM and EDX [Vieweg, 2007]. Cu-Se binaries were also found by others during selenization of metal/Se films [Hergert *et al.*, 2005] or in  $\text{H}_2\text{Se}$  [Hanket *et al.*, 2007]. Therefore it is concluded,

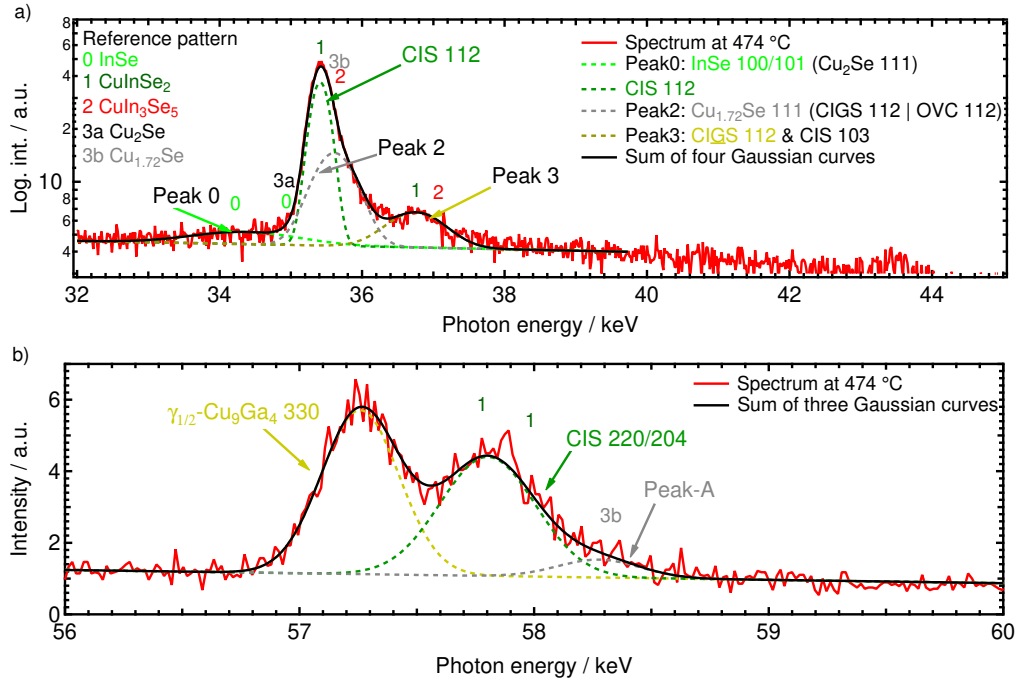


**Figure D.6.:** EDXRD spectrum at 474 °C for different energy ranges in a) and b). The signals can be described by a) four and b) three reflections with a Gaussian profile. A linear background is subtracted for the fit. Some reference peak positions are indicated with numbers.

that Peak-A and the shoulder correspond to Cu<sub>2-x</sub>Se. The composition is deduced to be Cu<sub>1.72</sub>Se by use of Vegard's law and literature values from [Tonejc *et al.*, 1975, Tonejc, 1980]. Fig. D.6 shows, that this assumption is sufficient to completely describe the signal and the evolution of  $I_{Cu-K\alpha}$ .

### Evaluation of depth position of $\gamma_{1/2}$ -Cu<sub>9</sub>Ga<sub>4</sub> at T<sub>2</sub>

The effect of the position of the  $\gamma_{1/2}$ -Cu<sub>9</sub>Ga<sub>4</sub> phase in the stack is studied at the instance of a few selected stacks. This will lead to the likeliest depth position of  $\gamma_{1/2}$ -Cu<sub>9</sub>Ga<sub>4</sub> and decrease the number of plausible permutations from generally 24 to 6. For simplicity, the possible Cu concentration range of  $64 \pm$  at.% Cu in  $\gamma_{1/2}$ -Cu<sub>9</sub>Ga<sub>4</sub> is set to the average value of 64 at.% Cu, for the moment. The  $\gamma_{1/2}$ -Cu<sub>9</sub>Ga<sub>4</sub> phase consists of Cu and Ga. It exhibits 92% of the total Ga amount. The main difference to all other phases is the high share of Ga. Hence, the  $I_{Ga-K\alpha}$  is a measure for the evaluation of calculated fluorescence intensities with varying depth position. Fig. D.7) shows, that the calculated  $I_{Ga-K\alpha}$  significantly increases with  $\gamma_{1/2}$ -Cu<sub>9</sub>Ga<sub>4</sub> phase positioned closer to the surface. Only the position of  $\gamma_{1/2}$ -Cu<sub>9</sub>Ga<sub>4</sub> at the back contact exhibits an  $I_{Ga-K\alpha}$  matching the experimental value. The stacking order above is irrelevant for

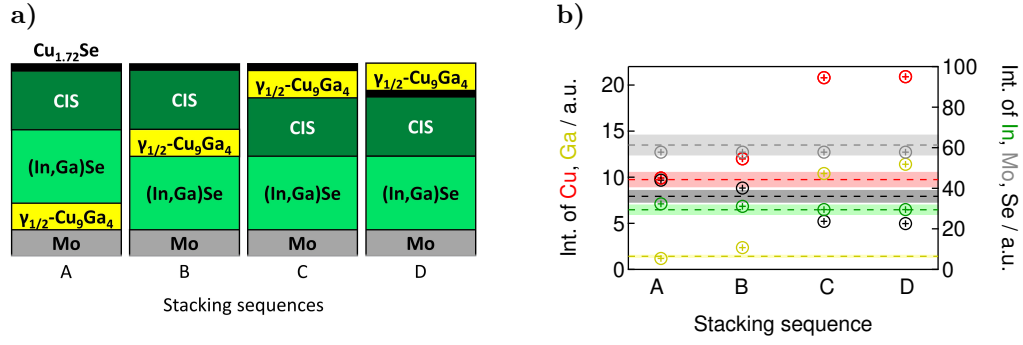


**Figure D.7.:** a) Stacking sequences with different positioning of  $\gamma_{1/2}$ -Cu<sub>9</sub>Ga<sub>4</sub> (64 at.% Cu) and b) corresponding calculated fluorescence intensities of Ga and Cu for each stack in contrast to the measured values at 447°C (dashed lines). The colors correspond to the element species as indicated at the left and right axis. The colored background ranges indicate the maximum uncertainty of the experimental values ( $\pm 8\%$ ).

$I_{Ga-K\alpha}$  and also the other fluorescence intensities. The position of  $\gamma_{1/2}$ -Cu<sub>9</sub>Ga<sub>4</sub> at the back contact is consistent with the presented reasons in Sec. 4.2.2.2.

### Evolution of calculated fluorescence intensities in the more surface sensitive detector:

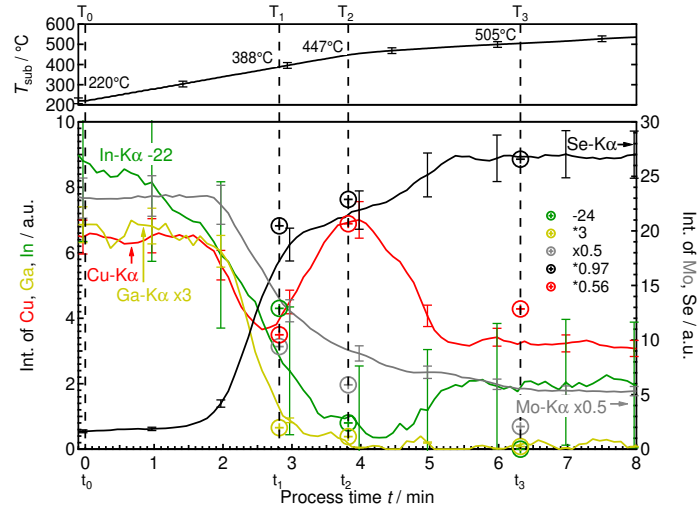


**Figure D.8.:** Experimental evolution and calculated fluorescence intensities for the respective stacking sequences (Fig. 4.11a) at  $T_{sub}$  of  $T_1=388^{\circ}C$  ( $t_1$ ),  $T_2=447^{\circ}C$  ( $t_2$ ) and  $T_3=505^{\circ}C$  ( $t_3$ ). The colors correspond to the element species as indicated at the left and right axis. The corresponding results regarding detector 1 can be found in Fig. 4.11b.

## D.4. Supplementary for Sec. 4.3

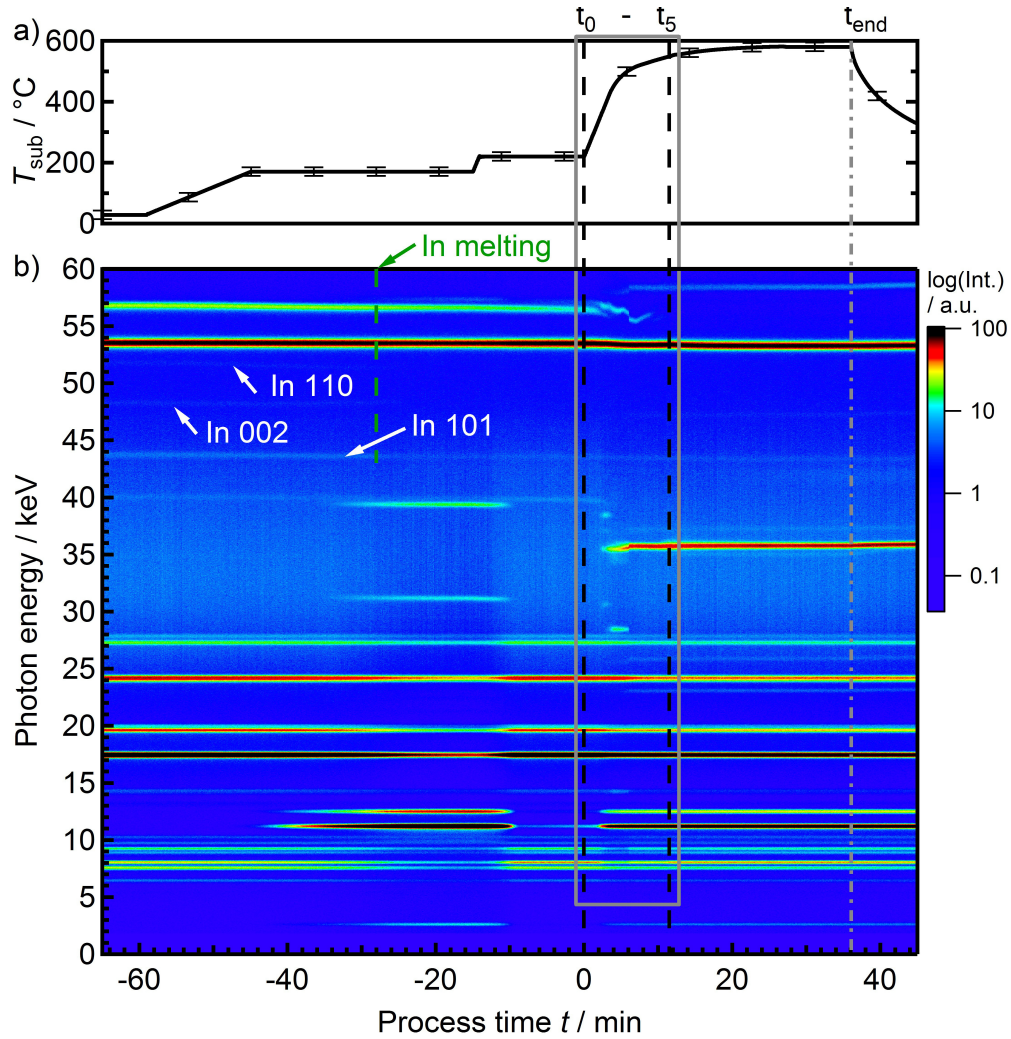


**Figure D.9.:** Evolution of intensities of phase reflection and fluorescence peaks over process time during selenization of a Cu-In-Ga multilayer precursor. a) Substrate temperature  $T_{\text{sub}}$  and b) time-resolved EDXRD/EDXRF signals over time. The intensity is color coded (as indicated on the right side). Points in time with characteristic signal intensities or changes are marked with dashed lines defined as  $t_i$  and  $t_0$  defines the start of the selenization process. The negative time indicates the process preparation before  $t_0$ . The measurements taken between 0 and 12 min (gray rectangle) are plotted in an extended scale in Fig. 4.12.

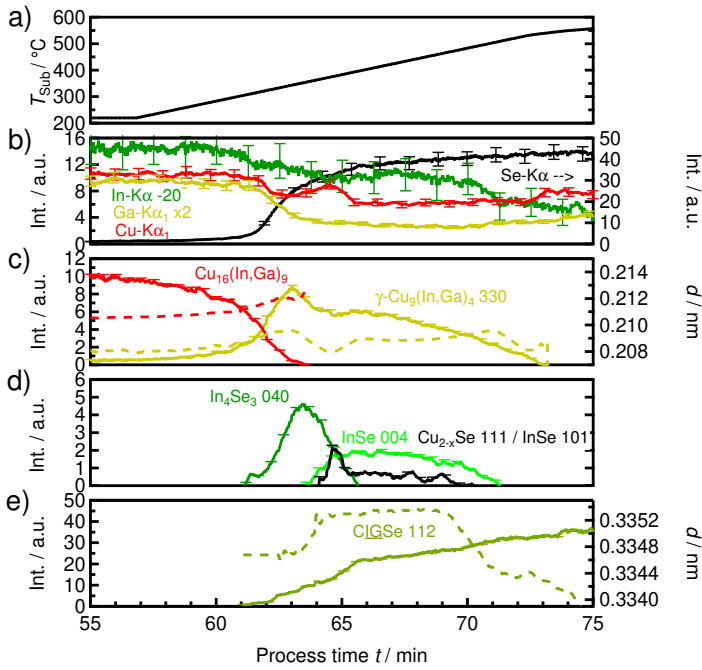


**Figure D.10:** Evolution of intensities of phase reflection and fluorescence peaks over process time during selenization of a Cu-In-Ga multilayer precursor. a) Substrate temperature profile. Evolution of integral intensities of b) fluorescence peaks and diffraction peaks of c) metallic alloys, d) binary selenides and e) CIGS. The final film exhibits an elemental depth distribution (especially regarding Ga) without final Ga segregation, similar to the one in Fig. 4.12. The difference to the previous process is the lower heating rate of  $0.1\text{ }^{\circ}\text{C/s}$  compared to the previous  $1\text{ }^{\circ}\text{C/s}$ . Dashed lines indicate the lattice plane distance (right axis).

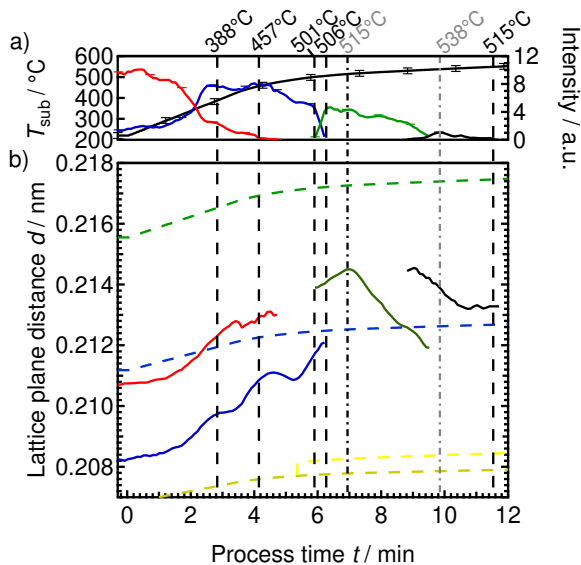


**Figure D.11:** Evolution of the reflections of the metallic alloys over process time, extracted from the EDXRD/EDXRF data in Fig. 4.12. a)  $T_{\text{sub}}$  and reflection intensities of  $\text{Cu}_{16}(\text{In,Ga})_9$  110/102 (red),  $\gamma\text{-Cu}_9(\text{In,Ga})_4$  330 (blue, green, black) and b) corresponding  $d_{330}$ . The dashed lines in b) represent the  $d_{330}$  of selected  $\gamma$ -phases calculated as function of  $T_{\text{sub}}$ , based on their value at RT and thermal expansion coefficient, given in literature (see sup. Tabs. E.2 and E.3).

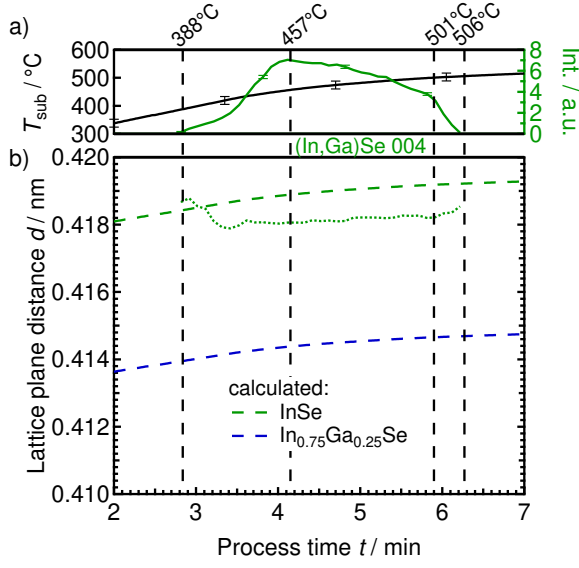


**Figure D.12:** Time evolution of the integral intensity and associated/related lattice plane distance of the (In,Ga)Se 004 reflection assigned in Fig. 4.12. a)  $T_{\text{sub}}$  and b) lattice plane distance (dotted, left axis) and intensity (line, right axis) of the observed (In,Ga)Se 004. The dashed lines represent the  $d_{004}$  of InSe, GaSe from literature taking  $T_{\text{sub}}$  into account.  $(\text{In}_{0.75}\text{Ga}_{0.25})\text{Se}$  is linearly interpolated. Initially (In,Ga)Se is nearly Ga free and increases its Ga content to  $(\text{In}_{0.95}\text{Ga}_{0.05})\text{Se}$  at its maximum 004 diffraction intensity at 457 °C ( $t_2$ ). During the decreasing  $I_{004}$ , its composition remains the same. Compare phase diagram of InSe-GaSe in Fig. E.7.

**Table D.1.:** Detailed composition of the  $\gamma\text{-Cu}_9(\text{In,Ga})_4$  phase for the different amounts of Cu assumed and calculated regarding the lattice plane distance of the 330 reflection at certain substrate temperatures ( $T_{\text{sub}}$ ), as described on page 157.

$T_{\text{sub}}$ / °C	$t_i$	Cu concentration / at.% Cu	composition of $\gamma\text{-Cu}_9(\text{In,Ga})_4$
388	$t_1$	66	$\text{Cu}_9(\text{In}_{0.27}\text{Ga}_{0.73})_{4.64}$
		67.5	$\text{Cu}_9(\text{In}_{0.28}\text{Ga}_{0.72})_{4.33}$
		69	$\text{Cu}_9(\text{In}_{0.29}\text{Ga}_{0.71})_{4.04}$
457	$t_2$	66	$\text{Cu}_9(\text{In}_{0.36}\text{Ga}_{0.64})_{4.64}$
		68	$\text{Cu}_9(\text{In}_{0.37}\text{Ga}_{0.63})_{4.24}$
		70	$\text{Cu}_9(\text{In}_{0.38}\text{Ga}_{0.62})_{3.86}$
501	$t_3$	66	$\text{Cu}_9(\text{In}_{0.43}\text{Ga}_{0.57})_{4.64}$
		68	$\text{Cu}_9(\text{In}_{0.44}\text{Ga}_{0.56})_{4.24}$
		70	$\text{Cu}_9(\text{In}_{0.45}\text{Ga}_{0.55})_{3.86}$
506	$t_4$	61	$\text{Cu}_9(\text{In}_{0.42}\text{Ga}_{0.58})_{5.75}$

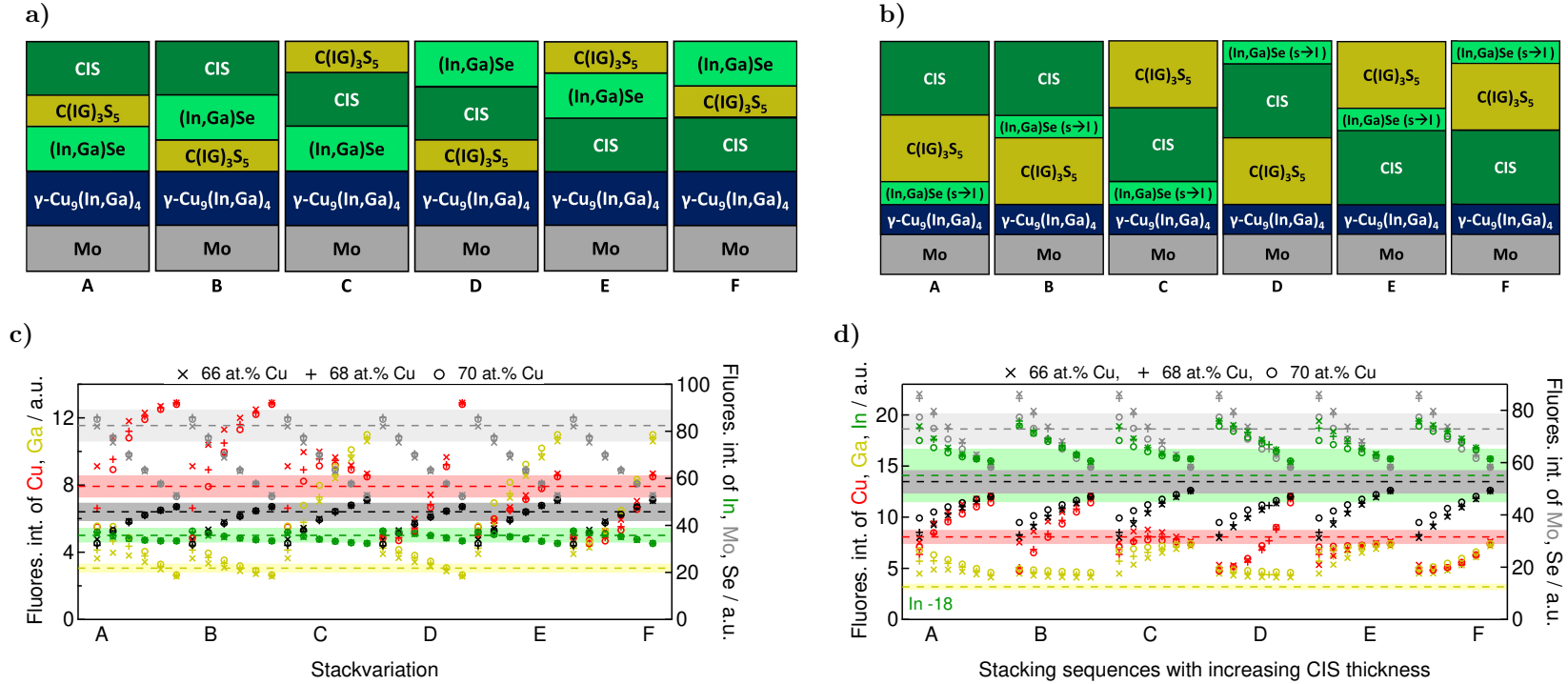


**Figure D.13.:** Possible permutations of the stacking sequence with a C(IG)<sub>3</sub>S<sub>5</sub> phase at a)  $T_{\text{sub}}=457^\circ\text{C}$  ( $t_2$ ) and at b)  $T_{\text{sub}}=501^\circ\text{C}$  ( $t_3$ ). c-d) Corresponding calculated fluorescence intensities (each with six values from lower to upper limit of the CIS thickness). The colors correspond to the element species as indicated at the left and right axis. x, +, o indicate the results for 66, 68 and 70 at.% Cu in  $\gamma$ -Cu<sub>9</sub>(In,Ga)<sub>4</sub>. Dashed lines illustrate the observed intensities from experiment at c)  $t_2$  and at d)  $t_3$ . The colored background ranges indicate the maximum uncertainty of the experimental values ( $\pm 8\%$ ). x, +, o indicate the results for different Cu concentrations in  $\gamma$ -Cu<sub>9</sub>(In,Ga)<sub>4</sub>. All  $I_{\text{In}-K\alpha}$  values in d) are reduced by 18 for a better visibility of the deviations.

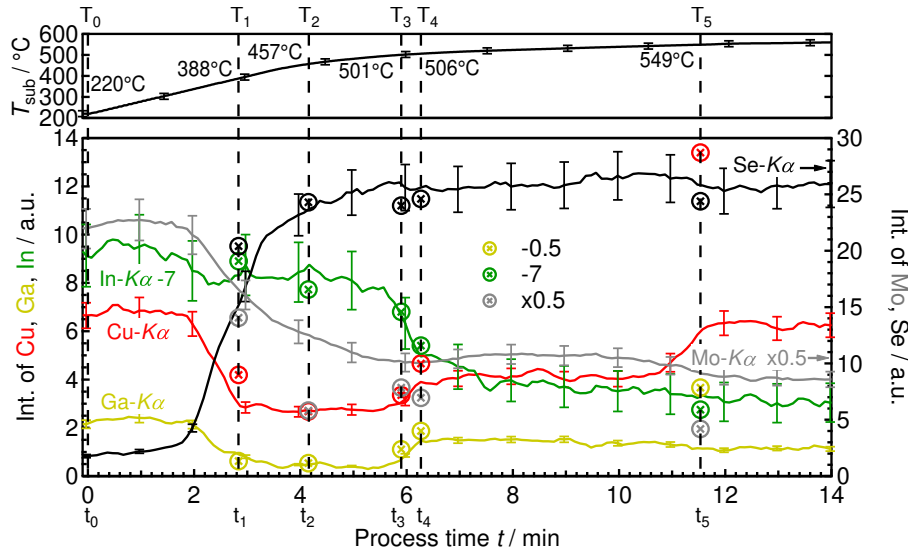


**Figure D.14.:** Calculated fluorescence intensities for the second detector of the respective stacking sequences (Fig. 4.22a) for the points in time at  $T_{\text{sub}}=388^\circ\text{C}$  ( $t_1$ ),  $T_{\text{sub}}=457^\circ\text{C}$  ( $t_2$ ),  $T_{\text{sub}}=501^\circ\text{C}$  ( $t_3$ ),  $T_{\text{sub}}=506^\circ\text{C}$  ( $t_4$ ) and  $T_{\text{sub}}=549^\circ\text{C}$  ( $t_5$ ) are shown together with the measured fluorescence intensities. The corresponding for detector 1 are shown in Fig. 4.22.

The Ga homogenization occurs at a temperature of  $501^\circ\text{C}$ , which is close to the temperature roughly approximated from the *ex situ* experiments to be above  $520^\circ\text{C}$  in the atmospheric selenization tool [Schmidt *et al.*, 2017]. It is likely to be the same mechanisms and not correlated to the loss of In.

#### D.4.1. Presence of a $\text{Cu}(\text{In,Ga})_3\text{Se}_5$ phase instead of a $\text{Cu}(\text{In,Ga})\text{Se}_2$ phase

Here, the phase mixture at  $T_{\text{sub}}=457^\circ\text{C}$  ( $t_2$ ) consists of  $\gamma\text{-Cu}_9(\text{In,Ga})_4$ ,  $(\text{In,Ga})\text{Se}$ , CIS and CIGS. The linear equation system can be solved for 66 at.% Cu and 68 at.% Cu in  $\gamma\text{-Cu}_9(\text{In,Ga})_4$ , but there is no solution for 70 at.% Cu. The mathematical set of solutions can be narrowed down, because there are solutions with no amount of a phase that was observed by *in situ* EDXRD. The reflection intensity of  $\gamma\text{-Cu}_9(\text{In,Ga})_4$  330 was similar to before at  $T_{\text{sub}}=388^\circ\text{C}$  ( $t_1$ ). The dimension of crystal amount could be similar too before. This limits the phase amount to the approximated range of fraction, with the CIS fraction as parameter, between 0.05 and 0.055 CIS for 66 at.% Cu. And the range of fraction for 68 at.% Cu is narrowed down between 0.009 and 0.017. The relative phase amount of CIS at  $T_{\text{sub}}=388^\circ\text{C}$  was concluded to be 0.06. This can not be used to reduce the range here, because CIS might have incorporated Ga and changed to the CIGS phase. But the total sum of both CIGS phases should

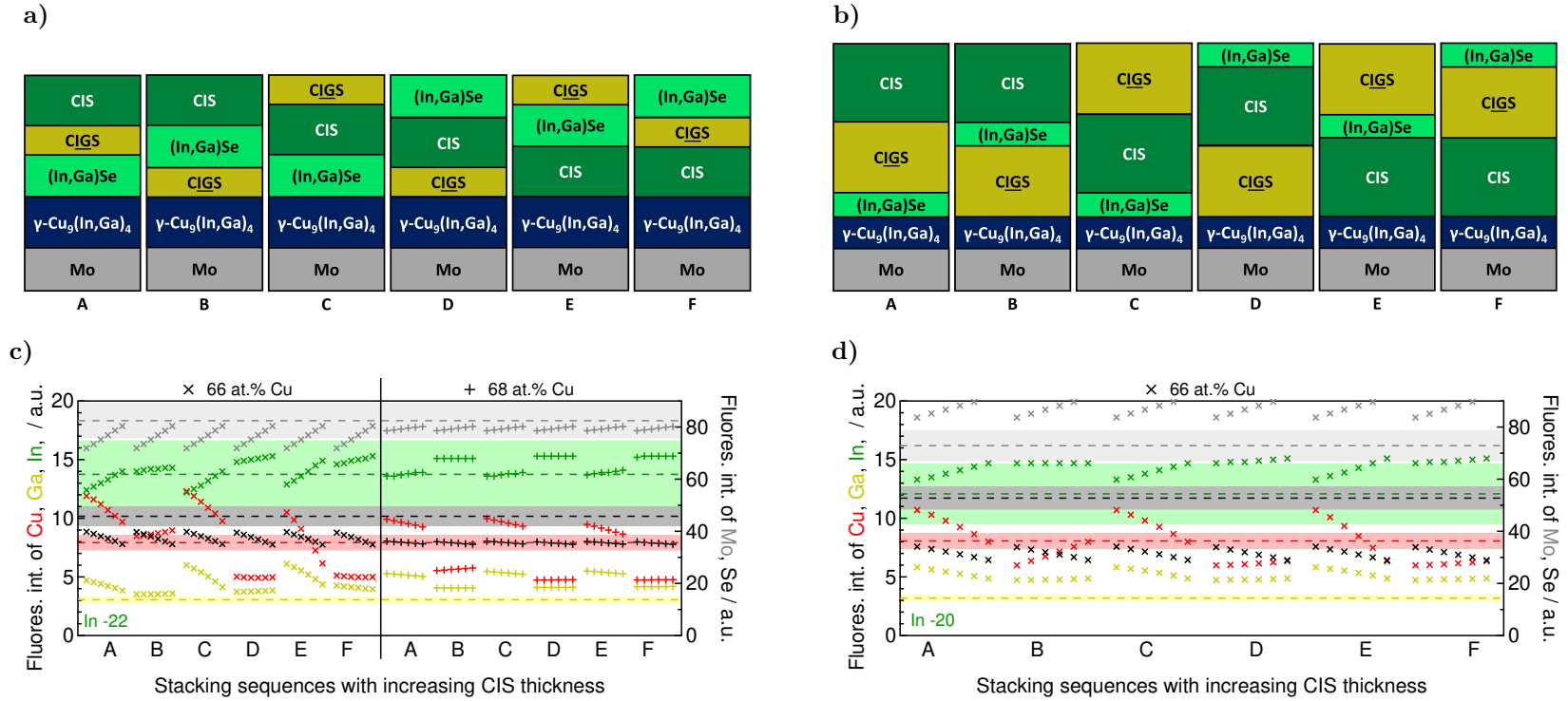


**Figure D.15.:** Possible permutations of the stacking sequence with a CIGS phase at a)  $T_{\text{sub}}=457^\circ\text{C}$  ( $t_2$ ) and at b)  $T_{\text{sub}}=501^\circ\text{C}$  ( $t_3$ ). c-d) Corresponding calculated fluorescence intensities (each with six values from lower to upper limit of the CIS thickness). The colors correspond to the element species as indicated at the left and right axis. c) x and + indicate the results for 66 and 68 at.% Cu in  $\gamma\text{-Cu}_9(\text{In,Ga})_4$ . d) x indicates the results for 66 at.% Cu in  $\gamma\text{-Cu}_9(\text{In,Ga})_4$ . Dashed lines illustrate the observed intensities from experiment at  $t_2$ . The colored background ranges indicate the maximum uncertainty of the experimental values ( $\pm 8\%$ ). All  $I_{\text{In-K}\alpha}$  values are reduced in c) by 22 and in d) by 20 for a better visibility of the deviations.

be bigger than the 0.06 before. This reduced the upper limit from 0.017 to 0.011 for 68 at.% Cu. The small amount of CIS results in very similar fluorescence intensities for the stacking sequences A, C and and, as well as for B, D and F, respectively (right side in Fig. D.15c).

The stacking sequence with the best matching  $I_{Cu-K\alpha}$  is E in Fig. D.15c but its difference for  $I_{Ga-K\alpha}$  is much higher than for B, which is outweighing. Stacking sequence E is unlikely.

At  $T_{\text{sub}}=501\text{ }^{\circ}\text{C}$  ( $t_3$ ), the linear equation system can only be solved for 66 at.% Cu in  $\gamma\text{-Cu}_9(\text{In,Ga})_4$  (and not for 68 at.% Cu and 70 at.% Cu). This is also the case for assuming a lower CGI of 0.9 instead of 1 in the chalcopyrite phases. The same loss of In as in Sec. 4.3.2 is assumed.

At  $T_{\text{sub}}=457\text{ }^{\circ}\text{C}$ , the only stacking sequence with CIGS slightly matching the measurement was sequence B. It would be reasonable, if at  $T_{\text{sub}}=501\text{ }^{\circ}\text{C}$  it is the same here as before. But the stacking sequence B shows no good accordance. The calculated  $I_{Mo-K\alpha}$  is always above the measured one, in contrast to the calculations for all other  $T_{\text{sub}}$  with a  $I_{Mo-K\alpha}$  smaller the measured one.

The set of solutions is between 0 bis 0.02586 CIS, with a phase fraction of CIGS decreasing to 0 for the upper limit of 0.02586 CIS. The fluorescence intensities closest to the measured values with maximum CIS amount is stacking sequence A, but it exhibits no CIGS amount and is therefore also unlikely, Fig. D.15d.

Overall, the maximum phase amount of CIS is only half the size it was found at  $T_{\text{sub}}=388\text{ }^{\circ}\text{C}$  ( $t_1$ ). The reflection intensity of CIS 112 increased by more than 3 times from  $T_{\text{sub}}=388\text{ }^{\circ}\text{C}$  (5.2) until  $T_{\text{sub}}=501\text{ }^{\circ}\text{C}$  (15.9) and should be related somehow to the phase amount. Thus, the whole set of solutions of the linear equation system is unlikely, if the fit of the CIS + CIGS signal is accurate.

The decreasing  $I_{In-K\alpha}$ , as measured, might indicate the time frame for the observed loss of In, thus, assuming a decreasing In amount, decreases  $I_{Se-K\alpha}$  and increases  $I_{Mo-K\alpha}$ , which is increasing the differences of the results even more. Only  $I_{Cu-K\alpha}$  is getting closer to the measured value, but can not outweigh the other differences of the fluorescence intensities.

No stack could be found with CIGS to reproduce the evolution of the measured elemental fluorescence intensities at  $T_{\text{sub}}=457\text{ }^{\circ}\text{C}$  and  $T_{\text{sub}}=501\text{ }^{\circ}\text{C}$ .

## D.5. Supplementary for Sec. 4.5

### D.5.1. Influence of total pressure on the film evolution during selenization

The influence of the total pressure on the selenization is evaluated by applying vacuum and atmospheric ( $N_2$ ) background conditions in the closed vacuum selenization tool. Two *in situ* EDXRD/EDXRF measurements were performed.

Fig. D.16 shows the evolution of integral peak intensities from reflection and fluorescence signals during selenization processes with a starting pressure of a) 100 mbar ( $N_2$ ) and b) in vacuum at  $\approx 10^{-5}$  mbar. The process with initial pressure of 100 mbar is raising its pressure during heating to nearly atmospheric pressure. Both processes result in similar final fluorescence and reflection intensities. The final spectra of both processes exhibit a CIS 112 reflection and a CIGS 112 reflection. No fundamental difference was observed. In case of the vacuum-based process, the CIGS reflection is getting slightly closer to the CIS 112 reflection. In summary, both processes resulted in Ga segregation. The kinetics are not fundamentally different by a different background pressure.

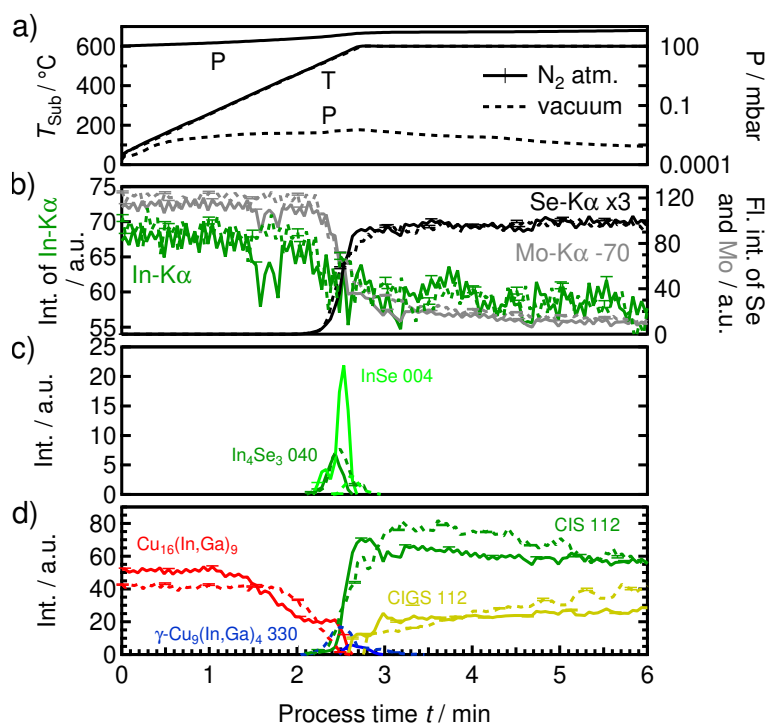


**Figure D.16.:** Evolution of reflection and fluorescence intensities over process time during selenization at different initial atmospheric (line) and low (dashed) pressure, extracted from the EDXRD/EDXRF measurement data shown in Fig. D.17. a)  $T_{\text{sub}}$  and pressure. Integral intensities of b) fluorescence as well as c) and d) reflection peaks.

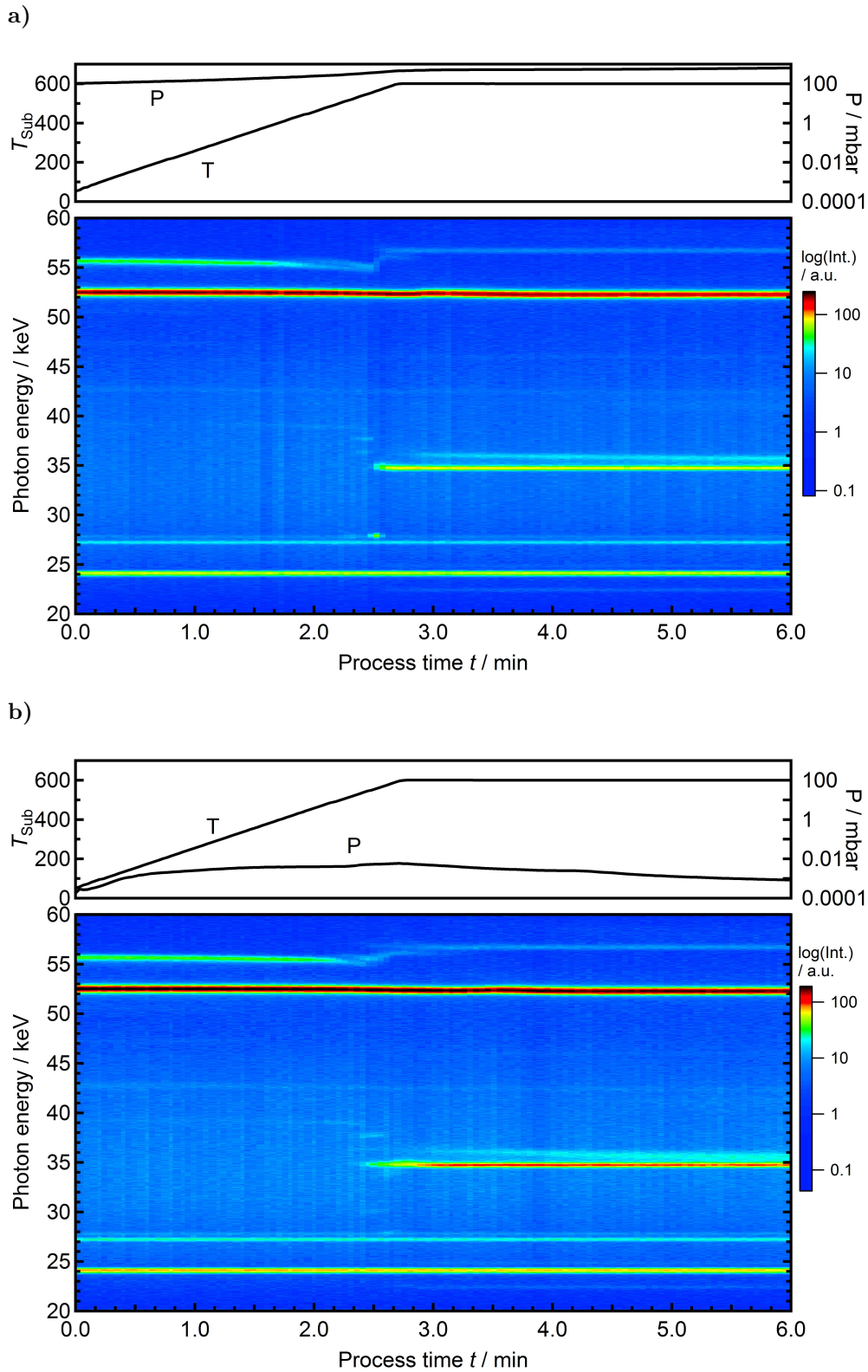


**Figure D.17.:** Evolution of reflection and fluorescence intensities over process time during selenization at different starting pressures. a) atmospheric and b) vacuum background pressure.  $T_{\text{sub}}$  and pressure on top of the EDXRD/EDXRF signal (color coded intensity).



# E. Data from literature

## Phase diagrams

The following phase diagrams are shown here: Phase diagrams in Ch. 1:

- Cu-Ga (Fig. E.1)
- $\gamma_{1/2/3}$ -Cu<sub>9</sub>Ga<sub>4</sub> a vs. Ga at.% (Fig. E.2a)
- $\gamma_{1/0}$ -Cu<sub>9</sub>Ga<sub>4</sub> a vs. T (Fig. E.2b)
- Cu-In (Fig. E.3)
- Cu-In-Ga (Fig. E.4)
- Cu-Se (Fig. E.5)
- In-Se (Fig. E.6)
- InSe-GaSe (Fig. E.7)
- Cu-In-Ga at 150 °C (Fig. 1.5a)
- Cu-In-Ga at 550 °C (Fig. 1.5b)
- Cu-In-Se at 300 °C (Fig. 1.6a)
- In<sub>2</sub>Se<sub>3</sub>-Cu<sub>2</sub>Se (Fig. 1.6b)

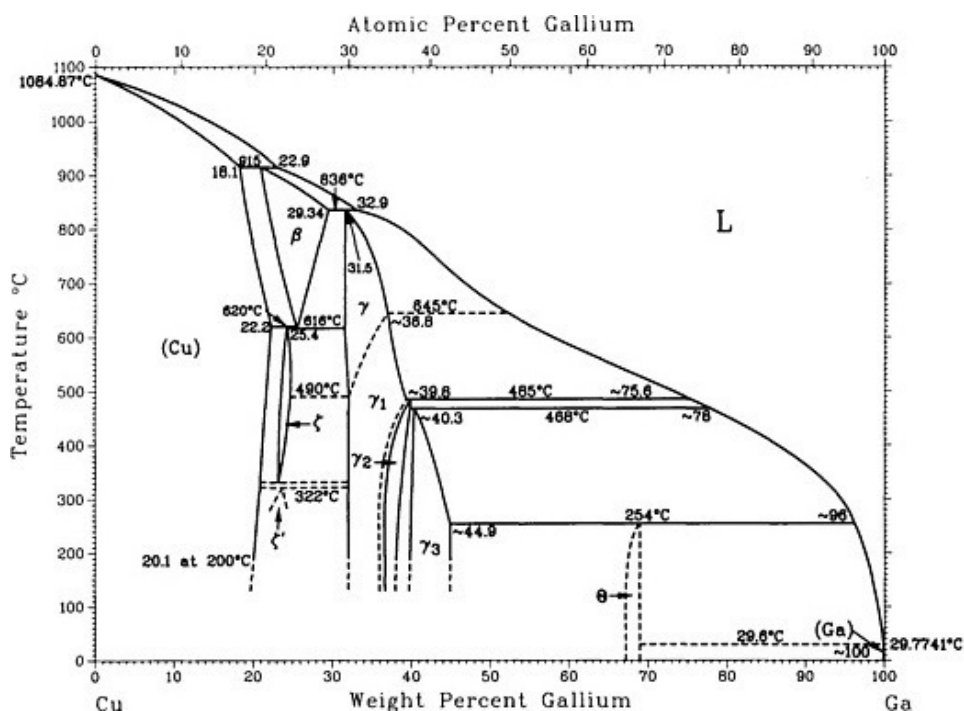


**Figure E.1.:** Phase diagram of Cu-Ga, various  $\gamma_i$ -Cu<sub>9</sub>Ga<sub>4</sub> phases.  $\gamma$  is denoted as  $\gamma_0$  during this work, [Subramanian and Laughlin, 1992].

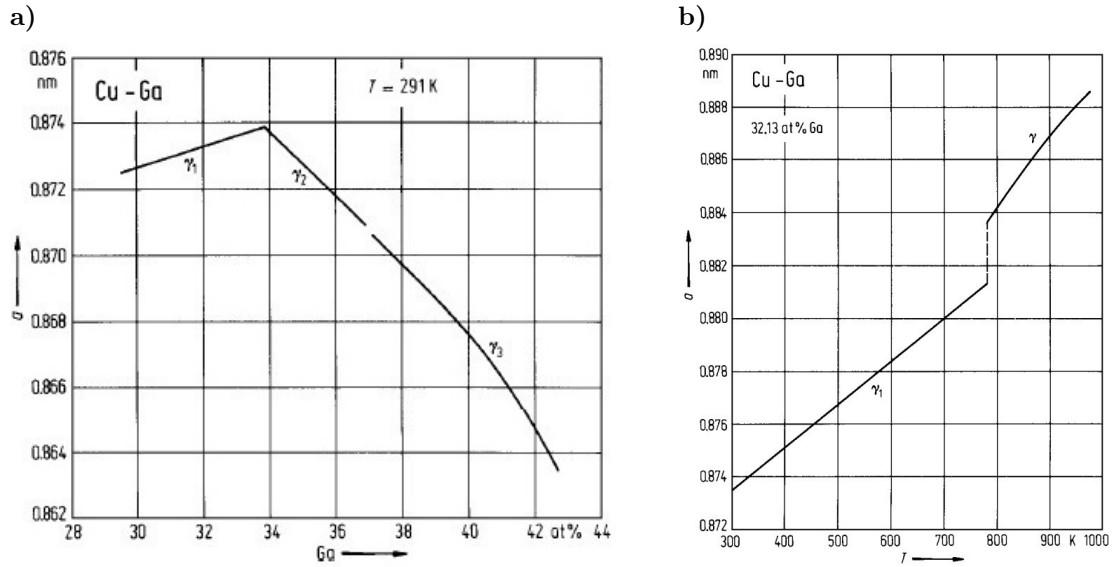


**Figure E.2.:** a) Lattice parameter for cubic  $\gamma_1$ ,  $\gamma_2$  and  $\gamma_3$  with the varying Ga concentration at 18 °C [Predel, 1994]. An overview of experimental data can be found on page 22 in [Hölzing, 2013]. b) lattice parameter for the cubic solid solution containing 32.13 at.% Ga vs. temperature [Predel, 1994]. The corresponding phase diagram of Cu-Ga is shown in Fig. E.1.

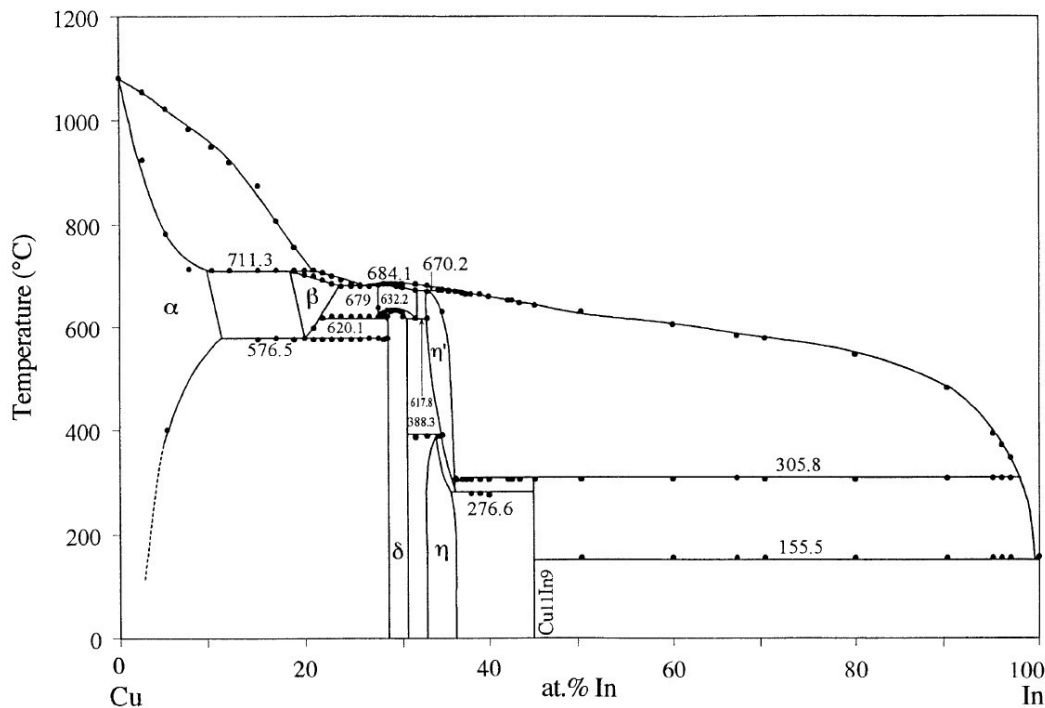


**Figure E.3.:** Phase diagram of Cu-In [Bahari *et al.*, 2003]. The  $\delta$  phase transforms to  $\gamma\text{-Cu}_9\text{In}_4$ , which is not marked.  $\eta$ :  $\text{Cu}_{16}\text{In}_9$ ,  $\alpha$ : Cu,  $\beta$ :  $(\text{Cu,In})_1$ .

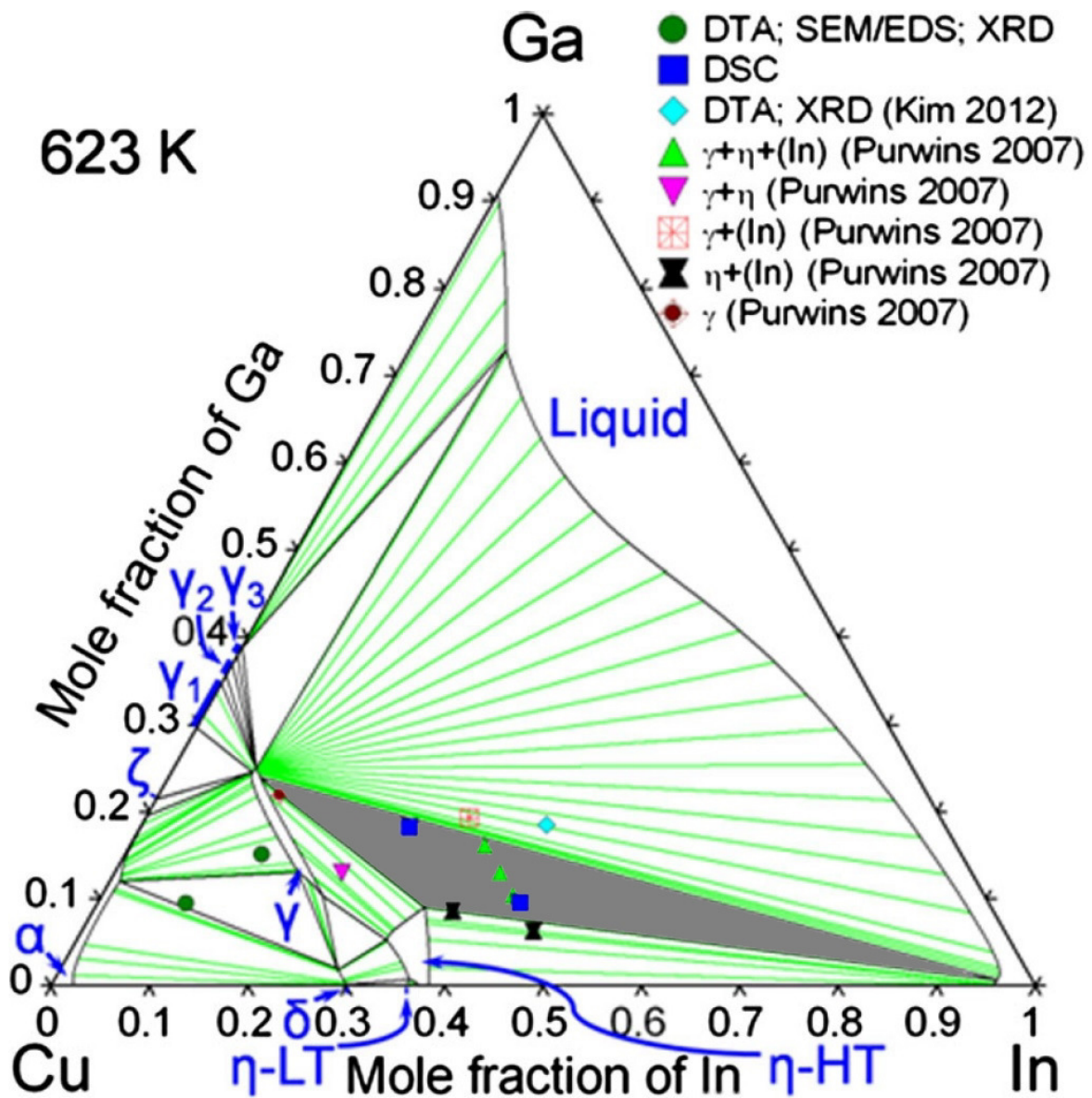


**Figure E.4.:** Calculated isothermal ternary phase diagram of Cu-In-Ga from Muzzillo *et al.* (2015) at 350 °C (623 K). The greek letters correspond to the following compounds:  $\alpha$ : Cu,  $\gamma_i$ : different  $\text{Cu}_9\text{Ga}_4$  (see text and Fig. E.1) with  $\gamma$  which is denoted as  $\gamma_0$  in this work, a low (LT) and high (HT) temperature phase of  $\eta$ :  $\text{Cu}_{16}\text{In}_9$ ,  $\phi$ :  $\text{Cu}_{11}\text{In}_9$ ,  $\zeta$ :  $\text{Cu}_{778}\text{Ga}_{222}$ . The area of the ternary phase mixture of  $\text{In}+\text{Cu}_{16}\text{In}_9+\text{Cu}_9(\text{In,Ga})_4$  is colored in gray.

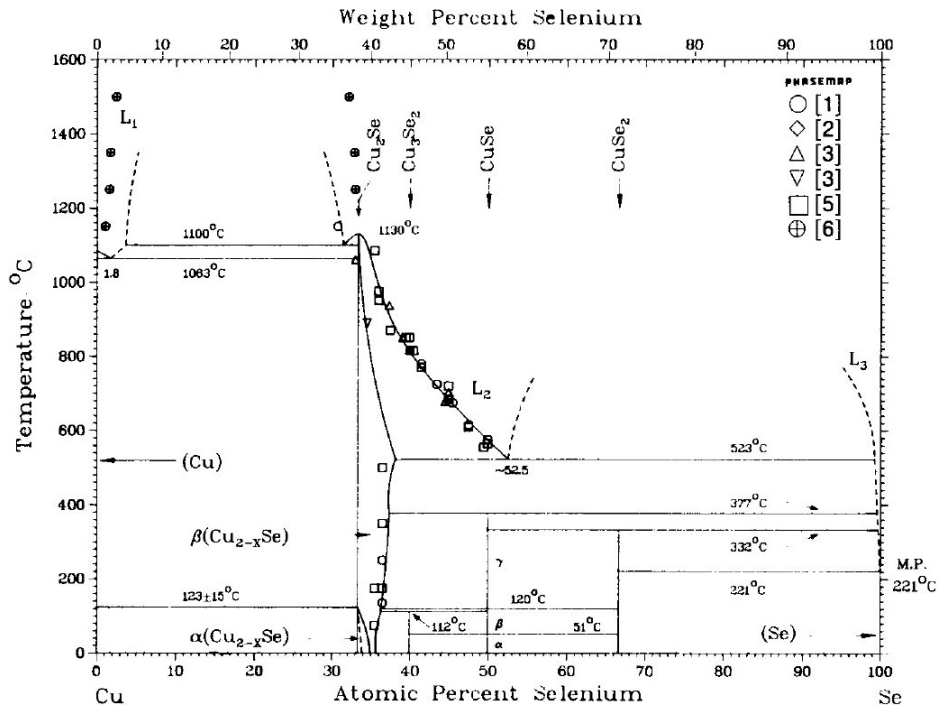


Figure E.5.: Phase diagram of Cu-Se [Chakrabarti and Laughlin, 1981].

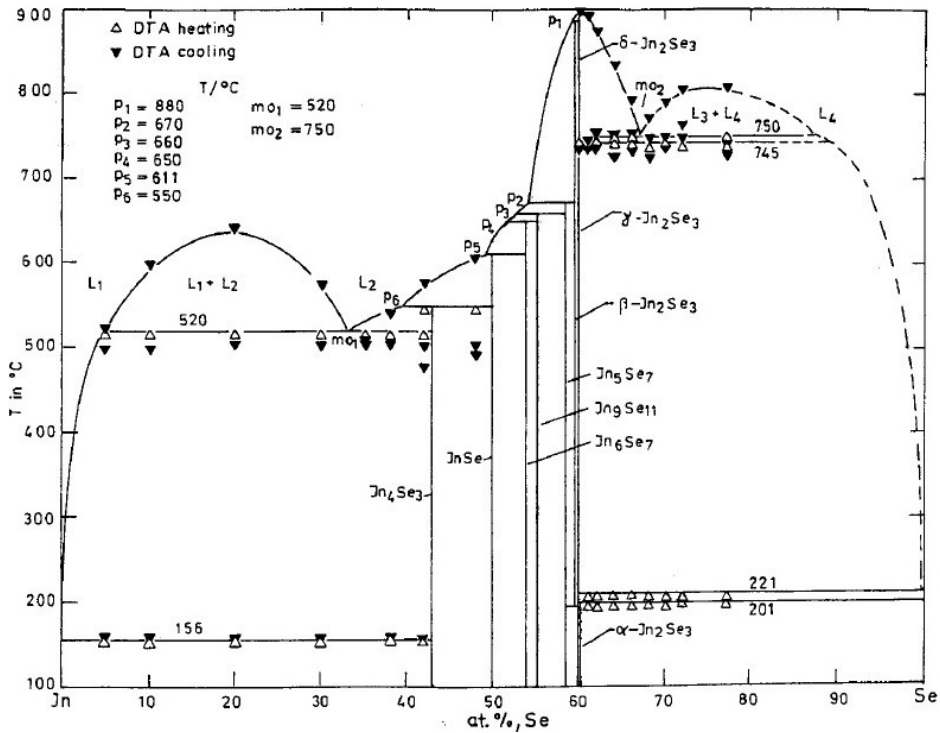
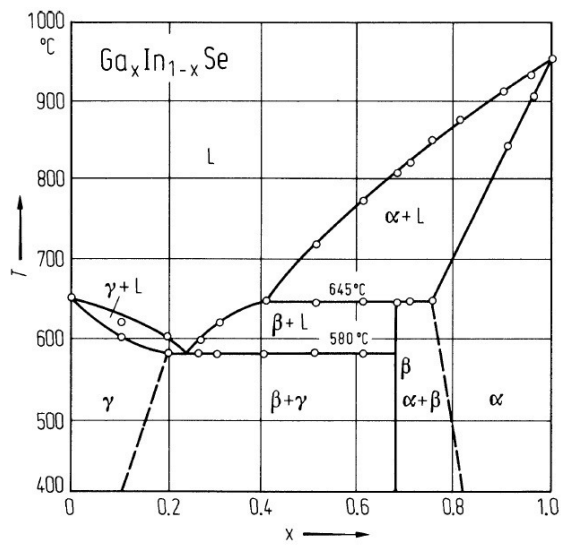


Figure E.6.: Phase diagram of In-Se [Gödecke *et al.*, 1998] with monotectic reaction at 520°C and peritectic phases:  $\text{In}_4\text{Se}_3$  (p6) at 550°C and InSe (p5) at 611°C.



**Figure E.7.:** Phase diagram of the pseudobinary GaSe-InSe system with temperature versus composition of  $x$  in  $\text{Ga}(x)\text{In}(1-x)\text{Se}$  [Muschinsky and Pawlenko, 1969].  $\alpha$  and  $\gamma$  are mixed crystals.  $\beta$  is the unstable component  $\text{Ga}_2\text{InSe}_3$ . Lattice constants for different  $x$  in  $\text{Ga}(x)\text{In}(1-x)\text{Se}$  are listed in [Madelung *et al.*, 1998].

## Data needed for the program EDXRdfit

For use of the program EDXRdfit, the amounts of atoms per area (element quantities) are needed. They are measured by *ex situ* XRF (at.%) and transformed to wt.% by  $w_i = \frac{a_i \cdot x_i}{\sum_{i=1}^4 a_i \cdot x_i}$ , with standard atomic weight  $a_i$  for the elements  $i$  [Cu (63.54 u), In (114.82 u), Ga (69.72 u), Se (78.96 u)], weight percentage  $w_i$ , atomic percentage  $x_i$ , avogadro constant  $N_A = 6.02214 \cdot 10^{23} \text{ mol}^{-1}$ , density of absorber  $\rho_{\text{absorber}}$  and thickness of absorber  $D_{\text{absorber}}$ . The quantity of Mo is calculated from the measured thickness  $D$  in nm, standard atomic weight for element  $i$  of  $a_{\text{Mo}} = 95.94 \text{ u}$ :  $N_{\text{Mo}} = D \cdot N_A \cdot a_{\text{Mo}}$ .

$$\text{Area density: } N_i = \rho_{\text{absorber}} \cdot D_{\text{absorber}} \cdot w_i / a_i \cdot N_A \quad (\text{E.1})$$

**Table E.1.:** Atomic densities of observed phases for use in the EDXRdfit program. Densities are calculated from the crystallographic data, taken from the references. Both references for  $\text{Cu}_2\text{Se}$  and  $\text{Cu}_{1.8}\text{Se}$  use the same space group Fm3m. For a  $\gamma$ - $\text{Cu}_9(\text{In}_{1-x}\text{Ga}_x)_4$  phase, the atomic density is weighted with the Ga to In ratio and the values of  $\gamma_i$ - $\text{Cu}_9\text{Ga}_4$  and  $\gamma$ - $\text{Cu}_9\text{In}_4$ . It is not distinguished between different  $\gamma_i$ - $\text{Cu}_9\text{Ga}_4$  ( $i=0,1,2,3$ ) due to the lack of information. For  $\text{Cu}_{16}\text{Ga}_9$ , the  $\rho$  ratio of  $\text{Cu}_9\text{Ga}_4/\text{Cu}_9\text{In}_4$  is assumed as an approximation.

Phase	$V_{\text{unit cell}} / \text{nm}^3$	No. of atoms per unit cell	Atomic density $\rho / \text{nm}^{-3}$	ICDD & Reference
$\text{Cu}_{16}\text{In}_9$	0.096	6	62.5	[Laves <i>et al.</i> , 1941], [Mainz, 2008]
$\gamma$ - $\text{Cu}_9\text{In}_4$	0.753	52	69.1	[Che and Ellner, 1992]
$\gamma_i$ - $\text{Cu}_9\text{Ga}_4$	0.669	52	77.7	[Stokhuyzen <i>et al.</i> , 1974]
$\text{CuGaSe}_2$	0.347	16	46.1	[Mandel <i>et al.</i> , 1977]
$\text{CuInSe}_2$	0.389	16	41.1	[Knight, 1992]
$\text{CuIn}_3\text{Se}_5$	0.382	15.3	40.1	[Marín <i>et al.</i> , 1998]
$\text{CuGa}_3\text{Se}_5$	0.331	15.3	46.2	[Marín <i>et al.</i> , 1998]
$\text{Cu}_{1.8}\text{Se}$	0.2023	11.2	55.4	at 360 °C, [Oliveria <i>et al.</i> , 1988]
$\text{Cu}_2\text{Se}$	0.2023	12	59.3	at 360 °C, [Oliveria <i>et al.</i> , 1988]
In	0.052	2	38.5	[Smith and Schneider, 1964]
In (l)			36.1	[Williams and Miller, 1950]
$\text{In}_4\text{Se}_3$	0.768	28	36.5	[Hogg <i>et al.</i> , 1973]
InSe	0.231	8	34.6	[Popović <i>et al.</i> , 1979]
Mo	0.031	2	64.5	[Swanson and Tatge, 1953]
$\text{MoSe}_2$	0.121	6	49.6	[Cech <i>et al.</i> , 1973]
Se (crys.)	0.0818	3	36.7	[Swanson and et al., 1955]

**Table E.2.:** Spacegroup and lattice parameter for the observed phases in the EDXRD measurements.

Compound	Spacegroup	Lattice const. / Å	ICDD & Reference
Cu <sub>16</sub> In <sub>9</sub> /Cu <sub>2</sub> In	194	a=b=4.2943 c=5.2328	03-065-0704 [Che and Ellner, 1992]
γ <sub>1</sub> -Cu <sub>9</sub> Ga <sub>4</sub>	215	a=b=c=8.7470	[Stokhuyzen <i>et al.</i> , 1974]
Cu <sub>9</sub> In <sub>4</sub> (RT)	215	a=b=c=9.0970	[Che and Ellner, 1992]
Cu <sub>9</sub> In <sub>4</sub> (650 °C)	215	a=b=c=9.2503	[Hume-Rothery <i>et al.</i> , 1951]
Cu <sub>9</sub> (In <sub>1-x</sub> Ga <sub>x</sub> ) <sub>4</sub>	215	a=b=c=8.95	[Mainz, 2008]
CuGaSe <sub>2</sub>	122	a=5.614 c=11.022	01-076-1735 [Mandel <i>et al.</i> , 1977]
CuInSe <sub>2</sub>	122	a=5.7810 c=11.6422	01-081-1936 [Knight, 1992]
CuIn <sub>3</sub> Se <sub>5</sub>	112	a=b=5.7541 c=11.538	00-051-1221 [Marín <i>et al.</i> , 1998]
CuGa <sub>3</sub> Se <sub>5</sub>	112	a=b=5.4996 c=10.946	[Marín <i>et al.</i> , 1998]
Cu <sub>1.8</sub> Se		a=5.765	[Heyding and Murray, 1976]
Cu <sub>2</sub> Se (210 °C)		a=5.854	01-071-4323 [Oliveria <i>et al.</i> , 1988]
Cu <sub>2</sub> Se (360 °C)		a=5.871	03-065-6556 [Oliveria <i>et al.</i> , 1988]
In	(I4/mmm)	a = 3.2512 c = 4.9467	00-005-0642 [Smith and Schneider, 1964]
In <sub>4</sub> Se <sub>3</sub>	58	a=15.297 b=12.308 c=4.081	00-051-0808 [Hogg <i>et al.</i> , 1973]
InSe (RT)	(P63/mmc) 194	a=b=4.0050 c=16.6400	034-1431 [Popović <i>et al.</i> , 1979]
GaSe (RT)		a=b=3.755 c=15.94	[Jellinek and Hahn, 1961]
Mo	229	a=b=c=3.1472 c=12.9250	00-042-1120 [Swanson and Tatge, 1953]
Se	152	a=b=4.3662 c=4.9536	00-006-0362 [Swanson, 1954]

**Table E.3.:** Thermal expansion coefficients  $\alpha$ , \*1: expected value from correlation with empirical pseudopotential determined from atomic spectra.  $\alpha_L(\text{Cu}_9\text{In}_4)$  is calculated by the lattice difference between RT from [Che and Ellner, 1992] and 650 °C from [Hume-Rothery *et al.*, 1951]. The values for  $\gamma_1\text{-Cu}_9\text{Ga}_4$  and  $\gamma\text{-Cu}_9\text{Ga}_4$  are calculated from Fig. 3 in [Predel, 1994], which are originally from [Pearson, 2013].

Compound	Temperature range (K)	Thermal expansion coefficient $\alpha$	Reference
$\text{Cu}_{16}\text{In}_9$	-	-	-
$\gamma_1\text{Cu}_9\text{Ga}_4$	300 to 780 K	$16.0 \cdot 10^{-6} K^{-1}$	s. caption
$\gamma\text{Cu}_9\text{Ga}_4$	780 to 980 K	$26.7 \cdot 10^{-6} K^{-1}$	s. caption
$\text{Cu}_9\text{In}_4$	RT to 923 K	$27.05 \cdot 10^{-6} K^{-1}$	s. caption
$\text{Cu}_9(\text{In,Ga})_4$	460 to 820 K	$30.2 \cdot 10^{-6} K^{-1}$	[Mainz, 2008]
$\text{CuGaSe}_2$	300 to 958 K	$\alpha_a=1.28 \cdot 10^{-6} K^{-1}$	[Kistaiah and Murthy, 1985]
$\text{CuGaSe}_2$	300 to 958 K	$\alpha_c=4.18 \cdot 10^{-6} K^{-1}$	[Kistaiah and Murthy, 1985]
$\text{CuInSe}_2$	300 to 573 K	$\alpha_a=11.0 \cdot 10^{-6} K^{-1}$	[Brühl <i>et al.</i> , 1981]
$\text{CuInSe}_2$	300 to 573 K	$\alpha_c=8.4 \cdot 10^{-6} K^{-1}$	[Brühl <i>et al.</i> , 1981]
$\text{CuGa}_3\text{Se}_5$	RT	$\alpha_a=7.7 \cdot 10^{-6} K^{-1}$	[Orlova <i>et al.</i> , 2002]
$\text{CuGa}_3\text{Se}_5$	RT	$\alpha_c=5.6 \cdot 10^{-6} K^{-1}$	[Orlova <i>et al.</i> , 2002]
$\text{CuIn}_3\text{Se}_5$	RT	$\alpha_a=10.4 \cdot 10^{-6} K^{-1}$	[Orlova <i>et al.</i> , 2002]
$\text{CuIn}_3\text{Se}_5$	RT	$\alpha_c=6.0 \cdot 10^{-6} K^{-1}$	[Orlova <i>et al.</i> , 2002]
$\text{Cu}_{1.72-1.86}\text{Se}$		$2.24 \cdot 10^{-5} K^{-1}$	[Tonejc <i>et al.</i> , 1975]
$\text{Cu}_{1.96}\text{Se}$		$2.20 \cdot 10^{-5} K^{-1}$	[Ogorelec and Čelustka, 1966]
$\text{GaSe}$	at 400+ K	$\alpha_a=9.5 \cdot 10^{-6} K^{-1}$	[Aliev <i>et al.</i> , 1972]
$\text{GaSe}$	at 400+ K	$\alpha_c=11.3 \cdot 10^{-6} K^{-1}$	[Aliev <i>et al.</i> , 1972]
$\text{In}$		$32 \cdot 10^{-6} K^{-1}$	*1 from Fig. 5 in [Gambino and Seiden, 1970]
$\text{In}_4\text{Se}_3$	300 K	$2.1 \cdot 10^{-6} K^{-1}$	[Logvinenko <i>et al.</i> , 1975]
$\text{InSe}$	at 400+ K	$\alpha_a=16.5 \cdot 10^{-6} K^{-1}$	[Aliev <i>et al.</i> , 1973]
$\text{InSe}$	at 400+ K	$\alpha_c=12.9 \cdot 10^{-6} K^{-1}$	[Aliev <i>et al.</i> , 1973]
$\text{Mo}$	at 853 K	$5.6 \cdot 10^{-6} K^{-1}$	from Fig. 2 in [White and Andrikidis, 1996]
$\text{Se}$	-	$36 \cdot 10^{-6} K^{-1}$	*1 from Fig. 5 in [Gambino and Seiden, 1970]

# List of Symbols and Abbreviations

## Symbols

$a_i$	standard atomic weight for element i
$h$	Planck constant
$\nu$	Photon frequency
$N_A$	Avogadro constant
$\sigma_A$	total atomic cross-section

## Abbreviations

ALD	atomic layer deposition
AFM	atomic force microscope
BESSY	<b>B</b> erlin <b>E</b> lectron <b>S</b> torage Ring Society for <b>S</b> ynchrotron Radiation
CBD	chemical bath deposition
CGI	or CuIII is the Cu to element III ratio: $[\text{Cu}]/([\text{In}]+[\text{Ga}])$
CIGS	$\text{Cu}(\text{In}_{1-x}\text{Ga}_x)\text{Se}_2$
$\text{C}(\text{IG})_3\text{S}_5$	$\text{Cu}(\text{In}_{1-x}\text{Ga}_x)_3\text{Se}_5$
<u>CIGS</u>	CIGS phase with a GGI above 0.35
CIGS	CIGS phase with a GGI between 0.25 and 0.35
<u>CIGS</u>	CIGS phase with a GGI between 0.1 and 0.25
CIS	CIGS phase with a GGI below 0.1
$D_{\text{absorber}}$	thickness of absorber
DTA	differential thermal analysis
EDDI	experimental station at BESSY II for <b>E</b> nergy <b>D</b> ispersive <b>D</b> iffraction
EDX	energy dispersive X-ray analysis
EDXRD	energy dispersive X-ray diffraction analysis
EDXRF	energy dispersive X-ray fluorescence analysis
$E_g$	band gap energy
EQE	external quantum efficiency
Esc	escape peak
FF	fill factor
GGI	or GaIII is the Ga to In ratio: $[\text{Ga}]/([\text{Ga}]+[\text{In}])$

GDOES	glow-discharge optical emission spectroscopy
HZB	Helmholtz Zentrum Berlin
ICDD	International Centre for Diffraction Data
$N_i$	general-area-density
ODC	ordered defect compound
OVC	ordered vacancy compound
PV	photovoltaics
PVD	physical vapor deposition
RMS	root mean square
$\rho_{absorber}$	density of absorber
RT	room temperature
RTA	rapid thermal annealing
RTP	rapid thermal processing
SEM	scanning electron microscopy
SRH	Shockley Read Hall recombination
TEM	transmission electron microscopy
$T_{max}$	maximum temperature during annealing
$T_{Se}$	Se source temperature
$T_{sub}$	substrate temperature
$V_{oc}$	open circuit voltage
$w_i$	weight percentage
$x_i$	atomic percentage
XRD	X-ray diffraction analysis
XRF	X-ray fluorescence analysis
WDXRF	wavelength dispersive X-ray fluorescence analysis

# Publications

## Peer-reviewed publications

### In the framework of this thesis

Bäcker, J.-P., Schmidt, S. S., Rodriguez-Alvarez, H., Wolf, C., Kaufmann, C. A., Hartig, M., Mainz, R., and Schlatmann, R. (2017). Lateral phase separation in Cu-In-Ga precursor and Cu(In,Ga)Se<sub>2</sub> absorber thin films. SOL ENERG MAT SOL C , 162:120-126.

Schmidt, S. S., Wolf, C., Rodriguez-Alvarez, H., Bäcker, J.-P., Kaufmann, C. A., Merdes, S., Ziem, F., Hartig, M., Cinque, S., Dorbandt, I., Köble, C., Abou-Ras, D., Mainz, R., and Schlatmann, R. (2017). Adjusting the Ga grading during fast atmospheric processing of Cu(In,Ga)Se<sub>2</sub> solar cell absorber layers using elemental selenium vapor. Prog. Photovolt.: Res. Appl. , 25(5):341-357.

### Not in the framework of this thesis

Stange, H., Brunken, S., Greiner, D., Marc Daniel Heinemann and, D. A. B. Y., Wägele, L. A., Schmidt, S. S., Bäcker, J.-P., Kaufmann, C. A., Klaus, M., Scheer, R., Genzel, C., and Mainz, R. (2018). Stacking fault energy as driving force for grain growth in CuInSe<sub>2</sub>. Phys. Rev. Applied.

Stange, H., Brunken, S., Greiner, D., Heinemann, M.-D., Kaufmann, C. A., Schmidt, S. S., Bäcker, J.-P., Klaus, M., Genzel, C., and Mainz, R. (2016). Diffusion-induced grain boundary migration as mechanism for grain growth and defect annihilation in chalcopyrite thin films. Acta Materialia , 111:377 - 384.

Morherr, A., Witt, S., Chernenkaya, A., Bäcker, J.-P., Schönhense, G., Bolte, M., and Krellner, C. (2016). Crystal growth of new charge-transfer salts based on  $\pi$ -conjugated donor molecules . Physica B: Condensed Matter , 496:98 - 105.

## Conference contributions as first author

Bäcker, J.-P., Schmidt, S.S., Rodriguez-Alvarez, H., Hartig, M., Kaufmann, C.A., Mainz, R., Wolf, C., Schlatmann, R. (2016). Phase separation in Cu-In-Ga precursor and Cu(In,Ga)Se<sub>2</sub> absorber thin films: Influences and reversibility. 7<sup>th</sup> International Workshop on CIGS Solar Cell Technology, Munich, conference poster.

Bäcker, J.-P., Rodriguez-Alvarez, H., Hartig, M., Kaufmann, C.A., Kavalakkatt, J., Lips, K., Mainz, R., Merdes, S., Schmidt, S.S., Wolf, C., Schlatmann, R. (2015). Kinetics of phase separation & coarsening in Cu-In-Ga precursor thin films for sequentially processed Cu(In,Ga)Se<sub>2</sub> solar cells. PVSEC-25, Busan, conference talk, honored with Paper Award.

Bäcker, J.-P., Rodriguez-Alvarez, H., Hartig, M., Kaufmann, C.A., Mainz, R., Merdes, S., Schmidt, S.S., Wolf, C., Ziem, F. and Schlatmann, R. (2015). Phase separation and the role of sodium during annealing and selenization of Cu-In-Ga precursors for sequentially processed Cu(In,Ga)Se<sub>2</sub> thin film solar cells. Solar Future Symposium, KAUST, Saudi-Arabia, conference poster.

Bäcker, J.-P., Rodriguez-Alvarez, H., Hartig, M., Kaufmann, C. A., Lips, K., Mainz, R., Merdes, S., Schmidt, S.S., Wolf, C., Ziem, F., Schlatmann, R. (2015). Kinetics of phase separation and coarsening in Cu-In-Ga precursor thin films for sequentially processed Cu(In,Ga)Se<sub>2</sub> solar cells, 6<sup>th</sup> International Workshop on CIGS Solar Cell Technology, Berlin, conference poster.

Bäcker, J.-P., Rodriguez-Alvarez, H., Wolf, C., Hartig, M., Merdes, S., Ziem, F., Kavalakkatt, J., Kaufmann, C.A., Schmidt, S.S., Mainz, R., Schlatmann, R. (2015). Kinetics of phase separation and coarsening in Cu-In-Ga precursor thin films for sequentially processed Cu(In,Ga)Se<sub>2</sub> solar cells, DPG Frühjahrstagung, Berlin, conference talk.

# Danksagung

An dieser Stelle möchte ich mich ganz herzlich bei allen bedanken, die mich bei meiner Promotionsarbeit unterstützt haben. Während meiner Zeit am HZB habe ich so viele tolle Leute kennengelernt, von denen ich zumindest einige erwähnen möchte.

Ich bedanke mich bei Prof. Klaus Lips und Prof. Rutger Schlatmann für die Möglichkeit und die Betreuung dieser Arbeit am HZB. Vielen Dank an Prof. Klaus Lips für die super QUANTSOL. Außerdem danke ich Prof. Schlatmann für die Finanzierung der Konferenzbesuche. Vielen Dank auch für die weitere Betreuung durch Dr. Sebastian Schmidt, Dr. Christian Kaufmann, Dr. Reiner Klenk und Dr. Roland Mainz.

Vielen dann für die finanzielle Unterstützung dieser Arbeit durch das Bundesministerium für Bildung und Forschung (BMBF) im Rahmen des ACCESS-CIGS Projektes (grant no. 0325903A) sowie des NeuMaS Projektes (Grant no. 13N11768) und der Landesregierung Berlin (SENBUF) im Rahmen des Programms für Spitzenforschung und Innovation in den Neuen Ländern (grant no. 03IS2151).

Sebastian und Reiner danke ich außerdem für die geduldige Hilfe, mich schriftlich besser auszudrücken.

Christian Kaufmann und Marc Heinemann danke ich für die super Zeit in Süd Korea.

Der Aufbau und Betrieb des RTP3 ging schon zu Beginn flott voran dank der technischen Hilfe von Anja Scheu und Sonja Cinque.

Auch Humberto Rodriguez-Alvarez danke ich für die anfängliche Einarbeitung und Hilfe beim Aufbau des Ofens.

Ich danke der ganzen CIGS Arbeitsgruppe sowie überhaupt allen am PVcomB, sei es für sehr gutes Arbeitsklima und Zusammenarbeit, Substratreinigung, Schichtabscheidungen, Kabel, Kuchen und vieles mehr.

Christoph Genzel und seiner Arbeitsgruppe danke ich für die tolle Unterstützung an EDDI. Die Auswertung der vielen Strahlzeitdaten und XRF-Berechnungen war nur dank der Programme von Roland Mainz so schnell möglich.

Frau Klimm danke ich für die Unterstützung mit REM Aufnahmen und Daniel Abou-Ras für Aufrechterhaltung eines funktionstüchtigen REMs an dem ich viele Messungen machen konnte.

Danke Manuel Hartig für die super Tipps und Hilfe bei Fahrradreparaturen.

Für die gemeinsame Zeit und vielen Diskussionen danke ich auch dem ganzen Doktorandenteam (u.a. Darja Erfurt, Stefan Körner, Tim Kodalle, Natalie Preissler, ...).

Paul, ich freue mich riesig, dass wir beim PhD-Retreat 2014 aneinander geraten sind und so eine tolle Freundschaft entstanden ist. Dank dir habe ich mich gleich viel wohler gefühlt in Berlin und schnell Anschluss gefunden. Die Zeit mit dir und mit Martin Liebhaber war fantastisch.

Von ganzem Herzen danke ich den beiden wichtigsten Frauen in meinem Leben, meiner Mutter Christine und meinem größten Schatz Jule. Auf zu neuen Abenteuern mein Schatz! Ebenso danke ich auch Jules ganzer Verwandtschaft, die mir sehr ans Herz gewachsen ist.

# Curriculum Vitae

The curriculum vitae is not included in the online version for data protection reasons.



# Selbständigkeitserklärung

Ich versichere hiermit, dass ich diese Arbeit selbstständig verfasst, alle benutzten Hilfsmittel angegeben, alle Stellen sowie alle Elemente, die zitiert oder dem Sinn nach aus anderen Werken entnommen sind mit Quellenangaben kenntlich gemacht habe. Außerdem versichere ich, dass diese Arbeit nicht schon einmal in einem früheren Promotionsverfahren angenommen oder als ungenügend beurteilt worden ist.

Berlin, den

.....

(JAN-PETER BÄCKER)